

TECHNICAL REPORT

# SPB/SFX Instrument Review Report

March 2022

*Adam R. Round and*

*Adrian P. Mancuso*

*on behalf of the SPB/SFX group*

*at European XFEL*

European X-Ray Free-Electron Laser Facility GmbH

Holzknappel 4

22869 Schenefeld

Germany





---

# Authorship contributions and acknowledgments

We would like to acknowledge, thank, and highlight the written contributions to this document from:

**Richard J. Bean, Valerio Bellucci, Johan Bielecki, Sarlota Birnsteinova, Fabio Dall'Antonia, Ibrahim Dawod, Raphael de Wijn, Thomas Dietze, Katerina Dörner, Juncheng E, Susanne Fangohr, Luca Gelisio, Gabriele Giovanetti, Huijong Han, Sravya Kantamneni, Chan Kim, Yoonhee Kim, Henry J. Kirkwood, Jayanath Koliyadu, Faisal H. M. Koua, Ruslan Kurta, Romain Letrun, Luis Lopez, Bradley Manning, Diogo Melo, Ladislav Mikeš, Grant Mills, Jaydeep Patel, Abhisakh Sarma, Tokushi Sato, Joachim Schulz, Marcin Sikorski, Nadja Reimers, Mattia Ronch, Cedric M. Signe Takem, Mohammad Vakili, Patrik Vagovič**

We also thank **Richard Neutze and the SFX User Consortium** for their ongoing contributions to the SPB/SFX instrument and its aims. We express thanks to the **European XFEL Management Board** for their feedback and guidance during the production of this report.

In addition, we would like to thank the **European XFEL support groups** for their contributions to the SPB/SFX instrument and the European XFEL, as well as the research outputs herein:

- Data Analysis
- Detector Development, Calibration
- DAQ and Controls
- Electronic and Electrical Engineering
- IT and Data Management
- Mechanical Engineering
- Optical Lasers
- Project Management Office
- Sample Environment and Characterisation
- Technical Services
- Undulator Systems
- Vacuum
- X-Ray Operations
- X-Ray Optics and Beam Transport
- X-Ray Photon Diagnostics

Finally all SPB/SFX staff, past and present, are thanked for their extreme dedication and professionalism. Without you, none of this exciting science would be possible.



---

# Contents

<b>1</b>	<b>Executive summary</b>	<b>5</b>
1.1	Context	5
1.1.1	Scope	6
1.1.2	Charge to the Committee	8
1.1.3	SFX User Consortium	10
1.1.4	Institutions contributing to the SFX User Consortium	10
1.1.5	Future opportunities	11
<b>2</b>	<b>Science and capability highlights from early operation</b>	<b>13</b>
2.1	High repetition rate serial femtosecond crystallography: A route to high data rate SFX	13
2.2	High repetition rate single particle imaging (SPI) for structural studies of heterogeneous populations of nanoparticles	17
2.3	Small angle scattering at XFELs: Results and opportunities	21
2.4	MHz repetition rate microscopy: Pilot experiment	21
2.5	Today's capabilities	23
<b>3</b>	<b>Instrumentation in operation</b>	<b>25</b>
3.1	Brief overview	25
3.2	Sample delivery methods	28
3.2.1	Liquid samples	28
3.2.1.1	Microfluidic device fabrication	29
3.2.1.2	High-viscosity extruders	31
3.2.2	Aerosols	31
3.2.3	Solid samples	32
3.3	Detectors in operation	32
3.3.1	AGIPD 1Mpix	33
3.3.1.1	General description	33
3.3.1.2	Detector calibration and commissioning	34
3.3.1.3	Baseline shift	35
3.3.1.4	"Snowy pixels"	35
3.3.2	Jungfrau 4M	38
3.3.2.1	General description	38
3.3.2.2	Commissioning, calibration, and maintenance	39
3.3.2.3	Status of the front-end modules	40
3.3.2.4	Multi memory cell operation	41
3.3.2.5	Upgrade of the detector's infrastructure	41

3.3.3	Coming detectors .....	42
3.4	Data analysis tools for SFX, SPI, and other purposes .....	43
3.4.1	Online analysis.....	44
3.4.2	Offline analysis.....	45
3.4.3	Extension to “non-standard” use-cases .....	48
<b>4</b>	<b>Future developments .....</b>	<b>49</b>
4.1	Overview vision .....	49
4.2	High repetition rate time-resolved SFX .....	50
4.3	LCP and fixed-target SFX (toward high repetition rate serial crystallography of viscous or fixed samples) .....	51
4.3.1	Sample-efficient methods are required.....	51
4.3.2	Path to automation .....	52
4.3.3	MHz SFX from “slow” samples .....	53
4.3.3.1	Beam sweeping concept.....	53
4.3.3.2	Route to implementation.....	54
4.4	XFEL single particle imaging.....	55
4.5	MHz X-ray microscopy: Route towards 3D information and hard X-ray acquisition .....	57
4.6	Form factor recovery from biological macromolecules in solution.....	59
4.7	FXS – Fluctuation X-ray scattering .....	60
<b>5</b>	<b>Retrospective: Metrics and the user community .....</b>	<b>63</b>
5.1	List of papers produced using beam.....	66
5.2	List of all papers from group by year.....	68
<b>6</b>	<b>SFX UC contributions and next steps.....</b>	<b>69</b>
<b>7</b>	<b>Conclusions and Outlook .....</b>	<b>73</b>
	<b>Appendices.....</b>	<b>79</b>
<b>A</b>	<b>Appendix: Requirements for future detector(s) .....</b>	<b>81</b>
A.1	Serial femtosecond crystallography and single particle imaging .....	81
A.2	Megahertz microscopy .....	83
A.2.1	CMOS cameras for indirect detectors.....	83
<b>B</b>	<b>Appendix: Selected publications elucidating scientific excellence .....</b>	<b>85</b>
B.1	User-driven publications.....	85
B.2	Staff-driven publications .....	136

---

# Executive summary

---

## Context

The Single Particles, Clusters, and Biomolecules & Serial Femtosecond Crystallography (SPB/SFX) instrument of the European XFEL is primarily concerned with three-dimensional diffractive imaging and structure determination of micrometre-scale and smaller objects at atomic or near-atomic resolution.

The SPB/SFX instrument has been in user operation since September 2017, one of the first two instruments to come online at the European XFEL. Active members of the SPB/SFX user community include scientists from all European XFEL member countries as well as from further afield, including the USA, China, and Australia. The research output metrics of the SPB/SFX instrument (primarily peer-reviewed research articles produced using European XFEL beam) are vastly above the European XFEL mean, with articles appearing in *Nature Methods*, *Nature Communications*, *Optica*, *IUCrJ*, and more.

The science scope at SPB/SFX places a particular emphasis on biological objects—including crystals of macromolecules and macromolecular complexes as well as viruses. More specifically, the SPB/SFX instrument aims to study structural *dynamics* in these biological systems on the millisecond to femtosecond timescale.

The SPB/SFX instrument is also capable of investigating non-biological samples using techniques similar to those described above. The investigation of material and other non-biological samples is now in increasing demand using scattering, diffraction, and imaging techniques. Recently, the SPB/SFX instrument has also been used for so-called “megahertz microscopy” to observe microscopic, stochastic processes on the sub-microsecond timescale using the natural time structure of the European XFEL.

Physically, the SPB/SFX instrument consists of two experiment endstations (upstream and downstream), based on the combined contributions of European XFEL and the SFX user consortium, contained in a single experiment hutch. In practice, five broad classes of experiment are performed at SPB/SFX (though a number of these utilize almost identical experimental configurations): 1) (time-resolved (TR)) serial crystallography from low viscosity, liquid jet injected samples, 2) TR small angle X-ray scattering (SAXS) of non-crystalline samples in low viscosity media, 3) TR-SFX of samples in high viscosity media, such as LCP, 4) single particle imaging of biological and inorganic samples using aerosol injection, and 5) megahertz microscopy of stochastic processes at micrometre length and sub-microsecond timescales. A key achievement of the SPB/SFX instrument group,

European XFEL supporting staff, and the SPB/SFX user community has been not only to successfully realize all these classes of experiment and collect data but also to successfully analyse this data and publish the results. Indeed, there are even analysis pipelines available for each of these classes of experiment (each in different levels of readiness and all with contributions or continuing contributions of the user community).

This document outlines the successful deployment of each of these methods, notes the opportunities and challenges for the immediate future, and describes opportunities for expansion and growth to meet the already high and growing community demand for each of these experiment classes.

## Scope

This document has been written in preparation for the instrument review of SPB/SFX scheduled for 15–16 March 2022. This will be the first instrument review conducted at European XFEL, as SPB/SFX was the first instrument (alongside FXE) to come online and perform user experiments at the European XFEL in September 2017. Since then, 36 experiments (as of December 2021) have been performed (of which 17 SFX and 4 SPI experiments used the standardized configurations). Fig. 1.1 shows a comparison of the number of finished experiments at SPB/SFX to those carried out at other instruments at the European XFEL. A total of 19 user-driven experiments have been published (so far) and more are in various stages of preparation. Of these 19 published articles, all present data collected using MHz repetition rates; 11 are SFX, 3 are SPI, and 5 present time-resolved data.

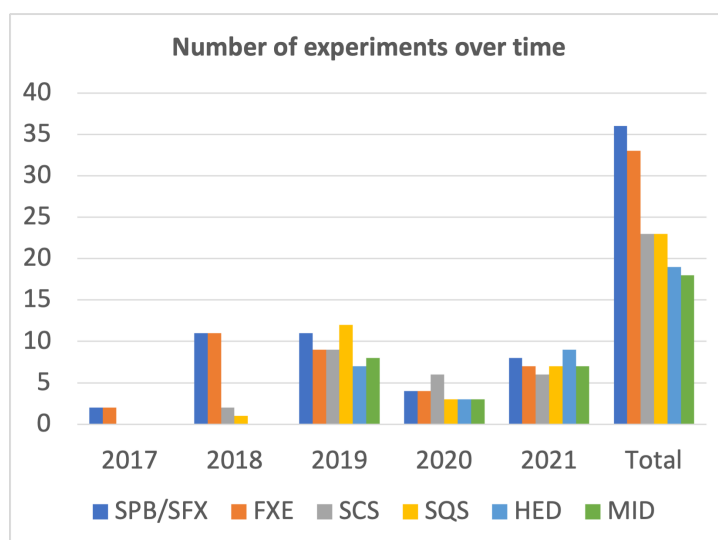


**Figure 1.1:** Number of experiments carried out at each of the six instruments between 2017 and 2021

This document looks back at what has been delivered by SPB/SFX in the past four and a half years and looks forward to a number of opportunities that this work at SPB/SFX has opened up for future scientific directions at European XFEL—most of which are wholly unique to this high repetition



rate and hard X-ray facility. Specific (though not yet detailed) examples of future directions will be presented that take into account these unique, future opportunities as well as exploiting the lessons learned from preliminary experiments already done at SPB/SFX.

The document is organized into a number of chapters mainly addressing issues of science scope, instrumentation capability, and future opportunities. Note that the future opportunities identified address both structural biology, the core remit of much of the SPB/SFX instrument, as well as subjects significantly beyond this field of science. Indeed, the high repetition rate of the European XFEL has opened up the possibility for both megahertz microscopy of fast, stochastic processes as well as the study of the three-dimensional structure of heterogeneous populations of material nanoparticles—both novel applications of a high repetition rate XFEL to materials science.

For convenience, the “Charge to the Committee” is reproduced below. Note that some aspects that are often part of instrument reviews in general, such as staff loading and graduate student planning, are out of scope for this first instrument review and are thus not comprehensively documented here. These topics may be addressed in discussion at the review meeting.

## Charge to the Committee

The six currently operating instruments were opened to user operation between summer 2017 and summer 2019, and will be reviewed in the period March 2022 — September 2023, after roughly five years of operation. All six instruments are teeming with scientific ambition. Each was planned to fulfil a broad variety of needs and requirements of a number of user communities, due to the global constraint of having only six instruments in the startup phase of the facility. The present instruments were intended to explore a large scientific space and volume that, by necessity, led to complex and demanding setups often requiring well-staffed and mature user groups to make effective use of beamtime. The experience of four years of operation shows that we are now ready to define more specialized setups and instruments that will allow for efficient studies in specific scientific and application areas.

The main goals of the instrument reviews are:

- 1 Assess past performance of the instrument and areas for improvement. Receive constructive feedback from:
  - Leaders in XFEL science and instrumentation to keep the instruments at a world-leading level
  - Science community—even beyond XFEL science—to provide broader perspectives
- 2 Receive advice on important future science directions. Your recommendation will be a precious aid in steering the scientific vision of the instrument for the next decade and will contribute to develop a foundation (and justification) for the strategic elements under consideration for the facility.

Your report shall detail responses to the questions below and, in addition, must include a summary of recommendations.

- Please summarize your recommendations in up to 10 short statements.
  - Please include specific recommendations given the perspective of future facility development plans.
- 1 Research by users and staff
    - Which experiments/results would you rank as outstanding?
    - How do you judge the quality of the major part of the experiments done?
    - Has the suite of experiments performed to date efficiently exploited the unique capabilities of this European XFEL instrument?
    - Should we concentrate activities and resources on specific scientific fields (differently to the present distribution of experiments)? If so, which?
    - Are there potential users or communities which have not yet been active?

## 2 Future scientific directions

- Do the short- and long-term research directions of the instrument address the key needs of users and the broader community?
- Are there outstanding areas that may require more emphasis or effort?

## 3 Technical status of the instrument

- Could you evaluate the technical status of the instrument?
- How do you judge technical developments initiated by the staff? Where do you see needs for improvement or additional development?
- Are the capabilities and components at the instrument sufficiently user-friendly?
- Do you see areas where more effort or even further development by expert (e.g. laser, optics, detectors, data, sample environment) groups is needed to improve quality, efficiency, or productivity?
- Please provide your evaluation of the instrument in the context of (international) competitors, both in terms of scope and performance.

## 4 Future technical developments

- Where do you see long-term needs for technical/capability developments?
- Would you recommend major refurbishment? If so, on which timescale?
- Are there areas where you would recommend a more detailed evaluation by experts in instrumentation?
- Do you see potential for development of common proposals with other X-ray facilities and/or different investigation techniques (n, e, otherwise)?

## SFX User Consortium

The SPB/SFX instrument is supported by a partnership between the European XFEL and the Serial Femtosecond Crystallography User Consortium (SFX UC). The SFX UC is a consortium of partners from the user community collaborating together to provide additional instrumentation, personnel, and expertise in serial crystallography for European XFEL. Indeed, the instrument was originally termed the SPB instrument, with its name later changed to “SPB/SFX” as an acknowledgment of the substantial contributions of the SFX UC.

Serial crystallography has become one of the leading applications of X-ray FELs, since it allows structure determination from samples too small for conventional analysis, avoids radiation damage, provides higher-quality data than achievable otherwise, and allows time-resolved measurements over timescales spanning 12 orders of magnitude. The popularity of the technique places demands on the availability of instrumentation and beamtime. Additionally, micro- or nano-crystals of macromolecules cannot easily be characterised to determine their suitability for serial crystallography with FEL pulses, other than measuring diffraction with FEL pulses. That is, there is a great need for sample screening where data may be collected in a minute or less per sample or sample condition, in combination with measurements of full datasets.

The SFX UC was thus formed with the goal of providing instrumentation for high-throughput serial femtosecond crystallography and related measurements. By refocusing the spent beam passing through the hole in the detector of the upstream region of the SPB/SFX instrument to a second downstream sample chamber, it would be possible to run two experiments at once. The efficient application of this idea requires a high level of automation and reliability, which needs dedicated, purpose-built instrumentation. Furthermore, for many macromolecular crystals, a diffraction camera consisting of a detector with about 2000 x 2000 pixels is required. The UC has already provided optics and components to refocus the beam, a measurement station with liquid-jet sample delivery, associated diagnostics, elements of a DAQ system, a pump laser system, and infrastructure modifications and additions to support the instrument. Outstanding is a suitable diffraction detector, in this case the larger 4 Mpx version of the AGIPD (1 Mpx version of which is already in use at SPB/SFX). Although the delivery of the AGIPD-4Mpx detector has been delayed, an external review and evaluation of the project was conducted and gives some confidence of improved design and reliability in operation once completed.

## Institutions contributing to the SFX User Consortium

- Centre for Free-Electron Laser Science, DESY, Hamburg, Germany
- Arizona State University, Tempe, Arizona, USA
- Diamond Light Source, Oxfordshire, UK
- Karolinska Institute, Solna, Sweden

- La Trobe University, Melbourne, Australia
- Lund University, Lund, Sweden
- Max Planck Institute for Medical Research, Heidelberg, Germany
- Medical Research Council, Laboratory of Molecular Biology, Cambridge, UK
- Paul Scherrer Institute, Villigen, Switzerland
- Slovak Academy of Sciences, Bratislava, Slovakia
- Stockholm University, Stockholm, Sweden
- University of Gothenburg, Gothenburg, Sweden
- University of Hamburg, Hamburg, Germany
- University of Lübeck, Lübeck, Germany
- University of St Andrews, St Andrews, UK
- Uppsala University, Uppsala, Sweden

## Future opportunities

At present, the SPB/SFX instrument serves a variety of science cases and communities across both the life sciences and the physical sciences. Most prominently, this includes structural biology, especially time-resolved structural biology, although time-resolved studies of material behaviour, synthesis, response to external forces, and stochastic processes are expected to become more and more prevalent. Figure 1.2 shows use cases that could benefit from dedicated instrumentation in the future, not only to alleviate over-subscription at SPB/SFX but to provide for more streamlined and efficient use of beamtime by users as well. Later in this document, we will explore more fully the possibilities to better exploit these opportunities in more efficient and effective ways in the future.

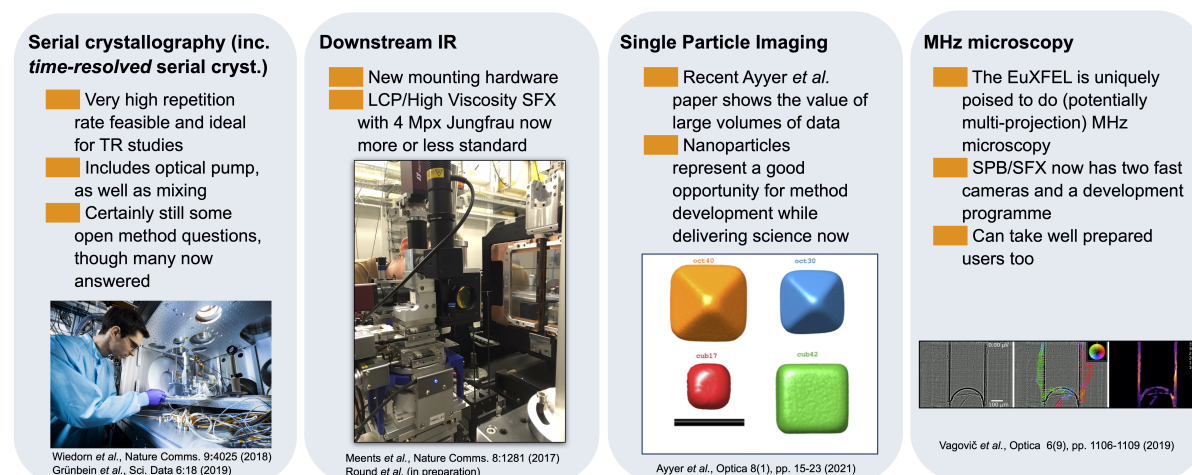


**Figure 1.2:** Possible suite of future, more specialized instrumentation to capitalize on the science presently performed at SPB/SFX



---

# Science and capability highlights from early operation

This chapter summarizes a selection of published science highlights from early operation at SPB/SFX. Some of the yet-to-be-published (and perhaps even more exciting) results are likely to be presented during the review meeting. At the time of writing, there are a number of finalized results that have been, or will soon be, submitted to various journals. For the readers' convenience, a limited selection of (open access) papers are reproduced in Appendix B. A list of published articles with beam is documented in Chapter 5. Early operation has, by necessity, predominantly focused on validating the capabilities of the instrument and extending the scope of existing modalities that can be achieved at the instrument. As such, there has been a visible bias towards methods and instrumentation in the highlights published to date. Nevertheless, interesting science questions have already been answered and more are, at the time of writing, being prepared for publication. In addition to the work of SPB/SFX users, the life science research of the SPB/SFX group is expanding and taking advantage of the defined standard configurations of the instrument, some examples of which are included in Appendix ???. Additionally, single particle imaging and megahertz microscopy for materials science becomes much more prevalent and very much capable of application.

---

## High repetition rate serial femtosecond crystallography: A route to high data rate SFX

One of the primary science drivers of the SPB/ SFX instrument is high repetition rate SFX [2]. The combination of a high repetition rate X-ray source and a high repetition rate capable detector (AGIPD) offers the possibility to collect SFX datasets within a matter of minutes. The unique train–pulse structure of the European XFEL presents opportunities, questions, and challenges for the SFX experimental process, from sample delivery to structural analysis.

The currently highest achievable data rate for SFX experiments at SPB/SFX is 30 times that of LCLS (3520 diffraction images per second vs. 120). The MHz intra-train pulse structure, however, represents a nearly four orders of magnitude increase in the X-ray pulse rate. One of the significant questions regarding a MHz data collection scheme was whether the increase in the X-ray pulse rate would have an effect on the subsequent analysis and data quality.

A series of early experiments and subsequent publications seek to address this question under conditions moving towards the current instrument performance, increasing from Beryllium compound refractive lens focusing of 15 [55] and later 50 pulses per train [17] to KB mirror focusing of 120 pulses per train [57]. A typical experimental setup for SFX experiments is shown in Fig. 2.1. The primary

concern was that the environment of the sample, or the sample itself, could be affected by previous pulses in a train—either by direct interaction with the X-ray beam or by the effect of the X-ray beam on the sample carrying jet. These investigations looked for correlations between pulse position in the train and various data metrics and found that there was no measurable difference in diffraction data or recovered structure quality with a MHz rate pulse delivery scheme.

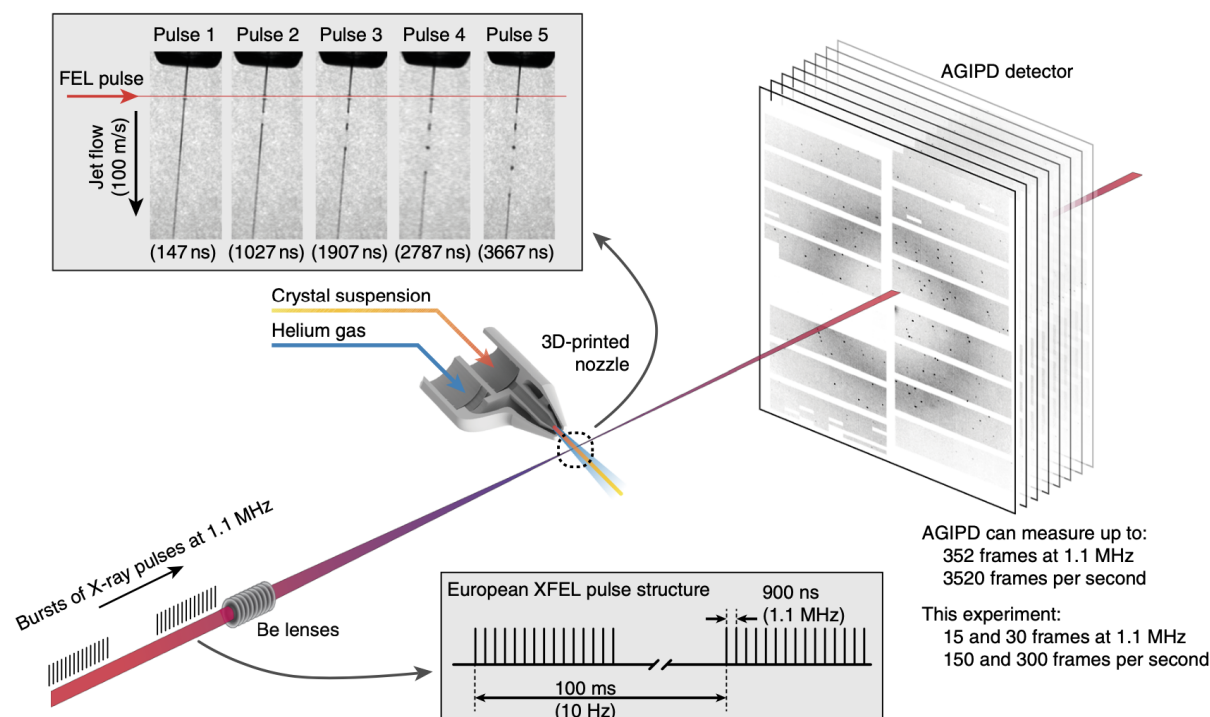


**Figure 2.1:** *Main:* Setup for early MHz SFX experiments with Be lenses producing a  $\approx 15$  micron focus. *Insert:* Jet imaged with fs laser after sequential X-ray pulses showing jet recovery has been shown to be possible in between pulses at up to 1.1 MHz (although the maximum facility and detector repetition rate is 4.5 MHz). Figure adapted from [55].

Wiedorn et al. [55] demonstrated that hit rate, indexing rate, and individual diffraction pattern resolution are unaffected by pulse position within the train (see Fig. 2.2), that the  $CC^*$  (data metric useful for comparing data and model quality) is similar for merged data split according to pulse ID, and that the correlation between merged data from the first and subsequent pulses is consistent.

With similar experimental conditions, Grünbein et al. [17] demonstrated that anomalous sulphur signal could be observed. In addition, the lengths of disulphide bonds, as a sensitive marker of radiation damage in lysozyme crystals, were compared from the first and later pulses in a train. No differences beyond experimental uncertainty were found.

With up to 120 pulses per train and a smaller focus of  $\approx 3$  microns, Yefanov et al. [57] compared hit rate probabilities and solved structures for each pulse of the train independently. A number of important conclusions for MHz rate serial crystallography were presented by Yefanov. These are consistent with,



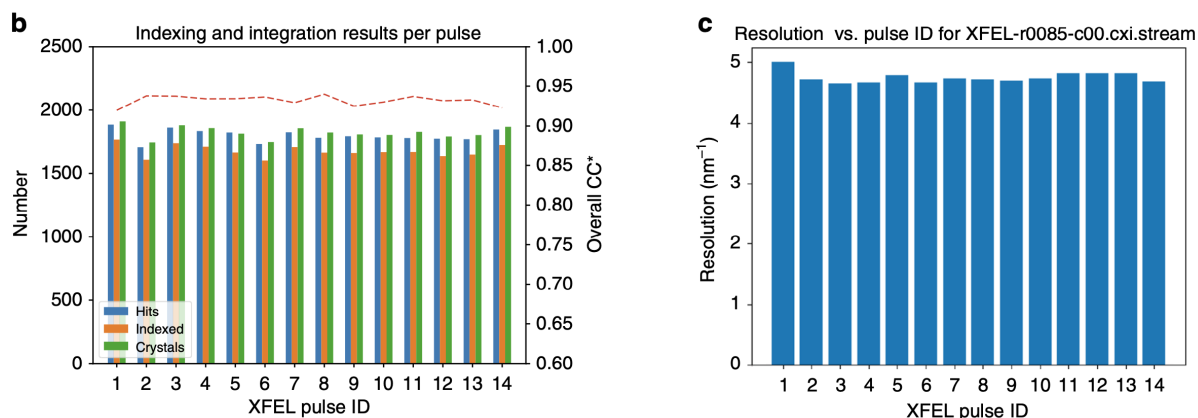


**Figure 2.2:** *Left:* Hit rate and “indexable” hit rate are consistent across pulse trains with no degradation in quality (CC\*). *Right:* CrystFEL resolution estimate as a function of pulse shows no decrease in estimated resolution. Figure adapted from [55].

and firmer than, those of both Wiedorn and Grünbein. They have also been further confirmed by subsequent experiments at the SPB/SFX instrument and highlighted in the resulting publications.

Those conclusions are re-formulated here:

- The structures generated from each ordinal pulse in a train show no significant differences from each other to 1.7 Å resolution (detector geometry / wavelength limited).
- Since the structures determined from each pulse are essentially identical, it is possible to merge data from all pulses in the pulse train into one dataset without having to account for changes due to the MHz repetition rate.
- It is therefore feasible to improve data quality by averaging over all pulses for large datasets, for time-resolved experiments, or for experiments using small or weakly diffracting crystals.
- Individual datasets with sufficient data for a molecular replacement structure determination can be completed significantly more quickly than at other sources (in a matter of minutes for a well-behaved experiment).

A MHz collection scheme does add important additional constraints to the sample delivery scheme. Liquid jets are often locally destroyed by interaction with the X-ray pulse. A jet must then re-establish in time to deliver a crystal to the interaction point for the next X-ray pulse. A given crystal (or section of jet) also must not have been exposed to X-rays from the tails of previous pulses. This results in a jet-speed requirement that is dependent on the time gap between X-ray pulses. For the commonly used 1.1 MHz rate, a jet speed of above  $\approx 50 \text{ ms}^{-1}$  is required [17; 55].

The continuous monitoring of jet behaviour is an important diagnostic for high repetition rate SFX experiments that has been implemented as a standard at SPB/SFX. The jet is imaged via either ns or fs optical laser pulses (depending on any additional optical pumping scheme required). Adjusting the

timing to compare images of the jet from adjacent X-ray pulses gives immediate feedback regarding jet re-formation (see Fig. 2.1). If the jet is not fast enough, either the jetting parameters can be adjusted to increase the jet speed or the X-ray pulse rate can be down-selected to increase the time gap between X-ray pulses. The European XFEL accelerator can now, at the switch of a button, alter its repetition rate to accommodate experimental needs. For SFX, this is predominantly between 1.1 MHz and 0.5 MHz.

Significant effort by colleagues from the Sample Environment and Characterisation (SEC) group is dedicated to the standardization of jets and delivery systems, especially via 3D printing of nozzles. This results in consistent liquid flow rate and gas parameters to achieve jets of reproducible size and speed as well as standardizing the day-to-day handling of these devices. This significantly decreases the barrier to fast nozzle and sample changes and reduces the change of instrument settings required from nozzle to nozzle. Further details are provided in Section 3.2.1.

A further consideration for the efficient completion of MHz SFX experiments is data handling and online experimental feedback. A number of user-developed software tools have been integrated at SPB/SFX, including OnDA [30]. A fraction of the online-corrected AGIPD data is output via the Karabo-bridge system (see Section 3.4). OnDA performs hit-finding on this data slice and displays live hit rate and recent hits. Taken together, this information can be used as a guide as to when sufficient data has been collected for a given sample or experimental condition.

Efforts are also ongoing in collaboration with colleagues from the Data Analysis and Controls groups to ease the flow of instrument metadata information to users. This information is also streamed via a Karabo bridge and can help the process of building an automated run log, or database, e.g. AMARCORD [32], and can help guide the experiment as well as spot instrument configuration issues quickly. Full information is always stored in the DAQ system for later in-depth analysis.

Early SFX experiments at SPB/SFX have laid the groundwork for successful execution of increasingly ambitious and complicated MHz rate SFX-based experiments. A dataset sufficient to reconstruct a high-quality structure can now be collected within a matter of minutes. This opens up the possibility to collect complex multi-dimensional datasets within reasonable experimental time, e.g. multiple time points for optically pumped systems and varied sample and substrate conditions in mix-and-inject experiments. Such experiments are now being performed successfully at SPB/SFX, described further in Section 4.2.

## High repetition rate single particle imaging (SPI) for structural studies of heterogeneous populations of nanoparticles

Structural determination of reproducible nano-particles without the need of forming crystals is one of the outstanding research avenues made possible by the extremely bright and short X-ray pulses from XFELs [35]. In contrast to the (now) more routine crystallography experiments, individual particles are delivered in a substrate-free fashion into the X-ray interaction region, usually as an aerosol with the help of an aerodynamic lens [28]. When an intense FEL pulse interacts with the particle, light is scattered in the forward direction, forming a diffraction pattern on the 2D photon detector, see Fig.2.3(a). This diffraction pattern corresponds to a (curved) slice through the 3D Fourier space of the particle. For large (>100 nm) particles, the signal level can be enough to perform a 2D reconstruction into real space of individual diffraction patterns, leading to images corresponding to projections of the particle density along the X-ray propagation direction. These images will have limited resolution. For smaller particles, the signal level is often too low to be successfully analysed in this manner. Instead, high-resolution reconstructions are made possible by the fact that the particles arrive into the X-ray interaction region with a random orientation. Thus, by collecting diffraction patterns on an ensemble of identical particles, one will eventually sample the full 3D Fourier space with enough signal to reconstruct the 3D structure of the particle as visualised in Fig. 2.3(b).

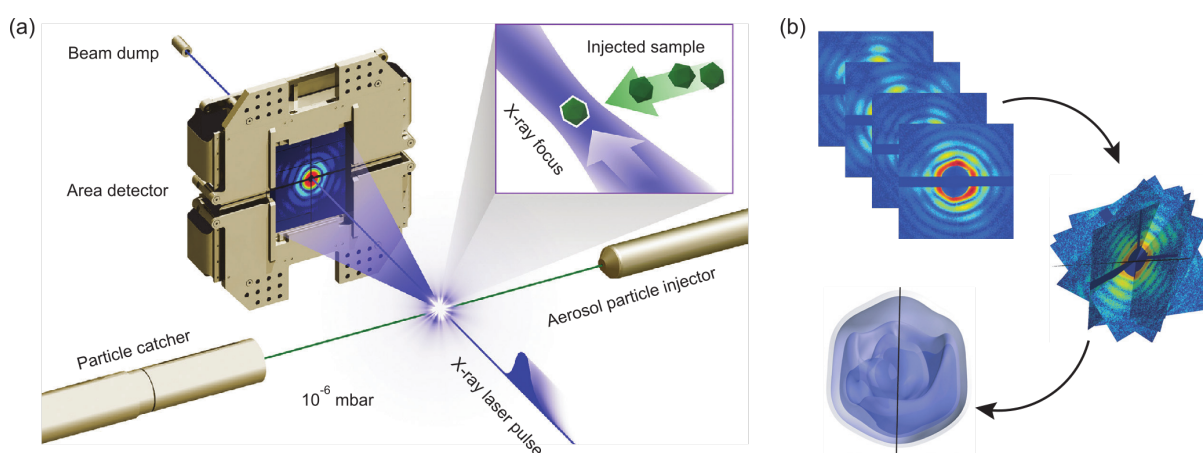


**Figure 2.3:** (a) Sketch of the setup for single particle imaging experiments. The aerosol injector delivers sample particles into vacuum, where they intersect with the X-ray beam. The resulting scattering is recorded shot-by-shot by an X-ray area detector. (b) Single diffraction patterns are oriented and assembled into a 3D Fourier volume, from which the real space object can be reconstructed using the smoothness of the diffraction pattern as the constraint used for phasing. Figure and caption adapted from Bielecki *et al.* [8].

There are two main factors that often limit the achievable resolution in this class of experiment. The first is the total number of scattered photons, and it relates to the highest resolution where sufficient signal level was recorded. As the number of photons per X-ray pulse is more or less fixed by the FEL and accelerator performance, the most reliable way to increase resolution is to collect more patterns. The second main aspect that limits the resolution is the degree of reproducibility of the

delivered particles, where the resolution will be limited to the length scale within which the particles are identical. Sample homogeneity is often characterized and optimized while the sample is in solution (independently of the diffraction analysis). This approach neglects the behaviour of the sample, and solution, when the aerosol is formed and liquid subsequently evaporates. Hence, sample delivery and its effect on sample homogeneity is an extremely important, and often overlooked, aspect of SPI experiments [7; 8].

At SPB/SFX, we have the unique opportunity to efficiently approach both of these limitations. The high repetition rate of the European XFEL, in conjunction with the MHz operation of both the accelerator and the Mpx AGIPD at SPB/SFX, makes it possible to record 3520 diffraction patterns per second. This is a factor of 30 higher collection rate than previously possible elsewhere, e.g. at LCLS. Secondly, our recently developed sample delivery scheme [7] and the aerosol characterization methods available in the SEC laboratories and SPB/SFX hutch, together with our in-house expertise, enable us to prepare and optimize the sample conditions in collaboration with users before the start of any given measurement with XFEL beam.

The potential enabled by these factors was first showcased during the Ayer p2160 experiment. The aim of the experiment was to collect an unprecedented one million pattern dataset from Au nano-particles in the shapes of cubes and octahedra with sizes between 17 and 60 nm. This dataset could then serve as a benchmark for data analysis and structure reconstruction algorithms. As a reference, the largest previous dataset from an SPI experiment contained approximately  $10^5$  patterns. Before the start of the beamtime, we worked closely with the sample preparation team to make sure that the sample was efficiently and homogeneously transferred into the aerosol phase. In this way, we managed, over the course of several months, to go from a sample that aggregated and clogged the sample delivery equipment, to a close-to-optimal sample with high throughput and sample-limited homogeneity. As a result, the aim to record one million diffraction patterns was achieved within only a few hours of measurement time, and, when the experiment was concluded, more than *10 million diffraction patterns* had been recorded.

The first paper published from the Ayer p2160 experiment presents 3D structure reconstruction to better than 2 nm resolution for all samples [5] (see Fig. 2.4). Even though we made sure that the sample delivery did not add heterogeneity to the sample, the Au nanoparticle synthesis inevitably leads to some degree of inherent heterogeneity in terms of size and shape. To achieve the 2 nm resolution reported in Ayer *et al.*, it was necessary to automatically sort amongst the structural variability in the Fourier domain. Due to the very low beamline background signal achieved by a two-plane beam cleaning slit procedure [21], the achievable resolution was finally limited by the AGIPD dark noise single-photon false-positive rate at 6 keV photon energy, a limit that can be improved by operating the detector in a higher gain mode.

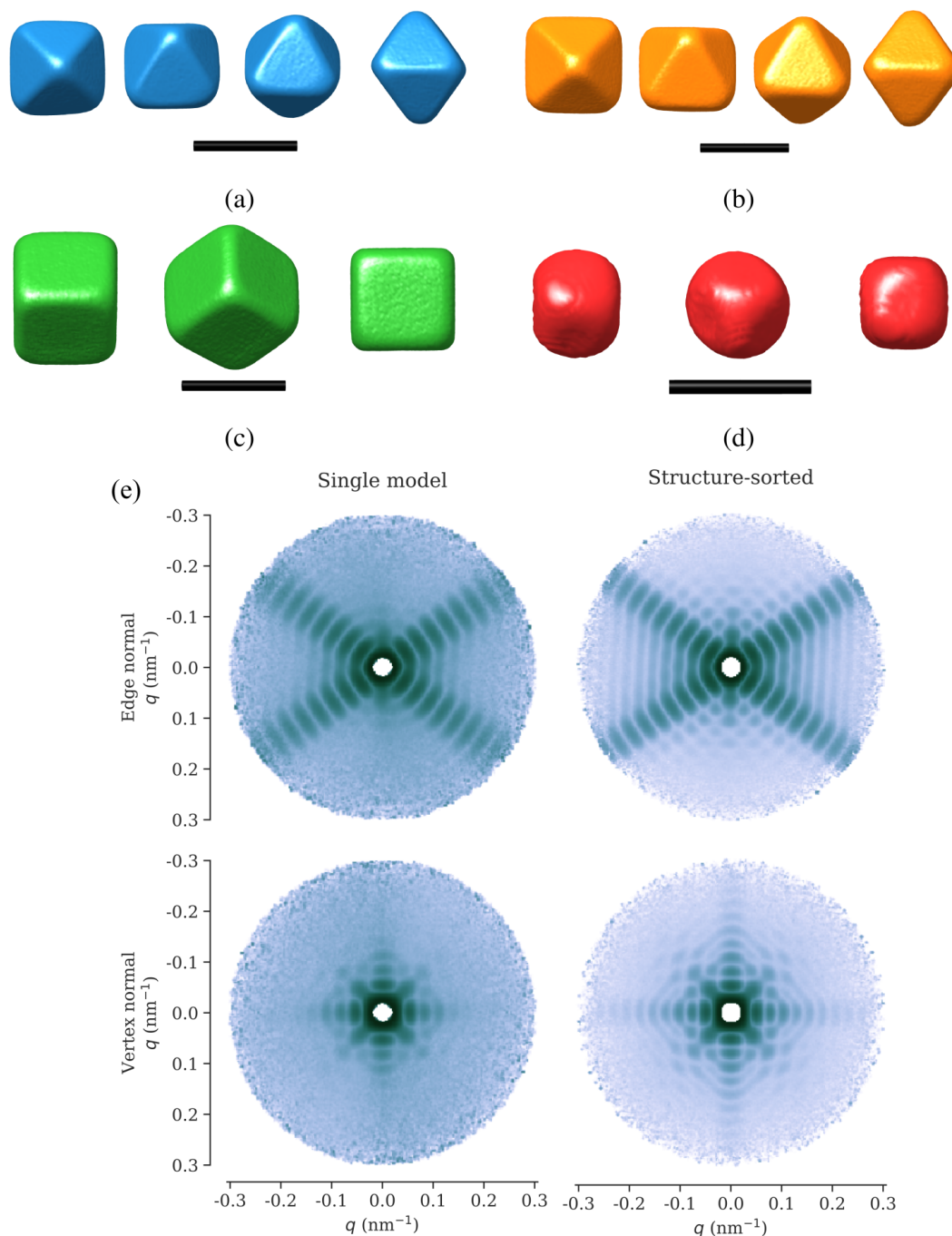


**Figure 2.4:** 3D structural reconstruction of (a) 30 nm octahedra, (b) 40 nm octahedra, (c) 42 nm cube, and (d) 17 nm cube samples with 40 nm scale bars as reference. (e) shows, with the 30 nm octahedra as an example, the improvement in Fourier domain contrast achieved after structurally sorting the sample ensemble. Figures adapted from Ayer *et al.* [5].

The ability to automatically sort weak patterns according to their structural classes in this way has been predicted from simulations but not before shown with real data. Similar problems with structural variability are to be expected when imaging single proteins, which has long been the ultimate goal of SPI. Thus, the results from inorganic samples are expected to be of great importance also in the pursuit of single protein imaging. The diffraction pattern sorting was further taken to the next level in the second paper [58], where machine-learning was employed to predict the real-space structure at arbitrary points in the continuous landscape spanned by the variations in question. In particular, this method was used to follow the melting that was observed by pre-exposure of the Au nano-particles in the wings of the FEL pulse arriving 880 ns prior to the main exposure.

Such developments are not only of value to the *biological* single particle imaging programme. There is increasing interest from the user community to investigate heterogeneous populations of material nanoparticles, either just across their population or in a time-resolved manner (such as observing NP synthesis). These experiments are possible already now, and proposals for material NP study are seen routinely.

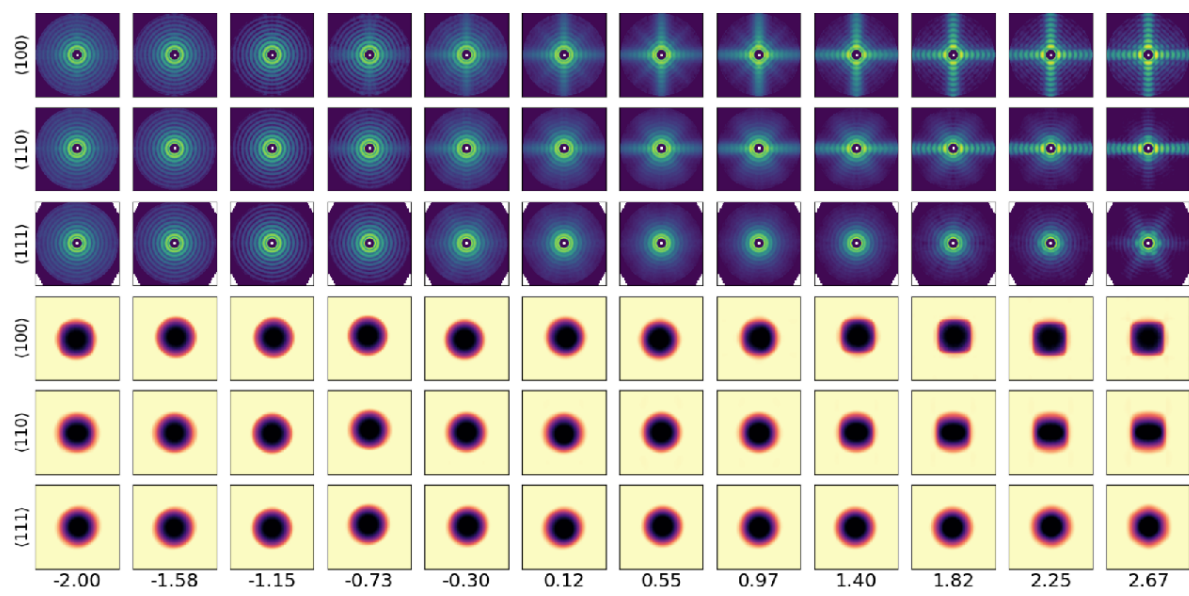


**Figure 2.5:** Neural network generated volumes along a latent “melting” coordinate. The melting occurs from left (spherical, melted) to right (cubic, intact). The top three rows show Fourier domain data along three directions, and the bottom three rows show the corresponding real space density projections.

---

## Small angle scattering at XFELs: Results and opportunities

Taking advantage of the MHz repetition rate to enable improved statistical analysis, filtering, and outlier rejection, proof of principle of the recovery of validated form factors from proteins in solution using XFEL pulses has been shown for what is believed to be the first time (see Section 4.6). A collaboration of motivated experts (EMBL Hamburg, CFEL, and European XFEL) measured standards and corona virus – related proteins of interest. Comparison of the same samples collected using an XFEL source and conventional synchrotron data collection, along with complementary measurements of samples using lab-based techniques, enabled validation of the data collected at the SPB/SFX instrument.

Further work to expand upon these results is already planned to enable small angle X-ray scattering experiments with XFEL pulses more routinely, and thereby enable time resolved studies of biological systems that can take advantage of the unique properties of FELs.

---

## MHz repetition rate microscopy: Pilot experiment

The development of XFELs has, in part, been driven by the very clear applications for imaging molecule-scale objects down to fs-scale temporal dynamics. The European XFEL uniquely provides MHz repetition rate, highly intense, fs-duration X-ray pulses with up to 24 keV photons (and possibly up to 60 keV in future). This opens up new possibilities for the imaging of matter such as fast, stochastic motion-tracking of objects with velocities up to km/s. Using full-field, single-shot microscopy techniques, the smooth evolution of certain processes can be observed with high contrast. EuXFEL provides a possible sampling time in the range of 222 ns – 282  $\mu$ s, with a burst duration of up to 600  $\mu$ s, meaning the tracking of objects at micron and sub-micron scales can be realized with velocities of up to km/s. Unlike pump and probe (PP) approaches, where the recording is done at a certain phase (delay time), MHz microscopy can record a sequence of images (movie) for a given probe signal and record the unique realization of a single stochastic event. Such a recording scheme can thereby provide significantly more information than averaged datasets obtained by PP or stroboscopic approaches.

The pilot experiment noted here has demonstrated the feasibility of XFEL MHz microscopy for tracking fast, stochastic phenomena by recording sequences of phase contrast images of laser-driven explosions [49], see Fig. 2.6.

Using a parasitic beam delivered by the SPB/SFX KB optics with a photon energy of 9.3 keV and a recording frequency of 1.1 MHz, clear tracking of individual debris exhibiting velocities of  $\approx 34$  m/s is demonstrated (Fig. 2.7).

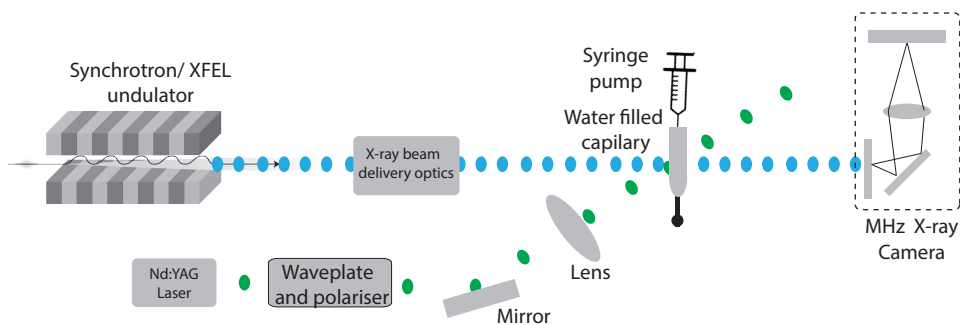


**Figure 2.6:** Schematics of the time-resolved MHz X-ray microscopy of laser-induced dynamics in a water-filled glass capillary.

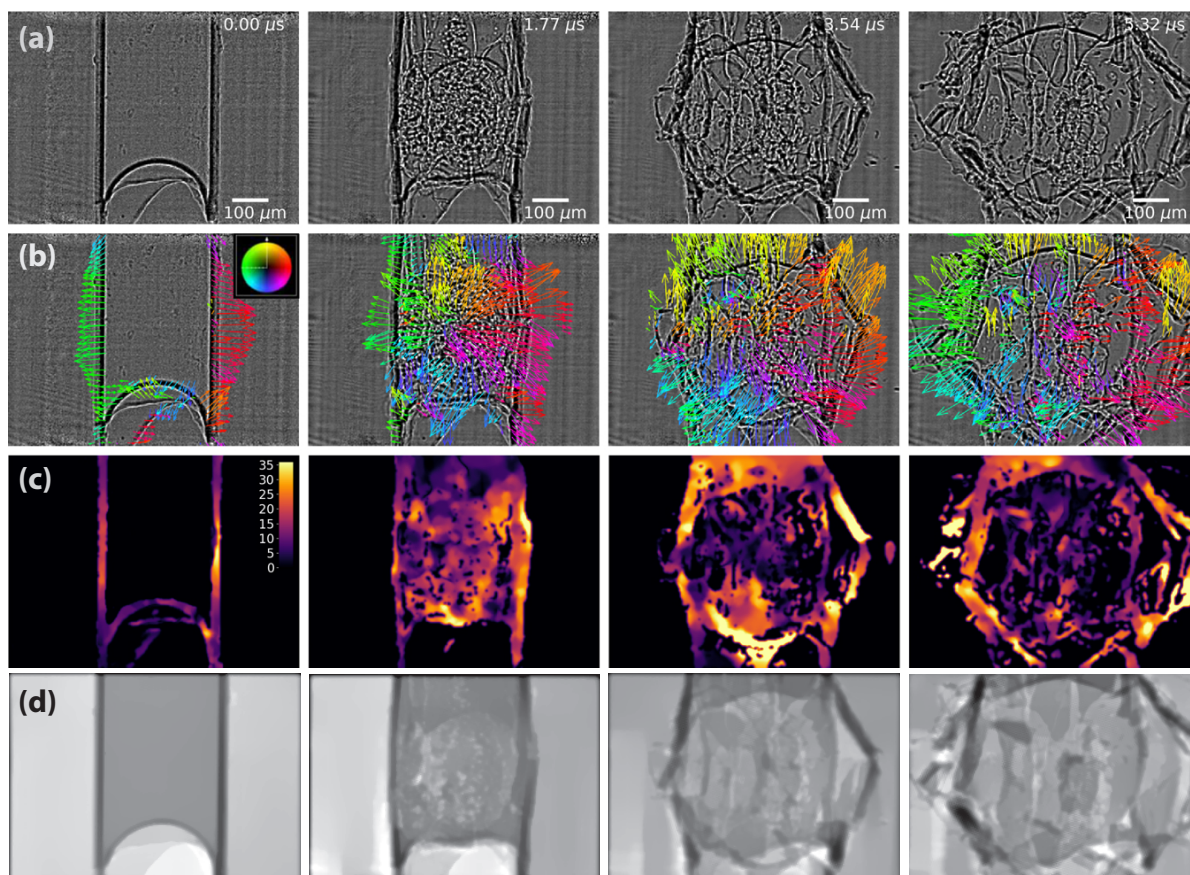


**Figure 2.7:** Image sequence of a laser-driven explosion of a capillary filled with water imaged at the European XFEL. Sequence (a) is the result of high-pass adaptive filtering to remove the high-frequency noise and image flickering, sequences (b) and (c) are the result of optical flow analysis [34] shown as a directional vector for the movement of debris (b) and the velocity maps (c) (see Visualization 1). The phase retrieval of the corresponding sequence (d) is performed using an ADMM-CTF algorithm [52].



These early results demonstrated that MHz Microscopy at EuXFEL is feasible and high resolution and high quality images can be recorded as compared to synchrotron sources (Fig. 2.8). This opens up new possibilities proposed in Section 4.5.

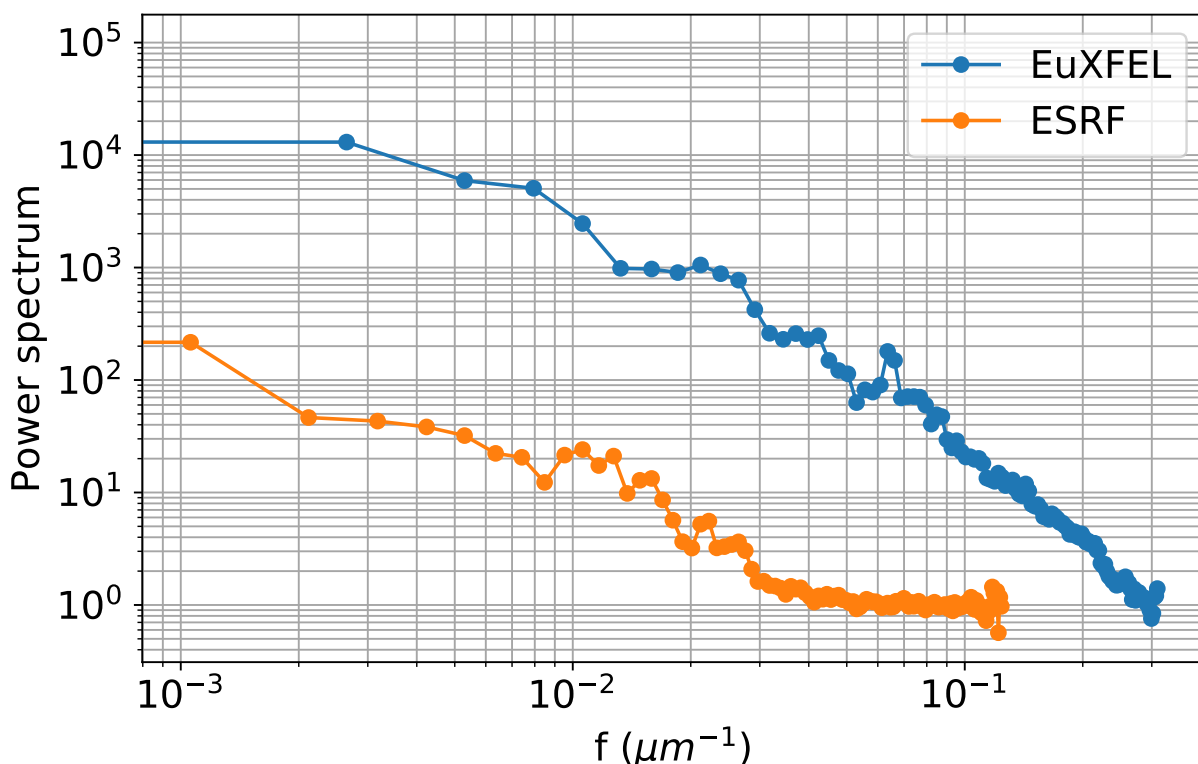


**Figure 2.8:** Power spectra of the frames with the highest SNR for the XFEL (SNR = 10.69) and the ESRF (SNR = 6.17) of the datasets compared in [49].

---

## Today's capabilities

In short, the SPB/SFX can routinely perform SFX and SPI experiments in regular operation. The SFX experiments are, as at all XFEL facilities, dependent on the behaviour of user sample in the sample delivery process and a program to screen sample delivery behaviour is commencing the second half of 2022 to address this potential limitation.

The very new methods of the XFEL SAXS and MHz microscopy have been demonstrated at SPB/SFX too with clear and successful results. While not yet as mature as SFX and SPI, they hold enormous promise for future application now that first experiments have been successfully completed.



# Instrumentation in operation

## Brief overview

The European XFEL accelerator delivers electron pulses into a fan of undulators [12], as shown in Fig. 3.1. The SPB/SFX instrument is located downstream of SASE1, a hard X-ray undulator producing X-rays from below 5 keV to above 20 keV (beyond the range of SPB/SFX’s operation in both directions). Currently, SASE1 and SASE3 (soft X-ray undulator) often operate in a so-called “interleaved” mode, where electron bunches within a bunch train are fed into each undulator alternately. The rate delivered to SPB/SFX can then be down-selected from the nominal (interleaved) rate of 1.13 MHz. The remainder of the electron pulse train is then conditioned for the SASE2 undulator. The total length of the operating window for SASE1 is restricted to (in practice) about 400  $\mu$ s per train. If the pulse repetition rate is reduced, fewer pulses are available per pulse-train given this finite window. Down-selecting the pulse rate therefore also reduces the overall achievable data rate.

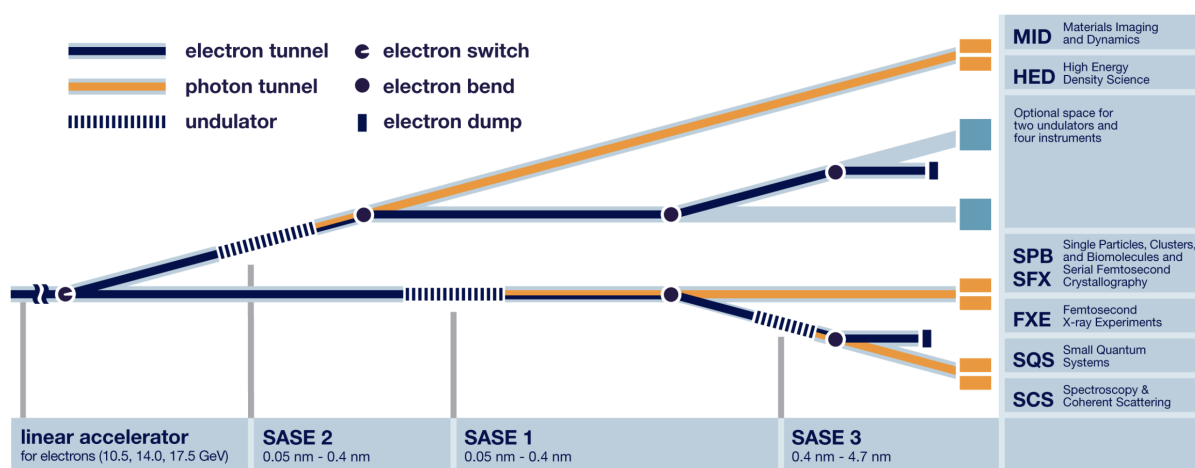


**Figure 3.1:** Layout of the photon beam systems at the European XFEL facility

The basic overview of the instrument is not repeated here for brevity. It is described in [29], and the downstream capabilities, including high viscosity SFX, MHz microscopy, and more, are described in [19]. In short, the SPB/SFX instrument is capable of many forward scattering techniques across photon energies from about 5 keV to greater than 15 keV.

Parameters offered to users are summarised in a two-page “fact sheet”. The most recent fact sheet, relevant to the call for the second half of 2022, is reproduced here for convenience.

# SPB/SFX Instrument Parameters for User Experiments (run 2022-02)

Version 1.0  
19/10/2021

Photon beam parameters		
<b>Photon energy</b>	6 - 12 keV	Up to 15 keV potentially possible
<b>Pulse energy</b>	≥2 mJ	Typical at 9.3 keV
<b>Photons per pulse (at source)</b>	~1 x 10 <sup>12</sup>	Derived from previous two fields (@ 9.3 keV)
<b>Pulse duration</b>	25 fs	Estimated
<b>Focal spot size (FWHM)</b>	~ 3 μm < 400 nm	Two KB mirror systems available
<b>Photons / μm<sup>2</sup> (at sample)</b>	> 10 <sup>10</sup>	Derived. Includes abs, expected spot size range.
<b>Train repetition rate</b>	10 Hz	
<b>Intra-train repetition rate</b>	1.1 MHz	(4.5 MHz, 100 kHz, some quasi-arbitrary patterns)
<b>ΔE/E</b>	~0.2%	Estimated
<b>No. of bunches per train</b>	≤352	Some quasi-arbitrary patterns possible.
Sample delivery systems: In vacuum (upstream, 1 Mpx AGIPD) and in-helium (downstream, roadrunner, Jungfrau 4M)		
<b>Liquid jet injector rod</b>	½" nozzle rod with M9x1 mm fine thread nozzle mount compatible with the CXI nozzle rod at LCLS (MPI design), 1030 mm in length. Additionally, 25mm nozzle rod with M23 fine thread.	
<b>Sample injection nozzles (GDVN and DFFN)</b>	3D printed nozzles to produce μm-sized liquid jets. Other nozzle types also possible. Nozzles are expected to be user-supplied unless otherwise arranged with SEC group prior to proposal.	
<b>High viscosity liquid jet</b>	Mounted on nozzle rod. ASU or EuXFEL design	
<b>Aerosol injector</b>	Aerosol produced by electrospray. Other nebulizers also possible	
<b>Fixed target sample holder</b>	Various available. Please consult with instrument scientists prior to proposal.	
<b>Pressure systems</b>	HPLC pumps, syringe pumps, gas-pressurised sample reservoirs	
AGIPD 1 Mpx detection properties		
<b>Number of pixels</b>	1024x1024	4 quadrants, each 512x512 pixels
<b>Pixel size</b>	200 μm x 200 μm	
<b>Minimum sample–detector distance*</b>	~129 mm	Maximum 200 mm stroke
<b>Resolution at edge @ 9.3 keV</b>	< 2 Å	At minimum distance from sample
<b>Max sample detector distance</b>	~ 5.5 m	
<b>Hole size</b>	8 mm. Possibly ~5 mm—large	

## SPB/SFX Instrument Parameters for User Experiments (run 2022-02) – page 2

Optical laser system 1 properties		
<b>Wavelength</b>	800 nm	From 740 to 840 nm (pulse duration is longer than 15 fs)
<b>Pulse duration</b>	15–300 fs	
<b>Repetition rate</b>	4.5 MHz	Down to 100 kHz
<b>Pulse energy</b>	50 $\mu$ J	
<b>Wavelength conversion</b>	SHG, THG (no OPA)	SHG (370–420 nm), THG (246–280 nm)
<b>Spot size</b>	30–50 $\mu$ m	Diameter (estimated, typical)
Optical laser system 2 properties		
<b>Wavelength</b>	1030 nm	No wavelength tunability
<b>Pulse duration</b>	1–400 ps	
<b>Repetition rate</b>	4.5 MHz	Down to 100 kHz
<b>Pulse energy</b>	1 mJ	
<b>Wavelength conversion</b>	SHG, THG, FHG	SHG (515 nm), THG (343 nm), FHG (258 nm)
<b>Spot size</b>	30–50 $\mu$ m	Diameter (estimated, typical)
Optical laser system 3 properties (Opolette 355 HE)		
<b>Wavelength</b>	210 – 2400 nm	OPO output
<b>Pulse duration</b>	3 – 7 ns	
<b>Repetition rate</b>	Single shot – 20Hz	Down to 100 kHz
<b>Pulse energy</b>	0.5 – 9 mJ	Dependent on wavelength
<b>Spot size</b>	4 mm	Near field
Three of these systems can be operated simultaneously		

Photon Arrival Monitor (PAM) timing tool available for micron beam experiments, depending on experimental configuration. TOPAS in commissioning and potentially available for experiments for run 2022-02. In Helium serial crystallography with Jungfrau 4M detector also available.

**In these cases, discussion with instrument scientists before proposal submission is essential**

Please discuss your experiment plans with an SPB/SFX instrument scientist **before** submitting your proposal. They can help you with any details that may have updated, assist with evaluating experiment feasibility, and much more.

Contacts:

[spb.sfx@xfel.eu](mailto:spb.sfx@xfel.eu)

[sample.environment@xfel.eu](mailto:sample.environment@xfel.eu)

[useroffice@xfel.eu](mailto:useroffice@xfel.eu)

---

## Sample delivery methods

A key group of technologies required for successful experimental outcomes requires the presentation or delivery of sample or samples—crystalline, non-crystalline, biological, inorganic, or otherwise—to the XFEL beam in order to have its structure interrogated. Traditionally, SFX has relied on the injection of micro-crystals in a liquid medium to present samples at a rate commensurate with XFEL repetition rates [11; 43]. This includes both lower viscosity media (with viscosities closer to that of water) as well as higher viscosity media, such as lipids in the cubic phase (LCP), which, in many cases, are more amenable to containing and transporting crystals of membrane proteins. Increasingly, systems presenting crystals on surfaces as so-called “fixed targets” are used too. As the European XFEL operates at extremely high repetition rates within the “train”, sample delivery methods compatible with MHz repetition rates are desirable. For methods that are not yet compatible with MHz rates (such as fixed target sample presentation) we have ongoing development projects to translate these methods to become MHz capable (such as a “beam sweeping” project that seeks to exploit fixed targets at high repetition rates by scanning the beam across targets, rather than trying to move them at speeds compatible with MHz rates).

### Liquid samples

For delivering liquid samples into the instrument, a nozzle rod and catcher system designed within the SFX User Consortium (SFX UC) has been installed and is presently in operation [45]. The standard rod system provides a load-lock mechanism to insert nozzles into the chamber without breaking vacuum. Recent developments in imaging hardware, control software, and organizational structure allow the exchanging of nozzles within 20 minutes. The system can be loaded with standard nozzles as well as high viscosity extruders and more complicated systems, such as a segmented flow setup in development with Arizona State University. The most widely used standard nozzles are gas dynamic virtual nozzles (GDVNs, [13; 22]) and double-flow-focusing nozzles (DFFNs, [37; 22]). GDVNs provide fast jets for MHz repetition rates with few- $\mu\text{m}$  diameter by compressing a liquid jet in a high-pressure helium stream. DFFNs add an additional liquid sheath layer between sample liquid and helium gas. For many samples, they provide more stable and reliable jetting.

Liquid sample delivery has been standardized as far as possible. Sample is loaded into reservoirs that can be mounted to a temperate-controlled shaking device in order to avoid settling. The reservoirs are pressurized using an HPLC pumping assembly. To ensure availability of the pumping system, the SEC group has standardized these systems, organizes regular maintenance, and keeps backup systems available. Switching between different samples, running water or empty buffer for alignment, and providing mixing agents is realized with a standard valve box. The entire system is Karabo controlled and can be accessed from the experiment hutch, the preparation lab, or the control room. During liquid jet beamtime, a SEC jetting expert is on shift to supervise jetting conditions and quickly react to any irregularities.

For many user groups, the sample consumption for a full dataset is a key parameter deciding on the feasibility of an experiment. We therefore have to efficiently use the sample provided by the users. In order to increase sample efficiency of the instrument, methods to reduce sample consumption are in development. For these methods, e.g. drop-on-demand sample delivery or segmented flow, lower flow rates are required. Actual flow rates are at the lower limit of the operation range of conventional HPLC pumps. To enable further flow-rate reduction, the SEC group is investigating the possibility of introducing syringe pumps for sample delivery. This technology has the potential to deliver liquids pulsation-free at extremely low flow rates. This is important because pulsation in the sample flow can induce instabilities that lead to nozzle clogging or synchronization loss.

### **Microfluidic device fabrication**

Microfluidic devices enable the precise control of fluids and the generation of micrometre-sized gas-focused liquid jets, high-viscous streams, and near-monodisperse droplets suitable for X-ray diffraction and scattering experiments at XFEL instruments.

Recent achievements and advances in liquid sample delivery methods for experiments at the SPB/SFX instrument are described in the article “3D printed devices and infrastructure for liquid sample delivery at the European XFEL” [50], which was compiled by SEC, SPB/SFX, FXE, and SQS group members as well as external collaborators. In this work, we present a variety of novel 3D printed liquid sample delivery devices (Fig. 3.2), whose construction is based on the two-photon polymerization (2PP) 3D printing technique. These devices encompass GDVNs for delivering microcrystals, mixing-GDVNs for time-resolved studies, high-viscosity extruders (HVEs) for studies of proteins within the LCP, and electrospray coned capillary tips (CCTs) for enabling aerosol-based samples. This fabrication method maintains the highly reproducible geometric features of the devices that are suitable for time-resolved SFX as well as SPI experiments at XFEL facilities.

Furthermore, all current and future 3D design files (with detailed descriptions of the design parameters and experimental requirements) are available for download through a GitHub repository, accessible under:

<https://github.com/flmiot/EuXFEL-designs>

With this repository, we hope to positively impact the quality of sample delivery devices, not only by fuelling new design ideas and improvements in the community but also by allowing users to facilitate sample injection tests at their home institute prior to an experiment at the European XFEL. Importantly for operation, we now also provide such 2PP 3D printed nozzles for users when required. This provides common quality control and more uniform conditions, ideally leading to improved experimental outcomes and better experiment risk mitigation.

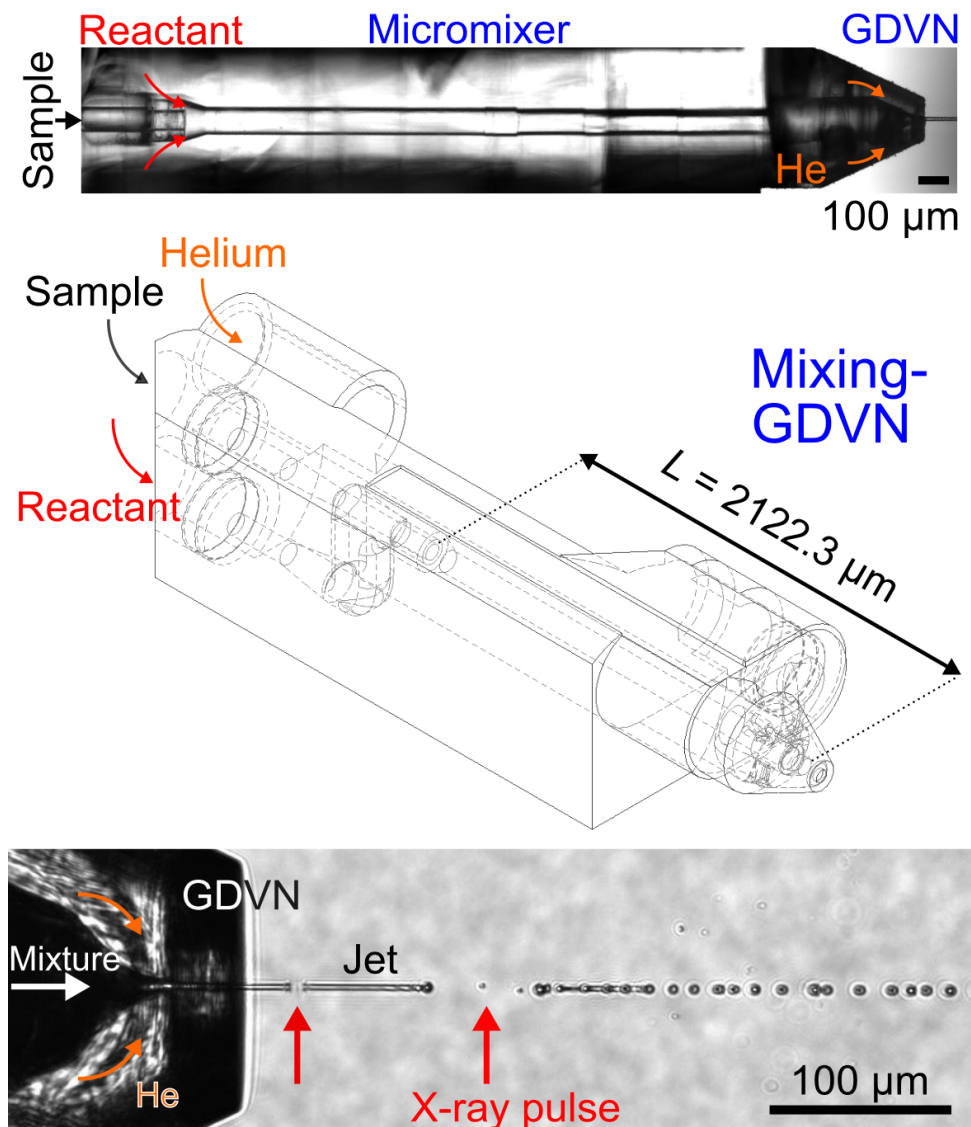


**Figure 3.2:** Overview of a 2PP 3D printed mix-and-inject device (i.e. mixing-GDVN) consisting of a 2 mm long micromixing channel (a microscopy image offers a view of the micromixing channel as seen from the top) fused to a GDVN tip. Magnification of the jetting region (bottom) demonstrates how a stable liquid jet inside the SPB/SFX sample chamber interacts with the X-ray pulses, which further create gaps into the liquid column. Upstream of the jet, throughout the micromixing channel, highly efficient and homogeneous mixing occurs via 3D diffusion across the flow direction, and retention times of several tens to several hundreds of milliseconds can be controlled. To access even longer retention/mixing times, a modular assembly approach can be pursued in which a printed micromixer and GDVN are connected by a liquid capillary extension of custom length.



## High-viscosity extruders

High viscosity samples, such as membrane proteins in lipid cubic phase, are mainly injected in the helium downstream sample environment. Because of low flow rate, these experiments are conducted at a 10 Hz repetition rate.

Two kinds of standard high-viscosity extruders are available for the SPB/SFX instrument: A modified version of the injector developed and distributed by Arizona State University [53] (ASU extruder) and a new design for the European XFEL (EuXFEL extruder). The ASU extruder provides a 40  $\mu\text{l}$  or a 120  $\mu\text{l}$  reservoir and has been used successfully for many experiments at LCLS and the European XFEL. The EuXFEL extruder provides a novel 440  $\mu\text{l}$  glass reservoir for longer operation time and easier filling. Both devices are compatible with the standard nozzle rods and can be used in the upstream sample environment.

For using the extruders in the downstream helium sample environment, a small helium chamber with a nozzle catcher has been built. The catcher accepts a short version of the standard nozzle rod. So we can use any nozzle rod compatible injection device in the downstream helium environment.

These higher viscosity extruders, while presently only 10 Hz compatible, are also potentially amendable to the benefits of “beam sweeping” and may be later high repetition rate compatible too. This would, naturally, increase the attractiveness of performing these experiments at the European XFEL compared to normal-conducting ( $\approx 100$  Hz) XFEL facilities elsewhere.

## Aerosols

Weakly scattering samples require a sample delivery method that introduces very little to no additional background scattering. For such samples, which typically are single particles or nano-crystals, an aerodynamic lens that focuses an aerosolized sample into the interaction region is used [28]. The aerodynamic lens is compatible with the standard catcher system used for SFX experiments at the SPB/SFX instrument and can utilize the full XFEL repetition rate. This capability is now routinely provided for users.

Typically, the sample, suspended in a volatile solution, is transferred into the gas phase by formation of nano-droplets, leaving behind naked sample particles/crystals after evaporation. In most cases it is of paramount importance to remove any non-volatile components in the solution in order to avoid signal contamination from the resulting covering of the particle. To reduce the effect of such non-volatile components, droplets as small as possible are used in the aerosol formation process [7]. The particles are subsequently transported by a sheath gas inside the aerodynamic lens, after which a particle beam with FWHM in the range between 10–100  $\mu\text{m}$  is achieved at the interaction region [18].

The electrospray nebulizer that is most commonly used produces droplets with diameters in the size range between 100–200 nm. Use of this nebulizer requires the sample solution conductivity to lie between 100–7000  $\mu\text{S}/\text{cm}$  and needs a combination of  $\text{N}_2$  and  $\text{CO}_2$  for stable operation. These relatively strongly scattering gases limit the achievable resolution for biological samples due to their contribution to background. A main focus in our internal research programme is to successfully replace most of the  $\text{N}_2$  and  $\text{CO}_2$  with He using novel microfluidic devices fabricated at the European XFEL, which in turn would greatly reduce the background scattering.

## Solid samples

A number of experiments require the sample to be presented on a solid substrate or in solid form itself. As one is generally unable to move a sample fast enough between MHz rate pulses to expose a fresh site, experiments using solid samples are constrained to collecting data either (a) from subsequent pulses in a train from the same position or (b) from a single pulse per train (i.e. 10 Hz).

A number of options exist for introducing solid samples to the X-ray pulses at SPB/SFX:

- Custom support attached to IRU nozzle rods
- Custom support attached to IRU hexapod
  - Use of SmarAct stages for additional X, Y, Z, and rotation axes
  - Sample scanner with standard frame
- Roadrunner installed at SPB/SFX (IRDa) [48]
  - Chips of varying designs can be mounted in a temperature and humidity controlled environment
  - Can also be used as the mounting point for other devices, i.e. drop on demand

These presently deployed methods are all constrained by collection mode (a) or (b), as described above. However, ongoing R&D is underway to avoid this constraint by clever manipulation of the incident beam, thus providing hope of enabling high-throughput and sample-efficient measurements (see Section 4.3.3).

---

## Detectors in operation

Two “large” 2D detectors support operation of two interaction regions at the SPB/SFX instrument. The one megapixel AGIPD (AGIPD 1Mpix) is an integral part of the upstream interaction region. It was developed specifically for European XFEL to enable wide spectrum of measurements, which utilize both time structure and brightness of the X-ray beam delivered at the European XFEL facility. The detector was delivered and commissioned in mid-2017 and has been in operation since then. The four megapixel unit of the AGIPD detector (AGIPD 4Mpix) was envisioned for the downstream interaction

region starting from 2017. Currently, due to delays in the AGIPD 4Mpix project, experiments at the downstream interaction region are realized with the help of the four megapixel Jungfrau (Jungfrau 4Mpix) detector, which is available for users since 2019. Nominally, this detector is compatible with 10 Hz operation at the European XFEL. The SPB/SFX instrument group is working with detector groups of European XFEL and Paul Scherrer Institute to enable operation of the additional 15 memory cells and therefore increase acquisition rate to 160 Hz.

## AGIPD 1Mpix

### General description

The AGIPD 1Mpix [1] is a 1 megapixel detector, which at SPB/SFX is part of the upstream interaction region. It was designed to operate in the photon energy range from 6 to 18 keV and to provide a dynamic range of  $10^4$  photons at 12 keV. The detector consists of 16 front-end modules (FEMs). Each FEM consists of  $512 \times 128$  pixels. All pixels, except double-sized pixels between the ASICs, have a pitch of  $200 \mu\text{m}$ . An array of memory cells behind the pixels enables acquisition of up to 352 images per train. The FEMs are grouped into quadrants (see Fig. 3.3). The relative position of the FEMs within each quadrant is fixed, while horizontal and vertical positions of the quadrants can be tailored to each experiment's needs. The relative position of the quadrants is evaluated with sub-pixel resolution using data from a reference sample, typically crystalline lysozyme.

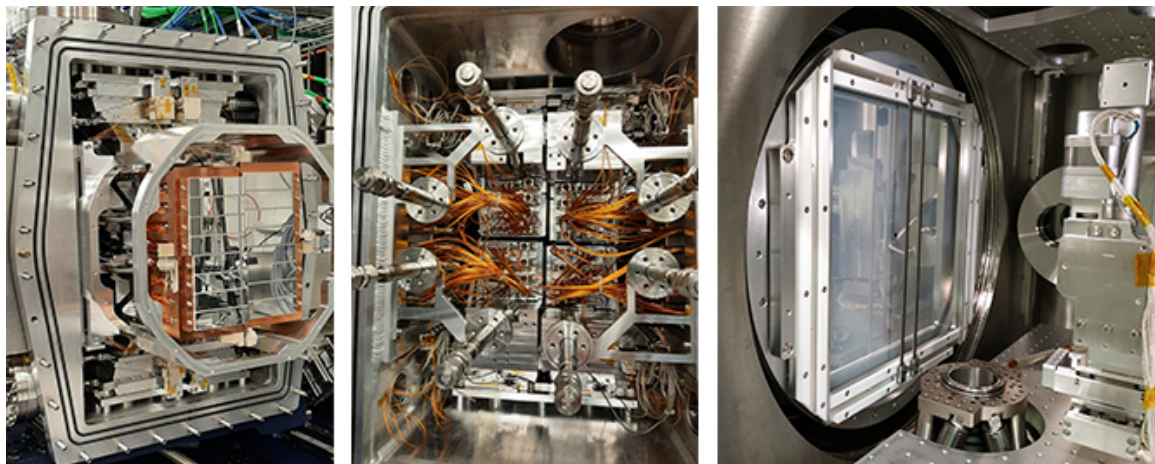


**Figure 3.3:** The AGIPD 1Mpix detector at the SPB/SFX instrument with the front (left) and rear (middle) panels of the detector vessel removed. *Left:* The front-end-modules are cooled using the four movable Cu blocks. The motor stacks visible beneath and above the quadrants are used to adjust the geometry of the detection plane. *Middle:* Electrical and cooling interfaces. Photos taken during the readout board upgrade in Dec. 2020. *Right:* Detector head in the nominal position during the SFX experiments. The Al-coated shield and Ta mask striped are visible. The sample delivery infrastructure (not shown) is aligned with respect to the X-ray beam with the help of hexapod shown at the bottom of the image.

Since its installation in 2017, the AGIPD 1Mpix became the main detector of the SPB/SFX instrument, and it is typically used for protein crystallography and single particle imaging. It was also successfully used for small angle scattering experiments and proof of principle MHz X-ray photon correlation spectroscopy [26], a technique routinely used now by the MID instrument with the second unit of the AGIPD detector.

The AGIPD 1Mpix operates in vacuum and is separated from the sample chamber by a DN500 valve, allowing access to the sample chamber during operation, while the detector remains cooled and under vacuum. During a typical experiment, a sample-to-detector distance of around 125 mm is achieved by translating the detector head into the sample chamber. To protect the detector against exposure to sample, an Aluminum-coated 13  $\mu\text{m}$  thick kapton shield is placed in front of the sensors (Fig. 3.3). The vacuum level inside the isolated detector chamber is on the order of  $10 \times 10^{-6}$  mbar. However, when connected to the sample chamber, pressure can exceed  $1 \times 10^{-4}$  mbar, depending on the gas load due to liquid jet operation. The detector is armed with interlocks to prevent electrical discharges at higher pressures or mechanical damage during operation.

By design, the AGIPD 1Mpix supports 4.5 MHz operation. However, during most experiments, the feasible acquisition rate is restricted by the sample delivery rate. For a given acquisition rate, the number of pulses per train recorded with the AGIPD 1Mpix is, in practice, often limited by the size of RF window assigned to SASE1. To account for the (unfortunate) dependency of the calibration constants on the acquisition rate and number of memory cells filled, only a few configurations are available: 352 memory cells at 1.13 MHz, 202 memory cells at 0.56 MHz, and 64 memory cells at 1.13 MHz. Operation of the AGIPD 1Mpix is supported by the online and the offline calibration pipelines.

It has to be stressed that the AGIPD 1Mpix is a one-of-a-kind detector that was developed specifically for the European XFEL. Since first light, two units have been deployed: one at SPB/SFX and the other at the MID instrument. Performance of the AGIPD 1Mpix is the subject of ongoing studies. Since its arrival at the SPB/SFX instrument, significant improvements have been made in terms of quality of the raw and corrected data. Further details regarding the detector calibration and operation procedures are described in internal European XFEL documentation, which can be provided on request.

### **Detector calibration and commissioning**

To ensure the data collected is of best quality, calibration constants are evaluated on a regular basis. Pedestals, thresholds, and bad pixels are estimated at least once per shift. The flat-field data is taken at the beginning of every experimental run as part of the instrument restart following each maintenance period. In addition to the regular detector calibration tasks, SPB/SFX supports a detector studies programme of the Detector group. For this purpose, several shifts per run are allocated by the instrument for detector studies. Two such projects are briefly summarized in the following section.

## Baseline shift

The AGIPD 1Mpix exhibits a so-called “baseline shift” towards negative values that is proportional to the total number of photons detected in a given front-end module. The “baseline shift” is a change in the pedestal (i.e. “baseline”) level as a function of the total number of photons detected by a FEM. To quantify and correct for this effect, a sufficient number of dark pixels are required. Therefore, 2 mm wide tantalum stripes were installed in front of the detector to fully shadow a fraction of each FEM (see Fig. 3.3) and therefore independently measure the baseline. This baseline shift was attributed to an error in the design of the readout circuit. The effect was mitigated by reducing the resistance of the selected resistors within the readout circuit. In February and March 2020, the slope of the baseline shift for various configurations of the readout boards was studied by the AGIPD developers, detector scientists, and members of the SPB/SFX group. For the optimal set of resistors, the baseline shift is around one order of magnitude lower than originally observed. Successful tests were followed by the upgrade of the AGIPD 1Mpix readout boards during the winter maintenance period of 2020. The tantalum mask is still required for measurements with high overall intensity.

## “Snowy pixels”

The “snowy pixels” effect is associated with the intensity levels around the transition region between high and medium gain. The AGIPD uses so-called “adaptive gain”, where the gain in a pixel reacts to the incident intensity. For AGIPD, there is a finite probability that a pixel may be read out in a transition state between gain levels, and the signal read no longer maps to the correct gain value. As a result, a much higher value is registered for such a pixel. Visually, for most colour scales, this effect manifests as some (seemingly arbitrary) pixels that should be part of a smooth signal being much brighter than their neighbours, hence the colloquial name “snowy pixels”. This effect is especially troublesome in the case of crystallographic data, as those pixels around may be incorrectly classified by algorithms as Bragg peaks. The severity of the effect depends strongly on the background level. For example, in case of an intense water ring, up to 10% of the pixels register unrealistically high values. Although, the ASIC would need to be redesigned in order to eliminate this effect, the probability of the pixel getting trapped in the transition phase is reduced in practice as far as possible by a practical and opportune tuning of the detector settings (see below).

One option to mitigate the “snowy pixels” is to operate the AGIPD 1Mpix in fixed medium gain—e.g. to suppress (or switch off) the adaptive gain and constrain the detector to only work in its “medium” gain range. This approach is suitable for measurements that do not require single photon sensitivity, i.e. potentially SFX type data collections. The fixed gain translates into reduced dynamic range in contrast with using the adaptive gain. For example, should the diffuse scatter between Bragg peaks also be of interest, fixed medium gain would no longer be appropriate, and variable gain used with efforts to mitigate the effect of “snowy pixels” would be necessary.

The fixed medium gain mode of operation was implemented at the beginning of 2021 and, since then, it was successfully used for a number of experiments, including the COVID-19 research programme. An alternative way to address the problem of “snowy pixels” is to extend the time between the arrival of the X-ray pulse (and the generation of charge in the pixel) and the onset of the readout by extending the exposure time. The frequency of the “snowy pixels” appearing as a function of the exposure time was studied at SPB/SFX in August 2021. Examples of the diffraction patterns from a water jet are shown in Fig. 3.4. For an exposure time  $t_{exp} = 200$  ns, the number of snowy pixels decreased by three orders of magnitude in comparison with the data taken with the nominal setting of  $t_{exp} = 120$  ns. To quantify the benefits for serial crystallography from using the longer integration time, lysozyme crystals were measured for both settings. Results are documented in Tab. 3.1 and 3.2. To summarize, an improvement of 30% in indexing rate and 25% in SNR was achieved. Note that the longer integration time implies that the maximum repetition rate is reduced, though 200 ns is still compatible with the 1.1 MHz rate, which is, at the time of writing, the highest practical (sample delivery limited) repetition rate achieved for serial crystallography.

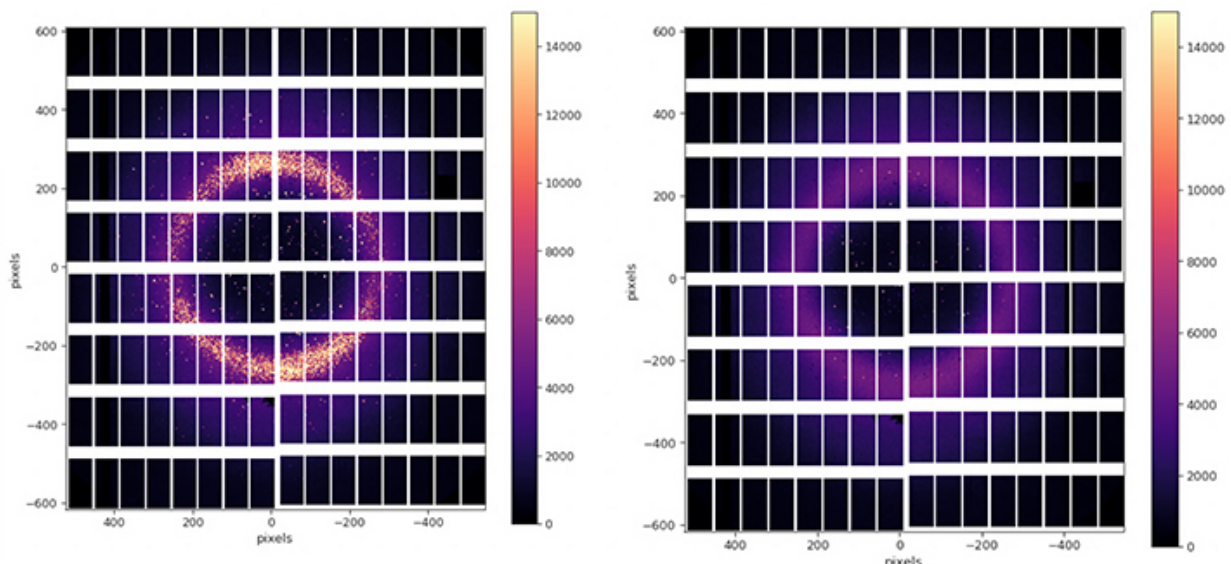


**Figure 3.4:** Lysozyme data collected for (left)  $t_{exp} = 120$  ns and (right)  $t_{exp} = 200$  ns

AGIPD 1Mpix data for $t_{exp} = 120$ ns					
Dataset	Hit/indexed rate	Overall indexing rate	N_crystals	N_frames	SNR
1	90.40	0.53	3187	605596	3.42
2	92.70	0.41	2540	613272	3.12
3	92.33	0.44	2708	608626	3.24
4	80.19	0.37	2389	652460	2.91
5	85.11	0.25	1309	516716	2.24
<b>Mean</b>	<b>88.15</b>	<b>0.4</b>			<b>2.99</b>
AGIPD 1Mpix data for $t_{exp} = 200$ ns					
Dataset	Hit/index rate	Overall indexing rate	N_crystals	N_frames	SNR
1	96.95	0.66	4476	677508	4.06
2	96.78	0.61	3848	630038	3.86
3	96.86	0.59	3823	647612	3.80
4	97.39	0.57	5627	984952	4.44
5	91.43	0.64	4013	623574	3.77
<b>Mean</b>	<b>95.88</b>	<b>0.61</b>			<b>3.99</b>

**Table 3.1:** Results of lysozyme SFX measurements for various exposure times  $t_{exp}$ . Hit finding was performed up to 2 Å, while indexing up to 4 Å.

AGIPD 1Mpix data for $t_{exp} = 120$ ns				
Dataset	Overall indexing rate (%)	N_crystals	N_frames	SNR
1	1.81	10935	605596	5.04
2	1.41	8671	613272	4.57
3	1.52	9228	608626	4.68
4	2.29	14936	652460	5.72
5	1.54	7974	516716	4.17
<b>Mean</b>	<b>1.71</b>			<b>4.84</b>
AGIPD 1Mpix data for $t_{exp} = 200$ ns				
Dataset	Overall indexing rate (%)	N_crystals	N_frames	SNR
1	2.11	14299	677508	5.84
2	1.96	12374	630038	5.46
3	1.92	12431	647612	5.41
4	1.82	17953	984952	6.45
5	3.24	20189	623574	7.01
<b>Mean</b>	<b>2.21</b>			<b>6.04</b>

**Table 3.2:** Results of lysozyme SFX measurements for various exposure times  $t_{exp}$ . Both hit finding and indexing were performed up to 4 Å.

## Jungfrau 4M

### General description

The downstream interaction region (IRD) is devoted, presently almost exclusively, to experiments in a Helium atmosphere. The AGIPD 4Mpix was originally planned to be the main detector for the IRD. However, due to delays in delivery and support from the SFX User Consortium (SFX UC), an alternate solution has been deployed in the form of a 4Mpix Jungfrau detector with 75  $\mu\text{m}$  pixel and 320  $\mu\text{m}$  silicon sensors. The detector head, along with a typical diffraction pattern, are shown in Fig. 3.5. Eight Jungfrau modules [33] are arranged into two columns; each column can be moved independently in the horizontal direction. The vertical gap between the modules is fixed, while the gap between both columns can be adjusted from 0 to 20 mm. Similarly to the AGIPD 1Mpix, the Jungfrau detector is protected against contamination (e.g. from sample debris) using a Kapton shield. Over the last few years of operation, several versions of the shield were developed to accommodate various experimental needs. Two examples are presented in Fig. 3.6.

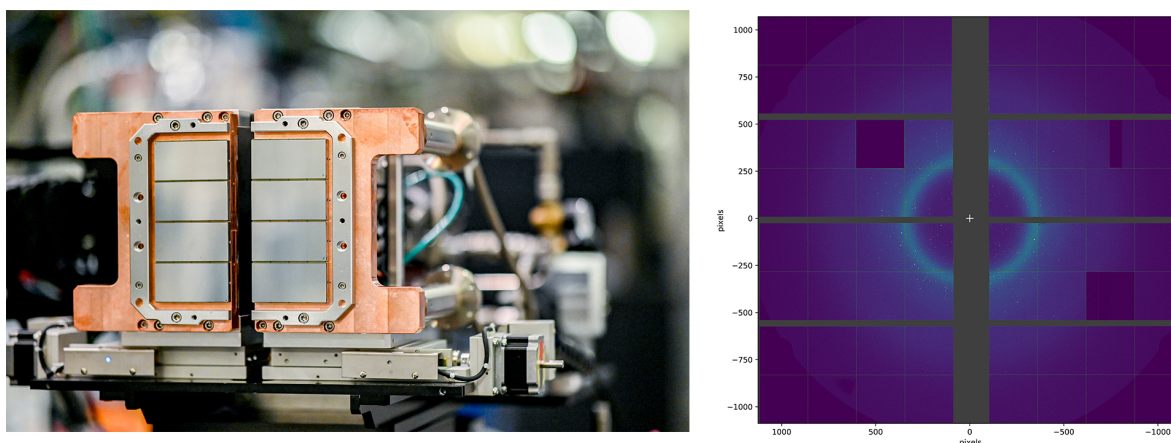


**Figure 3.5:** *Left:* Head of the 4Mpix Jungfrau detector at SPB/SFX. Two columns of Jungfrau modules are attached to copper cooling blocks and are installed on separate horizontal stages. Both the housing and protective shield were removed for this photograph *Right:* Example diffraction pattern. The signal is dominated by the water ring. The broken areas within the temporary modules are visible. (Imperfect “temporary” modules were delivered prior to the final, production quality modules, which have since been delivered to replace them). Round shadow at the edges and in the corners of the image corresponds to the part of the signal clipped by the exit aperture of the sample chamber.

Typically, the detection plane is positioned around 110–120 mm from the interaction region. However, the entire detector head can be translated downstream up to 300 mm to accommodate easier access to the sample region. The detector distance and geometry is calibrated (as with the AGIPD 1Mpix) using lysozyme as a reference sample. Nominally, the Jungfrau detector operates using a single memory cell, which, in the case of SFX measurements, translates into 10 Hz operation. To relax this limitation, SPB/SFX is collaborating with the detector groups of European XFEL and Paul Scherrer



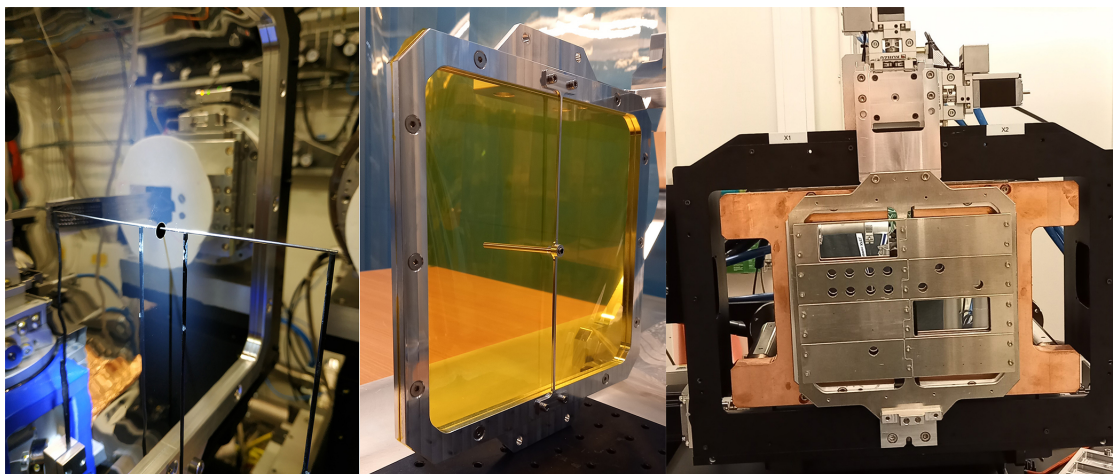


**Figure 3.6:** The Kapton shields used at SPB/SFX to protect the Jungfrau 4Mpix detector from exposure to the samples. *Left:* The Jungfrau 4Mpix with Aluminium-coated mask at the nominal distance from the interaction region. For this setup, the background on the detector was reduced with the help of straw guiding the direct beam out of the sample chamber. *Middle:* Shield with the additional straw, which guides the direct beam further downstream from the interaction region. *Right:* Shield with configurable panels used for detector studies. The shield motor stack is mounted on top of the detector housing.

Institute to enable operation of the 15 additional memory cells that the Jungfrau detector poses. Further details about the current status of the Jungfrau detector and the commissioning of the multi memory cell operation is detailed in European XFEL internal documentation, which can be provided upon request.

The online as well as offline calibration pipelines support the single memory cell operation of the Jungfrau detector. An upgrade of both pipelines to enable multi-cell operation is underway. From the control, the data acquisition, or the calibration point of view, each of the modules is treated as an independent detector. All units share only the trigger, with an option of individual adjustment of the delay between the trigger and acquisition start.

### **Commissioning, calibration, and maintenance**

Pedestals and bad pixels are evaluated at least once per shift, typically when dark images are acquired at the beginning and end of the shift. The flat-field data is taken at the beginning of every experimental run as part of the instrument restart after each maintenance period.

The current version of the readout boards only allows limited calibration of the Jungfrau front-end modules using the European XFEL infrastructure. In terms of gain, only the high gain stage calibration constants can be evaluated periodically at SPB/SFX. For the medium and the low gain stages, the gain constants provided by the supplier, PSI, are applied. The situation will improve with the

arrival of the latest version of the readout boards. Thanks to enabled back-plane pulsing, in-house characterization of the detector over the entire dynamic range will then be possible.

The relative position of the modules is evaluated for every experiment using the SFX data from the model sample, typically lysozyme. One of the ongoing projects between SPB/SFX and the Data Analysis group is automating generation of the geometry file, which encodes the specific geometry of detector modules.

The SPB/SFX group is responsible for assembly and maintenance of the detector. Replacement of the front-end modules and the readout boards is performed by designated scientists along with the engineers. To ease this task, specialized tools were developed by the engineers of the SPB/SFX group. As an example, the stand enabling safe rotation of the detector head and easier access to both FEM and readout board is presented in Fig. 3.7.



**Figure 3.7:** The Jungfrau 4Mpix during replacement of a front-end-module. The specialized stand allows easier access to all the components.

### Status of the front-end modules

Due to limited availability of the FEMs, the detector at SPB/SFX was, initially, equipped with only three top-quality modules. The remaining five slots were populated with so-called “temporary modules”, i.e. modules with minor defects (e.g. single broken ASIC). The defects are shown in Fig. 3.5. All the temporary modules are scheduled for replacement during the 2021–2022 winter maintenance period.

## Multi memory cell operation

It is clear that access to only a single memory cell of the Jungfrau pixel impairs productivity of the downstream interaction region. Faced with the accumulating delays of the AGIPD 4Mpix delivery, SPB/SFX put more effort into enabling access to the remaining 15 memory cells of the Jungfrau detector. In collaboration with PSI, the Detector and SPB/SFX groups performed systematic studies of the multi-cell operation mode.

Here, only the key findings are highlighted:

- In the case of the detector running in the adaptive gain mode, calibration of the raw data collected in the high gain is fully understood. Calibration of the medium and low gain data still poses a challenge. A large gap between pixel values corresponding to the high and medium gains points towards problems with the correct estimation of the pedestals.
- Analysis of data collected in the fixed medium gain mode yielded encouraging results. Although the lack of the incident intensity monitor at SPB/SFX prevents the absolute calibration of the detector in the fixed gain mode, it should not prevent the detector from being used successfully for SFX measurements. As the next step, the test protein crystallography experiment with Jungfrau detector using multiple memory cells at the fixed medium gain is scheduled for the first half of 2022. An absolute intensity monitor is scheduled for installation at time of writing.

## Upgrade of the detector's infrastructure

Based on the lessons learned during the first years of operation, the SPB/SFX instrument group decided to upgrade the detector. Engineers and scientists from the group are working on a new design of the Jungfrau detector and its immediate infrastructure. The conceptual engineering review was held on 10 November 2021, during which proposed solutions were presented to the engineers and scientists external to the project. The concept of the new Jungfrau 4Mpix detector is shown in Fig. 3.8. The final engineering review is planned for the beginning of 2022. The detector is scheduled for assembly during summer maintenance period of 2022. It will be commissioned and available to users in the second half of the year. Unfortunately, due to significant delays in the delivery of some critical electrical components, an intermediate solution will be implemented for the time period between the deployment of the detector in 2022 and the arrival of the desired parts in 2023.

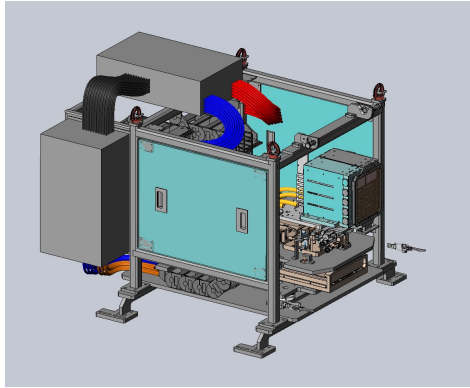


**Figure 3.8:** The Jungfrau 4Mpix during replacement of a front-end module. The specialized stand allows easier access to all of the components.

In the framework of this project, the following improvements are implemented:

- New readout boards, which will allow for calibration of the medium and low gains
- The interlock of the detector will include inputs from
  - Temperature of the cooling blocks
  - Temperature of the readout boards
  - Temperature of the coolant
  - Flow rate of the coolant
- Motorized vertical motion (40 mm travel range) of the detector head
- Adjustable limit and collision switches
- Redesigned shield motion
- Change from the TDK Lambda to MPOD power supplies
- New electrical interface to the control system and the detector diagnostics
- Detector cage providing safer hoisting and craning detector in and out of instrument

The upgrade will enable safer, more reliable, and more automated operation of the Jungfrau detector, which supports ongoing efforts to ease operational burden and focus on scientific data collection and results.

## Coming detectors

**AGIPD 4Mpix** By design, the four megapixel AGIPD (AGIPD 4Mpix) detector is planned to support operation of the downstream interaction region. At its core, the front-end module will resemble that of the AGIPD 1Mpix. Similarly, it will utilize 500  $\mu$  thick Si, 200  $\mu\text{m}$  x 200  $\mu\text{m}$  pixels, and array of capacitors will provide storage for 352 values (as per the 1Mpx version). The geometry of the FEMs will resemble the Jungfrau 4Mpix detector. The FEMs will be arranged into independently movable halves (Fig. 3.9). In contrast to the AGIPD 1Mpix at the upstream interaction region, the

entire electronics of the new AGIPD will be placed inside the vacuum chamber. The much greater dimensions of the AGIPD 4Mpix lead to a different concept for the detector motion. While the AGIPD 1Mpix remains fixed with respect to its vessel, and change in the sample-to-detector distance requires translation of the entire detector chamber, the detector plane of the AGIPD 4Mpix will move inside a stationary vessel. A great amount of heat to be dissipated from the detector combined with the in-vacuum motion poses a great challenge from the engineering point of view and is, in part, responsible for some of delays in detector delivery. According to the most recent estimates from the provider (DESY detector group), the AGIPD 4Mpix is expected to be delivered in 2023.

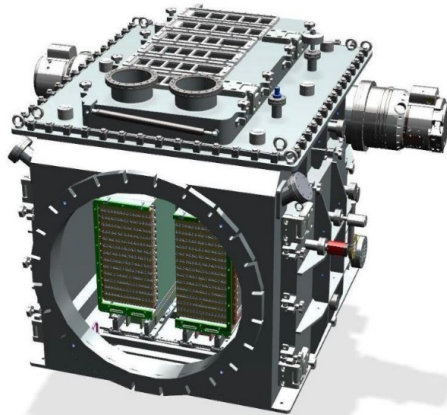


**Figure 3.9:** Model of the AGIPD 4Mpix planned for the downstream interaction region at SPB/SFX

**Gothard II** Six Gothard II detectors with 25  $\mu\text{m}$  pitch were ordered for SPB/SFX. Three of those are assigned for the X-ray diagnostics in the hutches, while the remaining three visible light sensitive units are planned to be used for the timing diagnostics.

---

## Data analysis tools for SFX, SPI, and other purposes

A particular challenge at high repetition rate XFEL facilities is making sense of the large volumes of data that can be collected, particularly 2D image data collected at high repetition rates. Different analysis steps can take place on different timescales, as it is almost impossible to both perform all desired analysis steps thoroughly and keep up with the acquisition rate overall.

In practice, a compromise between thorough analysis and immediate feedback is required. Data analysis is therefore grouped into the domains “online” (quasi live during an ongoing experiment with or without concurrent data acquisition), “near online” (analysis from file data directly or shortly after acquisition), and “offline” (any time after data acquisition, often even days or weeks after the beamtime).

## Online analysis

Online data analysis serves the main purpose of monitoring the experiment and previewing the soundness of produced data; as such, it is tightly linked to the control system. The online calibration of multi-gain megapixel area detector data can be seen as a first step of data processing and is implemented as a pipeline in the European XFEL control system, Karabo.

The major use cases in the broadest sense (SFX and SPI) at MHz rates have a fundamental similarity in that not every pulse will interact with the sample of interest. The resulting hits and misses need to be defined using the data itself. This necessitates initial processing and calibration as well as the definition of appropriate metrics for the data of interest (hits) in contrast to the background measured when no sample is present in the interaction region at the time of arrival of an X-ray pulse. The hit rate is dependent on the sample and delivery method and can routinely be less than 1%. Filtering the hits and minimizing the processing overhead for images not containing data related to the sample is a high priority and, as far as possible, common tools are used with optimized “hit” definitions for each type of experiment.

In some cases, specific analysis types are developed as part of the control system, i.e. implemented as Karabo devices, as well. An example is the pump–probe timing-jitter analysis tool described below, a collaboration between scientists from the SPB/SFX group and engineers from the Data Analysis group. Typically, data analysis within Karabo is of a general-diagnostic nature: pump–probe synchronization analysis, for instance, serves all time-resolved experiments, including the fields of SFX and SPI. Where online data analysis is to be performed by dedicated stand-alone software, it must receive the relevant data as exported from the control system. An infrastructural tool for this, called the “Karabo bridge”, has been developed by the Data Analysis group and is used at all of the European XFEL instruments, including SPB/SFX. On the client side, both a C++ and Python library exist to receive data streams over the bridge, using the ZeroMQ technology. This endpoint is currently embedded to European XFEL software tools (EXtra-foam, EXtra-metro) as well as user community-provided software (OnDA for SFX and Hummingbird for SPI).

EXtra-foam (Fast Online Analysis Monitor) [15] is a stand-alone GUI application based on a framework that provides real-time and offline data analysis (detector geometry, pump–probe, azimuthal integration, ROI, statistics, etc.) and visualization for experiments that use 2D area detectors (AGIPD, LPD, DSSC, FastCCD, JungFrau, ePix100, etc.) and 1D detectors (Gotthard, XGM, digitizer, etc.) at the European XFEL. EXtra-foam allows users to perform EDA (exploratory data analysis) in real time by “probing” the data with a combination of different analysis tools, e.g. monitoring individual pulses in a train, checking correlation, and trying different normalization methods, etc. This is particularly useful if users are not sure what the data really looks like or want to have a sanity check. EXtra-foam provides tailored data analysis configuration and visualization for specific experiments. For example, in a pump–probe setup, it allows users to choose how the pump and probe pulses are distributed (e.g. in the same train or a different train) by providing several typical “modes”. It also integrates

important plots in a single window so that users can gather abundant information at a glance. At SPB/SFX, EXtra-metro has been used for commissioning purposes as well as SAXS and fluctuation X-ray scattering user beamtimes.

EXtra-metro is a software solution for flexible user-defined online data analysis, abstracting away the processing machinery to a back-end framework (metropc), so that the actual pipeline of data transformations can be expressed as high-level, script-like Python code that becomes injected at runtime. This allows for convenient on-the-fly reprogramming of analysis workflows, with fast iterations and explicit implementations to solve a given problem in the very same moment. EXtra-metro connects to online data through a front-end device in Karabo and provides graphical visualization of results either in a separate lightweight GUI client or by sending reduced data back into the Karabo GUI. At SPB/SFX, it is increasingly used in the context of X-ray imaging and pump–probe experiment setup.

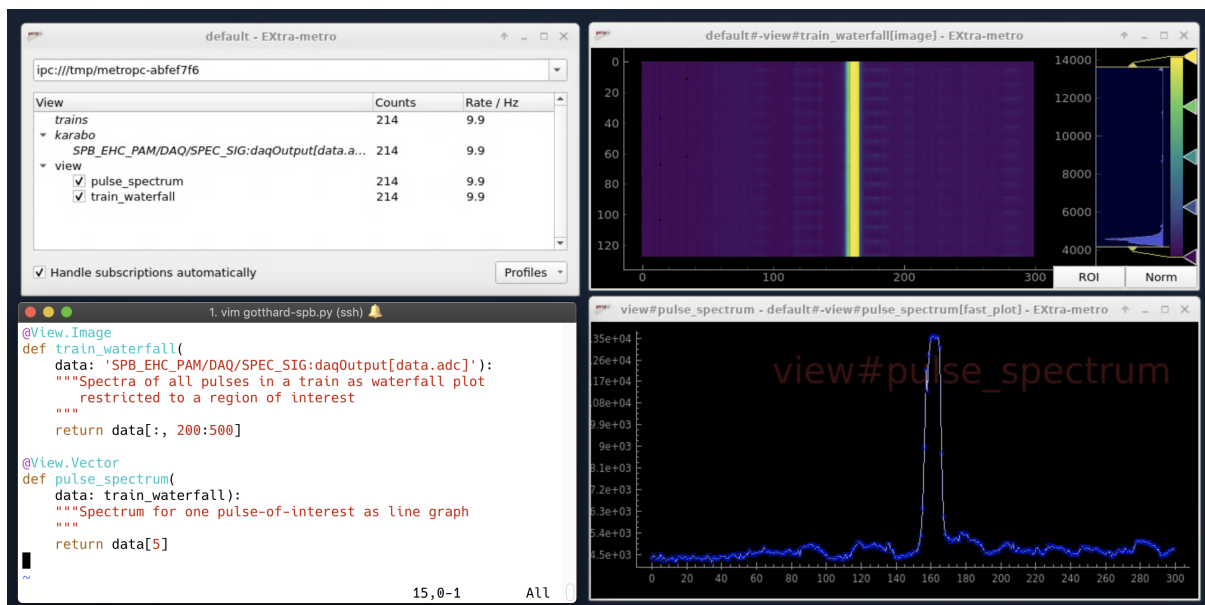


**Figure 3.10:** Example of basic EXtra-metro usage to visualize multi-pulse Gotthard detector traces from the SPB\_EHC\_PAM system. Both a 2D “waterfall” view with colour-coded intensity for all pulses in an XFEL train and a 1D line graph for one selected pulse are shown, as well as the “context” code to produce these.

## Offline analysis

For file-based SFX data processing and analysis, some well-established community software exists. The processing of “raw” (but, in case of European XFEL, already gain-corrected) pixel detector image data to structure factor intensity data in terms of peak finding, indexing, integration, scaling, and averaging is typically performed with either the CrystFEL package [54] or with the CCTBX/DIALS software [10]. The independent nature of single-shot diffraction images allows the distribution of data onto subsets of frames to be independently processed by different nodes of an HPC cluster. The

SLURM workload manager is used on the DESY HPC cluster Maxwell, including its relevant partitions for European XFEL staff and beamtime users.

In order to get closer to online data analysis in an “offline” file context, the Data Analysis group is working on pipelines to automate processing workflows, with the plan to trigger such pipelines automatically as soon as complete runs of acquired data are available at the relevant storage system. In the scope of an R&D project (an internal research and development scheme), the pipeline tool Extra-Xwiz is being developed for the SFX use case.

Currently, EXtra-xwiz serves as a wrapper around the CrystFEL software suite, with the following tasks:

- Presenting European XFEL format HDF5 data (a separate set of files per detector module) as coherent single-file “virtual” dataset (VDS) in CXI format as required by CrystFEL
- Configuring and launching (in case of multiple iterative) jobs of the CrystFEL programs *indexamajig* and *partialator* for crystallographic data reduction from raw detector images with Bragg diffraction patterns to crystallographic structure factor datasets.
- Distributing the computation onto chunks of data for parallel processing by employing the SLURM workload manager

Based on a well-annotated parameter configuration in a file—covering both input data/geometry file path specifications and CrystFEL parameters—the complete processing can be run in a fully automated fashion (Fig. 3.11), which is particularly useful for batch processing of multiple runs from identical experiment setups, given an established bad-pixel mask and CrystFEL-format detector geometry file. There are plans to include the steps of pixel outlier determination (hot pixels and other artifacts) and detector geometry optimization into the automated workflows. Xwiz features auxiliary data conversion steps for pixel masks from binary HDF5 arrays to rectangular mask objects in the geometry file and for the data layout (reference) in the geometry file from Cheetah-CXI to VDS-XCI.

One highlight from the broader analysis program was making sense of  $\approx 1$  PB of SFX data, collected in the frame of the COVID-19–related experiments during the beamtime and including the production of electron density maps. In general, for SFX users, we can now provide information that any crystallographer can make sense of, removing the need for specialist XFEL knowledge from the user.

Moreover, Xwiz has a module for multi-dimensional grid searches over the parameter space, varying different analysis aspects: peak-finding parameters, the indexing algorithm used, subsets of frames from a run, or even the version of CrystFEL, just to name some options.



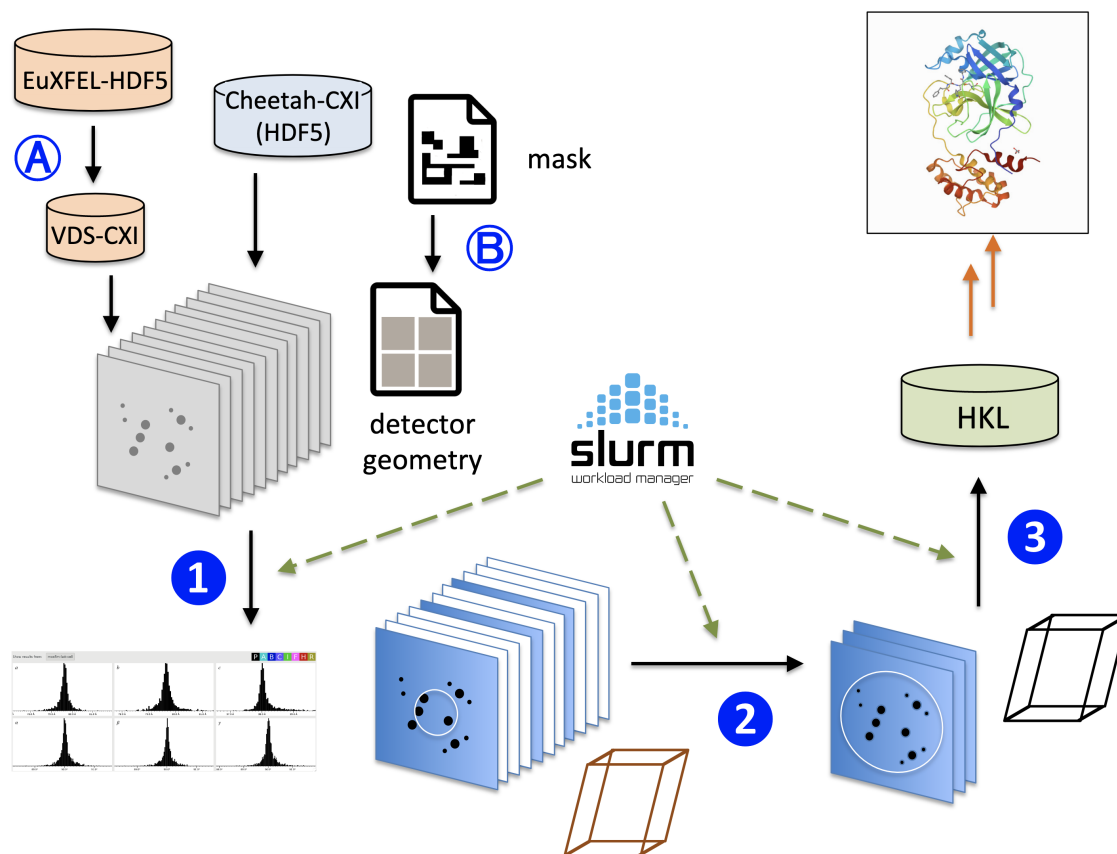


**Figure 3.11:** Schematic representation of a semi-automatic pipeline for SFX in its current implementation. Starting from HDF5 datasets in EuXFEL or Cheetah/CXI format, diffraction images are processed in three steps using CrystFEL tools, embedded in a workflow with a SLURM interface for distributed computing: (1) Initial crystallographic peak-finding and indexing of all detector images, followed by graphical determination of a crystal unit cell. (2) Peak-finding and indexing in a low-scattering-angle detector area using the preliminary unit cell, followed by selection of the indexable image subset (“crystal hit frames”) and unit cell refinement. (3) Peak-finding, indexing, and pixel intensity integration at predicted positions on a high-scattering-angle area using only the diffraction image subset, plus the refined unit cell. Crystallographic scaling and intensity averaging yields a unique reflection dataset, suited to reconstruct the macromolecular structure (not yet part of the pipeline). Preparative steps—such as (A) automatic conversion of EuXFEL data to the required CXI format in a “virtual” dataset or (B) optional import of pixel masks into the detector geometry description file—are also supported.

## **Extension to “non-standard” use-cases**

The tools presented above are developed as far as possible in a common framework to support all of the more standard use cases with minimised overheads (processing and staff support). At the same time, the possibility of optimisation for individual experiments and implementation of “user code” for specific tasks should be maintained. As such ongoing developments for optimisation of initial detector calibration and filtering combined with support for experiment specific user requests - with the caveat that implementations should be available for the wider community - give scope for supporting individual experiments as well as the development of the facility as a whole.

---

# Future developments

---

## Overview vision

Notwithstanding the relatively young age of the European XFEL and the SPB/SFX instrument, in this chapter, we present directions for medium-term development of the science possibilities presently covered by the SPB/SFX instrument. These are largely the science cases supported by the instrumentation highlighted earlier in Figure 1.2. Each of these fields—time resolved serial crystallography, single particle imaging, MHz microscopy, and the very nascent field of attempting what are traditionally low repetition rate serial crystallography experiments at MHz rates—are all now applicable to use cases in a broader scientific community, utilize the unique properties of European XFEL (including its high repetition rate, high pulse energy and higher photon energies), and have predominantly completed proof-of-principle demonstrations. In light of these benefits, ultimately, most of these applications warrant dedicated instrumentation for the improved efficiency, uptime, and experimental outcomes that come with specific hardware. This is also in line with overarching strategic ideas at European XFEL, where the need for future instruments to address more specific science capabilities will not only improve efficient and effective use of beamtime but will also improve access for new users who may not have (and should not need) a detailed background in facility-scale X-ray sources. The case for each of these science applications is made below, most urgently for serial crystallography, which offers concrete output though has specific needs for effective operation.

Even more immediately, the consolidation of best working practices and increasing automation is envisaged to reduce the human resource overheads for “standard” experiments and allow more efficient use of beamtime for collection of larger datasets, increasing the number of time points collected, statistics, and data quality parameters. These issues of automation and efficient operation are in discussion with the relevant supporting groups here at European XFEL.

In the meantime, ongoing and future planned projects of the SPB/SFX instrument group and collaborators are very broad and serve to

- Bring us towards the goal of efficient and effective use of beamtime
- Standardize the existing experiment configurations
- Extend the capabilities of the SPB/SFX instrument to enable new classes of experiments for the future

A non-exhaustive summary of the major development projects currently ongoing are detailed in this section and in Appendix ??.

---

## High repetition rate time-resolved SFX

Time-resolved SFX (TR-SFX) is an obvious scientific exploitation of the SFX capabilities of the SPB/SFX instrument, especially given the appetite for “dynamic structural biology”. See e.g. reviews by van den Bedem & Fraser [6] and Orville [38]. The goal of any TR-SFX experiment is to capture structural change during the course of a reaction or induced conformational change at appropriate temporal resolution.

The X-ray pulse structure of the European XFEL and the flexible optical laser pumping schemes available at SPB/SFX provide multiple opportunities to investigate reaction pathways on biologically relevant timescales. The combination of this experimental flexibility and fast data rate means that full reaction pathways can be investigated within reasonable experiment timeframes of a few beam shifts. The two principal experimental methods in TR-SFX are optically pumped or triggered reactions and mix-and-inject schemes.

In optically pumped schemes, a reaction or conformation change is triggered by output from a timed optical laser pulse. At SPB/SFX, a large range of pump wavelengths are available, including multi-pump schemes with ns lasers (see [29] for details). The fs pump–probe laser can deliver an arbitrary pulse pattern at the same intra-train rate as the X-ray pulses with an arbitrary delay to the X-ray pulses [39]. The time jitter (short term) between the laser and X-rays can be as low as 10 fs RMS, and the time drift (medium to long term) can be kept to a minimum, made possible by the optical locking scheme between the accelerator gun laser and the instrument pump laser [46]. User-defined laser pulse patterns allow for collecting a control, “unpumped” state at the same experiment conditions as a “pumped” or optically excited dataset, increasing the robustness of later analysis. User-defined X-ray pulse patterns offer the ability to collect diffraction with increasing delay after an initial pump. The 880ns (1.1 MHz) intra-train spacing typically used in SFX means that pump–probe delays from 1  $\mu$ s to 300  $\mu$ s can be collected in a single dataset.

Most biological systems are, however, not driven by light, and here mix-and-inject schemes may be appropriate [44]. In a mix-and-inject experiment, crystals and substrates or reagents are mixed at a well-defined point inside a delivery device, usually a more sophisticated version of the nozzle type used in other SFX experiments. For well-controlled experiments, the diffusion time of substrate through a crystal should be negligible compared to the reaction turnover time. This implies using crystals that are as small as possible; as a technique, this is very well-suited to FEL SFX instruments, which can collect analysable diffraction patterns from crystals of 100s of nm in size.

This mixing point of crystal and substrate can be altered within the nozzle design and, together with the diffusion time, this defines the time delay at which the reaction is probed by the X-ray pulse. Recent experiments at SPB/SFX have achieved delay times as low as 5 ms for crystals a few microns

in size [41]. In these cases, each X-ray pulse in a train can be considered to have probed essentially the same delay time (e.g. 5 ms + 0 to 300  $\mu$ s) and taking advantage of this allows multiple datasets with different delay settings to be collected in a few beam shifts.

Repeatable and tunable mixing nozzles are a key part of mix-and-inject experiments. New versions, based on 3D printing, are being developed within the European XFEL Sample Environment group, and we continue to accommodate advances in injector technology from the wider user community (see e.g. Knoška et al. [23]).

Multi-parameter TR-SFX experiments put high demand on instrument setup and alignment, and, to explore a large parameter space might require several changes during a single experiment week. These type of experiments would particularly benefit from close to real-time analysis. The ability to evaluate whether structural changes were visible or likely at a certain delay point or whether enough data had already been taken at a given delay point would increase the efficiency of the measurements and confidence in the data.

Notwithstanding these challenges, recent work (including work yet to be published) at SPB/SFX has shown that close to real-time analysis of large SFX datasets is not only possible, but such analysis can be used during beamtimes to make decisions relevant to live experiment design and success.

---

## **LCP and fixed-target SFX (toward high repetition rate serial crystallography of viscous or fixed samples)**

### **Sample-efficient methods are required**

SFX experiments and, in particular, SFX at MHz data collection rates, by necessity demand rapid sample delivery (for replenishment between each pulse). The consequence for this, however, is dramatically increased sample consumption (mL). Moreover, this can be highly inefficient, as the majority (more than 99%) of continuously delivered sample will pass through the interaction region while there are no X-rays—a direct consequence of the bunched time structure at the European XFEL. The amount of sample required is a significant and practical problem that is limiting for many samples (at all facilities). This is particularly so as production quantities can be highly cost- and time-limited when scaled up to be feasible for an experiment at an XFEL. A related issue is that many of the most scientifically interesting samples are sensitive or difficult to produce, and this is perhaps part of the reason they have not already been studied using traditional methods. Even for samples that can be scaled up by “only” accepting increased costs, this is not necessarily feasible for all groups currently engaged in XFEL research and is a preventative barrier, particularly for those with interesting science new to the field.

High viscosity jets can be more sample-efficient, utilizing slower injection speeds to more effectively use the sample. However, there is still a significant sample requirement for sample injection testing and, as the jet is larger than the beam, the injected sample is also not most efficiently used.

Fixed-target sample delivery is the most efficient method in terms of use of the available sample. Minimal testing is needed in most cases. Appropriate sample handling can keep the crystals hydrated even in the absence of excess mother liquor, which is preferable for data collection. Efficient chip loading can provide hit rates in excess of 90%, and nearly all crystals loaded onto a chip can be presented to the X-rays for data collection.

While high viscosity jets and fixed targets have two key benefits (lower sample consumption and preferred media for many interesting membrane proteins), such sample delivery schemes are inherently limited if only naively implemented at the European XFEL. This is fundamentally due to the European XFEL time structure, which forces a 10 Hz operation for experiments in this modality (these samples, in their simplest form, do not refresh quickly enough for high repetition rate operation). This case compares unfavourably with other XFEL facilities operating at 120 Hz, or even 60 Hz, as all other operating, normally conducting XFELs do today. Nevertheless, we will later outline methods that can make such delivery methods indeed higher repetition rate compatible, and hence very attractive at high repetition rate XFEL facilities, such as the European XFEL.

## **Path to automation**

Sample injection (both low and high viscosity) requires careful preparation, including jetting tests and optimization of delivery media parameters, crystal size, and concentration to minimize clogging. Furthermore, jets, being potentially unstable and prone to clogging, cannot always be reliably operated without supervision. These issues are addressed both by developments and activities within the SEC group as well as by user groups. Nevertheless, injection methods have specific challenges when aiming toward full automation, which would, in turn, reduce the barrier of entry for new and non-expert users.

Fixed-target sample delivery methods, on the other hand, are the standard for the majority of synchrotron crystallography endstations and potentially much simpler to automate. Although the specific methods of mounting the samples vary, the high level of automation (and sample tracking) facilitated by the fixed sample can support extremely high throughput with relatively low direct staff involvement [9; 47]. Moreover, serial data collection methods are increasingly employed at synchrotrons using fixed-targets arrays of micro-crystals (adaptation of mesh scans) with a high degree of automation. An automated instrument for SFX at the European XFEL based on fixed-target sample delivery would be highly beneficial to the community, not only for efficient data collection but also to facilitate crystal screening and testing independent of the ability to jet the sample reliably.

The downstream interaction region IRDa has now been commissioned, and 10 Hz operation at atmospheric pressure has been shown to be reliable. However, as the greater SPB/SFX instrument supports a very wide variety of science with varied instrument configurations, the installation and alignment overhead to set up IRDa for SFX is detrimental to efficiency and limits increasing the level of automation. These configuration changes are a consequence of the physical constraints for these other (also applicable and successful) experiments and are unavoidable even if efficient dual operation could be implemented with differing repetition rates. A dedicated location for testing IRDa apparatus and experiment setups outside the SPB/SFX experiment hutch would facilitate automation developments, though they would still not overcome the installation and reconfiguration overheads. Below (Section 4.3.3.2) we propose a way to address both this experimental overhead as well as provide a path to MHz-capable SFX for fixed-target and high-viscosity sample delivery systems, opening up the attractive world of (in viscous media) membrane protein crystallography to efficient interrogation by the European XFEL beam.

## **MHz SFX from “slow” samples**

Fixed targets and high viscosity injection, while amenable for the highly scientifically interesting and challenging samples, are limited by the rate at which fresh sample can be presented to the XFEL pulses. For example, the roadrunner design that is installed at SPB/SFX (IRDa) is capable of kHz data collection with synchrotron radiation [48]. However, this is still too slow to take advantage of the the European XFEL pulse train; therefore, these sample delivery methods are presently limited to only 10 Hz (single pulse per train).

Acceleration (and deceleration) of sample for a MHz scanning rate on a fixed target is a fundamental practical limitation and one of the reasons for the adoption of fast liquid injection as the preferred sample delivery method for MHz SFX. As high viscosity jets are also not able to be accelerated to the required speeds for MHz operation, moving the *beam* instead of the sample is a viable and achievable alternative, which could allow sample-efficient data collection at high repetition rates. The “holy grail” goal is to have the best of both worlds: minimal sample consumption, while still benefiting from data collection at very high repetition rates, which complete datasets in a fraction of the experiment time required at lower repetition rate facilities).

## **Beam sweeping concept**

Deflecting the XFEL beam via grazing incidence mirrors can provide angular displacements on the order of microradians, resulting in positional changes relative to the distance between mirrors and measurement plane. By sweeping a grazing incident mirror upstream of the sample plane, the beam can traverse fixed- and slow-sample delivery methods and illuminate “fresh” sample (a new location) at MHz rates. While oscillating such a mirror back and forth would require rapid acceleration and

potentially result in problematic vibrations, the suggested concept is to rotate a mirror at up to 10 Hz to sweep the beam across the sample during the train.

In the framework of a project funded by the Röntgen-Ångström Cluster, in close collaboration with the FS-CFEL-1/BMX group of Alke Meents, the development of this concept of beam sweeping to enable data collation with a fixed target and other slow delivery methods at the MHz repetition rate of the European XFEL facility is underway. Utilizing radial speeds of up to 6 rad/sec, two consecutive X-ray pulses are reflected at different angles from an X-ray mirror. Thus, individual crystals located in adjacent (vertical) positions in a sample holder will be exposed to separate pulses in the train. The fixed target is then able to be translated transversely at 10 Hz (which is already achieved), and data from individual crystals is collected at MHz rates as the beam sweeps over the sample vertically. Separation of the 4 micron diameter focused beam by 5 micron steps would allow measurement of separate crystals and, over the train (assuming 352 pulses maximum frame rate of AGIPD), the separation between the first and last pulses would be on the order of 1.75 mm. However, the possibility of radiation effects from previous pulses in neighbouring pores cannot be discounted and necessitates an increased pore spacing of up to 20  $\mu\text{m}$  (used in other studies [42; 48]), where radiation effects have not been observed. The resulting vertical displacement during the train in this case would be 7 mm.

### **Route to implementation**

The design of the beam-sweeping mirror is underway, and the construction and testing of the prototype is planned to begin in 2022. Validation of the prototype at synchrotron sources is envisaged to begin in late 2022 and early 2023 in preparation for testing at the SPB/SFX instrument. To facilitate this ongoing development and its commissioning and implementation, an expression of interest for a long-term proposal at the European XFEL as part of the call for proposals for Run 8 (deadline 3 December 2021) was submitted. This project is in line with the remit for the long-term proposal and will require an ongoing programme of testing to integrate building new instrumentation and new capabilities for the benefit of the user community.

Additionally, an R&D project as part of the European XFEL R&D programme, in collaboration with EMBL Hamburg and the Moscow Institute for Science and Technology (MIPT), has been implemented for systematic studies for SFX on membrane proteins (SSFEMP). The aim of this is optimize preparation, delivery, and data collection protocols for membrane proteins, including comparison and optimization of data collection approaches with fixed targets and high viscosity injection.

By combining the optimized workflows (for sample preparation, handling, and delivery) developed in the SSFEMP project with access to an optimized, automated instrument for sample efficient SFX samples, there is a route to enable access for not only new user groups but for samples that are not currently amenable to XFEL studies. Extending this beyond 10 Hz in the future with beam sweeping



or CW operation would provide unprecedented access, data collection, and extension of XFEL data collection to the wider user and structural biology community.

Finally, on a practical note, to address the obvious need for more beamtime for dedicated SFX at the European XFEL as well as to reduce the operational overhead of setting up the existing atmospheric pressure SFX sample environment, we propose to move the IRDa hardware (CRL lens stack and attenuator, sonic delay line, in-Helio YAG screen, RoadRunner, Jungfrau4M) to a dedicated instrument in the medium-term future. This is consistent with the European XFEL strategy process, which foresees eight (8) instruments in the medium-term future (an increase of one from the six presently in operation and the seventh under construction). This would allow not only user operation for standard SFX measurements without regular reconfiguration but also continued work on the realization of high repetition rate SFX on fixed and viscous samples. Operation of this dedicated fixed-target SFX station could simply be for one or two days per week, while configuration changes are underway in the other hutches, where even 10 Hz operation would be of direct benefit to the user programme and the number of deliverable hours. Furthermore, once the beam sweeping methodology is commissioned, such an endstation could operate almost transparently in parallel with other instrumentation. A movable mirror in the beam transport (in a tunnel) could pick off one train intermittently at a very low frequency. This would essentially reduce the delivered beam to parallel instruments by a negligible amount, but would allow such an SFX instrument to operate for almost all periods of time when beam is delivered. For example, one train “picked” every few seconds could provide competitive SFX data rates, and only a few percent reduction of total fluence (or number of pulses) to parallel instruments.

---

## XFEL single particle imaging

XFELs are perhaps synonymous, for some, with the idea of X-ray single particle imaging (SPI)—the concept that the structure of non-crystalline, yet mostly reproducible particles, can be determined to ideally atomic resolution through utilizing the sheer brilliance of individual XFEL pulses along with the spatial coherence of such a source [35; 3; 8].

The early user experiments at SPB/SFX have shown that we, indeed, have a good foundation for achieving high-resolution reconstructions from SPI experiments. Furthermore, the unique high repetition rate at the European XFEL confers significant benefits on this photon- and pulse-hungry technique [5; 58]. Nevertheless, there are a few outstanding issues to overcome before sub-nm resolutions can realistically be achieved. Perhaps most important is the parasitic diffraction signal from the carrier gas that is used to transport and focus the particles into a narrow beam at the interaction region. To enable the electrospray-based formation of droplets small enough to avoid substantial contamination from non-evaporative buffer compounds in a sample solution, a mixture of 90% N<sub>2</sub> and 10% CO<sub>2</sub> is used as the carrier gas. The scattering from these relatively heavy gas molecules creates a background scattering signal that adds incoherently to the sample diffraction. As the gas molecules are significantly smaller than the sample particles, this background signal drops off much

slower in the high-resolution regime compared to the sample signal. Thus, at high momentum transfer,  $q$ , the sample signal is drowned out by the gas scattering, and it is virtually impossible to discriminate between the two. The main effect of this background signal is the inability to accurately orient the 2D Fourier slices inside the full 3D domain, which, in turn, limits the achievable resolution even after background subtraction.

To overcome this signal contamination, we have developed, with the guidance of gas-mixing simulations, a 3D printed micro-fluidic electrospray capillary tip that incorporates a local low-flow  $N_2/CO_2$  atmosphere close to the Taylor cone, while the bulk of the transport gas is replaced with a He flow that transports the particles. Lab-based tests indicate that we can achieve a decrease close to a factor of 10 in background scattering with this scheme, although we still have development work to do before we are ready to deploy these devices. In a similar manner, we are working on improving the electrospray throughput. The standard electrospray geometry has been shown to have an intrinsic transmission of less than 10%, while relatively small changes in the design can bring the transmission up to 80% [16]. This should translate directly to an increased number of collected diffraction patterns and, hence, achievable resolution.

Another source of parasitic scattering comes from the beamline, especially with the highly divergent nano-KB beam. Here the solution is to re-imagine the beam cleanup slit-configuration and integrate sets of miniature slit-blades placed a few cm away from the interaction region. These have, at the time of writing, just been integrated into the sample chamber at SPB/SFX and are presently in test. This compares favourably to the 40 cm distance we previously had to the closest slits. This will enable us to achieve a proper beam cleanup configuration [21] also with the nano-focused beam.

In summary, we expect to see substantial improvements already in the short term with regards to the number of diffraction patterns we can collect as well as the data quality. Both of these gains will translate directly to higher achievable resolution.

Strategically, it is fair to ask what role single particle imaging can play at XFELs. There have been criticisms of SPI using XFELs from both within the XFEL community and also from the electron microscopy community, where static structures of biomolecules to applicable resolutions are an increasing success story. Here we propose to position SPB/SFX and the European XFEL to capitalize on present applications that can be performed today as well as being able to drive and take advantage of developments that may broaden XFEL SPI's applicability in the future. Today, SPI of higher atomic number nanoparticles (NPs) from heterogeneous populations is feasible, in no small part because of the unique, high repetition rate at the European XFEL. This capability potentially has a breadth of applications from optical behaviour of NPs, to quantitatively studying the structural heterogeneity of catalyst NPs, and much more. Simultaneously, the development of SPI will enable European XFEL to remain open to the possibility of SPI on biological particles in future, notwithstanding the present signal-to-background challenges for these lower atomic number systems we observe today. This remains an attractive, if further off, goal, as these particles can be delivered in number at the

European XFEL, in aqueous solutions and potentially even with time resolution. In the good news, as the instrumentation for both present materials' science applications and developing biological questions is essentially identical, we can pursue the latter, stretching goals while still harvesting science in materials science in what is now almost routine operation.

## MHz X-ray microscopy: Route towards 3D information and hard X-ray acquisition

Motivated by early results at SPB/SFX (see Section 2.4), we have performed several upgrades and improvements that resulted in significantly superior image quality and have facilitated data recording procedures. It is now possible to use the direct beam (Fig. 4.1) from the horizontal offset mirrors, which provides smooth illumination (Fig. 4.2). This is in contrast to previous, parasitic illumination delivered by the micron focusing KB (MKB) optics.

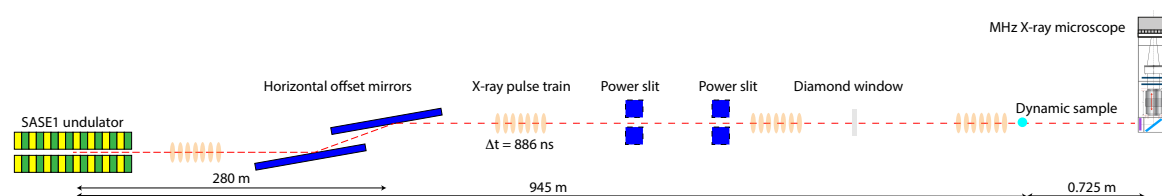


**Figure 4.1:** Direct beam configuration for MHz X-ray microscopy at the SPB/SFX instrument

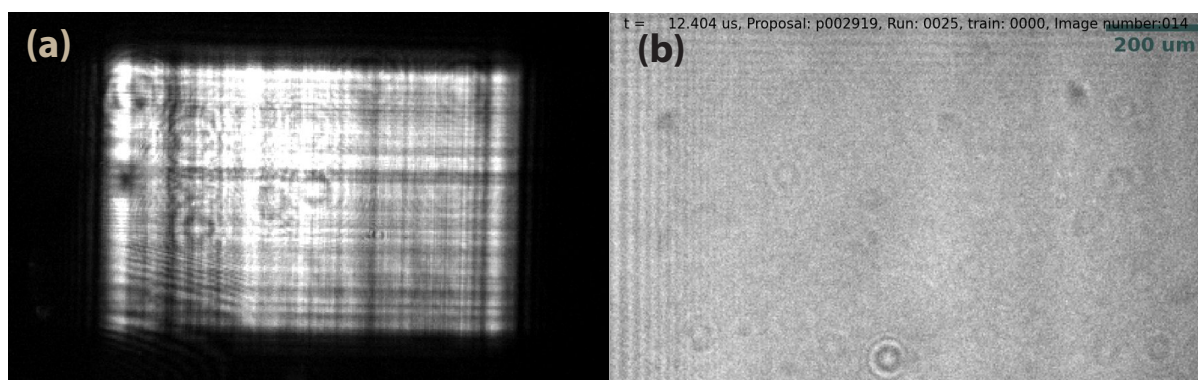


**Figure 4.2:** Images of the beam illumination using (a) the previous parasitic MKB illumination and (b) the direct beam illumination from the more recent experiment.

A recent pilot MHz microscopy experiment at SPB/SFX using 24 keV photons achieved, for the first time,  $\approx 800 \mu\text{J}$  per pulse. Using these conditions time dynamics in aluminium samples (see Fig. 4.3) and the pump laser driven explosion of a droplet held using acoustic levitation were recorded with unprecedented contrast.

We have demonstrated that XFEL MHz projection microscopy provides a unique tool to reveal fast stochastic dynamics showing superior contrast to synchrotron MHz microscopy. However, with just a

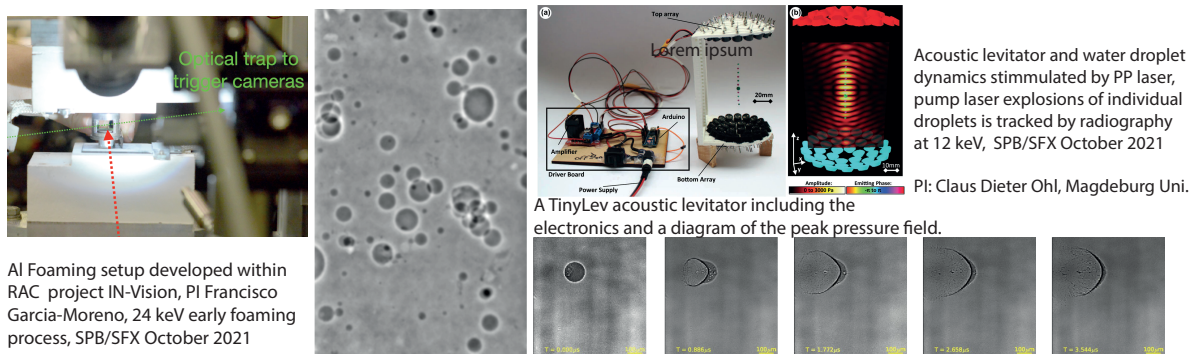


**Figure 4.3:** Example data recorded at the SPB/SFX instrument using direct beam illumination with 24 keV photons at  $\approx 800 \mu\text{J}$  per pulse showing an image of an Al foaming process (*left*) and PP laser driven explosion of a water droplet trapped in an acoustic levitator (*right*).

single projection, only simple objects can be studied, as complex dynamic objects might be difficult to interpret. Access to 3D information via conventional approaches is not applicable if one needs sampling of 3D frames with  $>1\text{kHz}$  repetition rates—one can simply not “spin” samples fast enough for traditional tomography at these rates. Due to XFELs having three orders of magnitude greater number of photons per pulse compared to synchrotrons and  $\approx 20\text{ eV}$  bandwidth, along with divergences in both orthogonal directions comparable to the angular acceptances of diffracting optics, the SASE1 source provides enough photons to employ crystal optics as beam splitters. Each splitter can redirect a portion of the beam ( $\approx 1 \times 10^{10}$  photons) through a point on the sample plane from a different relative angle. Such “views” will be imaged by MHz X-ray microscopes, and 3D information for each X-ray pulse will be recovered by software processing to provide a 4D sequence.

We have proposed two splitter systems and obtained third-party funding to enable their development. One is based on a Laue multi-beam splitter optimal for seeded beams, and a second (more recent design) is better suited for broader spectrum beams and optimized for SASE1 beams. The first design is currently characterised at synchrotrons, and the second design has already undergone first characterisation at the SPB/SFX instrument, providing promising results. These developments are proposed and driven by the Center for Free-Electron Laser Science (CFEL at DESY) and Lund University, in close collaboration with the European XFEL SPB/SFX instrument group and Industrial Liaison Office (ILO). Early developments are supported by the ongoing projects RAC INVISION 2020 (Total 1.5 M€) and an internal European XFEL R&D grant for MHz Microscopy (2021, 800 k€). Recently awarded grants ERC 3DX-FLASH 948426 (Lund University 2 M€) and EIC Pathfinder MHz-TOMOSCOPY (Coordinated by DESY, 3.5 M€) provide a significant boost to this development and will deliver a multi-projection MHz rate microscopy prototype that will be applied for the characterization of wet cavitation peening processes as an initial demonstration. The MHz-TOMOSCOPY consortium aims to build the new user base for microscopy applications at the European XFEL SPB/SFX instrument, which will enhance the user community of European XFEL and propose a dedicated endstation for the European XFEL.

The unique repetition rate and higher photon energy range, along with the plethora of scientific and industrially relevant systems that can be studied, make MHz microscopy and obvious development for European XFEL and a key plank in any medium-term plans for future development and dedicated instrumentation.

---

## Form factor recovery from biological macromolecules in solution

Small angle X-ray scattering (SAXS) methods are of great interest for understanding complex biological systems. From single particle imaging and fluctuation scattering up to and including solution scattering, the instrument geometry and constraints on the data are very similar. The main difference between these related techniques is the sample concentrations used and, therefore, the choice of sample delivery methods. SAXS experiments have been previously undertaken at XFELs and useful time-resolved data collected. However, to date, the results were obtained by subtracting the dark (unilluminated) signal from the pumped (laser excited) data, resulting in a *difference* curve that can be interpreted using *a-priori* information [4; 27]. To our knowledge, form factor recovery was not achieved until now because of difficulties associated with achieving reliable background subtractions, due to fluctuations in the X-ray source and sample delivery at XFELs (a natural consideration, given that both XFEL sources and sample delivery methods are often highly variable).

Direct duplication of experiment setups for solution scattering at synchrotrons to XFELs is not feasible due to the power per pulse of the XFELs. The rapid vapourization induced and resulting explosion, which are capable of destroying the sample containing capillary commonly used for sample delivery at synchrotrons, prevents this approach. Delivery of liquid-based samples at XFELs using gas dynamic virtual nozzles (GDVNs) enables sample replenishment (re-establishing the interrupted jet) between adjacent pulses. While GDVN liquid jets with water or homogeneous protein solutions are much more stable than with crystal slurries, they are still subject to instabilities. The observed scattering from shot to shot varies, as the jet and X-ray pulse intersect slightly differently, giving variation in incidence angle (and resulting flares), variation in path length due to movement from the centre of the jet, and variation in the jet thickness. Another complication is the possibility of interaction of subsequent pulses with debris from the exploding jet contributing to the observed scattering signal.

A collaborative effort (EMBL Hamburg, CFEL, and European XFEL) during the special rapid access call for COVID research has now provided proof of principle of the recovery of validated form factors from proteins in solution using XFEL pulses (paper in preparation). Taking advantage of the MHz repetition rate and the amount of data collected enabled statistical analysis of the obtained data, and using filtering and outlier rejection, shot-to-shot variations could be excluded from the average of the buffer and sample scattering, providing more reliable subtractions. Using systematic optimization of sample delivery, and the instrument parameters using online feedback from data processing, optimized experiment conditions were found *and* data could be collected from a number of samples.

Standards and proteins of interest were measured. Comparison of the same samples collected using an XFEL source and conventional synchrotron data collection, along with complementary measurements of samples using lab-based techniques, enabled validation of the resulting data from the SPB/SFX instrument.

Maintaining stable background scattering such that it can be reliably subtracted remains challenging. Further work to increase the reliability and improve the scattering signal and repetition rate, while avoiding the collection of signal from debris, will facilitate future use of this technique. The key aim is twofold: time-resolved studies at shorter timescales and measurements from ultradilute systems beyond what can be achieved at current synchrotron sources. A proposal for a follow-up experiment to build on the success of the recent proof of principle has been submitted as part of the ongoing collaboration to develop and exploit XFEL-SAS.

---

## **FXS – Fluctuation X-ray scattering**

Fluctuation X-ray scattering (FXS) is a technique that aims to recover the structure of biological particles from solution X-ray scattering [20; 24]. FXS proposes an alternative way for biological structure determination when more conventional serial crystallography or single-particle imaging (SPI) with an XFEL cannot be applied. This includes cases in which crystalline samples cannot be produced (e.g. for membrane proteins) or a single bioparticle is too small to be a subject of SPI. FXS relies on the detection of measurable angular correlations of photons scattered from bioparticles in solution, which are used as an additional source of information for structure determination. Model-based analyses or iterative phase retrieval can be applied to obtain information about structure of a bioparticle [14; 25; 40].

In terms of experimental realization, FXS is, at first glance, similar to small-angle X-ray scattering (SAXS) in which X-ray scattering is collected from many reproducible copies of a biological sample in solution. However, the request to measure angular intensity fluctuations imposes restrictions on the X-ray pulse duration, which should be shorter than the characteristic rotational diffusion time of bioparticles in solution [20]. This allows the avoidance of orientational averaging of fluctuations due to rotational diffusion of particles, characteristic of conventional SAXS measurements. Further contrast improvement in solution FXS can be achieved by optimizing the number of particles illuminated with the incident X-ray beam, which typically requires nanofocusing X-ray optics. High photon fluences are very beneficial in this case in order to measure sufficient scattering from a limited amount of weakly-scattering material in a short period of time. The eventual SNR can be improved by averaging the correlation functions over a large measured dataset (typically on the order of 100 scattering patterns). Therefore, availability of ultrashort and ultrabright focused pulses, combined with the possibility to record scattering data at a MHz repetition rate, make the SPB/SFX instrument especially suitable for FXS experiments. With this capacity, one can potentially collect an FXS dataset faster than at any other operating XFEL facility in the world.

Recent theoretical and experimental advances demonstrated the applicability of FXS to other research problems, e.g. structure characterization of disordered materials, crystallization studies, ultrafast structure dynamics [31; 51; 36]. First FXS experiments have been recently carried out at the SPB/SFX instrument; data evaluation is in progress. As the experimental conditions for FXS are readily realized at SPB/SFX, in the context of both SAXS and SPI, it is straightforward to enable FXS research too.





# Retrospective: Metrics and the user community

We note here various metrics for user operation, the SPB/SFX user community, and research output using beam at SPB/SFX since operation started in 2017. What is readily seen is that SPB/SFX attracts a diverse user community from all of the European XFEL member countries as well as from places further abroad, such as the USA, China, and Australia. The instrument has a healthy over-subscription ratio, though improving access—particularly for new users—is still needed, given the level of competition for beamtime. Finally, the instrument’s publication metrics, e.g. papers produced using the European XFEL beam, demonstrate a factor of two to three more papers per year of operation than the European XFEL mean, reflecting the highly productive, goal-oriented approach at SPB/SFX.

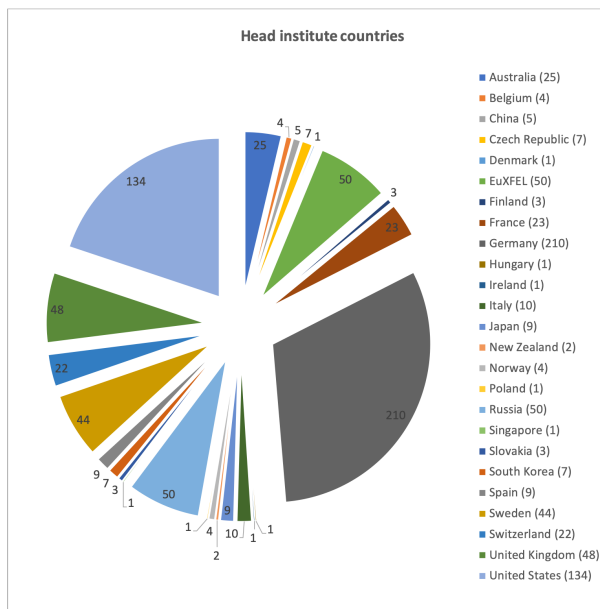


**Figure 5.1:** Head institute countries (2017–2021). The "head institute" here refers to the primary institute of a user.

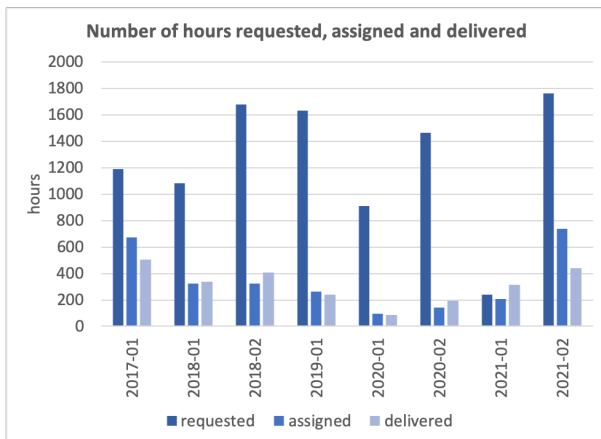


**Figure 5.2:** Number of hours of beamtime requested, assigned, and delivered by cycle (2017–2021)

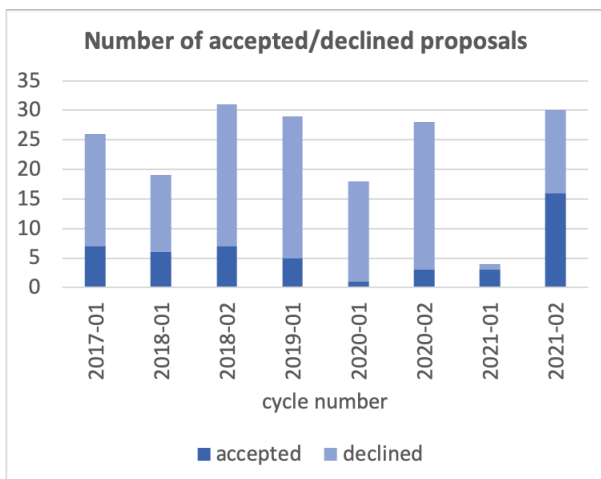


**Figure 5.3:** Number of proposals accepted and declined (2017–2021)

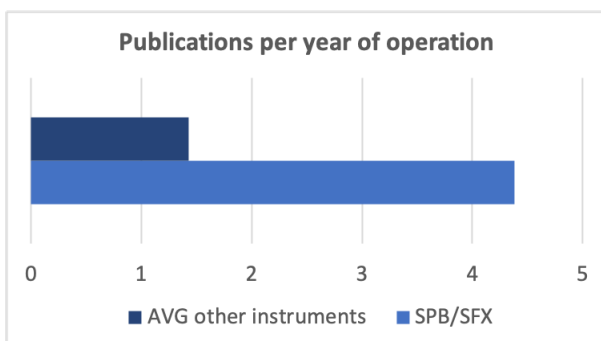


**Figure 5.4:** Papers published from work using beam at the European XFEL: SPB/SFX compared to the mean of the other five instruments of the facility (Sept 2021).

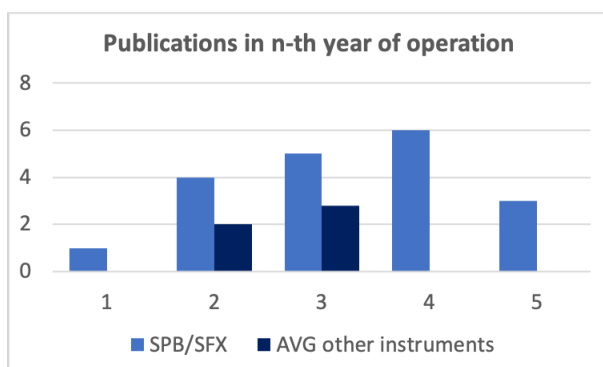


**Figure 5.5:** Number of papers using beam at European XFEL: SPB/SFX and other European XFEL instruments by year since their respective start of operation

**Table 5.1:** Overview of all instruments at the European XFEL and their dates of first operation

Instrument	Date of first operation	Years in operation in March 2022
SPB/SFX	September 2017	4.5
FXE	September 2017	4.5
SQS	November 2018	3.4
SCS	December 2018	3.3
MID	March 2019	3.0
HED	May 2019	2.9

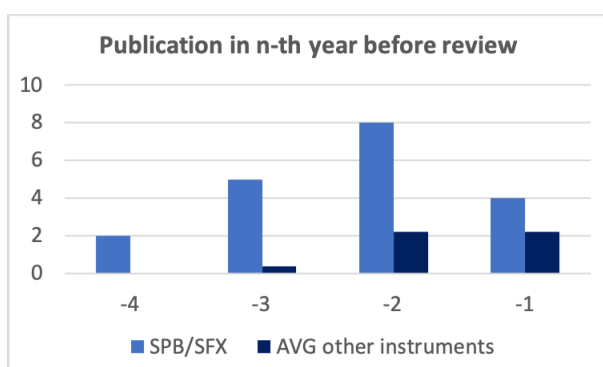


**Figure 5.6:** Number of publications using beam at SPB/SFX and other European XFEL instruments by year prior to this review (Year -1: Publication date between March 2020 and February 2021; Year -2: Publication date between March 2019 and February 2020; etc.)

---

## List of papers produced using beam

In Tab. 5.2 and 5.3, we provide for reference a non-exhaustive list of papers that have been produced to date which include data produced at the SPB/SFX instrument of the European XFEL. A selection of the most relevant publicly available papers is included in Appendix B.

**Table 5.2:** List of papers produced using beam at SPB/SFX

No	Date of publication	Publication details
1	Aug. 2018	M.L. Grünbein et al.: Megahertz data collection from protein microcrystals at an X-ray free-electron laser, <i>Nat. Commun.</i> 9 (1), 3487 (2018)
2	Oct. 2018	M.O. Wiedorn et al.: Megahertz serial crystallography, <i>Nat. Commun.</i> 9 (1), 4025 (2018)
3	Apr. 2019	M.L. Grünbein et al.: MHz data collection of a microcrystalline mixture of different jack bean proteins, <i>Sci. Data</i> 6 (1), 18
4	Apr. 2019	H.J. Kirkwood et al.: Initial observations of the femtosecond timing jitter at the European XFEL, <i>Opt. Lett.</i> 44 (7), 1650–1653 (2019)
5	Aug. 2019	P. Vagovic et al.: Megahertz x-ray microscopy at x-ray free-electron laser and synchrotron sources, <i>Optica</i> 6 (9), 1106
6	Nov. 2019	C. Gisriel et al.: Membrane protein megahertz crystallography at the European XFEL, <i>Nat. Commun.</i> 10 (1), 5021
7	Dec. 2019	O. Yevanov et al.: Evaluation of serial crystallographic structure determination within megahertz pulse trains, <i>Struct. Dyn.</i> 6, 064702
8	May. 2020	G. Mills et al.: First Experiments in Structural Biology at the European X-ray Free-Electron Laser, <i>Appl. Sci.</i> 2020, 10(10), 3642
9	May. 2020	E. Sobolev et al.: Megahertz single-particle imaging at the European XFEL, <i>Commun. Phys.</i> 3, 97 (2020)
10	Jun. 2020	T. Sato et al.: Femtosecond timing synchronization at megahertz repetition rates for an x-ray free-electron laser, <i>Optica</i> 7 (6), 716 (2020)
11	Sep. 2020	F. Lehmkuhler et al.: Emergence of anomalous dynamics in soft matter probed at the European XFEL, <i>PNAS</i> 117 (39), 24110–24111
12	Sep. 2020	A. Echelmeier et al.: Segmented flow generator for serial crystallography at the European X-ray free electron laser, <i>Nat Commun</i> 11 (1), 4511 (2020)

**Table 5.3:** List of papers produced using beam at SPB/SFX (continued)

No	Date of publication	Publication details
13	Nov. 2020	S. Pandey et al.: Time-resolved serial femtosecond crystallography at the European XFEL, <i>Nat. Methods</i> 17 (1), 73–78 (2020)
14	Dec. 2020	A. Gorel et al.: Shock Damage Analysis in Serial Femtosecond Crystallography Data Collected at MHz X-ray Free-Electron Lasers, <i>Crystals</i> 10 (12), 1145 (2020)
15	Jan. 2021	K. Ayyer et al.: 3D diffractive imaging of nanoparticle ensembles using an x-ray laser, <i>Optica</i> 8 (1), 15 (2021)
16	Jul. 2021	F. Dallari et al.: Microsecond hydrodynamic interactions in dense colloidal dispersions probed at the European XFEL, <i>IUCrJ</i> 8 (5), 775-783 (2021)
17	Sep. 2021	S. Pandey et al.: Observation of substrate diffusion and ligand binding in enzyme crystals using high-repetition-rate mix-and-inject serial crystallography, <i>IUCrJ</i> 8(6) (2021)
18	Sep. 2021	M. Hadian-Jazi et al.: Data reduction for serial crystallography using a robust peak finder, <i>Journal of Applied Crystallography</i> 54(5) (2021)
19	Feb. 2022	D. Doppler et al.: Co-flow injection for serial crystallography at X-ray free-electron lasers, <i>Journal of Applied Crystallography</i> 55, 1-13 (2022)
20	Mar. 2022	Y. Zhuang et al.: Unsupervised learning approaches to characterize heterogeneous samples using X-ray single particle imaging , <i>IUCrJ</i> (2022)
21	Mar. 2022	M. Vakili et al.: 3D printed devices and infrastructure for liquid sample delivery at the European XFEL, <i>J. Synchrotron Rad.</i> 29(2) (2022)
22	Mar. 2022	H. Kirkwood et al.: A multi-million image Serial Femtosecond Crystallography dataset collected at the European XFEL, <i>Scientific Data</i> , accepted (2022)

---

## List of all papers from group by year

Since 2015, a total of 119 articles have been published by the group (as of 8 Dec. 2021), with a further 6 preprints currently in review. Tab. 5.4 shows that the number of articles per year has steadily increased with time. Full details of all articles can be found [here](#). The table also shows a number of other publication types, including proceedings (10), preprints (6), posters (5), reports (3), talks (2), and books (2). A full list of all SPB/SFX publications can be found in the European XFEL Publication Database.

**Table 5.4:** Overview of papers produced by SPB/SFX group

Year	Number of published articles	Number of other publications
2015	4	2
2016	4	3
2017	9	4
2018	11	3
2019	15	1
2020	21	4
2021	11	4

---

# SFX UC contributions and next steps

The Serial Femtosecond Crystallography User Consortium (SFX UC) is dedicated to enhancing the life science capabilities of the Single Particles, Clusters, and Biomolecules & Serial Femtosecond Crystallography (SPB/SFX) instrument of the European XFEL. The consortium has provided scientific and technical expertise during the establishment of the instrument, has generated financing to expand the experimental capabilities of the instrument, and has created a network for the scientific user community in Europe and beyond. The scientific scope of the SFX UC emphasises the study of biological objects using XFEL radiation. This scope covers not only the study of microcrystals of macromolecules through serial femtosecond crystallography (SFX) and time-resolved SFX (TR-SFX), but also coherent diffractive imaging of single particles of macromolecular complexes including viruses, organelles, up to and including living cells.

In the next phase of the project, the SFX UC expects to reaffirm the successful establishment of the SPB/SFX instrument by lowering entry barriers to new users for a class of relatively standardized experiments and by continuing to push the limits of what is possible in life science using XFEL radiation. By volunteering scientific expertise, providing novel ideas that open up new scientific concepts, and critically over-viewing the technical capabilities and support structure of the instrument, we will support the growth of the user community. The SFX UC will continue to assist in acquiring and deploying new instrumentation and technologies, such as a 4 Mpixel AGIPD, following on from the significant contributions made in the first phase.

The consortium believes that it is critical for the SPB/SFX instrument to maintain competitive capabilities for SFX and TR-SFX, as these are the most widely used applications of XFEL radiation in the life sciences. Instrument reliability, ease of use and a highly effective duty cycle are considered priorities as these applications become increasingly streamlined. This vision includes the development of automation for sample delivery wherever appropriate. Moreover, as the field of time-resolved crystallography studies expands beyond the scope of naturally light-driven biological systems, it will be important to develop capability in mixing studies, temperature-controlled studies and the use of caged compounds.

Another aspect of the consortium's focus is efficient use of the sample and the available beamtime. This entails optimisation of the injection parameters and exploration of alternative approaches to enable projects where sample production is the limiting factor while maintaining MHz data collection rates. The scientific capabilities of sample environments are a critical part of any TR-SFX study and include mixing microjets, liquid and high-viscosity microjets, and fixed target systems. Several members of the SFX UC have been leading many of these innovations and can work with the SPB/SFX group to expand the scientific capability of the instrument. The SFX UC can also assist in the planning and development of potential future instruments that may be designed to meet the needs



**Figure 6.1:** SFX Users' Consortium funding partners.

of the TR-SFX community, while expanding the overall user support capabilities of European XFEL.

A second major entry barrier for new and experienced users is the overhead required for processing the large datasets and their subsequent analysis. It is clear that an overwhelming majority of users will require the support of European XFEL computing capabilities to be able to handle very large datasets in an efficient way. The SFX UC has a role to play by assisting with the development of streamlined protocols from the data being collected to the calculation of electron density, by incorporating appropriate quality control measures to guide users as they assess the scientific content of the experimental observations, and by training young scientists in data processing and analysis of SFX data. It is noteworthy that SFX UC members have been leading in the provision of open access software that fulfils these goals and are already collaborating very closely with data analysis experts at European XFEL to deploy these tools.

In parallel, the SFX UC will continue to push the limits of what is possible with XFEL radiation. The high repetition rates of the European XFEL create unique possibilities for high-throughput data collection of coherent diffraction imaging from biological samples. As with SFX, these very large datasets require specialist software and support as well as access to state-of-the-art computing facilities. In addition to including several leading scientists who are actively pushing these developments, the SFX UC can advise the European XFEL management about the needs of external users and help prioritize where the unique pulse structure of the European XFEL may have the most impact. Important areas of consideration include sample delivery, minimizing background, and which source characteristics are likely to have greatest impact, such as self-seeding, two-colour modes, or



shorter X-ray pulses.

On a medium- to long-term view, it is essential that the life science community becomes more engaged in utilizing the unique capabilities of the European XFEL. The SFX UC can assist through community outreach, by linking across Europe to complementary capabilities provided by synchrotron radiation facilities, and in developing serial synchrotron crystallography at high-brilliance beamlines. Moreover, the experience of synchrotron radiation facilities is that additional flexibility in beamtime scheduling—such as BAG formats, long-term projects, and protein crystal screening capabilities—could all assist in developing a stronger life science user base for the European XFEL.

Since 2014, the SFX UC has demonstrated the benefits of closely coupling a strong and innovative user community to a developing instrument at the European XFEL with unique potential to impact European life science. It is apparent that the SFX UC has a positive role to play as emphasis shifts from the establishment of the new capabilities of the SPB/SFX instrument to higher throughput use of the available beamtime and the expansion of the European XFEL life science user community.



---

# Conclusions and Outlook

The SPB/SFX instrument has been in operation since September 2017, after only some eleven weeks of time from first light in the experiment hall to user experiments. The instrument has been quantitatively and qualitatively successful, as evidenced by both the number of publications (when bench-marked at the still rather young EuXFEL) as well as by the breadth of demonstration of viable experimental techniques at EuXFEL's unique, MHz rate. This includes MHz serial crystallography (with both optical pump and mixing time-resolved cases), MHz Single Particle Imaging, MHz X-ray Photon Correlation Spectroscopy, MHz microscopy, MHz SAXS, MHz fs-scale timing and even more. All of this would not have been possible without an outstanding user community, and particularly the SFX Users' Consortium, which has helped to focus applications, provided material and scientific support, and taken leadership in growing the broader SPB/SFX user community. Nor without the dedicated staff of SPB/SFX and across European XFEL.

The next step in the life-cycle of the SPB/SFX instrument is to continue to exploit these demonstrated and unique capabilities for science. One criticism that has been leveled at the instrument is that a great number of demonstration and method experiments have been performed to date, with fewer applications. Of course, that the initial output of a new facility addresses issues around using the new capabilities (here particularly the high repetition rate) before exploiting them is only natural. Notwithstanding this, we see the SPB/SFX instrument at a turning point with most proposals and experiments now addressing *applications* of the SPB/SFX capabilities, rather than further method development. This includes things like structural studies of bacterial insecticides—an industrially relevant topic which has been uniquely investigated using both the intensity and sheer pulse number available at European XFEL [56]. Further examples are proposed, scheduled and submitted at time of writing, though it is not appropriate to disclose these here. Indeed, with the core capabilities of SPB/SFX—(TR-)SFX, SPI, MHz microscopy and SAXS—ready to exploit, the short and medium term future of SPB/SFX is bright and clear.

The medium to longer term future contains a number of opportunities which one can consider to take advantage of. As SPB/SFX has enabled a variety of experimental modalities that are both in demand and applicable to science of relevance to society, it would be attractive to build new, future instrumentation to focus on each of these topics. This would lead to both improved efficiency, but also better automation allowing access for users with novel science but not an X-ray facility background. Most urgently, and as described earlier, Serial Crystallography could sustain a dedicated instrument. MHz microscopy is similar, and would benefit from higher photon energies, which could be provided by a future undulator at European XFEL. Finally, an instrument dedicated to scattering studies alone (SPI, SAXS, FXS) would benefit enormously from a stable configuration and the improvements in background that can be made over longer periods of operational time (much like dedicated SAXS beamlines at synchrotrons).

Considering all these unique capabilities—particularly in time-resolution and especially where relevant to human health and new materials—the near future is incredibly exciting with opportunity not only to do great science at SPB/SFX, but also to do great science with real benefit to the community.

# References

- [1] A. Allahgholi, J. Becker, A. Delfs, et al.: “The Adaptive Gain Integrating Pixel Detector at the European XFEL”, *Journal of Synchrotron Radiation* **26**, 74–82 (2019) doi:10.1107/S1600577518016077
- [2] M. Altarelli, R. Brinkmann, M. Chergui, et al. (eds.): “Technical Design Report: The European X-Ray Free-Electron Laser”, DESY Report 2006-097 (2006)
- [3] A. Aquila, A. Barty, C. Bostedt, et al.: “The linac coherent light source single particle imaging road map”, *Structural Dynamics* **2**, 041701 (2015) doi:10.1063/1.4918726
- [4] D. Arnlund, L. C. Johansson, C. Wickstrand, et al.: “Visualizing a protein quake with time-resolved X-ray scattering at a free-electron laser”, *Nature methods* **11**, 923–926 (2014)
- [5] K. Ayer, P. L. Xavier, J. Bielecki, et al.: “3D diffractive imaging of nanoparticle ensembles using an x-ray laser”, *Optica* **8**, 15–23 (2021) doi:10.1364/OPTICA.410851
- [6] H. van den Bedem, J. S. Fraser: “Integrative, dynamic structural biology at atomic resolution—it’s about time”, *Nature Methods* **12**, 307–318 (2015) doi:10.1038/nmeth.3324
- [7] J. Bielecki, M. F. Hantke, B. J. Daurer, et al.: “Electrospray sample injection for single-particle imaging with x-ray lasers”, *Science Advances* **5** (2019) doi:10.1126/sciadv.aav8801
- [8] J. Bielecki, F. R. N. C. Maia, A. P. Mancuso: “Perspectives on single particle imaging with x rays at the advent of high repetition rate x-ray free electron laser sources”, *Structural Dynamics* **7**, 040901 (2020) doi:10.1063/4.0000024
- [9] M. W. Bowler, D. Nurizzo, R. Barrett, et al.: “MASSIF-1: a beamline dedicated to the fully automatic characterization and data collection from crystals of biological macromolecules”, *Journal of synchrotron radiation* **22**, 1540–1547 (2015)
- [10] A. S. Brewster, D. G. Waterman, J. M. Parkhurst, et al.: “Improving signal strength in serial crystallography with *DIALS* geometry refinement”, *Acta Crystallographica Section D Structural Biology* **74**, 877–894 (2018) doi:10.1107/S2059798318009191
- [11] H. N. Chapman, P. Fromme, A. Barty, et al.: “Femtosecond X-ray protein nanocrystallography”, *Nature* **470**, 73–77 (2011) doi:10.1038/nature09750
- [12] W. Decking, F. Brinker, L. Froehlich, et al.: “Status of the European XFEL”, *Energy [GeV]* **17**, 10–16 (2019)
- [13] D. P. DePonte, U. Weierstall, K. Schmidt, et al.: “Gas dynamic virtual nozzle for generation of microscopic droplet streams”, *Journal of Physics D: Applied Physics* **41**, 195505 (2008) doi:10.1088/0022-3727/41/19/195505
- [14] J. J. Donatelli, P. H. Zwart, J. A. Sethian: “Iterative phasing for fluctuation X-ray scattering”, *Proceedings of the National Academy of Sciences* **112**, 10286–10291 (2015)
- [15] *EXtra-foam*, original-date: 2019-11-27T09:16:11Z, 2022
- [16] H. Fu, A. C. Patel, M. J. Holtzman, et al.: “A New Electrospray Aerosol Generator with High Particle Transmission Efficiency”, *Aerosol Science and Technology* (2011) doi:10.1080/02786826.2011.582899

- [17] M. L. Grünbein, J. Bielecki, A. Gorel, et al.: “Megahertz data collection from protein microcrystals at an X-ray free-electron laser”, *Nature communications* **9**, 3487 (2018)
- [18] M. F. Hantke, J. Bielecki, O. Kulyk, et al.: “Rayleigh-scattering microscopy for tracking and sizing nanoparticles in focused aerosol beams”, *IUCrJ* **5**, 673–680 (2018)  
doi:10.1107/S2052252518010837
- [19] A. R. et al. In Submission: “EThe Single Particle, Clusters, and Biomolecules and Serial Femtosecond Crystallography Instrument of the European XFEL: Interaction Region Downstream at Atmospheric pressure (IRDa)”, *JSR* (2022)
- [20] Z. Kam: “Determination of macromolecular structure in solution by spatial correlation of scattering fluctuations”, *Macromolecules* **10**, 927–934 (1977)
- [21] N. M. Kirby, S. T. Mudie, A. M. Hawley, et al.: “A low-background-intensity focusing small-angle X-ray scattering undulator beamline”, *Journal of Applied Crystallography* **46**, 1670–1680 (2013)  
doi:10.1107/s002188981302774x
- [22] J. Knoška, L. Adriano, S. Awel, et al.: “Ultrapact 3D microfluidics for time-resolved structural biology”, *Nature communications* **11**, 1–12 (2020)
- [23] J. Knoška, L. Adriano, S. Awel, et al.: “Ultrapact 3D microfluidics for time-resolved structural biology”, *Nature Communications* **11**, 657 (2020) doi:10.1038/s41467-020-14434-6
- [24] R. P. Kurta, M. Altarelli, I. A. Vartanyants: “Structural analysis by x-ray intensity angular cross correlations”, *Adv. Chem. Phys* **161** (2016)
- [25] R. P. Kurta, J. J. Donatelli, C. H. Yoon, et al.: “Correlations in scattered X-ray laser pulses reveal nanoscale structural features of viruses”, *Physical review letters* **119**, 158102 (2017)
- [26] F. Lehmkuhler, F. Dallari, A. Jain, et al.: “Emergence of anomalous dynamics in soft matter probed at the European XFEL”, *Proceedings of the National Academy of Sciences* **117**, 24110–24116 (2020) doi:10.1073/pnas.2003337117 eprint:  
<https://www.pnas.org/content/117/39/24110.full.pdf>
- [27] M. Levantino, G. Schiro, H. T. Lemke, et al.: “Ultrafast myoglobin structural dynamics observed with an X-ray free-electron laser”, *Nature communications* **6**, 1–6 (2015)
- [28] P. Liu, P. J. Ziemann, D. B. Kittelson, et al.: “Generating particle beams of controlled dimensions and divergence: I. Theory of particle motion in aerodynamic lenses and nozzle expansions”, *Aerosol Science and Technology* **22**, 293–313 (1995)
- [29] A. P. Mancuso, A. Aquila, L. Batchelor, et al.: “The single particles, clusters and biomolecules and serial femtosecond crystallography instrument of the European XFEL: Initial installation”, *Journal of synchrotron radiation* **26**, 660–676 (2019)
- [30] V. Mariani, A. Morgan, C. H. Yoon, et al.: “*OnDA*: online data analysis and feedback for serial X-ray imaging”, *Journal of Applied Crystallography* **49**, 1073–1080 (2016)  
doi:10.1107/S1600576716007469
- [31] A. V. Martin: “Orientational order of liquids and glasses via fluctuation diffraction”, *IUCrJ* **4**, 24–36 (2017)
- [32] P. Middendorf: *Amarcord documentation pages*, <https://cfel-sc-public.pages.desy.de/amarcord/amarcord/index.html>, Accessed: 2022-01-14

- [33] A. Mozzanica, A. Bergamaschi, S. Cartier, et al.: “Prototype characterization of the JUNGFRUA pixel detector for SwissFEL”, *Journal of Instrumentation* **9**, C05010–C05010 (2014)  
doi:10.1088/1748-0221/9/05/c05010
- [34] A. Myagotin, A. Ershov, L. Helfen, et al.: “Coalescence analysis for evolving foams via optical flow computation on projection image sequences”, *J Synchrotron Radiat* **19**, 483–491 (2012)  
doi:10.1107/S0909049512015099
- [35] R. Neutze, R. Wouts, D. van der Spoel, et al.: “Potential for biomolecular imaging with femtosecond X-ray pulses”, *Nature* **406**, 752–757 (2000)
- [36] A. Niozu, Y. Kumagai, T. Nishiyama, et al.: “Characterizing crystalline defects in single nanoparticles from angular correlations of single-shot diffracted X-rays”, *IUCrJ* **7**, 276–286 (2020)
- [37] D. Oberthuer, J. Knoška, M. O. Wiedorn, et al.: “Double-flow focused liquid injector for efficient serial femtosecond crystallography”, *Scientific reports* **7**, 1–12 (2017)
- [38] A. M. Orville: “Recent results in time resolved serial femtosecond crystallography at XFELs”, *Current Opinion in Structural Biology* **65**, 193–208 (2020) doi:https://doi.org/10.1016/j.sbi.2020.08.011
- [39] G. Palmer, M. Kellert, J. Wang, et al.: “Pump-probe laser system at the FXE and SPB/SFX instruments of the European X-ray Free-Electron Laser Facility”, *Journal of synchrotron radiation* **26**, 328–332 (2019)
- [40] K. Pande, J. J. Donatelli, E. Malmerberg, et al.: “Ab initio structure determination from experimental fluctuation X-ray scattering data”, *Proceedings of the National Academy of Sciences* **115**, 11772–11777 (2018)
- [41] S. Pandey, G. Calvey, A. M. Katz, et al.: “Observation of substrate diffusion and ligand binding in enzyme crystals using high-repetition-rate mix-and-inject serial crystallography”, *IUCrJ* **8**, 878–895 (2021) doi:10.1107/S2052252521008125
- [42] P. Roedig, H. M. Ginn, T. Pakendorf, et al.: “High-speed fixed-target serial virus crystallography”, *Nature methods* **14**, 805–810 (2017)
- [43] I. Schlichting: “Serial femtosecond crystallography: the first five years”, *IUCrJ* **2**, 246–255 (2015)  
doi:10.1107/s205225251402702x
- [44] M. Schmidt: “Reaction Initiation in Enzyme Crystals by Diffusion of Substrate”, *Crystals* **10** (2020) doi:10.3390/cryst10020116
- [45] J. Schulz, J. Bielecki, R. B. Doak, et al.: “A versatile liquid-jet setup for the European XFEL”, *Journal of Synchrotron Radiation* **26**, 339–345 (2019) doi:10.1107/S1600577519000894
- [46] S. Schulz, M. Czwalinna, M. Felber, et al.: “Few-Femtosecond Facility-Wide Synchronization of the European XFEL”, 39th Free Electron Laser Conf. (FEL’19), Hamburg, Germany, 26-30 August 2019, 318–321 (JACOW Publishing, Geneva, Switzerland 2019)  
doi:10.18429/JACoW-FEL2019-WEB04
- [47] O. Svensson, S. Malbet-Monaco, A. Popov, et al.: “Fully automatic characterization and data collection from crystals of biological macromolecules”, *Acta Crystallographica Section D: Biological Crystallography* **71**, 1757–1767 (2015)

- [48] A. Tolstikova, M. Levantino, O. Yefanov, et al.: “1 kHz fixed-target serial crystallography using a multilayer monochromator and an integrating pixel detector”, *IUCrJ* **6**, 927–937 (2019) doi:10.1107/S205225251900914X
- [49] P. Vagovič, T. Sato, L. Mikeš, et al.: “Megahertz x-ray microscopy at x-ray free-electron laser and synchrotron sources”, *Optica* **6**, 1106–1109 (2019) doi:10.1364/OPTICA.6.001106
- [50] M. Vakili, J. Bielecki, J. Knoška, et al.: “3D printed devices and infrastructure for liquid sample delivery at the European XFEL”, *Journal of Synchrotron Radiation* **29** (2022) doi:10.1107/S1600577521013370
- [51] P. Vester, I. A. Zaluzhnyy, R. P. Kurta, et al.: “Ultrafast structural dynamics of photo-reactions observed by time-resolved x-ray cross-correlation analysis”, *Structural Dynamics* **6**, 024301 (2019)
- [52] P. Villanueva-Perez, F. Arcadu, P. Cloetens, et al.: “Contrast-transfer-function phase retrieval based on compressed sensing”, *Opt. Lett.* **42**, 1133–1136 (2017) doi:10.1364/OL.42.001133
- [53] U. Weierstall, D. James, C. Wang, et al.: “Lipidic cubic phase injector facilitates membrane protein serial femtosecond crystallography”, *Nature Communications* **5**, 3309 (2014) doi:10.1038/ncomms4309
- [54] T. A. White, V. Mariani, W. Brehm, et al.: “Recent developments in *CrystFEL*”, *Journal of Applied Crystallography* **49**, 680–689 (2016) doi:10.1107/S1600576716004751
- [55] M. O. Wiedorn, D. Oberthür, R. Bean, et al.: “Megahertz serial crystallography”, *Nature communications* **9**, 4025 (2018)
- [56] L. J. Williamson, M. Galchenkova, H. L. Best, et al.: “Structure of the *Lysinibacillus sphaericus* Tpp49Aa1 pesticidal protein elucidated from natural crystals using MHz-SFX” (2022) doi:10.1101/2022.01.14.476343
- [57] O. Yefanov, D. Oberthür, R. Bean, et al.: “Evaluation of serial crystallographic structure determination within megahertz pulse trains”, *Structural Dynamics* **6**, 064702 (2019)
- [58] Y. Zhuang, S. Awel, A. Barty, et al.: “Unsupervised learning approaches to characterizing heterogeneous samples using X-ray single-particle imaging”, *IUCrJ* **9** (2022) doi:10.1107/S2052252521012707



# Appendices



---

# Appendix: Requirements for future detector(s)

The AGIPD 1Mpix detector plays a critical role in ensuring the high quality of the scientific output of the upstream interaction region at the SPB/SFX instrument. The Jungfrau 4Mpix detector enables operation at the downstream interaction region, although, even with the 16 memory cells in use, it will not allow users to take advantage of the high repetition rate of the European XFEL. Potential arrival of the AGIPD 4Mpix would improve the operation capabilities of the instrument. However, the AGIPD 4Mpix will share characteristics with the AGIPD 1Mpix and will pose similar constraints on scientific questions that could be answered at SPB/SFX. It is clear that access to improved detectors plays a critical role in the continuous growth of the instrument.

Serial femtosecond crystallography, coherent diffraction imaging (with the stress on single particle imaging), and MHz X-ray microscopy were identified as the key scientific areas of interest for SPB/SFX in the future. Although the optimal detectors for each of those fields would have very different characteristics, there is a subset of common requirements, such as a small ( $< 100 \mu\text{m}$ ) pixel size, a greater number of memory cells, or the ability to veto individual frames.

A short summary of the detector characteristics desired for those experiments are listed below.

---

## Serial femtosecond crystallography and single particle imaging

From the perspective of protein crystallography, two main limitations posed by the AGIPD 1Mpix are the maximum achievable resolution and maximum size of the unit cell of the measured crystals.

The area of the detector is also a limitation for SPI and also in this case a larger active area is desirable. In addition to this the signal expected for SPI experiments is significantly weaker. This requires a narrower dynamic range than SFX, though ideally requires the capability of counting single photons with high fidelity.

It is desirable for the next generation detector to meet the requirements outlined in Tab. A.1 for both SFX and SPI.

**Table A.1:** Detector parameters for SFX and SPI experiments

Parameter	Value for SFX	Value for SPI	Comment
Detector size (mm)	350 × 350	350 × 350	Determines the resolution of measurement (distance to the smallest observable feature of the studied protein). For a given resolution shell, the fraction of the arc covered by the detector determines the number of patterns that are needed to achieve desired completeness.
Min. number of memory cells	500	500	Throughput of measurement is proportional to the number of memory cells; therefore, the detector should be able to handle a greater number of pulses per train than AGIPD 1Mpix.
Gain mode	Adaptive/fixed	Fixed	Control over gain setting on the ASIC. level
Dynamic range (photons)	1–10 000	1–1000	At 12 keV.
SNR	5–6	5–6	Ensures sufficiently low false–positive events per million pixels.
Linearity	Better than 1%	Better than 1%	Required for phasing studies.
Pixel size (μm)	75–100	75–100	Enables measurements of units cell several hundreds of Å.
Veto	Yes	Yes	The ability to discard (empty) data online would alleviate data storage issues, speed up online data processing, and improve data acquisition efficiency.

---

## Megahertz microscopy

There are two types of detectors that can be used for MHz microscopy: (a) indirect detectors and (b) direct-conversion MHz-sampling integrating detectors. The indirect detector is composed of light emission material (scintillator) that, under X-ray illumination, generates fluorescence emission in the green to near-ultraviolet light range (550 nm –  $\approx$ 350 nm), containing a latent image of the sample. Such an image is then magnified using a diffraction-limited visible light microscope and projected onto a CCD, sCMOS, or CMOS detector. Current state-of-the-art CMOS detectors suitable for MHz indirect detectors are limited to a small number of pixels and a small dynamic range. For example, the Shimadzu HPV-X2 have 400 pixels  $\times$  250 pixels with a dynamic range of 10 bits. Spatial resolutions down to micron scales are achievable with indirect detectors.

### CMOS cameras for indirect detectors

The camera should be able to synchronise to a pulse pattern selected from a master frequency of 1.3 GHz. The recording sequence should be possible to trigger with an external synchronised TTL signal. The jitter between the external trigger and the start of the acquisition should be  $\leq 5$  ns. The camera should be able to record a larger portion of the train, at least 300 frames (current state-of-the-art is 256 frames per buffer). Readout and saving of the image sequence should ideally be completed in the time between trains in order to be ready to record the next sequence when the next train arrives. Camera control software should be implementable in modern control systems of large-scale facilities (Tango, Karabo, etc.). The software should provide an absolute timestamp of acquired sequences so that these can be easily related to a specific XFEL train id. Ideally, Linux SDK should be available.

**Table A.2:** Major parameters for indirect detector CMOS cameras

Parameter	Required value
Chip format	$\geq 1024 \times 1024$ pixels <sup>2</sup>
Pixel size	$\leq 32$ $\mu$ m
Dynamic range	$\geq 12$ bit (14 bit)
Minimum buffer length	$\geq 300$ frames
Readout time	$< 99.4$ ms (to be ready before next train)
Maximum recording frequency	4.5 MHz (9 Mhz)

The ideal detector would combine sub-micron resolution with high efficiency, high dynamic range, and X-ray magnification with direct conversion X-ray. X-ray magnification can be achieved via focusing lenses or crystal magnifiers, and the magnified X-ray image can be then projected onto

direct conversion detectors. The pixel size required should be smaller than 200  $\mu\text{m}$  to avoid long sample-to-detector distances in case of focusing geometry. The minimum number of pixels should be  $\geq 512 \times 512$  for a reasonable field of view. The repetition rate should be able to match the European XFEL with a reasonable number of frames recorded per train. As the European XFEL competitive advantage is a possibility to deliver pulses in the very hard X-ray regime, high Z materials for the chip have to be considered. We plan to explore the possibility to combine direct conversion detectors with a Ge220 Bragg magnifier, which can provide 250x magnification and record 40 mm x 40 mm (existing prototypes on a small footprint 0.5 m; new system can be designed with optimized parameters for given available detector). Another option is to combine focusing lenses with a direct conversion detector. Such a combination can reach nm scale spatial resolution with a high numerical aperture of the lenses to keep such a microscope short in profile. Ideal candidates for focusing optics are Laue lenses, which can efficiently work above 60 keV. The direct conversion detector described above is required.

---

# Appendix: Selected publications elucidating scientific excellence

This appendix reproduces some (open access) publications for the reader's convenience. All those noted here have used European XFEL beam at the SPB/SFX instrument.

For clarity, the publications are grouped into user-driven publications and staff-driven publications.

---

## User-driven publications

This section includes the following user-driven publications.

### **Megahertz data collection from protein microcrystals at an X-ray free-electron laser**

M.L. Grünbein et al.: Nat. Commun. **9** (1), 3487 (2018)

doi:10.1038/s41467-018-05953-4

### **Megahertz serial crystallography**

M.O. Wiedorn et al.: Nat. Commun. **9** (1), 4025 (2018)

doi:10.1038/s41467-018-06156-7

### **Observation of substrate diffusion and ligand binding in enzyme crystals using high-repetition-rate mix-and-inject serial crystallography**

S. Pandey et al.: IUCrJ **8** (6), 878–895 (2021)

doi:10.1107/S2052252521008125

### **3D diffractive imaging of nanoparticle ensembles using an x-ray laser**

K. Ayyer et al.: Optica **8** (1), 15 (2021)

doi:10.1364/OPTICA.410851





ARTICLE

DOI: 10.1038/s41467-018-05953-4

OPEN

# Megahertz data collection from protein microcrystals at an X-ray free-electron laser

Marie Luise Grünbein<sup>1</sup>, Johan Bielecki<sup>2</sup>, Alexander Gorel<sup>1</sup>, Miriam Stricker<sup>1</sup>, Richard Bean<sup>2</sup>, Marco Cammarata<sup>3</sup>, Katerina Dörner<sup>2</sup>, Lars Fröhlich<sup>4</sup>, Elisabeth Hartmann<sup>1</sup>, Steffen Hauf<sup>2</sup>, Mario Hilpert<sup>1</sup>, Yoonhee Kim<sup>2</sup>, Marco Kloos<sup>1</sup>, Romain Letrun<sup>2</sup>, Marc Messerschmidt<sup>2,5</sup>, Grant Mills<sup>2,6</sup>, Gabriela Nass Kovacs<sup>1</sup>, Marco Ramilli<sup>2</sup>, Christopher M. Roome<sup>1</sup>, Tokushi Sato<sup>2,7</sup>, Matthias Scholz<sup>4</sup>, Michel Sliwa<sup>8</sup>, Jolanta Sztuk-Dambietz<sup>2</sup>, Martin Weik<sup>9</sup>, Britta Weinhausen<sup>2</sup>, Nasser Al-Qudami<sup>2</sup>, Djelloul Boukhelef<sup>2</sup>, Sandor Brockhauser<sup>2,10</sup>, Wajid Ehsan<sup>2</sup>, Moritz Emons<sup>2</sup>, Sergey Esenov<sup>2</sup>, Hans Fangohr<sup>2</sup>, Alexander Kaukher<sup>2</sup>, Thomas Kluyver<sup>2</sup>, Max Lederer<sup>2</sup>, Luis Maia<sup>2</sup>, Maurizio Manetti<sup>2</sup>, Thomas Michelat<sup>2</sup>, Astrid Münnich<sup>2</sup>, Florent Pallas<sup>2</sup>, Guido Palmer<sup>2</sup>, Gianpietro Previtali<sup>2</sup>, Natascha Raab<sup>2</sup>, Alessandro Silenzi<sup>2</sup>, Janusz Szuba<sup>2</sup>, Sandhya Venkatesan<sup>2</sup>, Krzysztof Wrona<sup>2</sup>, Jun Zhu<sup>2</sup>, R. Bruce Doak<sup>1</sup>, Robert L. Shoeman<sup>1</sup>, Lutz Foucar<sup>1</sup>, Jacques-Philippe Colletier<sup>9</sup>, Adrian P. Mancuso<sup>2</sup>, Thomas R.M. Barends<sup>1</sup>, Claudiu A. Stan<sup>11</sup> & Ilme Schlichting<sup>1</sup>

X-ray free-electron lasers (XFELs) enable novel experiments because of their high peak brilliance and femtosecond pulse duration. However, non-superconducting XFELs offer repetition rates of only 10–120 Hz, placing significant demands on beam time and sample consumption. We describe serial femtosecond crystallography experiments performed at the European XFEL, the first MHz repetition rate XFEL, delivering 1.128 MHz X-ray pulse trains at 10 Hz. Given the short spacing between pulses, damage caused by shock waves launched by one XFEL pulse on sample probed by subsequent pulses is a concern. To investigate this issue, we collected data from lysozyme microcrystals, exposed to a  $\sim 15\ \mu\text{m}$  XFEL beam. Under these conditions, data quality is independent of whether the first or subsequent pulses of the train were used for data collection. We also analyzed a mixture of microcrystals of jack bean proteins, from which the structure of native, magnesium-containing concanavalin A was determined.

<sup>1</sup>Max Planck Institute for Medical Research, Jahnstrasse 29, 69120 Heidelberg, Germany. <sup>2</sup>European XFEL GmbH, Holzkoppel 4, 22869 Schenefeld, Germany. <sup>3</sup>Department of Physics, UMR 625, UBL, University of Rennes 1, 35042 Rennes, France. <sup>4</sup>Deutsches Elektronensynchrotron DESY, Notkestraße 85, 22607 Hamburg, Germany. <sup>5</sup>BioXFEL STC, 700 Ellicott Street, Buffalo, NY 14203, USA. <sup>6</sup>ARC Centre of Excellence for Advanced Molecular Imaging, La Trobe Institute for Molecular Science, La Trobe University, Melbourne, VIC 3086, Australia. <sup>7</sup>Center for Free-Electron Laser Science, Deutsches Elektronensynchrotron, Notkestraße 85, 22607 Hamburg, Germany. <sup>8</sup>Laboratoire de Spectrochimie Infrarouge et Raman, CNRS, UMR 8516, Université de Lille, 59000 Lille, France. <sup>9</sup>Institut de Biologie Structurale, Université Grenoble Alpes, CEA, CNRS, 38044 Grenoble, France. <sup>10</sup>Biological Research Centre (BRC), Hungarian Academy of Sciences, Temesvári krt. 62, Szeged 6726, Hungary. <sup>11</sup>Department of Physics, Rutgers University Newark, 101 Warren Street, Newark, NJ 07102, USA. Correspondence and requests for materials should be addressed to T.R.M.B. (email: [Thomas.Barends@mpimf-heidelberg.mpg.de](mailto:Thomas.Barends@mpimf-heidelberg.mpg.de)) or to C.A.S. (email: [claudiu.stan@rutgers.edu](mailto:claudiu.stan@rutgers.edu)) or to I.S. (email: [Ilme.Schlichting@mpimf-heidelberg.mpg.de](mailto:Ilme.Schlichting@mpimf-heidelberg.mpg.de))

X-ray free-electron lasers (XFELs) are novel X-ray sources that provide femtosecond pulses of a peak brilliance that exceeds that of synchrotron sources by nine orders of magnitude. The short duration of the pulses matches the chemical time scale of femtoseconds, allowing the investigation of the dynamics of matter in a time-resolved manner<sup>1–3</sup>, and enables the analysis of highly radiation-sensitive objects<sup>4,5</sup>. The high intensity of the pulses enables the study of weakly scattering objects such as very small crystals<sup>6–8</sup> and the coherence of the beam enables the imaging of non-crystalline particles<sup>9,10</sup>. In line with these transformative capabilities, demand for beam time at XFELs is very high. For this reason, MHz repetition rate XFELs have been awaited eagerly, since they can deliver X-ray pulses with an up to ~10,000-fold higher maximum repetition rate than the first hard X-ray FEL that came online in 2009<sup>11</sup>. An increase in pulse rate is expected to speed up data collection, thereby accommodating more users and allowing the collection of enough data to study systems with very weak signals. Also, high pulse rates make for better use of the often highly valuable samples that are generally delivered continuously into the X-ray beam by means of liquid jets, aerosols or molecular beams. However, data collection at MHz rates brings with it many new challenges including the rapid delivery of samples to present fresh material for each pulse, and the development of high frame rate detectors, allowing fast data acquisition and storage<sup>12</sup>.

The European XFEL (EuXFEL) in Germany is the first MHz XFEL. Its unique design values of up to 27,000 pulses per second (delivered in 10 trains per second with a 4.5 MHz repetition rate within each train) and a peak brilliance of  $5 \times 10^{33}$  photons  $s^{-1}$   $mm^{-2}$   $mrad^{-2}$  (0.1% bandwidth)<sup>13–15</sup> provide unprecedented possibilities for experiments in biology, materials science, chemistry and physics by increasing the average pulse rate almost 300-fold compared to any previous XFEL. Here we report serial femtosecond crystallography (SFX) experiments on protein microcrystals carried out at MHz data acquisition rate at the SPB/SFX instrument of the EuXFEL<sup>16,17</sup> (June 2018, proposal number 2038). As well as addressing the challenges associated with MHz data repetition rates using a model system (lysozyme protein crystals), we investigated a microcrystalline preparation of jack bean proteins precipitated with acetone, a preparation described by James Sumner, who used this technique for the first crystallization of an enzyme (urease) in 1926<sup>18</sup>, resulting in a Nobel Prize in 1946<sup>19</sup>. That work ultimately showed that enzymes are proteins. We demonstrate here that it is possible to separate the data of the three types of protein crystals in such a microcrystalline mixture of jack bean proteins (urease, concanavalin A and B), and to determine the structures of the two concanavalins, using data collected at the first MHz XFEL.

## Results

**Injection and data collection.** Full exploitation of the MHz repetition rate for SFX data collection requires three conditions to be fulfilled: (i) when using microjets for sample delivery, high-intensity XFEL pulses induce explosions that generate a gap in the liquid jet<sup>20</sup> and a fresh section of the running jet must advance to the X-ray interaction region before arrival of the subsequent XFEL pulse. (ii) Sample that is exposed to an XFEL pulse should not have been exposed to (stray) X-rays from the previous pulse, as this can cause radiation damage. (iii) It has been shown that the impact of an XFEL pulse on the liquid jet may launch shock waves travelling upstream of the jet before onset of the explosion<sup>20</sup>. These may cause mechanical damage to crystals before they even reach the interaction region, which must be prevented for a successful measurement. Issue (i) can be addressed by using a sufficiently high speed of the jet. Challenge

(ii) requires more displacement of the sample than the size of the X-ray beam and its wings. Problem (iii) is far less trivial as it is not a local effect but one capable of affecting samples far away from the actual exposure site. It is therefore critical to verify that, at the short spacing between two X-ray pulses at MHz repetition rate (~1  $\mu$ s), such shock waves do not affect the sample under investigation. While a model exists to predict the jet gap size in case (i)<sup>20</sup> and the region affected in case (ii) is given by the X-ray beam properties, no predictions exist for the shock wave damage in case (iii). Therefore, now that the first MHz XFEL has become available, we investigated this issue at current EuXFEL operating parameters, using microcrystals of the model protein lysozyme.

Lysozyme microcrystals were injected in a thin liquid microjet into the XFEL beam<sup>21,22</sup>. The sample was probed using trains of 50 XFEL pulses with an 886 ns interval between pulses (1.128 MHz intra-train repetition rate which was the highest available operating rate at the time of the experiment). The time interval between each 50-pulse train was ~100 ms ensuring that the first pulse in a train always probed an undamaged sample. To identify possible damage due to the short pulse intervals within a train, we compared the quality of data collected from the first pulse in a train with those from subsequent pulses in a train.

Diffraction data was recorded at 7.47 and 9.22 keV photon energy using a 1 megapixel Adaptive Gain Integrating Pixel Detector (AGIPD)<sup>12</sup>. The X-ray focal size was ~15  $\mu$ m diameter at 7.47 keV and ~28  $\mu$ m diameter at 9.22 keV, and each pulse had ~0.9–1.5 mJ pulse energy. The pulse length was likely around 50 fs (FWHM) based on electron beam diagnostics. Since a sufficiently high jet velocity is critical to avoid sample damage by the previous pulses, we used a time-resolved optical imaging system using a fs optical pump laser<sup>23</sup> for jet illumination to observe the effects of the interaction with the XFEL pulses, and to determine the jet velocity during each XFEL pulse train. To avoid radiation damage from the previous pulse, the jet must advance by at least the XFEL beam diameter between pulses. The velocity required to reestablish a jet in time for the next pulse after the XFEL-induced explosion was 40–50  $m s^{-1}$  and was determined by recording images of the jet 13 or 124 ns after the second pulse in the train. These time delays were chosen such that the jet gaps caused by both the first and second pulses were clearly visible in the optical image. Figure 1a shows a typical jet image for a jet carrying lysozyme crystals. The presence of two distinct gaps displaced by 2.7 beam diameters and separated by a section of contiguous jet indicates that the second pulse indeed intercepted a recovered jet, and the distance between the centers of the gaps is given by the jet velocity multiplied by the in-train pulse interval. Moreover, consecutive X-ray pulses in the same train were observed to probe different crystals, further verifying that jet speed was indeed high enough to transport new sample into the interaction region (Fig. 1b, c).

The presence of shock waves could not be detected optically in the small jets used for crystal delivery since the visibility of shocks decreases rapidly with jet diameter<sup>20</sup>. Due to the X-ray focus being much larger than the jet diameter, the shock waves were considerably weaker than the ones launched at similar pulse energies by beams smaller than the jet diameter, as shown in Supplementary Fig. 1 for two larger diameter water jets (12 and 27  $\mu$ m).

## Correlating data quality to pulse number within pulse train.

The issues of potential radiation damage and shock wave effects were addressed by collecting extensive data sets on the model protein lysozyme at both 7.47 and 9.22 keV photon energy (87,000 and 45,000 indexed images, respectively) to compare the

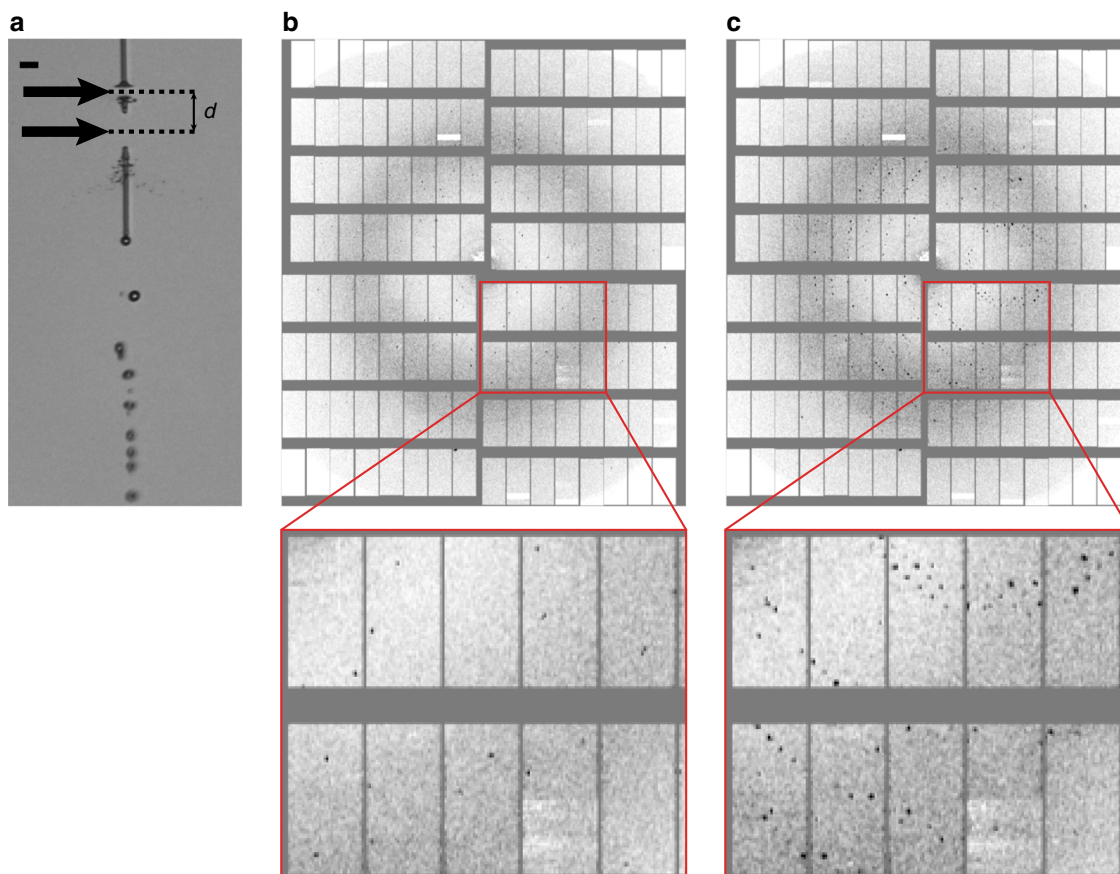


**Fig. 1** Consecutive X-ray exposures. **a** Liquid microjet (lysozyme microcrystals in mother liquor,  $\sim 4\ \mu\text{m}$  jet diameter) after being hit by the first two consecutive X-ray pulses of a pulse train separated by 886 ns, as viewed by the off-axis camera using fs laser illumination shortly after the second X-ray pulse. Flow direction is pointing down in the image. Each X-ray pulse leads to an explosion in the jet, opening up a gap (black arrows). The jet is sufficiently fast ( $\sim 45\ \text{m s}^{-1}$ ) to close the gap created by the first pulse (lower gap) in time for the second pulse to hit the jet (upper gap). The distance  $d$  between both gap centers is  $\sim 40\ \mu\text{m}$ . The scale bar is  $20\ \mu\text{m}$ . **b, c** Diffraction patterns of lysozyme microcrystals recorded with the first (**b**) and second (**c**) X-ray pulse of the same pulse train (886 ns time delay between pulses) showing that the two pulses probed different crystals. **a–c** All data were recorded from the same sample suspension, using the same nozzle and flow parameters

different amounts of energy deposited in the sample at these photon energies, and by then comparing the data obtained from each pulse number within a train for a given photon energy (see Fig. 2 and Supplementary Information). The diffraction data were indexed and integrated using CrystFEL<sup>24,25</sup>.

Notably, the quality of the data is very good, allowing observation of the anomalous sulphur signal as shown in Fig. 2a. Statistics for the full data sets are given in Table 1.

Since the integrity of disulfide bonds is a sensitive marker for radiation damage in lysozyme crystals<sup>26</sup>, we compared the bond length of the disulfide bridges derived from data collected using the first pulse and those of later pulses, respectively. Since these refined to the same value within experimental error (Supplementary Table 1), significant radiation damage caused by previous pulses appears unlikely.

We then investigated other statistical indicators of diffraction data quality to check for shock wave-induced damage. Importantly, at both 7.47 and 9.22 keV photon energy, the diffraction resolution, as well as other quality measures such as  $R_{\text{work}}/R_{\text{free}}$  and  $\text{CC}^*$ <sup>27</sup> (Fig. 2b–d and Supplementary Figures 2 and 3) do not show a dependence on the position in the pulse train. In particular, there is no difference in resolution between the diffraction data collected by the first and second X-ray pulse (Fig. 2c, Supplementary Fig. 4), both distributions having a peak at the same resolution ( $\sim 2.2\ \text{\AA}$  in case of the 7.47 keV data). The

hit rate (the ratio between the number of detected diffraction patterns and the total number of images) shows some variation (Fig. 2e, and Supplementary Fig. 2c), as does the signal-to-noise ratio (Supplementary Fig. 3a, e),  $R_{\text{split}}$  (Supplementary Fig. 3c, g) and the Wilson B factor (Supplementary Fig. 3b, f); however, this can be explained by the variation of the pulse intensity over the train, which decreases with pulse number (Fig. 2d, e, Supplementary Fig. 2). For some quality indicators, the data statistics show a discontinuity between the first and the last half of the pulse train (Supplementary Figure 3c, g, Supplementary Figure 5, Supplementary Figure 6 and Supplementary Note 1), for reasons that are currently unclear. Since the pulse energy does not show a similarly abrupt behavior (Fig. 2d, e and Supplementary Fig. 2b, c), possible explanations could include a change in e.g. the calibration and/or offset parameters for the various memory cells of the detector. Indeed, we found that in the detector calibration data recorded using copper fluorescence in a series of flat field measurements, stronger intensity signals occur much more frequently for the second half of the memory cells. This increase in the calibration measurements shows the same trend with the memory cell number as the jump we observed using diffraction data. Moreover, given that radiation- and/or shock wave-induced damage should affect the whole pulse train either as a smooth trend (i.e., as a cumulative effect over the pulses) or as a sudden change from the first to the second pulse in the train, it is highly

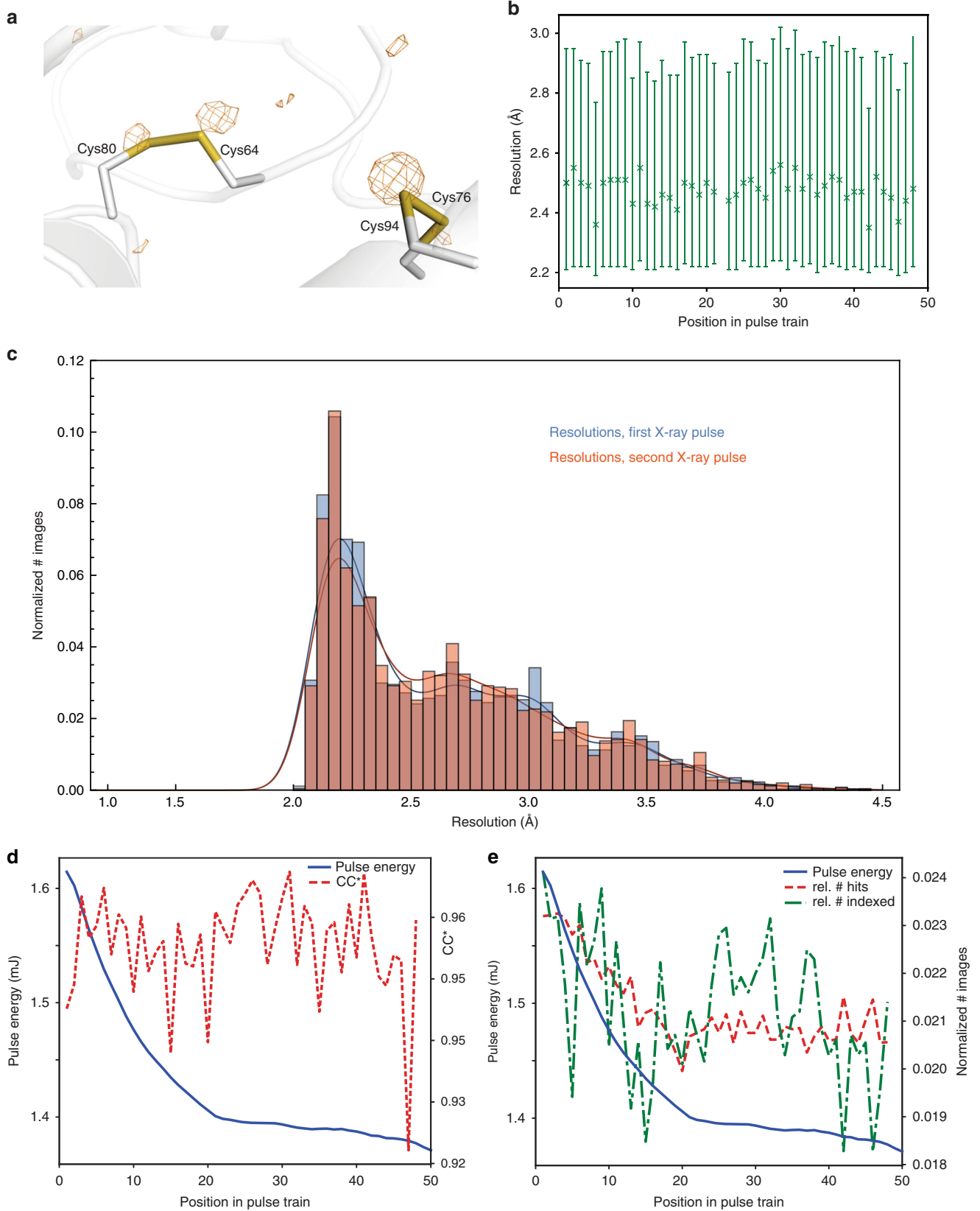


**Fig. 2** Quality of lysozyme control data collected at 7.47 keV photon energy. **a** Anomalous difference density map contoured at  $3.0\sigma$ , calculated using data to 2.2 Å resolution from 87,000 images. The main peaks are associated with the sulfur atoms (shown: two disulfide bridges). **b** Diffraction resolution as a function of the position in the pulse train. Symbols show the median resolution of all indexed images. The error bars indicate the 0.25 and 0.75 quantiles. **c** Histograms of the resolutions of lysozyme microcrystals of the 7.47 keV dataset for the first (blue, 2109 indexed images) and second (red, 1924 indexed images) pulses in the pulse trains. **d**  $CC^{*27}$  of partial datasets (red line) and pulse energy (blue line) as a function of the position in the pulse train. **e** Hit- and indexing rate (red and green lines, as the normalized number of images) as well as pulse energy (blue line) as a function of the position in the pulse train. The total number of hits and indexed images was 421,705 and 106,661, respectively

**Table 1** Data collection and refinement statistics

	Lysozyme, 7.47 keV (6HOK)	Lysozyme, 9.22 keV (6HOL)	Concanavalin A (6GW9)	Concanavalin B (6GWA)
<b>Data collection</b>				
Space group	$P4_32_12$	$P4_32_12$	$I222$	$P6_1$
Cell dimensions				
<i>a</i> , <i>b</i> , <i>c</i> (Å)	79.9, 79.9, 38.5	80.1, 80.1, 38.6	63.9, 88.1, 90.2	82.3, 82.3, 103.4
$\alpha$ , $\beta$ , $\gamma$ (°)	90.0, 90.0, 90.0	90.0, 90.0, 90.0	90.0, 90.0, 90.0	90.0, 90.0, 120.0
Resolution (Å)	35–2.2 (2.3–2.2) <sup>a</sup>	35–1.9 (2.0–1.9)	45–2.1 (2.2–2.1)	42–2.2 (2.3–2.2)
$R_{\text{split}}$	0.077 (0.374)	0.154 (0.591)	0.128 (0.694)	0.146 (0.560)
$CC_{1/2}$	0.994 (0.249)	0.973 (0.387)	0.984 (0.333)	0.967 (0.232)
$CC^*$	0.999 (0.631)	0.993 (0.747)	0.996 (0.706)	0.992 (0.614)
$I/\sigma(I)$	12.0 (4.1)	6.3 (2.9)	7.2 (2.0)	7.6 (3.2)
Completeness (%)	100.0 (100.0)	100.0 (100.0)	100.0 (100.0)	100.0 (100.0)
Multiplicity	1160 (690)	278 (186)	715 (146)	723 (241)
<b>Refinement</b>				
Resolution (Å)	35.0–2.2	35.0–1.9	45.0–2.1	42.0–2.2
No. of reflections	6717	10,346	15,227	20,161
$R_{\text{work}}/R_{\text{free}}$	0.196/0.240	0.188/0.237	0.186 / 0.238	0.161 / 0.213
No. of atoms				
Protein	992	992	1778	2274
Ligand/ion	—	—	2 (Ca <sup>2+</sup> , Mg <sup>2+</sup> )	—
Water	73	80	72	159
<i>B</i> -factors				
Protein	36.2	19.2	29.4	26.5
Ligand/ion	—	—	20.9 (Ca <sup>2+</sup> ), 21.8 (Mg <sup>2+</sup> )	—
Water	45.0	26.7	35.8	35.2
R.m.s. deviations				
Bond lengths (Å)	0.002	0.008	0.002	0.009
Bond angles (°)	0.619	1.054	0.577	1.210

The number of indexed crystals used for structure determination was 86,807 for lysozyme at 7.47 keV, 45,799 for lysozyme at 9.22 keV, 76,803 for concanavalin A and 23,719 for concanavalin B  
<sup>a</sup>Values in parentheses are for the highest-resolution shell.

unlikely that the observed effect is caused by damage to the sample.

**Analysis of microcrystals of jack bean proteins.** In addition to the comprehensive analysis of SFX data collected for each shot in the pulse train using microcrystals of the well-established model system lysozyme, we were also interested to explore whether the data collected at MHz rate using a novel X-ray detector would be of sufficient quality to permit the analysis of an uncharacterized, complex system. To this end, we collected SFX data of a microcrystalline mixture of jack bean proteins, crystallized using acetone as published previously<sup>18</sup>. The microcrystalline slurry contained at least three different crystal forms (Fig. 3a). Due to their small size (on the order of 5–10 μm) the crystals could not be further characterized before the beam time and it thus remained unclear which proteins had in fact crystallized. Indexing with CrystFEL<sup>24,25</sup> revealed the presence of three different crystal lattices corresponding to one protein each. In line with expectations from the purification protocol<sup>28,29</sup> and SDS PAGE of the microcrystals (Supplementary Fig. 7), a search for known unit cell constants from the PDB resulted in identification of

diffraction patterns from urease, concanavalin A and concanavalin B crystals. In contrast to the concanavalin A and B microcrystals, which diffracted strongly, urease microcrystals diffracted only to low resolution and with low signal-to-noise ratio, and no structure was refined. In total, 1,333,750 images were collected, and the final number of indexed diffraction patterns was 76,803 for concanavalin A and 23,719 for concanavalin B, with the resolution limit of the Monte-Carlo integrated data being 2.1 Å for concanavalin A and 2.2 Å for concanavalin B. The structures of concanavalin A and B were solved by molecular replacement, and data and refinement statistics are shown in Table 1.

Given the lysozyme results, it appears unlikely that our jack bean protein data are compromised by radiation damage or by shock wave effects in the current experiment. Indeed, the electron density maps are of excellent quality (Fig. 3b, c) and the overall structures are virtually identical to those determined using macroscopic crystals, with core RMSDs on Ca atoms against reference structures of 0.31 Å for concanavalin A (vs. PDB entry 1JBC<sup>30</sup>) and 0.24 Å for concanavalin B (vs. PDB entry 1CNV<sup>31</sup>). Notably, in contrast with all other concanavalin A structures in the PDB, our structure contains a magnesium ion in one of the

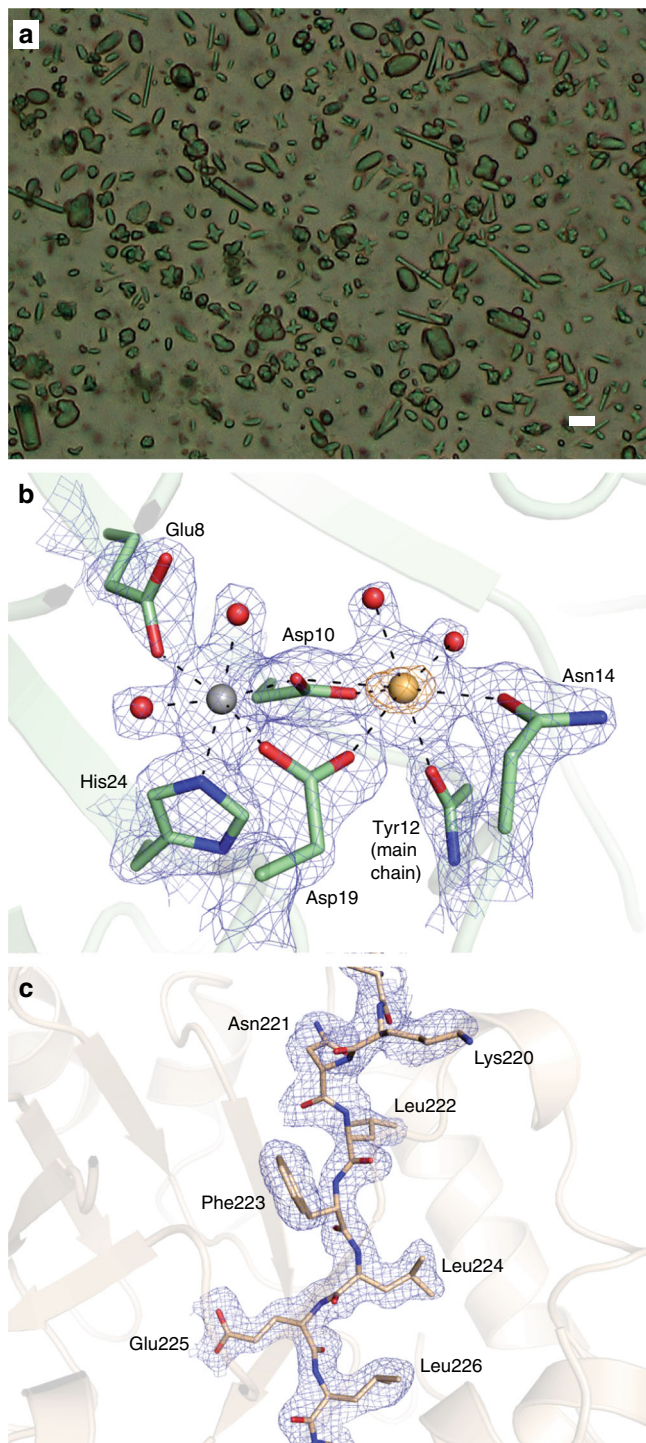


**Fig. 3** MHz serial femtosecond crystallography of jack bean proteins. **a** Microscope image of the microcrystalline mixture of jack bean proteins that was injected into the X-ray beam, clearly showing different types of crystal forms. The scale bar is 10  $\mu\text{m}$ . **b** Map quality for the concanavalin A structure. The metal binding site is shown, with the simulated annealing composite omit map contoured at  $1.0\sigma$  shown as a blue mesh and the anomalous difference density map ( $5.0\sigma$ ) shown as an orange mesh. Selected residues are shown as sticks, the calcium and magnesium ions as yellow and grey spheres, respectively. Water molecules are shown as red spheres. **c** Map quality for the concanavalin B structure. Part of one of the  $\beta$ -strands of the TIM-barrel is shown as sticks, with the simulated annealing composite omit map ( $1.0\sigma$ ) shown as a blue mesh

main metal binding sites, as expected given the metal content of native concanavalin A<sup>32</sup>. In structures determined from macroscopic crystals this site is typically occupied by a manganese ion, which increases diffraction quality<sup>33</sup>.

## Discussion

Taken together, our present data suggest that under the conditions used, neither protein structure nor crystal quality is affected by previous X-ray pulses. While these results are very promising for MHz data collection, it must be noted that the conditions of the experiment were fairly mild in terms of X-ray exposure due to the current large focus spot size of  $\sim 15\ \mu\text{m}$  (FWHM) and an intra-train repetition rate of 1.128 MHz. The final design characteristics of the SPB/SFX instrument at EuXFEL foresee an X-ray focus of hundreds of nanometers (nanofocus) to a few micrometers (microfocus) resulting in a much higher fluence, combined with the possibility of a 4.5 MHz intra-train repetition rate<sup>13,14</sup> which will therefore require a reassessment of this issue.

Our results demonstrate that MHz XFELs can be used to collect high-quality serial femtosecond crystallography data, and that under the conditions used in the current experiment, shock waves caused by the interaction between the sample jet and the XFEL pulses do not compromise the data to a measurable extent. The data are good enough to evaluate a previously uncharacterized sample. As shown by the electron density maps of the concanavalin A and B structures determined in this study, the data are of high quality and this is likely to improve as experience with ultrafast detectors such as the AGIPD increases. Moreover, in just one shift (12 h) of data collection,  $\sim 77,000$  indexed images were collected of concanavalin A and  $\sim 24,000$  of concanavalin B, despite this being one of the very first experiments at a new facility.

The findings presented here are of interest for a large and continuously growing community of scientists interested in using MHz XFELs. The possibility of recording data  $>100$  times faster than previously possible means that XFEL technology will in the near future become available to many more scientists since the cost of these measurements will decrease greatly as the time spent to acquire the data is reduced. Notably, the techniques we used in our present work and the underlying physics of operating sequential experiments at MHz rates are also directly relevant to other subfields of XFEL science, from physicists interested in extreme interactions between radiation and matter, to chemists focused on ultrafast reactions, and to other scientists interested in “big data” measurements.

## Methods

**Crystallization.** Jack bean meal was obtained as a fine powder from Sigma (J0125). Proteins were extracted following published procedures<sup>28,29</sup>. To this end, 50 g of jack bean powder were suspended in 200 ml of phosphate buffer (100 mM, pH 8.0) and stirred for 1 h at 4  $^{\circ}\text{C}$ . After centrifugation, acetone was added to the supernatant to yield 28% and incubated overnight at 4  $^{\circ}\text{C}$ . After centrifugation the acetone concentration was increased to 31.6% and stirred for 1 h at RT. Upon further centrifugation the acetone concentration was increased to 50% and stirred 1 h at RT. After a final round of centrifugation the pellet was dissolved in 50 ml 50 mM Tris pH 8.0. This solution was dialyzed for 48 h against water at 4  $^{\circ}\text{C}$ . Rod- and rugby-ball-shaped crystals appeared overnight. After 2 weeks of storage at 4  $^{\circ}\text{C}$ , needle-shaped crystals appeared. Lysozyme microcrystals were grown by rapidly mixing 2.5 ml of protein solution (hen egg white lysozyme (Sigma) in 0.1 M sodium acetate buffer pH 3.0) and 7.5 ml precipitate solution (20% NaCl, 6% PEG 6000, 0.1 M sodium acetate pH 3.0). The mixture was left overnight on a slowly rotating wheel shaker. After gravity-induced settling, the crystalline pellet was washed several times in crystal storage solution (10% NaCl, 0.1 M sodium acetate buffer, pH 4.0). The microcrystal size depends on protein concentration and temperature:  $\sim 1\ \mu\text{m}$  crystals were obtained using a protein concentration of 32  $\text{mg ml}^{-1}$  at 4  $^{\circ}\text{C}$ <sup>22</sup>; the microcrystals were slightly larger ( $\sim 2 \times 2 \times 3\ \mu\text{m}$ ) when using a protein concentration of 50  $\text{mg ml}^{-1}$  at room temperature<sup>34</sup>.

**Injection.** A suspension of microcrystals in their mother liquor was injected into the X-ray interaction region via a liquid microjet produced by a gas dynamic virtual nozzle (GDVN)<sup>35</sup> using helium as the focusing gas. The sample flow rate was 30–40  $\mu\text{l min}^{-1}$ , and gas pressure 400–500 psi at the inlet of the GDVN's gas supply line, corresponding to a flow rate of 140–250  $\text{ml min}^{-1}$ . All samples were 20  $\mu\text{m}$  filtered prior to injection, and the suspension was adjusted to contain 10–15% (v/v) settled crystalline material. During injection the sample was kept in a rotating temperature-controlled reservoir (20 °C for lysozyme microcrystals, 4 °C for jack bean protein microcrystals) to prevent crystal settling<sup>36</sup>.

Jet speed is a parameter of utmost importance for our experiment, determining not only the rate at which sample is replenished in the X-ray interaction region but also the distance of microcrystals probed by consecutive X-ray pulses. Jet speed was therefore measured in situ (described below) during data collection both on a regular basis and for each change in flow conditions (e.g., new sample, crystal concentration, change in liquid flow rate or helium pressure, new GDVN, etc.). To enable comparison of all data collected in a liquid jet, jet speed was always set to a value of 40–50  $\text{m s}^{-1}$ , typically  $\sim 45 \text{ m s}^{-1}$ , by adjusting the sample flow rate and the pressure of the focusing gas.

**Imaging the jet.** The liquid jet was imaged from an off-axis perspective (orthogonal to both X-rays and jet flow direction) using a 10 $\times$  infinity-corrected objective in combination with a 200 mm tube lens and a camera (Basler pilot pIA2400-17gm, Basler AG, Germany). The optical resolution of the imaging system, determined with a resolution target (Edmund Optics), was 1.6  $\mu\text{m}$ . During data collection the camera pixels were 2  $\times$  2-binned, resulting in recorded images with a scale of 0.68  $\mu\text{m pixel}^{-1}$ . To illuminate the jet for high time resolution imaging while preventing motion-induced blurring, which may preclude any speed analysis for liquid jets running at the speeds required for MHz data collection<sup>37</sup>, the femtosecond (fs) SASE1 optical pump laser<sup>23</sup> was employed for jet illumination as described in ref. 20. The fs laser pulse and the camera were triggered by the EuXFEL global trigger (10 Hz) that indicates the arrival of an X-ray pulse train, thus the images were recorded at a set delay relative to the arrival of the pulse train. We set this delay to image the jet shortly after the second pulse generated a visible gap in the jet, thus imaging the effect of the first two pulses on the jet (see Fig. 1a). The optical images were recorded 124 ns (lysozyme) and 13.4 ns (jack bean proteins) after the second XFEL pulse. The imaging time delay was chosen such that the gap made by the second pulse in the jet was clearly visible during the experiment, in order to provide feedback for the proper alignment of the jet (i.e., the best alignment occurred when the gap size was maximized, which indicates that the jet acquired the maximum possible radiation dose). The jets carrying lysozyme, because they were less stable in shape than the urease/concanavalin jets, required a longer imaging delay such that a larger gap size compensated for the jet's shot-to-shot jitter.

**Jet speed determination.** In situ measurement of jet speed is constantly required for MHz data collection to verify that the gap produced by one X-ray pulse has moved downstream before arrival of the subsequent X-ray pulse. This is particularly important when flow conditions change. Measuring jet speed is generally done by tracking a feature over time. In our case, the tracked "feature" was the center of the gap produced by the XFEL interaction with the jet, which is flushed downstream by the subsequently injected sample at the speed of the jet itself<sup>20</sup>. Imaging two gaps in the jet that are produced by two X-ray pulses therefore allows determining jet speed in a single image provided the imaging quality and time resolution is high enough to determine the center of both gaps: If the two gaps are located at distance  $d$  from each other, and the corresponding X-ray pulses were spaced by  $\Delta t$ , then jet speed  $v$  is obtained as  $v = d/\Delta t$  (see Fig. 1a).

**Data collection.** The experiment was performed at the SPB/SFX instrument of the EuXFEL<sup>16,17</sup>. Ten pulse trains per second consisting of 50 pulses at 1.128 MHz intra-train repetition rate (886 ns spacing between pulses as measured during the experiment) were used for data collection. We note that during our experiment, the EuXFEL could deliver up to 60 pulses per train to SPB/SFX and that the accelerator was indeed running in 60-pulse mode, with the first 10 pulses used for electron orbit feedback and then being sent to the pre-undulator dump, without lasing. While an increase in the electron orbit stability has been observed in the accelerator with this procedure, possible increases in positional or intensity stability of X-rays at the SPB/SFX instrument have not yet been determined. We chose to discard the first 10 pulses before the sample, due to the possibility that the first pulses in a full train currently may have lower intensities due to the feedback loop requiring the first pulses in a train to optimize beam properties over the remainder of a given train. Thus, using the first several pulses in a maximum-size train could have led to an underestimate of sample damage. The photon energy was tuned to 7.47 and 9.22 keV for the lysozyme control data sets and to 7.48 keV for the jack bean protein microcrystals data set. For the lysozyme control data, the crystal size was chosen so as to have the diffraction limit fall within the boundary of the detector, to be able to see any damage effects on the diffraction resolution ( $1 \times 1 \times 1 \mu\text{m}$  for the 7.47 keV data,  $2 \times 2 \times 3 \mu\text{m}$  for the 9.22 keV data). At the beginning of each shift the X-ray focus size was minimized by adjusting the photon energy, and then measured, by imaging the size of the fluorescent spot produced by single focused XFEL pulses on a YAG screen (Ce:YAG, 20  $\mu\text{m}$  thickness, Crytur) placed at the

interaction region. The X-ray focus was  $\sim 15 \mu\text{m}$  for the 7.47 keV lysozyme and the 7.48 keV jack bean protein data and  $\sim 28 \mu\text{m}$  for the 9.22 keV lysozyme data. For each individual X-ray pulse, the pulse energy was recorded by an X-ray gas monitor detector (XGMD) upstream of the experimental hutch. Microcrystals were injected into the X-ray interaction region using a GDVN as described above.

**Data processing and structure solution.** Data from the AGIP detector was calibrated using the calibration pipeline established at EuXFEL<sup>38,39</sup>, with constants provided by the facility and the AGIPD consortium. CASS<sup>40</sup> was used for online data analysis, hit identification and data preprocessing. Indexing and integration were performed with CrystFEL version 0.6.3. The detector distance was the same for each of the five shifts of data collection. The position of the sample jet was continuously adjusted to maximize the hit rate. The positions and orientations of individual sensor modules of the AGIPD were refined as described<sup>1</sup>. The quality of the lysozyme control data was investigated using custom-written python- and mathematica scripts as well as programmes from the CCP4 suite<sup>41</sup>. Lysozyme structures were refined against the 7.47 and 9.22 keV datasets using PHENIX<sup>42</sup> (including simulated annealing), after molecular replacement with PHASER<sup>43</sup>. In the 7.47 keV structure, 99.2%, 0.8%, and 0.0% of residues are in the preferred, allowed and disallowed regions of the Ramachandran plot, respectively. For the 9.22 keV structure, these numbers are 99.2%, 0.8%, and 0.0%. Complete data and model statistics are given in Table 1.

The concanavalin A data were phased by molecular replacement with PHASER<sup>43</sup>, using PDB entry 1JBC<sup>30</sup> as the search model after removal of the waters and the metal ions. A clear solution (TFZ = 8.9) was found, and the structure was refined by iterative cycles of rebuilding in COOT<sup>44</sup> and refinement in PHENIX<sup>42</sup>, including simulated annealing. The final model has excellent geometry, with 97.4% of residues in the preferred regions of the Ramachandran plot, 2.6% in allowed regions and 0.0% in disallowed regions. A phased anomalous difference density map was calculated to help identify the metal ions bound to the protein. As expected at the photon energy used for data collection (7.48 keV), clear anomalous difference density (6.9 $\sigma$  peak height) was found at the position of the calcium ion, but none was found for the other metal ion, which was modeled as a magnesium ion based on the lack of anomalous signal, the coordination as well as the expected metal content for native concanavalin A<sup>32</sup>.

The concanavalin B data were treated by AMBIGATOR to remove the indexing ambiguity<sup>25,45</sup>. These data were then also phased by molecular replacement with PHASER using PDB entry 1CNV<sup>31</sup> as the search model after removal of the waters, again resulting in a very clear solution (TFZ = 12.6). The final structure was obtained using iterative cycles of rebuilding in COOT and refinement in PHENIX (including simulated annealing), resulting in a model with excellent geometry, with 97.9% of residues in preferred regions, 1.7% in allowed regions and 0.4% (1 residue) in disallowed regions of the Ramachandran plot. This latter residue is in a highly strained part of the main chain, involved in a cis peptide known to occur in concanavalin B.

Simulated annealing composite omit maps of representative regions of both structures are shown in Fig. 3. Atomic coordinates and structure factor amplitudes have been deposited in the Protein Data Bank under entry codes 6GW9 (concanavalin A) and 6GWA (concanavalin B). Data and model statistics for both structures are given in Table 1.

**Code availability.** Analysis scripts are available from the authors upon request.

**Data availability.** Coordinates and structure factor amplitudes have been deposited in the Protein Data Bank under accession codes 6H0K (lysozyme, 7.47 keV), 6H0L (lysozyme, 9.22 keV), 6GW9 (concanavalin A) and 6GWA (concanavalin B). Data from this experiment have been registered under DOI 10.22003/XFEL.EU-DATA-002038-00. Other data are available from the corresponding authors upon reasonable request.

Received: 11 July 2018 Accepted: 1 August 2018

Published online: 28 August 2018

## References

- Barends, T. R. M. et al. Direct observation of ultrafast collective motions in CO myoglobin upon ligand dissociation. *Science* **350**, 445–450 (2015).
- Pande, K. et al. Femtosecond structural dynamics drives the trans/cis isomerization in photoactive yellow protein. *Science* **352**, 725–729 (2016).
- Coquelle, N. et al. Chromophore twisting in the excited state of a photoswitchable fluorescent protein captured by time-resolved serial femtosecond crystallography. *Nat. Chem.* **10**, 31–37 (2018).
- Kern, J. et al. Simultaneous femtosecond X-ray spectroscopy and diffraction of photosystem II at room temperature. *Science* **340**, 491–495 (2013).
- Suga, M. et al. Native structure of photosystem II at 1.95 angstrom resolution viewed by femtosecond X-ray pulses. *Nature* **517**, 99–103 (2015).

6. Colletier, J. P. et al. *De novo* phasing with X-ray laser reveals mosquito larvicide BinAB structure. *Nature* **539**, 43–47 (2016).
7. Sawaya, M. R. et al. Protein crystal structure obtained at 2.9 Ångstrom resolution from injecting bacterial cells into an X-ray free-electron laser beam. *Proc. Natl Acad. Sci. USA* **111**, 12769–12774 (2014).
8. Ginn, H. M. et al. Structure of cpv17 polyhedrin determined by the improved analysis of serial femtosecond crystallographic data. *Nat. Commun.* **6**, 6435 (2015).
9. Seibert, M. M. et al. Single mimivirus particles intercepted and imaged with an X-ray laser. *Nature* **470**, 78–81 (2011).
10. Kassemeyer, S. et al. Optimal mapping of X-ray laser diffraction patterns into three dimensions using routing algorithms. *Phys. Rev. E* **88**, 042710 (2013).
11. Bostedt, C. et al. Linac coherent light source: the first five years. *Rev. Mod. Phys.* **88**, 015007 (2016).
12. Henrich, B. et al. The adaptive gain integrating pixel detector AGIPD: a detector for the European XFEL. *Nucl. Instrum. Meth. Phys. Res. A* **633**, S11–S14 (2011).
13. Altarelli, M. The European X-ray free-electron laser facility in Hamburg. *Nucl. Instrum. Meth. Phys. Res. B* **269**, 2845–2849 (2011).
14. Altarelli, M. The European X-ray free-electron laser: toward an ultra-bright, high repetition-rate X-ray source. *High Power Laser Sci. Eng.* **3**, <https://doi.org/10.1017/hpl.2015.17> (2015).
15. Tschentscher, T. et al. Photon beam transport and scientific instruments at the European XFEL. *Appl. Sci.* **7**, 592 (2017).
16. Mancuso, A. P. *Conceptual Design Report: Scientific Instrument Single Particles, Clusters, and Biomolecules (SPB)*. XFEL.EU Technical Report 1–96, <https://doi.org/10.3204/XFEL.EU/TR-2011-007> (2011).
17. Mancuso, A. P., Aquila, A., Borchers, G., Giewekemeyer, K. & Reimers, N. *Technical Design Report: Scientific Instrument Single Particles, Clusters, and Biomolecules (SPB)*. XFEL.EU Technical Report 1–232, <https://doi.org/10.3204/XFEL.EU/TR-2013-004> (2013).
18. Sumner, J. B. The isolation and crystallization of the enzyme urease. *Prelim. Pap. J. Biol. Chem.* **69**, 435–441 (1926).
19. Edsall, J. T. 50 years ago: James Sumner and the crystallization of urease. *Trends Biochem. Sci.* **1**, 21 (1976).
20. Stan, C. A. et al. Liquid explosions induced by X-ray laser pulses. *Nat. Phys.* **12**, 966–971 (2016).
21. Chapman, H. N. et al. Femtosecond X-ray protein nanocrystallography. *Nature* **470**, 73–77 (2011).
22. Boutet, S. et al. High-resolution protein structure determination by serial femtosecond crystallography. *Science* **337**, 362–364 (2012).
23. Pergament, M. et al. Versatile optical laser system for experiments at the European X-ray free-electron laser facility. *Opt. Express* **24**, 29349–29359 (2016).
24. White, T. A. et al. CrystFEL: a software suite for snapshot serial crystallography. *J. Appl. Crystallogr.* **45**, 335–341 (2012).
25. White, T. A. et al. Recent developments in CrystFEL. *J. Appl. Crystallogr.* **49**, 680–689 (2016).
26. Southworth-Davies, R. J., Medina, M. A., Carmichael, I. & Garman, E. F. Observation of decreased radiation damage at higher dose rates in room temperature protein crystallography. *Structure* **15**, 1531–1541 (2007).
27. Karplus, P. A. & Diederichs, K. Linking crystallographic model and data quality. *Science* **336**, 1030–1033 (2012).
28. McPherson, A., Geller, J. & Rich, A. Crystallographic studies on concanavalin-B. *Biochem. Biophys. Res. Commun.* **57**, 494–499 (1974).
29. Jabri, E., Lee, M. H., Hausinger, R. P. & Karplus, P. A. Preliminary crystallographic studies of urease from jack bean and from *Klebsiella aerogenes*. *J. Mol. Biol.* **227**, 934–937 (1992).
30. Parkin, S., Rupp, B. & Hope, H. Atomic resolution structure of concanavalin A at 120 K. *Acta Crystallogr. D* **52**, 1161–1168 (1996).
31. Hennig, M., Jansonius, J. N., Terwisscha Van Scheltinga, A. C., Dijkstra, B. W. & Schlesier, B. Crystal-structure of concanavalin-B at 1.65 Ångstrom resolution - an inactivated chitinase from seeds of *Canavalia ensiformis*. *J. Mol. Biol.* **254**, 237–246 (1995).
32. Yariv, J., Kalb, A. J. & Levitzki, A. Interaction of concanavalin A with methyl alpha-d-glucopyranoside. *Biochim. Biophys. Acta* **165**, 303–30 (1968).
33. Kalb, A. J., Yariv, J., Helliwell, J. R. & Papiz, M. Z. The effect of metal-ion homogeneity on the diffraction limit of orthorhombic (I222) crystals of concanavalin-A. *J. Cryst. Growth* **88**, 537–540 (1988).
34. Gorel, A. et al. Multi-wavelength anomalous diffraction *de novo* phasing using a two-colour X-ray Free-Electron Laser with wide tunability. *Nat. Commun.* **8**, 1170 (2017).
35. Weierstall, U., Spence, J. C. H. & Doak, R. B. Injector for scattering measurements on fully solvated biospecies. *Rev. Sci. Instrum.* **83**, 035108 (2012).
36. Lomb, L. et al. An anti-settling sample delivery instrument for serial femtosecond crystallography. *J. Appl. Crystallogr.* **45**, 674–678 (2012).
37. Grünbein, M. L., Shoeman, R. L. & Doak, R. B. Velocimetry of fast microscopic liquid jets by nanosecond dual-pulse laser illumination for megahertz X-ray free-electron lasers. *Opt. Express* **26**, 7190–7203 (2018).
38. Kuster, M. et al. Detectors and calibration concept for the European XFEL. *Synchrotron Radiat. News* **27**, 35–38 (2014).
39. Fangohr, H. et al. Data analysis support in KARABO at European XFEL. TUCPA01 (2018). <https://doi.org/10.18429/JACoW-ICALPCS2017-TUCPA01>
40. Foucar, L. et al. CASS-CFEL-ASG software suite. *Comput. Phys. Commun.* **183**, 2207–2213 (2012).
41. The CCP4 suite. Programs for protein crystallography. *Acta Crystallogr. D* **50**, 760–763 (1994).
42. Adams, P. D. et al. Phenix: a comprehensive python-based system for macromolecular structure solution. *Acta Crystallogr. D* **66**, 213–221 (2010).
43. McCoy, A. J. et al. Phaser crystallographic software. *J. Appl. Cryst.* **40**, 658–674 (2007).
44. Emsley, P. & Cowtan, K. *Coot*: model-building tools for molecular graphics. *Acta Crystallogr. D* **60**, 2126–2132 (2004).
45. Brehm, W. & Diederichs, K. Breaking the indexing ambiguity in serial crystallography. *Acta Crystallogr. D* **70**, 101–109 (2014).

## Acknowledgements

We acknowledge European XFEL in Schenefeld, Germany, for provision of X-ray free-electron laser beamtime at the SPB/SFX instrument and thank the instrument group and facility staff for their great assistance. We thank Oleksandr Yefanov for helpful discussions on detector geometry optimization, as well as Harald Sinn and Winfried Decking for helpful discussions on beam- and pulse train properties. We thank the AGIPD consortium for providing some of the calibration constants for the detector. We also thank Melanie Müller for peptide mass fingerprinting. The authors are indebted to the SFX User Consortium for the provision of instrumentation and personnel that has enabled this experiment. This research was supported by the Max Planck Society and travel grants from the European XFEL. J.-P.C., M.W., M.C. and M.S.I. acknowledge support from ANR Grant (BioXFEL). J.-P.C. acknowledges financial support by CEA, CNRS, Université Grenoble Alpes, and the Agence Nationale de la Recherche (Grants Nr. ANR-15-CE18-0005-02, ANR-17-CE11-0018-01). C.A.S. was supported by startup funds from Rutgers University Newark. G.M. acknowledges the support of the Australian Research Council Centre of Excellence in Advanced Molecular Imaging [CE140100011]. G.M. also acknowledges the Australian Nuclear Science and Technology Organisation (ANSTO) in providing financial support for this work. We also acknowledge the travel funding provided by the International Synchrotron Access Program (ISAP) managed by the Australian Synchrotron, part of ANSTO, and funded by the Australian Government.

## Author contributions

M.L.G., M.St., M.K., R.L.S. and R.B.D. performed injection, E.H. and I.S. prepared crystals, M.H. and L.Fou. performed online data analysis, A.G., J.-P.C., and T.R.M.B. performed offline analysis. J.B., M.Me., K.D., R.B., T.S., Y. K., A.P.M. and R.L. performed data collection. M.Me., J.S.-D., S.H., N.R., A.Mü., A.K. and M.R. developed, controlled and operated the detector. M.Sch. and L.Fr. prepared and tested the specific repetition rates of the accelerator. H.F., T.M., A.S., S.B., J.Z., T. K., S. E. and W.E. developed control and online analysis software. K.W., D.B., L.M., G.P., J.S., N.Al Q. and M. Ma. performed data management. T.S., J.B., R.L., M. L. G. and C.A.S. set up femtosecond jet imaging, I.S. and C.A.S. conceived the experiment. I.S., C.A.S., J.B., B.W. and A.P.M. designed the experiment. M.L.G., A.G., M.St., R.B., J.B., M.C., K.D., E.H., M.H., Y.K., M.K., R.L., J.S.-D., A.P.M., M.Me., G.M., G.N.K., C.M.R., T.S., M.S.I., M.W., B.W., G. M., M.R., R.B.D., R. L.S., L.Fou., J.-P.C., T.R.M.B., C.A.S. and I.S. prepared the experiment. F.P., S.V., G.P., M. E. and M.L. designed and set up the femtosecond laser. M.L.G., T.R.M.B., C.A.S. and I.S. wrote the paper with input from all authors.

## Additional information

**Supplementary Information** accompanies this paper at <https://doi.org/10.1038/s41467-018-05953-4>.

**Competing interests:** The authors declare no competing interests.

**Reprints and permission** information is available online at <http://npg.nature.com/reprintsandpermissions/>

**Publisher's note:** Springer Nature remains neutral with regard to jurisdictional claims in published maps and institutional affiliations.





**Open Access** This article is licensed under a Creative Commons Attribution 4.0 International License, which permits use, sharing, adaptation, distribution and reproduction in any medium or format, as long as you give appropriate credit to the original author(s) and the source, provide a link to the Creative Commons license, and indicate if changes were made. The images or other third party material in this article are included in the article's Creative Commons license, unless indicated otherwise in a credit line to the material. If material is not included in the article's Creative Commons license and your intended use is not permitted by statutory

regulation or exceeds the permitted use, you will need to obtain permission directly from the copyright holder. To view a copy of this license, visit <http://creativecommons.org/licenses/by/4.0/>.

© The Author(s) 2018



ARTICLE

DOI: 10.1038/s41467-018-06156-7

OPEN

# Megahertz serial crystallography

Max O. Wiedorn  et al.<sup>#</sup>

The new European X-ray Free-Electron Laser is the first X-ray free-electron laser capable of delivering X-ray pulses with a megahertz inter-pulse spacing, more than four orders of magnitude higher than previously possible. However, to date, it has been unclear whether it would indeed be possible to measure high-quality diffraction data at megahertz pulse repetition rates. Here, we show that high-quality structures can indeed be obtained using currently available operating conditions at the European XFEL. We present two complete data sets, one from the well-known model system lysozyme and the other from a so far unknown complex of a  $\beta$ -lactamase from *K. pneumoniae* involved in antibiotic resistance. This result opens up megahertz serial femtosecond crystallography (SFX) as a tool for reliable structure determination, substrate screening and the efficient measurement of the evolution and dynamics of molecular structures using megahertz repetition rate pulses available at this new class of X-ray laser source.

---

Correspondence and requests for materials should be addressed to H.C. (email: [henry.chapman@desy.de](mailto:henry.chapman@desy.de)) or to A.B. (email: [anton.barty@desy.de](mailto:anton.barty@desy.de)). <sup>#</sup>A full list of authors and their affiliations appears at the end of the paper.

The development of serial femtosecond crystallography (SFX) using intense femtosecond-duration pulses from X-ray free-electron lasers has opened up new avenues for the measurement of macromolecular structures and macromolecular dynamics. SFX has found particular application for room temperature measurements using micron-sized and smaller protein crystals, time-resolved studies of biomolecular dynamics at physiologically relevant temperatures, and the measurement of radiation-sensitive structures<sup>1–7</sup>. The pressing challenge facing serial crystallography has been efficiently measuring diffraction data from the large number of individual micro- or nanocrystals required for the serial crystallography approach. Now, the new European X-ray Free-Electron Laser (EuXFEL) is the first X-ray free-electron laser capable of delivering X-ray pulses with a megahertz inter-pulse spacing, a peak pulse rate four orders of magnitude higher than previously possible<sup>8</sup>. However, to date, it has been unclear whether it would indeed be possible to measure high-quality structures using an XFEL beam with a microsecond X-ray pulse separation. Here, we show that high-quality structures can indeed be obtained using 1.1 MHz repetition rate pulses from the European XFEL using currently available operating conditions (September 2017 and March 2018, proposal p2012). We present two complete data sets, one from the well-known model system in crystallography, lysozyme and the other from a so far unknown complex of a  $\beta$ -lactamase from *Klebsiella pneumoniae* involved in antibiotic resistance. This result opens up the possibility of SFX structure determination at a far higher rate than previously possible, enabling the efficient measurement of the evolution and dynamics of molecular structures using megahertz repetition rate pulses available at this new class of X-ray laser source.

Ultra-short and extremely intense X-ray pulses from XFELs can outrun X-ray-induced damage processes to obtain practically

unperturbed structures before the onset of sample explosion<sup>9,10</sup>. "Diffraction before destruction" has enabled the recent development of SFX at FELs using sub-micron-sized crystals at room temperature using doses far exceeding conventional radiation damage limits<sup>11,12</sup>. To date, SFX measurements have been limited by facility pulse repetition rates to measuring at 120 frames per second or 8 ms between pulses<sup>13–15</sup>. The EuXFEL design produces bursts of X-ray pulses at a megahertz repetition rate, repeating at 10 Hz frequency (Fig. 1). At the current EuXFEL, intra-bunch repetition rate of 1.1 MHz the pulse spacing is less than 1  $\mu$ s, nearly four orders of magnitude shorter than previously available<sup>8</sup>. The decreased time between X-ray pulses enables the EuXFEL to deliver more pulses per second while maintaining the same X-ray peak power, but simultaneously poses several challenges for SFX. Exposed samples must clear the X-ray interaction point in less than 1  $\mu$ s before the arrival of the next X-ray pulse requiring sample to be delivered four orders of magnitude faster than previously required. Additionally, detecting full-frame diffraction patterns with megahertz pulse repetition rates requires a totally new class of detector. Further complicating matters, the high dose deposited by a single FEL pulse can cause the jet to explode. This creates a void which must also clear the interaction point before the next X-ray pulse arrives. The explosion has been observed to send a shock wave back up the liquid column under certain conditions<sup>16</sup>, while high levels of ionization produced in a small area also create free electrons which can damage as yet unexposed sample. Any of these effects could damage the incoming protein crystals resulting in either modification of the molecular or crystalline structure, possibly preventing structural information to be acquired from diffraction measurements altogether.

We demonstrate here that serial femtosecond crystallography using bursts of megahertz repetition rate X-ray pulses is capable

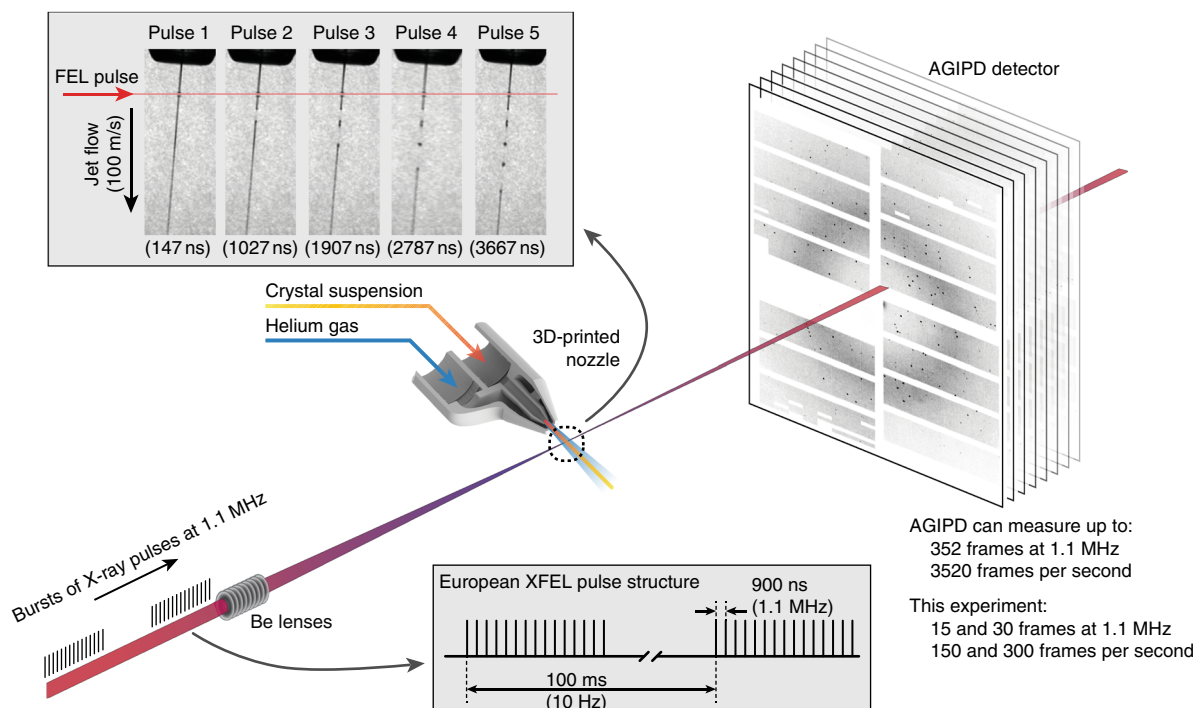


**Fig. 1** Megahertz serial crystallography. Pulses from the European XFEL were focused on the interaction region using a set of Beryllium lenses. Protein crystals in crystallization solution were introduced into the focused XFEL beam using a liquid jet of 1.8  $\mu$ m diameter moving at speeds between 50 m/s and 100 m/s. Diffraction from the sample was measured using an AGIPD, which is capable of measuring up to 3520 pulses per second at megahertz frame rates. In-situ jet imaging (inset) showed that the liquid column does explode under the X-ray illumination conditions of this experiment using a jet with a speed of 100 m/s, but that the liquid jet recovered in less than 1  $\mu$ s to deliver fresh sample in time for arrival of the next X-ray pulse. Images and movies of jets at different speeds are included in the supplementary material

of high-resolution structure determination using high-speed liquid jets as the sample delivery medium and hen egg white lysozyme (HEWL) as a known and well-characterized model system. HEWL is an extremely well-characterized system that crystallizes easily into a range of crystal sizes, making it an excellent system for demonstrating SFX at MHz pulse rates. We further demonstrate that MHz SFX is suitable for structural discovery by determining the structure of a so far unknown complex of a  $\beta$ -lactamase from *K. pneumoniae*. This enzyme belongs to the extended spectrum  $\beta$ -lactamases (ESBLs) that play an important role in emerging multi-antibiotic resistance mechanisms. This class of enzymes is able to hydrolyze the  $\beta$ -lactam ring structure of most prominent antibacterial agents used in medicine and render them ineffective. The constantly evolving resistance to penicillin and penicillin-derived antibiotics is forcing the development of new antibiotics, as particular ESBLs including CTX-M-14 from *K. pneumoniae* are already able to cleave even antibiotics specifically developed against pathogens with high  $\beta$ -lactamase stability including third-generation cephalosporins such as cefotaxime or ceftazidime<sup>17</sup>. These cephalosporins have bulky R1 residues, which means that they no longer fit into the binding pocket of  $\beta$ -lactamases and thus are no longer cleaved by them. The so-called activity-stability compromise for the observed substrate-spectrum-expanding mutations in ESBL describing an enlargement of the binding pocket at the expense of the overall stability of the enzyme<sup>18</sup> is a suspected cause of inhibition<sup>19</sup>. To obtain structural insights into the molecular basis and spectrum of CTX-M-14 inhibition, we analyzed the complex with the inhibitor avibactam. Furthermore, studying  $\beta$ -lactamase binding is an important demonstration towards both high-throughput substrate screening and future time-resolved diffusion-based SFX experiments in which inhibitor and crystals are mixed on the fly to enable time-resolved structural studies of substrate binding<sup>20</sup>.

## Results

**Megahertz serial crystallography.** Our experiment was conducted at the SPB/SFX (single particles, clusters and biomolecules and serial femtosecond crystallography) instrument of the European XFEL<sup>21</sup>. For the HEWL measurements, X-ray pulses with a mean photon energy of 9.3 keV (1.3 Å wavelength), a mean pulse energy of 580  $\mu$ J and pulse length of approximately 50 fs duration (derived from the electron bunch length) were focused by beryllium compound refractive lenses into a focal spot of 16  $\mu$ m diameter full width at half maximum (FWHM) in the SPB/SFX interaction region (Fig. 1). The European XFEL pulse structure for this experiment comprised 15 X-ray pulses at 1.1 MHz repetition rate repeating at 10 Hz, for a total of 150 pulses per second. Microcrystals of HEWL of 6–8  $\mu$ m size were introduced into the X-ray interaction region in a 1.8  $\mu$ m diameter liquid jet by a gas dynamic virtual nozzle at speeds of between 50 and 100 m/s. Jet speed was measured using direct imaging in the laboratory under the same conditions as used in the EuXFEL experiment (Table 1). Measurements were made at room temperature and the absorbed dose for each crystal was estimated to be 0.5 MGy using RADDOSE-3D version 2.1<sup>22</sup> based on an estimated 50% beamline transmission and a 16  $\mu$ m focal spot size. Diffraction from each X-ray pulse was measured using a 1-megapixel AGIPD (adaptive gain integrating pixel detector) located 0.12 m downstream of the interaction region as shown in Fig. 1. A sample crystal diffraction pattern is shown in Fig. 2 demonstrating the quality of diffraction patterns measured. An image of an HEWL crystal in liquid jet under the same sample delivery conditions used in this experiment is shown in Supplementary Figure 1, which also illustrates how jet

**Table 1 Measured jet speeds**

Condition	50 m/s	75 m/s	100 m/s	25 m/s
Liquid flow ( $\mu$ L/min)	15	13	13	41
Gas flow (mg/min)	23	50	80	20
<b>Water</b>				
Delay time (ns)	200	130	80	~2000
Distance by imaging in lab ( $\mu$ m)	10	10	9	~50
Speed by imaging in lab (m/s)	50	77	110	25
<b>Lysozyme crystal suspension</b>				
Delay time (ns)	500	400	200	-
Distance by imaging in lab ( $\mu$ m)	21	31	21	-
Speed by imaging in lab (m/s)	42	78	105	-

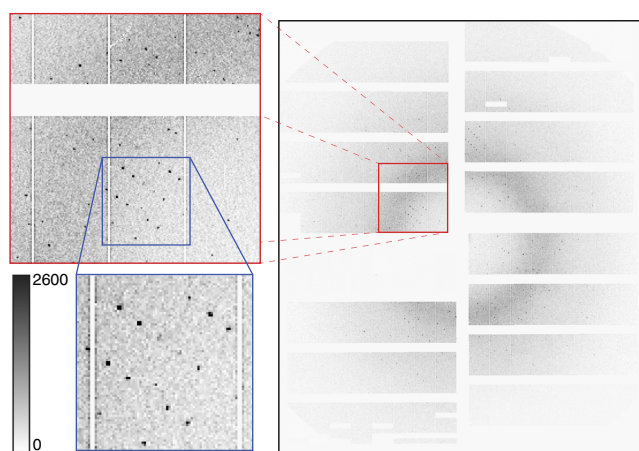


**Fig. 2** Diffraction pattern from HEWL. Diffraction pattern from a single HEWL microcrystal measured using MHz pulses of 50 fs duration X-rays at 9.3 keV using the AGIPD 1M detector in the SPB/SFX instrument. Dynamic gain switching of the AGIPD detector enables simultaneous low noise and high dynamic range: each pixel has three gain settings which are automatically selected depending on the per-pixel cumulative intensity to simultaneously maximize sensitivity and dynamic range. Image clipped at 2600 counts to show content, full dynamic range of brightest spots extends to 109,000 counts

speed for crystal solution was directly measured using double exposure illumination.

An important consideration is whether data can be collected from any pulse in the EuXFEL pulse train, or only from the first pulse due to jet destruction or crystal damage. Direct imaging of the liquid jet using stroboscopic laser illumination shows that the XFEL pulse initially vaporizes the jet but that the liquid column does indeed recover in time for the next X-ray pulse for jets with a diameter of less than 2  $\mu$ m and speeds between 50 and 100 m/s, while jets with a speed of 25 m/s do not recover in time (Fig. 3 and Supplementary Movie 1, Supplementary Movie 2, Supplementary Movie 3, Supplementary Movie 4). Imaging reveals that explosion dynamics for jet speeds of between 50 and 100 m/s are qualitatively different from those previously reported<sup>16</sup>, showing a clean break in the liquid stream rather than the rapid expansion shapes reported in ref. <sup>16</sup>, reflecting the smaller jet size and larger focus compared to previous studies. Results using lower photon energies at FLASH suggest this behaviour will scale to GGy doses expected to be available due to smaller focal spot sizes at the SPB/SFX instrument in the near future<sup>23</sup>. The ratio of focal spot size to jet diameter may also affect explosion dynamics

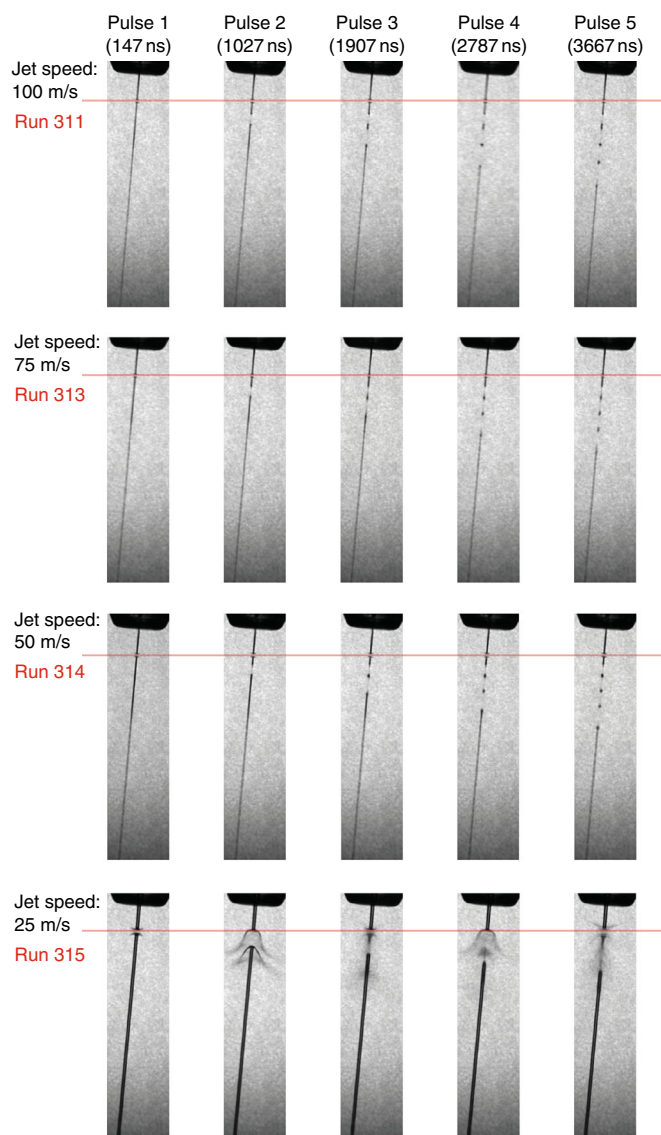


**Fig. 3** Images of interaction of the EuXFEL liquid jet for the first 5 pulses in a train. Jets in the range of 50–100 m/s recover in time for the next pulse (first three rows), whereas slower jets of the type commonly used at LCLS do not recover in time for the next XFEL pulse at MHz repetition rates (bottom row). The bottom line provides linkage back to the results presented in ref. <sup>1</sup>. Red line shows the intersection point with X-ray pulses. Images obtained by synchronized laser back illumination. Movies with finer time steps are included as supplementary material

and will be the subject of future studies when smaller focal spot sizes become available.

**Lysozyme reference data.** We collected 749,874 diffraction patterns from HEWL crystal solution in 83 min of measurement time at 150 pulses per second, of which 25,193 images (3.4%) were found to contain crystal diffraction as identified by Cheetah<sup>24</sup>. We observed that diffraction from microcrystals could be observed on both the first and subsequent pulses in the XFEL pulse train and that detected crystal “hits” were distributed roughly evenly through the pulse train (Fig. 4). This indicates that the first pulse does not destroy the liquid jet for the rest of the pulse train across the range of jet speeds and X-ray pulse intensities tested. From the identified hits, 24,733 images (95%) could

be indexed using the CrystFEL software suite<sup>25,26</sup> yielding 25,531 indexed crystal lattices for structure determination when allowing for multiple lattices per image. Indexing results further indicate that crystals were equally distributed among pulses in the MHz XFEL pulse train with no obvious signs of degradation in data quality through the pulse train (Fig. 4). Additionally, the CC\* data metric is similar for merged data split according to pulse ID, and that the correlation between merged data from the first and subsequent pulses is consistent showing no visible signs of degradation under the conditions of this experiment (Fig. 4).

Merging reflection intensities using the program partialator in CrystFEL produced a data set with an error metric  $R_{\text{split}}$  of 0.105 to 1.8 Å resolution and CC\* of 0.995 (Table 2). The structure was determined by molecular replacement using Phenix<sup>27</sup> using a solvent-free version of the 4ET8 SFX lysozyme structure<sup>2</sup> as the starting model with an  $R_{\text{work}}/R_{\text{free}}$  of 0.151/0.176 to 1.8 Å resolution (Fig. 5a and Table 2). Calculation of a composite simulated annealing omit map and, separately, complete rebuilding of the structure from a truncated starting model using Autobuild<sup>28</sup> after removal of residues 1–16 and 40–60 of the polypeptide chain indicate that the measured data contain meaningful and sufficient information to rebuild the structure (Fig. 5b and Supplementary Figure 2). No obvious signs of damage are visible at the disulfide bond sites at this dose (Supplementary Figure 3).

**CTX-M-14  $\beta$ -lactamase.** Measurements for CTX-M-14  $\beta$ -lactamase were made in the same manner as for HEWL, except the EuXFEL delivered 300 pulses per second with a mean photon energy of 9.15 keV and a higher mean pulse energy of 1.05 mJ per pulse, giving an absorbed dose of 0.9 MGy using RADDOSE-3D version 2.1<sup>22</sup>. Microcrystals of CTX-M-14  $\beta$ -lactamase were of 3–8  $\mu\text{m}$  size and delivered using similar jet speeds and diameters as for HEWL. A total of 3,215,616 diffraction patterns were collected from CTX-M-14 from which 14,445 (0.4%) were identified as crystal hits by Cheetah<sup>24</sup>, of which 12,474 could be indexed using the CrystFEL software suite<sup>25,26</sup>. Merging reflection intensities using the program partialator in CrystFEL produced a data set with an error metric  $R_{\text{split}}$  of 0.197 and CC\* of 0.984 to 1.7 Å resolution (Table 2). A solvent-free version of 5TWD CTX-M-14<sup>18</sup> was applied to refine the model of CTX-M-14 in complex with avibactam. The SFX data collected to 1.7 Å show a complex with diazabicyclooctane avibactam, covalently bound to OG of Ser70 of the  $\beta$ -lactamase, as also reported similar by King et al.<sup>29</sup> for other  $\beta$ -lactamases. The crystals are in a space group with only one molecule in the asymmetric unit (AU), an active site fully accessible to solvent, and were soaked with avibactam just before the SFX data collection. The electron density as well as the resulted and refined model are of high quality, without any indication of radiation damage and show avibactam complexed covalently to OG of Ser70 of the  $\beta$ -lactamase (Fig. 6a, b). As CTX-M  $\beta$ -lactamases are known to demonstrate a unique capacity to expand their substrate profile, via active site region amino acid changes, thereby conferring resistance which in turn leads to therapy failure, the obtained CTX-M-14 structure is most useful and complements information already obtained from other  $\beta$ -lactamases<sup>29</sup>. The data will support drug discovery investigations to extend the spectrum of inhibition to a wider range of serine  $\beta$ -lactamases. Experimental procedures applied for crystal preparation, soaking and SFX data collection pave the way for time-resolved SFX experiments applying  $\beta$ -lactamase microcrystals at EuXFEL with different  $\beta$ -lactam antibiotics, such as cefotaxime, to unravel the structural mystery and conformational changes involved in sequential acylation and deacylation of the  $\beta$ -lactam ring.

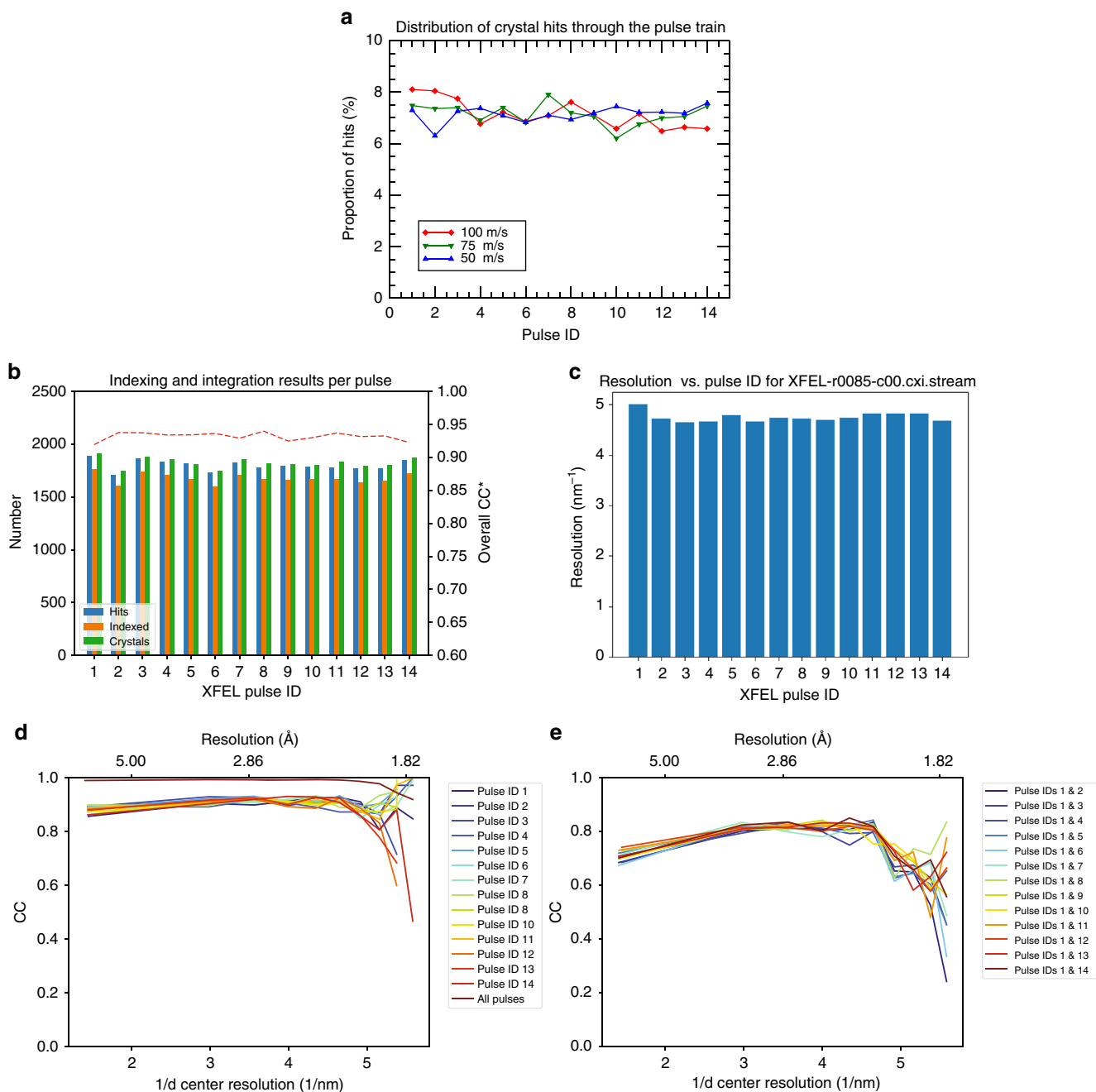


**Fig. 4** HEWL diffraction was measured on all pulses in the pulse train. **a** Hit fraction as a function of pulse number indicates that crystals are hit randomly on any pulse within the MHz EuXFEL pulse train, and not only on the first pulse in the pulse train. **b** Indexable lattices were equally distributed among the MHz XFEL pulse trains and no sign of degradation in data quality is observed through the pulse train as measured by the overall  $CC^*$  for subsets of the data corresponding to each pulse. **c** CrystFEL resolution estimate as a function of X-ray pulse within a train shows no decrease in estimated resolution through the course of the pulse train. **d**  $CC^*$  for data separated from each pulse indicates similar data quality for each pulse in the pulse train. Merging all pulses produces higher data quality (as expected). **e** Correlation of merged data from the first pulse relative to each subsequent pulse in the pulse train indicates that data are similar on each pulse to the limit of data quality available in this experiment. Both **d** and **e** are generated from the same stream files used for structure determination sorted according to pulse ID

## Discussion

The results obtained for HEWL and CTX-M-14 demonstrate that SFX using X-ray pulses with megahertz repetition rates is suitable for high-resolution structure determination using the methods described in this paper under the exposure conditions currently available at the European XFEL. This work was performed with pulse trains of 15 and 30 X-ray pulses delivered in bursts with a 1.1 MHz inter-pulse repetition rate, for a total of 150 and 300 pulses per second—the number of pulses available at the time of

the experiment during instrument commissioning. However, the advance to exploiting sub-microsecond inter-pulse spacing demonstrated here is the key to high speed data acquisition using MHz pulse rates. Subsequent experiments have already been able to take advantage of 500 pulses per second<sup>30</sup>, and at the time of writing SFX experiments at the European XFEL are already performed using 1200 pulses per second at 1.1 MHz pulse rates enabling data to be measured at a rate 10 times higher than previously possible at hard X-ray XFELs. 3520 pulses per second

is planned to be available for EuXFEL users in 2019 enabling even higher data acquisition rates in the near future. The results presented here demonstrate that SFX using X-ray pulses with sub-microsecond inter-pulse spacing is suitable for high-resolution structure determination, and thus the results scale to even more pulses per train up to and beyond the current AGIPD memory cell limit of 352 pulses per train.

We can therefore look forward to measurements using more pulses per unit time as the number of pulses per train delivered by European XFEL continues to increase. For example, when the number of pulses in the European XFEL pulse train is increased to match the maximum AGIPD detector frame rate of 3520

frames per second, the HEWL data set presented here could be collected in as little as 3.5 min while consuming only 50  $\mu$ L of crystal solution. Under such conditions the  $\beta$ -lactamase measurements could be completed in only 15 min despite the low hit fraction of 0.4% obtained. Further reduction to less than 1 min per data set consuming only 15  $\mu$ L of solution should be possible by increasing the hit fraction and reducing dead time through improvements in sample delivery. Moving beyond 352 pulses per train at EuXFEL would require either a new detector able to detect more pulses per pulse train or exploitation of the real-time veto capabilities of AGIPD. Meanwhile, the planned LCLS-II facility promises up to  $10^5$ – $10^6$  equally spaced pulses per second increasing the rate of structure determination even further. In particular, the structural data obtained for the CTX-M14 avibactam complex demonstrates the potential of megahertz SFX for structural discovery at newly available high repetition rate sources, opening up new possibilities for rapid screening for drug targets using on-the-fly substrate mixing, while the potential for rapid data acquisition will facilitate the generation of time-resolved movies of macromolecules in action at physiological temperature.

**Table 2 SFX data and refinement statistics**

Parameter	Lysozyme	CTX-M-14
Photon energy (mean value)	9300 eV	9150 eV
X-ray focus	15 $\mu$ m (FWHM)	15 $\mu$ m (FWHM)
Pulse energy at sample (assuming 50% beamline transmission)	290 $\mu$ J	526 $\mu$ J
Pulse length	50 fs	50 fs
Space group	P 4 <sub>3</sub> 2 <sub>1</sub> 2	P 3 <sub>2</sub> 2 1
Unit cell		
<i>a</i> , <i>b</i> , <i>c</i>	79.6, 79.6, 38.3 Å	41.8, 41.8, 233.3 Å
$\alpha$ , $\beta$ , $\gamma$	90, 90, 90°	90, 90, 120°
No. of hits/indexed lattices	25,193/25,531	14,445/12,474
No. of unique reflections	12,387 (1171)	27,838 (2715)
Resolution range	21.99–1.76 (1.82–1.76) Å	34.6–1.69 (1.75–1.69) Å
Completeness	99.64% (97.25%)	99.89% (99.45%)
$R_{\text{split}}$	0.106 (0.446)	0.197 (0.476)
$I/\sigma(I)$	7.36 (2.62)	4.37 (2.30)
$CC_{1/2}$	0.98 (0.79)	0.93 (0.63)
$CC^*$	0.99 (0.94)	0.98 (0.88)
Wilson <i>B</i> -factor	26.18 Å <sup>2</sup>	26.80 Å <sup>2</sup>
$R_{\text{Work}}$	0.157 (0.211)	0.176 (0.27)
$R_{\text{Free}}$	0.173 (0.218)	0.21 ((0.30)
Rmsd bonds/Rmsd angles	0.010 Å/0.994°	0.008 Å/1.22°
Ramachandran favored	99.21%	98.1%
Ramachandran allowed	0.79%	1.5%
Ramachandran outliers	0.00%	0.4%
Average <i>B</i> -factor	30.0 Å <sup>2</sup>	27.6 Å <sup>2</sup>
Macromolecules	28.9 Å <sup>2</sup>	27.1 Å <sup>2</sup>
Ligands	45.8 Å <sup>2</sup>	22.2 Å <sup>2</sup>
Solvent	40.3 Å <sup>2</sup>	37.0 Å <sup>2</sup>
PDB code	6FTR	6GTH
CXIDB data deposition	CXIDB ID-80	CXIDB ID-83

Statistics for the highest-resolution shell are shown in parentheses

## Methods

**Sample preparation.** Crystals of HEWL were grown by the rapid-mixing batch method<sup>31</sup>. Crystals with sizes of between 6 and 8  $\mu$ m in diameter were obtained by adding three parts of precipitant (1 M NaCl, 40% (v/v) ethylene glycol, 15% (w/v) PEG 4000, 50 mM acetate buffer pH 3.5 filtered through a 450 nm filter) to one part of HEWL (Sigma–Aldrich; dissolved to 126 mg/mL in 50 mM acetate buffer pH 3.5 and filtered through a 100 nm filter) at 1 °C (ThermoStat C, Eppendorf, Germany). The resulting mixture was immediately subjected to rapid mixing and incubated for 30 min at 1 °C<sup>32</sup>. Crystal sizes were estimated through image analysis by optical microscopy. Crystals were resuspended before injection to yield a homogeneous suspension of HEWL microcrystals.

For the CTX-M-14  $\beta$ -lactamase the gene was cloned into a pRSET A plasmid and transformed into competent *Escherichia coli* BL21DE3 cells (BL21(DE3) pLyS, Novagen, Schwalbach, Germany). Chromosomal DNA from clinical *K. pneumoniae* DT1 (GenBank CP019077.1) served as a template. The amplicon was cloned into pCR4 and introduced into *E. coli* TOP10 cells (Invitrogen), giving *E. coli* TOP10 x pCR4::blaCTX-M-14. TOP10 x pCR4::blaCTX-M-14 was used to isolate CTX-M14. The primers used to amplify blaCTX-M14 were Prom-CTX-M14-for GCCAAAAGTTATTCTACTACTACT and CTX-M14-rev TTACAGCCCTTCGGCGATG. BL21DE3 cell were grown in LB medium at 37 °C containing 100  $\mu$ g/mL ampicillin for plasmid selection. Gene expression was induced by supplementation of IPTG (isopropyl  $\beta$ -D-1-thiogalactopyranoside) to a final concentration of 1 mM at an optical density (OD) of 0.7. Cells were harvested 3 h after induction by centrifugation with 4000  $\times$  g at 4 °C. The cell pellet was resuspended in 20 mM MES pH 6 and sonicated for lysis. Cell debris were separated by centrifugation at 17000  $\times$  g for 1 h at 4 °C. Supernatant was supplemented by addition of 1  $\mu$ L DNase and dialyzed overnight against a large volume of 20 mM MES pH 6 at 4 °C. Dialyzed sample was filtered using a 0.2  $\mu$ m syringe filter and applied onto a cation exchange column (HiTrap SP XL) using a Äkta Pure chromatography system. The column was pre-equilibrated with 20 mM MES pH 6 and CTX-M-14 was eluted using a gradient over 20 column volumes with 50 mM NaCl, 20 mM MES pH 6. Elution peak was concentrated using a

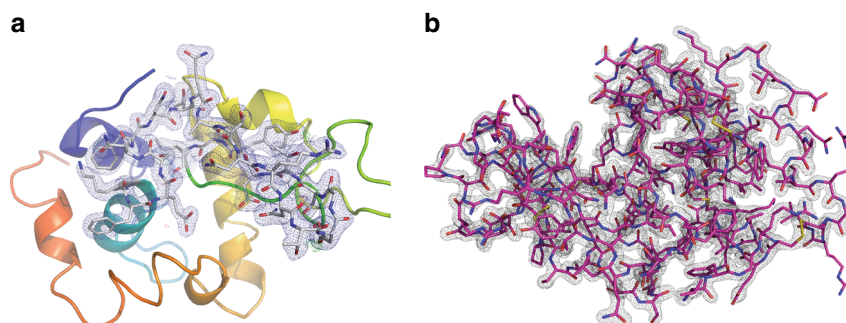


**Fig. 5** Electron density map for HEWL by MHz SFX. **a** 2Fo-Fc map at 1 sigma overlaid on Fo-Fc map at 3 sigma from molecular replacement using a solvent-free version of the 4ET8 lysozyme structure<sup>2</sup> as the starting model. **b** Integrity of the measured data is verified by complete rebuilding of the structure from a truncated starting model after removal of residues 1–16 and 40–60 of the polypeptide chain using Autobuild<sup>28</sup>



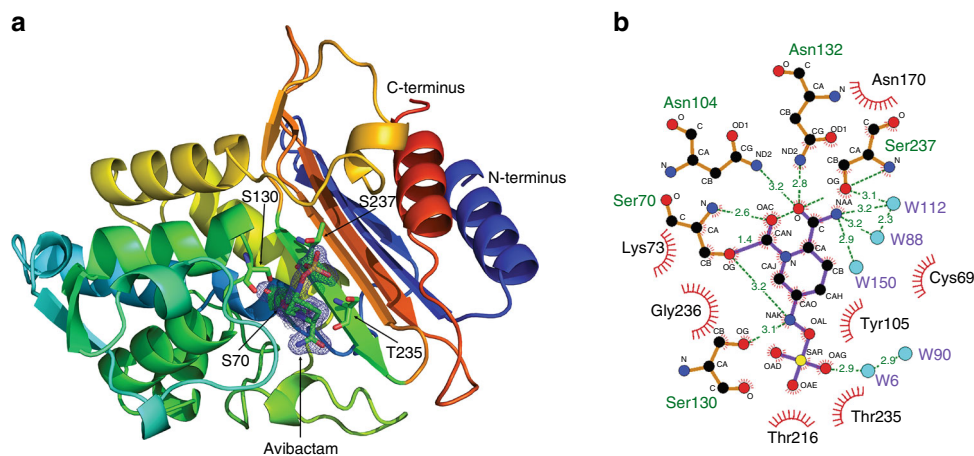


**Fig. 6** Structure of CTX-M-14  $\beta$ -lactamase determined by MHz SFX. **a** 2Fo-Fc map at 1 sigma overlaid on Fo-Fc map at 3 sigma around covalently bound avibactam from molecular replacement using a solvent-free version of the 5TWD  $\beta$ -lactamase structure from ref. <sup>18</sup> as the starting model. **b** Representation of covalently bound avibactam to OG of Ser70, stabilized by hydrogen bonds and hydrophobic interactions with surrounding amino acids of CTX-M-14. Figure was prepared using Ligplot<sup>53</sup>

10 kDa Amicon concentrator to a final CTX-M-14 concentration of 20 mg/mL. CTX-M-14 microcrystals for SFX were produced using a seeding approach. Crystals were grown by sitting drop vapor diffusion at 20 °C overnight mixing 1  $\mu$ L CTX-M-14 at 20 mg/mL and 1  $\mu$ L precipitant (40% PEG8000, 200 mM lithium sulfate, 100 mM sodium acetate). Obtained crystals (space group P2<sub>1</sub>2<sub>1</sub>2<sub>1</sub>) were crushed and a seed stock was prepared. To obtain microcrystals the undiluted seed stock was used for batch crystallization setups by mixing volumes of 50% CTX-M-14 with 10% undiluted seed stock and 40% precipitant solution. Resulting microcrystals were centrifuged at 200  $\times$  g for 5 min and the pellet was crushed using a glass tissue homogenizer. This procedure was repeated 10 times and the supernatant of a final centrifugation step was used for two successive rounds of seed stock preparation, resulting in approximately 1 mL of highly concentrated seed stock that was used for following CTX-M-14 batch crystallization setups. CTX-M-14 microcrystals prepared by this approach grew within 1 h and had a homogeneous size distribution ranging from 3 to 8  $\mu$ m, scored by light microscopy. Prior to sample loading into the reservoir container the crystal suspension was filtered using a 20  $\mu$ m gravity flow filter and mixed at this time with avibactam to obtain a final avibactam concentration of 20 mM.

**Fast jets.** Delivery of suspensions of crystal solution followed the principle of a gas dynamic virtual nozzle<sup>33–35</sup> in which a liquid stream is focused and accelerated by the virtual orifice created by a co-propagating helium gas flow. The sample was delivered to the injector using a syringe approach in which a high-pressure liquid chromatography (HPLC) pump (Shimadzu) delivered water to drive the plunger in a sample reservoir, forcing sample through a syringe into the injector lines. The pump delivers a constant flow even at high pressures and thus allows for stable and steady delivery of the sample suspension. The sample flow rate was additionally monitored by a liquid flow meter (Sensirion) located in the water stream between the HPLC pump and the sample syringe/reservoir. Gas flow was controlled using a GPI gas pressure regulator (Proportion-air) and the flow rate was monitored with a gas flow meter (Bronkhorst). Nozzle tips were produced by three-dimensional (3D) printing<sup>36</sup> following the design shown in Fig. 1. A 50  $\mu$ m internal diameter injector sample line was used for improved stability with the crystal sizes used, placing an upper limit on achievable jet speed in this experiment. Three different conditions were chosen for sample delivery spanning the range of 50–100 m/s jet speed, significantly faster than previous jet velocities that were usually below 30 m/s<sup>37</sup>. Jet speeds were estimated during the experiment based on the flow conditions and known geometry of the 3D-printed nozzle, and subsequently verified by high-speed imaging in the laboratory using the same flow conditions as listed in Table 1. Laboratory measurement with both water and HEWL crystal suspension showed similar jet speeds, as reported in Table 1. The speed of the 25 m/s jet was calculated with less precision from movement of the X-ray-induced gaps at EuXFEL. No crystal diffraction data were collected with the 25 m/s jet. For simplicity in the main text and figures we refer to these conditions as jets with a speed of 100, 75, 50 and 25 m/s, values which retain physical meaning but do not over-estimate the stability of the jet speed over time.

Placement of injector nozzles near the XFEL interaction region was achieved using a “nozzle rod” mount provided by the EuXFEL sample environment group, providing the ability to optimize overlap between the focused X-ray beam and the sample-containing liquid jet. Interaction of the jet with the XFEL was imaged using an in-situ microscope with pulsed laser back illumination (Coherent Minilite-II, pulse duration of 3–5 ns for the frequency doubled 532 nm pulse) synchronized to the XFEL pulses similar to the arrangement in ref. <sup>16</sup>. Jet explosion movies were collected using the higher pulse energy of the  $\beta$ -lactamase measurements.

**SPB/SFX instrument.** Experiments were performed at the SPB/SFX instrument at the European XFEL X-ray free-electron laser in September 2017 (HEWL) and April 2018 (CTX-M-14) as part of EuXFEL experiment p2012 using parameters as described in the main text. The size of the focal spot in the interaction region was estimated to be 16  $\mu$ m  $\pm$  4  $\mu$ m FWHM diameter based on optical imaging of single shots using Ce:YAG screens of various thicknesses (15, 20 and 50  $\mu$ m). An analysis of the scattered signal on the detector suggests it is possible the actual focal spot was somewhat smaller in size. The liquid jets (described above) were positioned in the interaction region by mounting nozzles on a movable “nozzle rod” which held the jets just above the

X-ray focal position and aligned to the X-ray beam using an in-line microscope viewing system. Diffraction from the sample was measured using an AGIPD 1M located 0.12 m downstream of the sample interaction region, with the direct beam passing through a central hole in the detector to a beam stop further downstream.

The AGIPD (Supplementary Figure 4) is a new charge integrating detector built for the European XFEL that is capable of measuring full frames at the EuXFEL pulse repetition rate. The AGIPD is designed to read out in burst mode because the EuXFEL delivers trains of X-ray pulses at MHz repetition rate, repeating at 10 Hz repetition rate. This experiment was performed with 30 pulses per burst at 1.1 MHz repetition rate. The EuXFEL design parameters extend to bursts of up to 2700 pulses at 4.5 MHz repetition rate, and thus each AGIPD pixel contains 352 analog memory cells which can be addressed at MHz repetition rates enabling the AGIPD to measure bursts of up to 352 individual X-ray pulses at MHz repetition rate. Subsequently, all memory cells are read out in the less than 100 ms before arrival of the next burst of X-ray pulses. This enables up to 352 pulses per train to be measured, or when fewer than 352 pulses populate a pulse train allows all pulses to be measured, as is this case here. The maximum frame rate of AGIPD is therefore 3520 frames per second matched to the EuXFEL pulse structure. Each pixel of AGIPD has three gain settings which are automatically selected on a frame-by-frame basis depending on the signal present in each pixel (Supplementary Figure 4). The AGIPD 1M detector used here consists of 16 tiles of 128  $\times$  512 pixels each arranged as shown in Fig. 1 and Supplementary Figures 4 and 5. Calibration of the AGIPD readout requires measurement of the pedestal, gain and gain switching threshold for each of the three gain stages in each memory cell of each pixel. In this experiment the detector readout was initially limited to the first 15 X-ray pulses during instrument commissioning (HEWL), and later 30 pulses (CTX-M-14).

**XFEL data analysis.** Experiment progress was monitored online using OnDA<sup>38</sup> for serial crystallography reading data in real time from the EuXFEL control system Karabo<sup>39</sup> using the Karabo bridge<sup>40</sup>. Of the 749,874 diffraction patterns collected during HEWL data acquisition runs used for final analysis, 25,193 (3.4%) images were found by Cheetah<sup>24</sup> to contain crystal diffraction (peakfinder8, minSNR = 8, minADC = 200, minPix = 2, minPeaks = 20). The same procedure was followed for CTX-M-14, except with the peakfinder8 parameters minSNR = 8, minADC = 250, minPix = 1, minPeaks = 20. Data from each AGIPD module was saved into separate files, and thus Cheetah<sup>24</sup> was updated to match data from each of the 16 separate modules by train and pulse number. This ensured data was processed from the same X-ray pulse even in the presence of missing data frames, for example, if not all modules were present in the saved data for all train and pulse ID combinations. Data were read from uncalibrated (RAW\_) data files in European XFEL format, and thus detector calibration was required. See Supplementary Figure 4 for operation of the AGIPD multiple-gain mode. AGIPD calibration was performed in Cheetah as follows: first the memory cell in use for the given Train ID

and Pulse ID combination was determined, and then the recorded gain switch level was compared against the gain threshold for that memory cell to determine which gain mode the pixel was in for that particular measurement. The pedestal and gain correction for that memory cell and gain stage was then applied, and a per-memory cell and gain stage bad pixel mask was applied. Bad pixels were identified as statistical outliers in dark data sets and flagged to be ignored. The density of bad pixels across the detector areas used for analysis was 2.5% (Supplementary Figure 5). Calibration constants were obtained using software from both EuXFEL and the AGIPD detector consortium<sup>41</sup>. The output from Cheetah was stored in .cxi format for compatibility with downstream processing. Corrected data frames as well as raw data for both data sets have been deposited in the CXIDB.

**SFX data processing.** Indexing was done for both data sets applying CrystFEL v.0.6.3 to peaks found by Cheetah using the indexing packages MOSFLM<sup>42</sup>, DirAx<sup>43</sup> and asdf<sup>26</sup>. Since detector panel locations were not measured to adequate precision before the experiment, lithium titanate powder diffraction rings were used for rough detector panel alignment followed by fine refinement from HEWL and CTX-M-14 diffraction data using geoptimiser<sup>44</sup> and Slip-n-slide<sup>45</sup>. Combined with a 1% uncertainty in photon energy and uncertainty in the detector-to-sample distance, final indexing involved an iterative process with refinement of all unknown values using geoptimiser<sup>44</sup>. Indexing of multiple lattices per image sometimes resulted in a higher number of indexed lattices than number of input images. Merging and scaling of the Bragg peaks intensities were performed using partialator program from CrystFEL. To avoid the integration of noise for weakly scattering patterns, reflections were included up to  $0.2 \text{ nm}^{-1}$  above a conservative resolution estimate for each crystal ( $-\text{push-res} = 0.2$ ) for both HEWL and CTX-M-14. Since the space group of the CTX-M-14 crystals ( $P 3_2 2 1$ ) is merohedral and will exhibit indexing ambiguities, we processed the stream-file using ambigator in CrystFEL<sup>46</sup> to resolve the indexing ambiguity before scaling and merging. MTZ-files for crystallographic data processing were generated from CrystFEL merged reflection data files using f2mtz of CCP4<sup>47</sup>. Figures of merit were calculated using compare\_hkl (Rsplit,  $CC_{1/2}$ ,  $CC^*$ ) and check\_hkl (SNR, multiplicity, completeness), both a part of CrystFEL. The distribution of peak intensities and Wilson plot for the HEWL data set also reflect good data quality and dynamic range (Supplementary Figures 6 and 7).

**Structure determination.** A solvent-free version of the 4ET8 lysozyme structure<sup>2</sup> and the solvent-free structure of the 5TWD  $\beta$ -lactamase structure<sup>18</sup> were used each as a starting model for molecular replacement in Phaser<sup>48</sup>. Due to non-isomorphism of the collected data set with the data set in 4ET8 and 5TWD  $R_{\text{free}}$ -flags were generated randomly using phenix.refine<sup>49</sup> and the same set of  $R_{\text{free}}$ -flags were then used throughout the refinement process. Initial refinement was carried out for both structures using phenix.refine, with all isotropic atomic displacement parameters set to 20 and using simulated annealing. This was followed by iterative cycles of restrained maximum-likelihood refinement using phenix.refine and manual model re-building using COOT<sup>50</sup>. Polygon<sup>51</sup> and MolProbity<sup>52</sup> were used for the validation of the final model.

To assess the quality of data we followed two separate approaches. In the first approach, firstly we calculated a composite simulated annealing omit map for the HEWL structure, using phenix.composite\_omit\_map<sup>27</sup> (Supplementary Figure 2), and secondly we generated a polyAla-model of the final refined model, truncated residues 1–16 and 40–60 and used AutoBuild<sup>28</sup> to see whether the final model could be rebuilt correctly and completely starting from just the X-ray-data and the truncated model (Supplementary Figure 2). Figures were generated using PyMOL. For CTX-M-14 the quality of the data and electron density was proven by the clear difference electron density of avibactam complexed in the active site, allowing an unambiguous interpretation of the inhibitor and identification of the covalent bond to OG of Ser70 of the  $\beta$ -lactamase.

**Code availability.** The versions of Cheetah and CrystFEL used in this work are available from the respective websites: <https://www.desy.de/~barty/cheetah> and <https://www.desy.de/~twhite/crystfel>.

### Data availability

Source data have been deposited with the Coherent X-ray Imaging Databank (CXIDB) with reference number CXIDB-ID-80 (HEWL) and CXIDB-ID-83 (CTX-M-14). Data deposition with CXIDB includes: Raw EuXFEL data files (/raw); Cheetah folder (results and calibrations); Stream files generated by CrystFEL; Detector geometry files; Data calibrated by the European XFEL (/proc). The DOI for the original data at EuXFEL is: <https://doi.org/10.22003/XFEL.EU-DATA-002012-00>. Structures have been deposited with the Protein Data Bank (PDB) with the accession codes 6FTR (HEWL) and 6GTH (CTX-M-14). Other data are available from the corresponding authors upon reasonable request.

Received: 5 August 2018 Accepted: 21 August 2018

Published online: 02 October 2018

### References

- Chapman, H. N. et al. Femtosecond X-ray protein nanocrystallography. *Nature* **470**, 73–77 (2011).
- Boutet, S. et al. High-resolution protein structure determination by serial femtosecond crystallography. *Science* **337**, 362–364 (2012).
- Kang, Y. et al. Crystal structure of rhodopsin bound to arrestin by femtosecond X-ray laser. *Nature* **523**, 561–567 (2015).
- Pande, K. et al. Femtosecond structural dynamics drives the trans/cis isomerization in photoactive yellow protein. *Science* **352**, 725–729 (2016).
- Stagno, J. R. et al. Structures of riboswitch RNA reaction states by mix-and-inject XFEL serial crystallography. *Nature* **541**, 242–246 (2017).
- Gati, C. et al. Atomic structure of granulysin determined from native nanocrystalline granulovirus using an X-ray free-electron laser. *Proc. Natl. Acad. Sci. USA* **114**, 2247–2252 (2017).
- Suga, M. et al. Native structure of photosystem II at  $1.95 \text{ \AA}$  resolution viewed by femtosecond X-ray pulses. *Nature* **517**, 99–103 (2015).
- Altarelli, M. & Mancuso, A. P. Structural biology at the European X-ray free-electron laser facility. *Philos. Trans. R. Soc. B Biol. Sci.* **369**, 20130311–20130311 (2014).
- Neutze, R., Wouts, R., van der Spoel, D., Weckert, E. & Hajdu, J. Potential for biomolecular imaging with femtosecond X-ray pulses. *Nature* **406**, 752–757 (2000).
- Chapman, H. N. et al. Femtosecond diffractive imaging with a soft-X-ray free-electron laser. *Nat. Phys.* **2**, 839–843 (2006).
- Holton, J. M. A beginner's guide to radiation damage. *J. Synchrotron Rad.* **16**, 133–142 (2009).
- Holton, J. M. & Frankel, K. A. The minimum crystal size needed for a complete diffraction data set. *Acta Crystallogr. D Biol. Crystallogr.* **66**, 393–408 (2010).
- Ishikawa, T. et al. A compact X-ray free-electron laser emitting in the sub-ångström region. *Nat. Photonics* **6**, 540–544 (2012).
- Yabashi, M., Tanaka, H. & Ishikawa, T. Overview of the SACLA facility. *J. Synchrotron Rad.* **22**, 477–484 (2015).
- White, W. E., Robert, A. & Dunne, M. The Linac coherent light source. *J. Synchrotron Rad.* **22**, 472–476 (2015).
- Stan, C. A. et al. Liquid explosions induced by X-ray laser pulses. *Nat. Phys.* **12**, 966–971 (2016).
- Both, A. et al. Emergence of ceftazidime/avibactam non-susceptibility in an MDR *Klebsiella pneumoniae* isolate. *J. Antimicrob. Chemother.* **72**, 2483–2488 (2017).
- Patel, M. P. et al. The drug-resistant variant P167S expands the substrate profile of CTX-M  $\beta$ -lactamases for oxymino-cephalosporin antibiotics by enlarging the active site upon acylation. *Biochem.-Us* **56**, 3443–3453 (2017).
- Chen, Y., Delmas, J., Sirot, J., Shoichet, B. & Bonnet, R. Atomic resolution structures of CTX-M beta-lactamases: Extended spectrum activities from increased mobility and decreased stability. *J. Mol. Biol.* **348**, 349–362 (2005).
- Olmos, J. L. et al. Enzyme intermediates captured 'on the fly' by mix-and-inject serial crystallography. *BMC Biol.* **16**, 1–15 (2018).
- Altarelli, M. et al. XFEL: The European X-Ray Free-Electron Laser. *Technical Design Report* (DESY, Hamburg, 2006).
- Zeldin, O. B., Gerstel, M., & Garman, E. F. RADDOS-3D: time- and space-resolved modelling of dose in macromolecular crystallography. *J. Appl. Crystallogr.* **46**, 1225–1230 (2013).
- Wiedorn, M. O. et al. Rapid sample delivery for megahertz serial crystallography at X-ray FELs. *IUCrJ* **5**, 1–11 (2018).
- Barty, A. et al. Cheetah: software for high-throughput reduction and analysis of serial femtosecond X-ray diffraction data. *J. Appl. Crystallogr.* **47**, 1118–1131 (2014).
- White, T. A. et al. CrystFEL: a software suite for snapshot serial crystallography. *J. Appl. Crystallogr.* **45**, 335–341 (2012).
- White, T. A. et al. Recent developments in CrystFEL. *J. Appl. Crystallogr.* **49**, 680–689 (2016).
- Adams, P. D. et al. PHENIX: a comprehensive Python-based system for macromolecular structure solution. *Acta Crystallogr. D Biol. Crystallogr.* **66**, 213–221 (2010).
- Terwilliger, T. C. et al. Iterative model building, structure refinement and density modification with the PHENIX AutoBuild wizard. *Acta Crystallogr. D Biol. Crystallogr.* **64**, 61–69 (2008).
- King, D. T., King, A. M., Lal, S. M., Wright, G. D. & Strynadka, N. C. J. Molecular mechanism of avibactam-mediated  $\beta$ -lactamase inhibition. *ACS Infect. Dis.* **1**, 175–184 (2015).
- Grünbein, M. L. et al. Megahertz data collection from protein microcrystals at an X-ray free-electron laser. *Nat. Commun.* **9**, 3487 (2018).
- Stellato, F. et al. Room-temperature macromolecular serial crystallography using synchrotron radiation. *IUCrJ* **1**, 204–212 (2014).
- Beyerlein, K. R. et al. Mix-and-diffuse serial synchrotron crystallography. *IUCrJ* **4**, 769–777 (2017).

33. DePonte, D. P. et al. Gas dynamic virtual nozzle for generation of microscopic droplet streams. *J. Phys. D Appl. Phys.* **41**, 195505 (2008).
34. Oberthuer, D. et al. Double-flow focused liquid injector for efficient serial femtosecond crystallography. *Sci. Rep.* **7**, 1–10 (2017).
35. Gañán-Calvo, A. M. Generation of steady liquid microthreads and micron-sized monodisperse sprays in gas streams. *Phys. Rev. Lett.* **80**, 285–288 (1998).
36. Nelson, G. et al. Three-dimensional-printed gas dynamic virtual nozzles for x-ray laser sample delivery. *Opt. Express* **24**, 11515–11516 (2016).
37. Beyerlein, K. R. et al. Ceramic micro-injection molded nozzles for serial femtosecond crystallography sample delivery. *Rev. Sci. Instrum.* **86**, 125104 (2015).
38. Mariani, V. et al. OnDA: online data analysis and feedback for serial X-ray imaging. *J. Appl. Crystallogr.* **49**, 1073–1080 (2016).
39. Heisen, B. et al. Karabo: An integrated software framework combining control, data management, and scientific computing tasks. In *Proc. International Conference on Accelerator & Large Experimental Physics Control Systems*, FRCOAAB02, 1465–1468 (San Francisco, 2013).
40. Fangohr, H. et al. Data analysis support in Karabo at European XFEL. In *Proc. 16th Int. Conf. on Accelerator and Large Experimental Control Systems*, TUCPA01, 245–252 (Barcelona, Spain, 2017).
41. Kuster, M. et al. Detectors and calibration concept for the European XFEL. *Synchrotron Radiation News* **27**, 35–38 (2014).
42. Powell, H. R. The Rossmann Fourier autoindexing algorithm in MOSFLM. *Acta Crystallogr. D Biol. Crystallogr.* **55**, 1690–1695 (1999).
43. White, T. A. et al. Crystallographic data processing for free-electron laser sources. *Acta Crystallogr. D Biol. Crystallogr.* **69**, 1231–1240 (2013).
44. Yefanov, O. et al. Accurate determination of segmented X-ray detector geometry. *Opt. Express* **23**, 28459–12 (2015).
45. Ginn, H. M. & Stuart, D. I. The slip-and-slide algorithm: a refinement protocol for detector geometry. *J. Synchrotron Rad.* **24**, 1–11 (2017).
46. Brehm, W. & Diederichs, K. Breaking the indexing ambiguity in serial crystallography. *Acta Crystallogr. D Biol. Crystallogr.* **70**, 101–109 (2014).
47. Winn, M. D. et al. Overview of the CCP4 suite and current developments. *Acta Crystallogr. D Biol. Crystallogr.* **67**, 235–242 (2011).
48. McCoy, A. J. et al. Phaser crystallographic software. *J. Appl. Crystallogr.* **40**, 658–674 (2007).
49. Afonine, P. V. et al. Towards automated crystallographic structure refinement with phenix.refine. *Acta Crystallogr. D Biol. Crystallogr.* **68**, 352–367 (2012).
50. Emsley, P., Lohkamp, B., Scott, W. G. & Cowtan, K. Features and development of Coot. *Acta Crystallogr. D Biol. Crystallogr.* **66**, 486–501 (2010).
51. Urzhumtseva, L., Afonine, P. V., Adams, P. D. & Urzhumtsev, A. Crystallographic model quality at a glance. *Acta Crystallogr. D Biol. Crystallogr.* **65**, 297–300 (2009).
52. Chen, V. B. et al. MolProbity: all-atom structure validation for macromolecular crystallography. *Acta Crystallogr. D Biol. Crystallogr.* **66**, 12–21 (2010).
53. Wallace, A. C., Laskowski, R. A. & Thornton, J. M. LIGPLOT: a program to generate schematic diagrams of protein-ligand interactions. *Protein Eng. Des. Sel.* **8**, 127–134 (1995).

## Acknowledgements

We acknowledge European XFEL in Schenefeld, Germany, for provision of X-ray free-electron laser beamtime at Scientific Instrument SPB/SFX and would like to thank the instrument group and facility staff for their assistance. We also acknowledge useful discussions with John Spence, ASU; Arwen Pearson, UHH; and Ilme Schlichting, MPI-MF. We acknowledge the support of funding from: The excellence cluster "The Hamburg Center for Ultrafast Imaging-Structure, Dynamics and Control of Matter at the Atomic Scale" of the Deutsche Forschungsgemeinschaft (CUI, DFG-EXC1074); the European Research Council, "Frontiers in Attosecond X-ray Science: Imaging and Spectroscopy (AXSIS)", ERC-2013-SyG 609920 (2014–2018); the Gottfried Wilhelm Leibniz Program of the DFG; the project "X-probe" funded by the European Union's 2020 Research and Innovation Program under the Marie Skłodowska-Curie grant agreement 637295; the BMBF German-Russian Cooperation "SyncFELMed" grant 05K14CHA; European Research Council under the European Union's Seventh Framework Programme (FP7/2007–2013) through the Consolidator Grant COMOTION (ERC-614507-Küpper); the Helmholtz Gemeinschaft through the "Impuls und Vernetzungsfond"; Helmholtz Initiative and Networking Fund through the Young Investigators Program and by the Deutsche Forschungsgemeinschaft SFB755/B03; the DLR (Deutsche Zentrum für Luft und Raumfahrt) via project 50WB142, the Swedish Research Council; the Knut and Alice Wallenberg Foundation; the Röntgen-Angström Cluster; the BMBF via projects 05K13GU7 and 05E13GU1; from Ministry of Education, Science, Research and Sport of the Slovak Republic; the Joachim Herz Stiftung; the Deutsche Forschungsgemeinschaft (DFG) Cluster of Excellence "Inflammation at interfaces" (EXC 306); the Swedish Research Council; the Swedish Foundation for Strategic Research; the Australian Research Council Center of Excellence in Advanced Molecular Imaging (CE140100011); the Australian Nuclear Science and Technology Organisation (ANSTO); the International Synchrotron Access Program (ISAP) managed by the Australian Synchrotron, part of ANSTO, and funded by the Australian Government; The projects Structural dynamics of biomolecular systems (CZ.02.1.01/0.0/0.0/15\_003/0000447) (ELIBIO) and Advanced research using

high-intensity laser produced photons and particles (CZ.02.1.01/0.0/0.0/16\_019/0000789) (ADONIS) from European Regional Development Fund, the Ministry of Education, Youth and Sports as part of targeted support from the National Programme of Sustainability II; the Röntgen-Ångström-Cluster; the Chalmers Area of Advance, Material science; the Project DPI2016-78887-C3-1-R, Ministerio de Economía y Competitividad; the Wellcome Trust (studentship 075491/04); Rutgers University, Newark; the Max Planck Society; the NSF-STC "BioXFEL" through award STC-1231306; the Slovak Research and Development Agency under contract APVV-14-0181; the Wellcome Trust; Helmholtz Strategic Investment funds; Australian Research Council Centre of Excellence in Advanced Molecular Imaging (CE140100011), Australian Nuclear Science and Technology Organisation (ANSTO); The Swedish Research Council, the Knut and Alice Wallenberg Foundation, and the Röntgen-Angström Cluster, Ministry of Education, Science, Research and Sport of the Slovak Republic; BMBF grants 05K16GUA and 05K12GU3; the Joachim Herz Foundation through and Add-on Fellowship; NHMRC project grants 1107804 and 1108859, ARC Discovery Early Career Research Award (DE170100783); National Health and Medical Research Council (NHMRC) project grants 1107804, 1071659, 1071659 and Principal Research Fellowship (1110971). ARC Discovery Early Career Research Award (DE170100783); National Science Foundation Grant # 1565180, "ABI Innovation: New Algorithms for Biological X-ray Free Electron Laser Data"; Diamond Light Source and from a Strategic Award from the Wellcome Trust and the Biotechnology and Biological Sciences Research Council (grant 102593); use of the XBI biological sample preparation laboratory, enabled by the XBI User Consortium. This work was performed, in part, under the auspices of the U.S. Department of Energy by Lawrence Livermore National Laboratory under Contract DE-AC52-07NA27344. M.L.S., M.A.C. and M.F. were supported by the NIH grant 1R01GM117342-01.

## Author contributions

The experiment was conceived by H.C., A.B. and A.P.M. as an open experiment for the EuXFEL user community. A.B. coordinated and led the collaboration. M.O.W. and Saš.B. led the sample injection team. D.O. and C.S. led the sample team. A.B. and St.A. led the data processing team. C.B. and M.P. led the CTX-M-14 studies. R.B. was the instrument scientist responsible for this experiment. A.P.M. led development of the SPB/SFX instrument, and H.G. led development of the AGIPD detector. J.K., M.H. developed and optimized 3D printed nozzle. D.O., C.S., B.A., Sad.B., I.B., M.A.C., C.D., M.F., P.F., S.H., M.H., B.K., C.K., Ann.M., K.M., M.M., K.A.N., G.P., L.R., J.M.L.-R., W.M.R., I.S., M.L.S., M.M.S., R.S., N.W., T.V. and P.L.X. contributed to sample preparation. M.O.W., Saš.B., Ju.K., Sa.A., L.A., Y.D., H.F., L.G., M.D., T.S., S.I., Jo.K., D.H., M.T., D.C.F.M., J.N., M.H., F.C.-M., A.M.G.-C., C.A.S., J.A., A.M.O., R.B.D. and R.L.S. contributed to sample delivery. A.B., H.C., St.A., V.M., H.M.G., M.O.W., O.Y., T.A.W., And.M., K.A., W.B., Y.G., A.T., P.V.-P., F.R.N.C.M., J.A.S., N.Z., J.H., M.S. and S.P. contributed to data processing and analysis. A.P.M., R.B., J.B., K.D., K.G., R.G., Y.K., R.L., M.M., G.M., A.R., T.S., M.S., P.V., B.W., and J.S. developed and operated the SPB/SFX instrument at EuXFEL. K.W., D.B., L.M., G.P., J.S., N.A.-Q., S.B., H.F., T.M., C.D., A.S. and C.X. developed EuXFEL DAQ and controls. H.G., A.A., D.G., A.K., M.K., T.L., D.M., J.P., U.T., I.C., P.G., B.S., X.S. and J.Z. developed the AGIPD detector. J.S.-D., S.H., A.K. and A.M. were responsible for the detector at EuXFEL. C.B., R.S., N.W., M.P., T.N., S.B., K.L.C., M.A., and H.R. contributed to the CTX-M-14 sample and analysis. The manuscript was written by A.B., M.O.W., D.O. and C.B. with input from all authors.

## Additional information

**Supplementary Information** accompanies this paper at <https://doi.org/10.1038/s41467-018-06156-7>.

**Competing interests:** The authors declare no competing interests.

**Reprints and permission** information is available online at <http://npg.nature.com/reprintsandpermissions/>

**Publisher's note:** Springer Nature remains neutral with regard to jurisdictional claims in published maps and institutional affiliations.



**Open Access** This article is licensed under a Creative Commons Attribution 4.0 International License, which permits use, sharing, adaptation, distribution and reproduction in any medium or format, as long as you give appropriate credit to the original author(s) and the source, provide a link to the Creative Commons license, and indicate if changes were made. The images or other third party material in this article are included in the article's Creative Commons license, unless indicated otherwise in a credit line to the material. If material is not included in the article's Creative Commons license and your intended use is not permitted by statutory regulation or exceeds the permitted use, you will need to obtain permission directly from the copyright holder. To view a copy of this license, visit <http://creativecommons.org/licenses/by/4.0/>.

© The Author(s) 2018

Max O. Wiedorn<sup>1,2,3</sup>, Dominik Oberthür<sup>1</sup>, Richard Bean<sup>4</sup>, Robin Schubert<sup>3,5,6</sup>, Nadine Werner<sup>5</sup>, Brian Abbey<sup>7</sup>, Martin Aepfelbacher<sup>8</sup>, Luigi Adriano<sup>9</sup>, Aschkan Allahgholi<sup>9</sup>, Nasser Al-Qudami<sup>4</sup>, Jakob Andreasson<sup>10,11,12</sup>, Steve Aplin<sup>1</sup>, Salah Awel<sup>1,3</sup>, Kartik Ayyer<sup>1</sup>, Saša Bajt<sup>9</sup>, Imrich Barák<sup>13</sup>, Sadia Bari<sup>9</sup>, Johan Bielecki<sup>4</sup>, Sabine Botha<sup>3,5</sup>, Djelloul Boukhelef<sup>4</sup>, Wolfgang Brehm<sup>1</sup>, Sandor Brockhauser<sup>4,14</sup>, Igor Cheviakov<sup>8</sup>, Matthew A. Coleman<sup>15</sup>, Francisco Cruz-Mazo<sup>16</sup>, Cyril Danilevski<sup>4</sup>, Connie Darmanin<sup>7</sup>, R. Bruce Doak<sup>17</sup>, Martin Domaracky<sup>1</sup>, Katerina Dörner<sup>4</sup>, Yang Du<sup>1</sup>, Hans Fangohr<sup>4,18</sup>, Holger Fleckenstein<sup>1</sup>, Matthias Frank<sup>15</sup>, Petra Fromme<sup>19</sup>, Alfonso M. Gañán-Calvo<sup>16</sup>, Yaroslav Gevorkov<sup>1,20</sup>, Klaus Giewekemeyer<sup>4</sup>, Helen Mary Ginn<sup>21,22</sup>, Heinz Graafsma<sup>9,23</sup>, Rita Graceffa<sup>4</sup>, Dominic Greiffenberg<sup>24</sup>, Lars Gumprecht<sup>1</sup>, Peter Göttlischer<sup>9</sup>, Janos Hajdu<sup>10,11</sup>, Steffen Hauf<sup>4</sup>, Michael Heymann<sup>25</sup>, Susannah Holmes<sup>7</sup>, Daniel A. Horke<sup>1,3</sup>, Mark S. Hunter<sup>26</sup>, Siegfried Imlau<sup>1</sup>, Alexander Kaukher<sup>4</sup>, Yoonhee Kim<sup>4</sup>, Alexander Klyuev<sup>9</sup>, Juraj Knoška<sup>1,2</sup>, Bostjan Kobe<sup>27</sup>, Manuela Kuhn<sup>9</sup>, Christopher Kupitz<sup>28</sup>, Jochen Küpper<sup>1,2,3,29</sup>, Janine Mia Lahey-Rudolph<sup>1,30</sup>, Torsten Laurus<sup>9</sup>, Karoline Le Cong<sup>5</sup>, Romain Letrun<sup>4</sup>, P. Lourdu Xavier<sup>1,31</sup>, Luis Maia<sup>4</sup>, Filipe R.N.C. Maia<sup>10,32</sup>, Valerio Mariani<sup>1</sup>, Marc Messerschmidt<sup>4</sup>, Markus Metz<sup>1</sup>, Davide Mezza<sup>24</sup>, Thomas Michelat<sup>4</sup>, Grant Mills<sup>4</sup>, Diana C.F. Monteiro<sup>3</sup>, Andrew Morgan<sup>1</sup>, Kerstin Mühligh<sup>10</sup>, Anna Munke<sup>10</sup>, Astrid Münnich<sup>4</sup>, Julia Nette<sup>3</sup>, Keith A. Nugent<sup>7</sup>, Theresa Nuguid<sup>5</sup>, Allen M. Orville<sup>22</sup>, Suraj Pandey<sup>28</sup>, Gisel Pena<sup>1</sup>, Pablo Villanueva-Perez<sup>1</sup>, Jennifer Poehlsen<sup>9</sup>, Gianpietro Previtali<sup>4</sup>, Lars Redecke<sup>8,30</sup>, Winnie Maria Riekehr<sup>30</sup>, Holger Rohde<sup>8</sup>, Adam Round<sup>4</sup>, Tatiana Safenreiter<sup>1</sup>, Iosifina Sarrou<sup>1</sup>, Tokushi Sato<sup>1,4</sup>, Marius Schmidt<sup>28</sup>, Bernd Schmitt<sup>24</sup>, Robert Schönherr<sup>30</sup>, Joachim Schulz<sup>4</sup>, Jonas A. Sellberg<sup>33</sup>, M. Marvin Seibert<sup>10</sup>, Carolin Seuring<sup>1,3</sup>, Megan L. Shelby<sup>15</sup>, Robert L. Shoeman<sup>17</sup>, Marcin Sikorski<sup>4</sup>, Alessandro Silenzi<sup>4</sup>, Claudiu A. Stan<sup>34</sup>, Xintian Shi<sup>24</sup>, Stephan Stern<sup>1,4</sup>, Jola Sztuk-Dambietz<sup>4</sup>, Janusz Szuba<sup>4</sup>, Aleksandra Tolstikova<sup>1</sup>, Martin Trebbin<sup>3,35,36</sup>, Ulrich Trunk<sup>9</sup>, Patrik Vagovic<sup>1,4</sup>, Thomas Ve<sup>37</sup>, Britta Weinhausen<sup>4</sup>, Thomas A. White<sup>1</sup>, Krzysztof Wrona<sup>4</sup>, Chen Xu<sup>4</sup>, Oleksandr Yefanov<sup>1</sup>, Nadia Zatsepin<sup>38</sup>, Jianguo Zhang<sup>24</sup>, Markus Perbandt<sup>3,5,8</sup>, Adrian P. Mancuso<sup>4</sup>, Christian Betzel<sup>3,5,6</sup>, Henry Chapman<sup>1,2,3</sup> & Anton Barty<sup>1</sup>

<sup>1</sup>Center for Free-Electron Laser Science, Deutsches Elektronen-Synchrotron DESY, Notkestrasse 85, 22607 Hamburg, Germany. <sup>2</sup>Department of Physics, Universität Hamburg, Luruper Chaussee 149, 22761 Hamburg, Germany. <sup>3</sup>The Hamburg Center for Ultrafast Imaging, Universität Hamburg, Luruper Chaussee 149, 22761 Hamburg, Germany. <sup>4</sup>European XFEL GmbH, Holzkoppel 4, 22869 Schenefeld, Germany. <sup>5</sup>Institute for Biochemistry and Molecular Biology, Laboratory for Structural Biology of Infection and Inflammation, Universität Hamburg, Notkestrasse 85, 22607 Hamburg, Germany. <sup>6</sup>Integrated Biology Infrastructure Life-Science Facility at the European XFEL (XBI), Holzkoppel 4, 22869 Schenefeld, Germany. <sup>7</sup>Australian Research Council (ARC) Centre of Excellence in Advanced Molecular Imaging, Department of Chemistry and Physics, La Trobe Institute for Molecular Sciences, La Trobe University, Bundoora, VIC 3086, Australia. <sup>8</sup>Institute of Medical Microbiology, Virology and Hygiene, University Medical Center Hamburg-Eppendorf (UKE), 20246 Hamburg, Germany. <sup>9</sup>Deutsches Elektronen-Synchrotron DESY, Notkestrasse 85, 22607 Hamburg, Germany. <sup>10</sup>Laboratory of Molecular Biophysics, Department of Cell and Molecular Biology, Uppsala University, Uppsala 751 24, Sweden. <sup>11</sup>ELI Beamlines, Institute of Physics of the Czech Academy of Sciences, Na Slovance 2, 182 21 Prague, Czech Republic. <sup>12</sup>Condensed Matter Physics, Department of Physics, Chalmers University of Technology, Gothenburg 412 96, Sweden. <sup>13</sup>Institute of Molecular Biology, SAS, Dubravská cesta 21, 845 51 Bratislava, Slovakia. <sup>14</sup>Biological Research Centre (BRC), Hungarian Academy of Sciences, Temesvári krt. 62, Szeged 6726, Hungary. <sup>15</sup>Lawrence Livermore National Laboratory, 7000 East Avenue, Livermore, CA 94550, USA. <sup>16</sup>Depart. Ingeniería Aeroespacial y Mecánica de Fluidos ETSI, Universidad de Sevilla, 41092 Sevilla, Spain. <sup>17</sup>Max Planck Institute for Medical Research, Jahnstr. 29, 69120 Heidelberg, Germany. <sup>18</sup>Engineering and the Environment, University of Southampton, SO17 1BJ Southampton, UK. <sup>19</sup>School of Molecular Sciences and Biodesign Center for Applied Structural Discovery, Arizona State University, Tempe, AZ 85287-1604, USA. <sup>20</sup>Hamburg University of Technology, Vision Systems E-2, Harburger Schloßstr. 20, 21079 Hamburg, Germany. <sup>21</sup>Division of Structural Biology, Headington, Oxford OX3 7BN, UK. <sup>22</sup>Diamond Light Source, Research Complex at Harwell, and University of Oxford, Diamond House, Harwell Science and Innovation Campus, Didcot, Oxfordshire OX11 0DE, UK. <sup>23</sup>Mid Sweden University, Holmgatan 10, 85170 Sundsvall, Sweden. <sup>24</sup>Paul Scherrer Institut, Forschungsstrasse 111, 5232 Villigen, Switzerland. <sup>25</sup>Department of Cellular and Molecular Biophysics, Max Planck Institute of Biochemistry, 82152 Martinsried, Germany. <sup>26</sup>Linac Coherent Light Source, SLAC National Accelerator Laboratory, Menlo Park 94025 CA, USA. <sup>27</sup>School of Chemistry and Molecular Biosciences, Institute for Molecular Bioscience and Australian Infectious Diseases Research Centre, University of Queensland, Brisbane, QLD 4072, Australia. <sup>28</sup>Physics Department, University of Wisconsin-Milwaukee, 3135 N. Maryland Ave, Milwaukee, WI 53211, USA. <sup>29</sup>Department of Chemistry, Universität Hamburg, Martin-Luther-King Platz 6, 20146 Hamburg, Germany. <sup>30</sup>Institute of Biochemistry, Center for Structural and Cell Biology in Medicine,

University of Lübeck, Ratzeburger Allee 160, 23562 Lübeck, Germany. <sup>31</sup>Max-Planck Institute for the Structure and Dynamics of Matter, Luruper Chaussee 149, 22761 Hamburg, Germany. <sup>32</sup>NERSC, Lawrence Berkeley National Laboratory, Berkeley 94720 CA, USA. <sup>33</sup>Biomedical and X-Ray Physics, Department of Applied Physics, AlbaNova University Center, KTH Royal Institute of Technology, Stockholm 106 91, Sweden. <sup>34</sup>Physics Department, Rutgers University Newark, Newark, NJ 07102, USA. <sup>35</sup>Department of Chemistry, University at Buffalo, 359 Natural Sciences Complex, Buffalo, NY 14260, USA. <sup>36</sup>Institute of Nanostructure and Solid State Physics, Department of Physics, Universität Hamburg, Luruper Chaussee 149, 22761 Hamburg, Germany. <sup>37</sup>Institute for Glycomics, Griffith University, Southport, QLD 4222, Australia. <sup>38</sup>Department of Physics, Arizona State University, Tempe, AZ 85287, USA





Received 21 June 2021

Accepted 6 August 2021

Edited by K. Moffat, University of Chicago, USA

# Observation of substrate diffusion and ligand binding in enzyme crystals using high-repetition-rate mix-and-inject serial crystallography

Suraj Pandey,<sup>a</sup> George Calvey,<sup>b</sup> Andrea M. Katz,<sup>b</sup> Tek Narsingh Malla,<sup>a</sup> Faisal H. M. Koua,<sup>c</sup> Jose M. Martin-Garcia,<sup>d,e</sup> Ishwor Poudyal,<sup>a</sup> Jay-How Yang,<sup>d</sup> Mohammad Vakili,<sup>f</sup> Oleksandr Yefanov,<sup>c</sup> Kara A. Zielinski,<sup>b</sup> Sasa Bajt,<sup>g,h</sup> Salah Awel,<sup>c</sup> Katarina Doerner,<sup>f</sup> Matthias Frank,<sup>i</sup> Luca Gelisio,<sup>c</sup> Rebecca Jernigan,<sup>d</sup> Henry Kirkwood,<sup>f</sup> Marco Kloos,<sup>f</sup> Jayanath Koliyadu,<sup>f</sup> Valerio Mariani,<sup>c,j</sup> Mitchell D. Miller,<sup>k</sup> Grant Mills,<sup>f</sup> Garrett Nelson,<sup>l</sup> Jose L. Olmos Jr,<sup>k,m</sup> Alireza Sadri,<sup>c</sup> Tokushi Sato,<sup>f</sup> Alexandra Tolstikova,<sup>c</sup> Weijun Xu,<sup>k</sup> Abbas Ourmazd,<sup>a</sup> John C. H. Spence,<sup>l</sup> Peter Schwander,<sup>a</sup> Anton Barty,<sup>g</sup> Henry N. Chapman,<sup>c,h,m</sup> Petra Fromme,<sup>d</sup> Adrian P. Mancuso,<sup>f,o</sup> George N. Phillips Jr,<sup>k,p</sup> Richard Bean,<sup>f</sup> Lois Pollack<sup>b</sup> and Marius Schmidt<sup>a\*</sup>

In memoriam of John Spence.

**Keywords:** substrate diffusion in crystals; antibiotic resistance;  $\beta$ -lactamases; enzyme kinetics; irreversible inhibition; mix-and-inject serial crystallography; serial femtosecond crystallography; European X-ray Free-Electron Laser; megahertz pulse-repetition rate; protein structure determination; drug discovery; ceftriaxone; sulbactam; X-ray crystallography; enzyme mechanisms.

**PDB references:** BlaC, unmixed, 7k8l; mixed with ceftriaxone, 5 ms, 7k8e; 10 ms, 7k8f; 50 ms, 7k8h; mixed with sulbactam, 66 ms, 7k8k

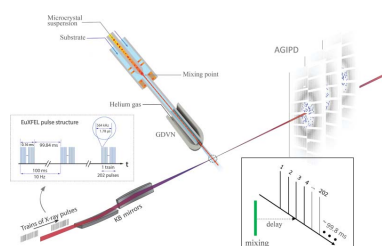
**Supporting information:** this article has supporting information at [www.iucrj.org](http://www.iucrj.org)

<sup>a</sup>Physics Department, University of Wisconsin-Milwaukee, 3135 North Maryland Avenue, Milwaukee, WI 53211, USA, <sup>b</sup>School of Applied and Engineering Physics, Cornell University, 254 Clark Hall, Ithaca, NY 14853, USA, <sup>c</sup>Center for Free-Electron Laser Science, Deutsches Elektronen-Synchrotron DESY, Notkestrasse 85, 22607 Hamburg, Germany, <sup>d</sup>School of Molecular Sciences and Biodesign Center for Applied Structural Discovery, Arizona State University, Tempe, AZ 85287-1604, USA, <sup>e</sup>Institute of Physical Chemistry Rocasolano, Spanish National Research Council, Calle de Serrano 119, 28006 Madrid, Spain, <sup>f</sup>European XFEL, Holzkoppel 4, 22869 Schenefeld, Germany, <sup>g</sup>Deutsches Elektronen-Synchrotron DESY, Notkestrasse 85, 22607 Hamburg, Germany, <sup>h</sup>The Hamburg Centre for Ultrafast Imaging, Luruper Chaussee 149, 22761 Hamburg, Germany, <sup>i</sup>Lawrence Livermore National Laboratory, 7000 East Avenue, Livermore, CA 94550, USA, <sup>j</sup>SLAC National Accelerator Laboratory, 2575 Sand Hill Rd, Menlo Park, California 94025, USA, <sup>k</sup>Department of BioSciences, Rice University, 6100 Main Street, Houston, TX 77005, USA, <sup>l</sup>Department of Physics, Arizona State University, Tempe, AZ 85287, USA, <sup>m</sup>Department of Bioengineering and Therapeutic Sciences, University of California San Francisco, San Francisco, CA 94158, USA, <sup>n</sup>Department of Physics and Universitat Hamburg, Luruper Chaussee 149, 22761 Hamburg, Germany, <sup>o</sup>Department of Chemistry and Physics, La Trobe Institute for Molecular Science, La Trobe University, Melbourne, Victoria 3086, Australia, and <sup>p</sup>Department of Chemistry, Rice University, 6100 Main Street, Houston, TX 77005, USA. \*Correspondence e-mail: [m-schmidt@uwm.edu](mailto:m-schmidt@uwm.edu)

Here, we illustrate what happens inside the catalytic cleft of an enzyme when substrate or ligand binds on single-millisecond timescales. The initial phase of the enzymatic cycle is observed with near-atomic resolution using the most advanced X-ray source currently available: the European XFEL (EuXFEL). The high repetition rate of the EuXFEL combined with our mix-and-inject technology enables the initial phase of ceftriaxone binding to the *Mycobacterium tuberculosis*  $\beta$ -lactamase to be followed using time-resolved crystallography in real time. It is shown how a diffusion coefficient in enzyme crystals can be derived directly from the X-ray data, enabling the determination of ligand and enzyme–ligand concentrations at any position in the crystal volume as a function of time. In addition, the structure of the irreversible inhibitor sulbactam bound to the enzyme at a 66 ms time delay after mixing is described. This demonstrates that the EuXFEL can be used as an important tool for biomedically relevant research.

## 1. Introduction

Combating the rise of infectious diseases requires a collaborative and interdisciplinary approach. Structural biologists can contribute by investigating the reaction mechanisms of biomedically significant enzymes as a structural basis to develop cures for diseases. Bacterial infections with strains that are resistant to currently available antibiotics are on the rise (Cassini *et al.*, 2019). A study sponsored by the British government projected that in the near future more people will die from untreatable bacterial infections than from cancer (<https://amr-review.org/>). Bacterial enzymes that inactivate



OPEN ACCESS

currently available drugs are central to antibiotic resistance (Fair & Tor, 2014), and unraveling the catalytic mechanism of these enzymes will be beneficial for the development of novel antibiotics (Imming *et al.*, 2006).  $\beta$ -Lactamases such as the *Mycobacterium tuberculosis*  $\beta$ -lactamase [BlaC; Fig. 1(a)] catalytically inactivate  $\beta$ -lactam antibiotics.  $\beta$ -Lactamases are responsible for the emergence of multidrug- and extensively drug-resistant bacterial strains (Smith *et al.*, 2013). Infectious diseases that could be treated with antibiotics in the past may become untreatable. This warrants the investigation of the structure and function of these enzymes.

Using time-resolved crystallography, structures of intermediates and kinetic mechanisms can be extracted simultaneously from the same set of X-ray data (Moffat, 2001; Schmidt, 2008). At free-electron lasers (XFELs) small, micrometre- and submicrometre-sized, crystals can be examined due to the immense X-ray pulse intensity (Chapman *et al.*, 2011). The microcrystals are destroyed by the pulses, and new crystals must be delivered to the X-ray interaction point in a serial fashion. This method has been termed serial femtosecond crystallography (SFX; Chapman *et al.*, 2011; Boutet *et al.*, 2012). Since the XFEL pulses are of femtosecond duration, diffraction patterns are collected before the crystals suffer significant radiation damage, resulting in X-ray structures that are essentially damage-free (Lomb *et al.*, 2011; Nass, 2019; Neutze *et al.*, 2000) and are suspended in their current reaction state. Most time-resolved crystallographic experi-

ments at XFELs are of the pump–probe type. An optical laser pulse triggers a reaction in the crystallized molecules. Structures are probed by X-ray pulses after a controlled delay (Tenboer *et al.*, 2014; Barends *et al.*, 2015; Coquelle *et al.*, 2018; Nogly *et al.*, 2018; Kern *et al.*, 2018; Pandey *et al.*, 2019; Skopintsev *et al.*, 2020; Dods *et al.*, 2021; Yun *et al.*, 2021). Due to the ultrashort nature of both X-ray and optical laser pulses, the experiments can reach subpicosecond time resolutions (Hartmann *et al.*, 2014; Barends *et al.*, 2015; Pande *et al.*, 2016; Skopintsev *et al.*, 2020). Photoactivation requires a light-sensitive cofactor, a chromophore, located in the protein to absorb the light. Light absorption must trigger a reaction that either promotes catalysis directly (Holtorf *et al.*, 1995; Li *et al.*, 2010; Sorigué *et al.*, 2017, 2021) or regulates the activity of the enzyme (Takala *et al.*, 2014; Gourinchas *et al.*, 2017; Carrillo *et al.*, 2021). Most enzymes, however, are neither activated nor regulated by light, meaning that the technique can only be directly applied in a narrow range of cases. Broader application requires great effort and chemical expertise to either engineer photoactive enzymes or to design photoactive compounds that can be soaked into, and activated in, enzyme crystals (Šrajter & Schmidt, 2017; Zaitsev-Doyle *et al.*, 2019; Mehrabi, Schulz, Dsouza *et al.*, 2019).

With the ‘mix-and-inject’ technique (Schmidt, 2013; Stagno *et al.*, 2017; Kupitz *et al.*, 2017; Olmos *et al.*, 2018; Mehrabi, Schulz, Agthe *et al.*, 2019) photoactivation is not necessary. The substrate is rapidly mixed with small enzyme crystals

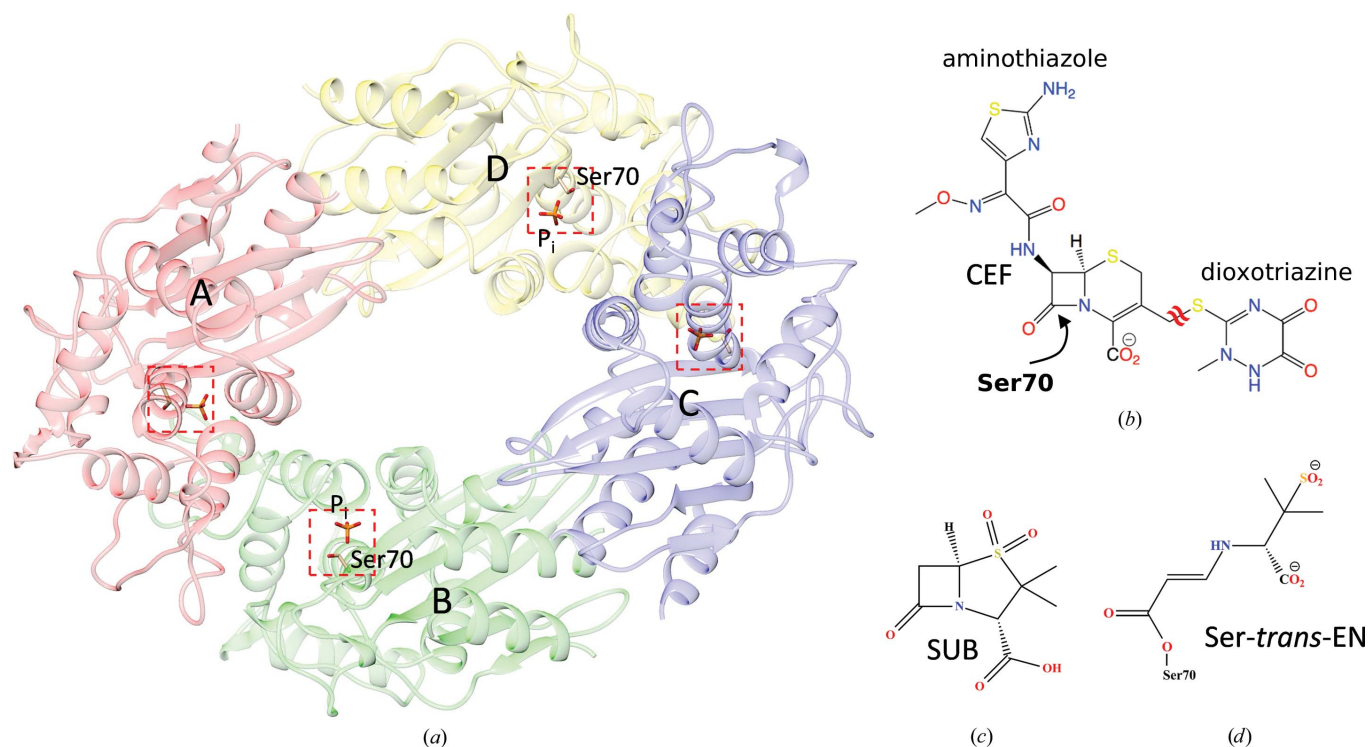


**Figure 1**  
The structures of BlaC and the ligands investigated here. (a) Structure of BlaC in the orthorhombic crystal form. The four subunits of BlaC are shown in red (A), green (B), blue (C) and yellow (D). The red dotted box shows the position of the active site. A phosphate ( $P_i$ ) is present in all active sites. The catalytically active Ser70 is marked in subunits B and D. (b) The chemical structure of ceftriaxone (CEF). The leaving group (dioxotriazine; the double tilde shows the cleaved bond) and the thiazole ring are marked. (c) The chemical structure of subactam (SUB). (d) The covalently bound *trans*-EN. Ser70 of BlaC opens the  $\beta$ -lactam ring of SUB. The structure rearranges to a *trans*-enamine. This inactivates BlaC.



**Table 1**  
Data-collection statistics [30 ms data from Olmos *et al.* (2018)].

	Water (reference)	5 ms CEF	10 ms CEF	50 ms CEF	66 ms SUB	30 ms CEF (LCLS)
Temperature (K)	293	293	293	293	293	293
Space group	$P2_1$	$P2_1$	$P2_1$	$P2_1$	$P2_1$	$P2_1$
EuXFEL train pulse rate (kHz)	564	564	564	564	564	564
$a, b, c$ (Å)	80.9, 99.5, 112.6	80.6, 98.7, 113.1	80.6, 98.5, 113.5	80.4, 98.2, 115.2	81.0, 99.5, 112.6	78.7, 96.8, 112.6
$\alpha, \beta, \gamma$ (°)	90, 108.4, 90	90, 108.6, 90	90, 108.8, 90	90, 110.0, 90	90, 108.4, 90	90, 109.7, 90
Resolution (Å)	2.8	2.4	2.6	2.6	2.7	2.7
Hits	51980	110698	85775	85914	35886	35065
Indexed patterns	31812	105495	52323	36256	25013	24397
Hit/indexing rate (%)	2.98/61.2	0.65/95.3	1.33/61.0	2.26/42.2	0.78/69.7	3.87/69.5
Observed reflections	31572191	114717921	49576617	38055135	21034155	14588166
Unique reflections	41870	65232	51595	50760	45344	40340
Multiplicity	754 (236)	1758 (1246)	966.3 (580.4)	749.7 (449.4)	463.8 (307.4)	526 (142)
Completeness (%)	100 (100)	100 (100)	100 (100)	100 (100)	100 (100)	100 (100)
$R_{\text{split}}$ (%)	20.6 (988)	15.6 (303.7)	17.8 (334)	20.9 (198.1)	21.4 (459.2)	14.2 (121.1)
$CC_{1/2}$ (%)	96.5 (22.9)	99.2 (26.9)	99.6 (58.4)	99.5 (58.4)	96.9 (20.5)	98.6 (34.5)

during sample delivery (Calvey *et al.*, 2019). Mixing occurs at a well controlled location ‘en route’ to the X-ray beam. During the time delay  $\Delta t_m$  that occurs between mixing and injection, the substrate diffuses into the crystals and binds to the enzyme. The complex formed by the substrate and the enzyme then initiates the enzymatic cycle. Variation of  $\Delta t_m$  allows the measurement of rate coefficients together with atomic resolution structures which can be associated with intermediate states of the protein reactions (Kupitz *et al.*, 2017; Olmos *et al.*, 2018; Mehrabi, Schulz, Agthe *et al.*, 2019). This can reveal the mechanism of enzyme action at the molecular level or the binding of a drug molecule. The combination of serial femtosecond crystallography with mixing before injection has been denoted ‘mix-and-inject serial crystallography’ (MISC; Kupitz *et al.*, 2017; Olmos *et al.*, 2018). The feasibility of MISC has previously been demonstrated with BlaC on longer millisecond timescales (Kupitz *et al.*, 2017; Olmos *et al.*, 2018). The observation of intermediate-state structures, and the maximization of the potential time resolution in both photoactivation and mix-and-inject techniques, relies on an accurately gauged start time of the reaction inside the crystals. In photoactivation experiments this requires a sufficient penetration of optical laser light into the crystal to ensure that a reaction is simultaneously triggered in a significant fraction of the molecules. In mix-and-inject experiments, the diffusion time of the substrate into the crystal may limit the ability to discriminate diffusion and kinetics, including substrate binding. To overcome this limitation, micrometre or sub-micrometre crystal sizes are required that ensure that the substrate diffuses rapidly into the crystals and the reaction is triggered swiftly and much faster than the lifetime of the reaction intermediates of interest (Schmidt, 2013).

The reaction of the cephalosporin antibiotic ceftriaxone [CEF; Fig. 1(b)] with BlaC is an excellent candidate for exploration with MISC. Previously, this reaction was investigated for  $\Delta t_m$  of longer than 30 ms (Kupitz *et al.*, 2017; Olmos *et al.*, 2018). At 30 ms, however, the CEF binding sites in BlaC were essentially fully occupied (Olmos *et al.*, 2018), a state also reached on similar timescales for other proteins and enzymes (Stagno *et al.*, 2017; Mehrabi, Schulz, Agthe *et al.*, 2019; Ishigami *et al.*, 2019). The substrate-binding phase and the

formation of the enzyme–substrate complex, however, remain elusive. Here, we aim to characterize the early phase of substrate binding with single-millisecond time delays by using the megahertz X-ray pulse-repetition rate of the European XFEL (EuXFEL; Decking *et al.*, 2020).

In addition, we aim to investigate the reaction of BlaC with an inhibitor, sulbactam [SUB; Fig. 1(c)], on a millisecond timescale. The biochemistry of SUB and its application in combination with  $\beta$ -lactam antibiotics have been described in detail elsewhere (Totir *et al.*, 2007). SUB binds to the active site of BlaC and reacts with the catalytically active serine of  $\beta$ -lactamases to form a covalently bound species. Most abundant is the so-called *trans*-enamine (*trans*-EN) species [Fig. 1(d)] that inhibits  $\beta$ -lactamases and helps to eliminate  $\beta$ -lactamase-induced antibiotic resistance. Static structures of *trans*-ENs with  $\beta$ -lactamases, including BlaC, have recently been characterized (Cheng *et al.*, 2020; Tassoni *et al.*, 2019), but structures of the early species that form during SUB binding remain elusive.

## 2. Methods

### 2.1. BlaC crystals

Platelet-shaped crystals of BlaC with approximate dimensions of  $10 \times 10 \times 2 \mu\text{m}$  (Appendix A) were produced by a stirring method on site in the XBI facility of the EuXFEL (Han *et al.*, 2021) using ammonium phosphate (AP) as described by Olmos *et al.* (2018). The crystals belonged to space group  $P2_1$  (Table 1), with four BlaC subunits in the asymmetric unit [Fig. 1(a)] (Olmos *et al.*, 2018). Only two subunits bind CEF in their catalytic cleft, as demonstrated previously (Olmos *et al.*, 2018). The concentration of BlaC subunits in the crystals is 15.5 mM, so that the concentration of active subunits is 7.8 mM. When this concentration is matched by substrate, the substrate concentration is called ‘stoichiometric’ in the following description.

### 2.2. Data collection at the EuXFEL

The platelets were mixed with ceftriaxone [CEF; Fig. 1(b); molecular mass  $554.6 \text{ g mol}^{-1}$ ; 200 mM in 0.8 M AP] or

sublactam (SUB) inhibitor [Fig. 1(c), molecular mass  $223.2 \text{ g mol}^{-1}$ ,  $100 \text{ mM}$  in  $0.8 \text{ M AP}$ ] using optimized mixing injectors (Calvey *et al.*, 2019) which were adapted to operate at the SPB/SFX instrument (Mancuso, 2019) of the EuXFEL. Flow rates and mixer geometries are shown in Table 2. The mixture was intercepted after a delay  $\Delta t_m$  by X-ray pulses from the EuXFEL. The EuXFEL delivers X-ray pulses in pulse trains that repeat ten times per second (Fig. 2). Each train contained 202 X-ray pulses with approximately 40 fs full-width at half-maximum (FWHM) pulse duration and about 1.5 mJ pulse energy. The pulse-repetition rate within a pulse train was 564 kHz, a reduction from the possible 4.5 MHz to avoid pristine, upstream jet volumes being affected by previous X-ray pulses (Yefanov *et al.*, 2019; Pandey *et al.*, 2020; Grünbein *et al.*, 2021). Given a flow rate of about  $80 \text{ } \mu\text{l min}^{-1}$  (Table 2) and an assumed jet diameter of  $8 \text{ } \mu\text{m}$ , the jet advances 26.5 m in a second. With a 564 kHz pulse rate the jet is intercepted every  $47 \text{ } \mu\text{m}$ , which is much larger than the gap ( $\sim 20 \text{ } \mu\text{m}$ ; Wiedorn, Oberthür *et al.*, 2018) in the jet produced by the intense X-ray pulse. The X-ray beam size at the jet position was  $\sim 3 \text{ } \mu\text{m}$ . The design of the mixers allowed us to

recapture the record (Mehrabi, Schulz, Agthe *et al.*, 2019) for the shortest MISC time point, while maintaining the high jet speed necessary for the 564 kHz measurements (Wiedorn, Oberthür *et al.*, 2018). Reference data were obtained by mixing with water.

Diffraction patterns (DPs) were collected using the Adaptive Gain Integrating Pixel Detector (AGIPD; Allahgholi *et al.*, 2019) operating at a 565 kHz frame rate. The experiment was monitored using *OnDA* (Mariani *et al.*, 2016), which is designed to estimate hit rates and spatial resolution in real time. DPs with Bragg reflections were selected by *Cheetah* (Barty *et al.*, 2014) and indexed, integrated, scaled and merged by *CrystFEL* (White *et al.*, 2016) in a manner consistent with previous work (Pandey *et al.*, 2020). In brief, diffraction images with Bragg reflections were found by *Cheetah* (peakfinder8, minSNR=8, minADC=200, minPix=1, minPeaks=25) using the calibration process described by Wiedorn, Awel *et al.* (2018). Careful masking of shadowed and unreliable regions of the detector was performed on a run-by-run basis (Appendix B). Independent masks were used for peak finding to avoid false hits, for example due to ice formation. Indexing

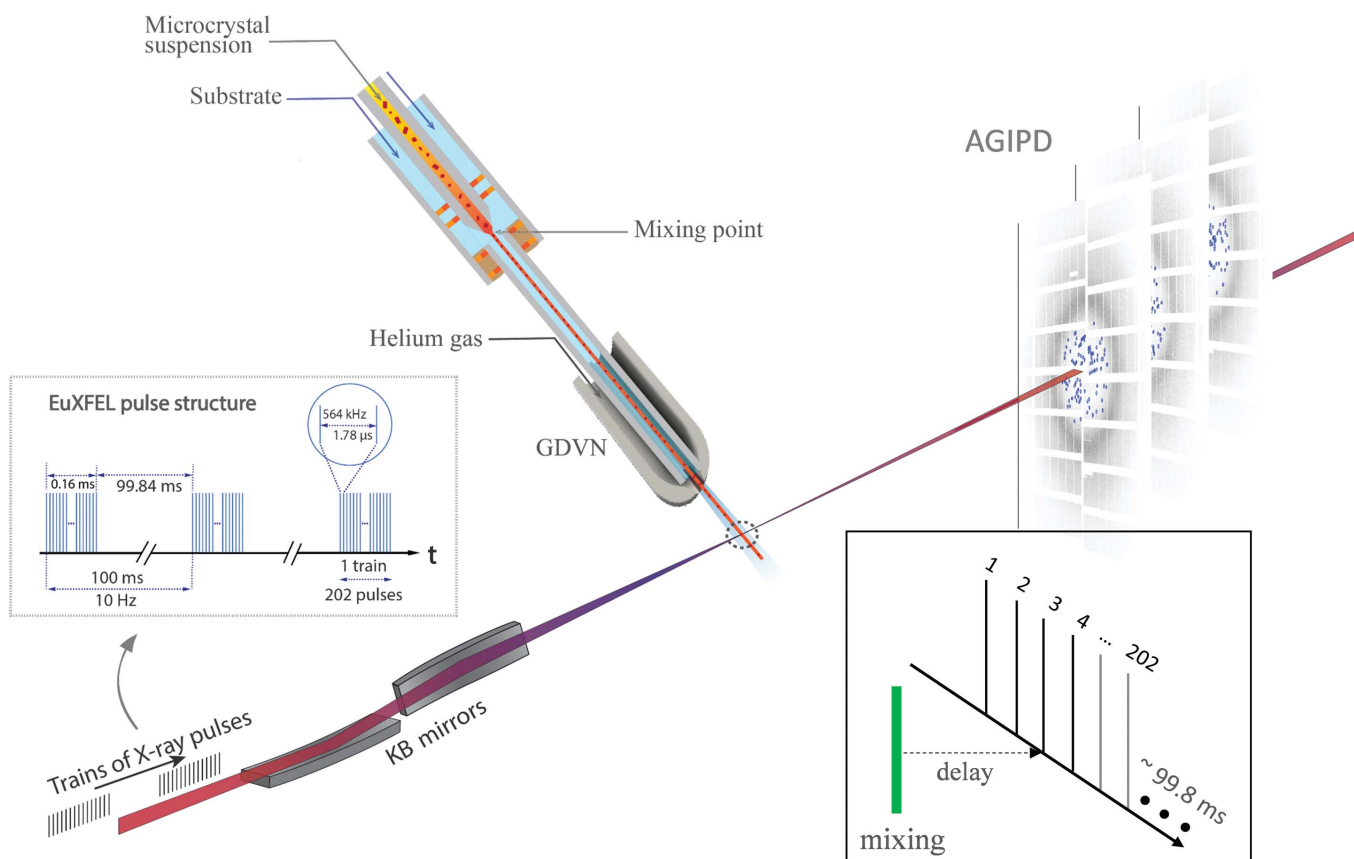


**Figure 2** Experimental setup at the European XFEL. BlaC microcrystals are mixed with substrate and injected into the X-ray interaction region (dotted circle) after a delay determined by the distance between the mixing region and the X-rays, the capillary width and the flow rate. Diffusion of substrate into the crystals occurs during this time. The mixture is probed by trains of X-ray pulses. The trains repeat ten times per second. Pulses within the trains repeat at 564 kHz, hence the pulses are spaced by  $1.78 \text{ } \mu\text{s}$ . 202 pulses were in each train for this experiment. The AGIPD collects the diffraction patterns and reads them out for further analysis. Inset: data collection. With a selected injector geometry and flow rate, the delay is fixed by the distance of the mixing region from the X-ray interaction region. All pulses in all trains (here pulse 3) probe the same time delay. The EuXFEL pulse structure is most efficiently used.

Table 2

Parameters for the mix-and-inject experiments.

Concentrations of ceftriaxone (CEF) and sulbactam (SUB) are shown as were flowed through the outer capillary line of the mixing injectors. Time delays are achieved after mixing in a constriction as per Calvey *et al.* (2019).

	Water	SUB	CEF	CEF	CEF
$\Delta t_m$ (ms)	(10)	66	5	10	50
Ligand concentration (mM)	—	100	200	200	200
Ligand buffer	—	0.8 M AP pH 4.6	0.8 M AP pH 4.6	0.8 M AP pH 4.6	0.8 M AP pH 4.6
Ligand flow ( $\mu\text{l min}^{-1}$ )	74.5	54.5	76.7	74.5	71.8
Crystal flow ( $\mu\text{l min}^{-1}$ )	5.5	11.6	3.3	5.5	8.2
Mixing injector capillary internal diameter ( $\mu\text{m}$ )	50	75	50	50	75
Constriction length (mm)	17.8	36.1	9.3	17.8	36.1
Timing uncertainty (ms)	—	9.3	1.8	3.0	10.4
Experimental time to collect the data set (min)	50	56	138	250	32

was performed with *CrystFEL* (version 0.9.0) using the indexing package *XGANDALF* (Gevorkov *et al.*, 2019) with the following parameters: `peaks=peakfinder8`, `Min-SNR=5`, `Min-pixel-count=1`, `Threshold=400`. The detector geometry was refined using *geoptimiser* (Yefanov *et al.*, 2015). Merging and scaling of the Bragg peak intensities were performed using the *partialator* program from *CrystFEL*. To avoid the integration of noise for weakly scattering patterns, reflections were included up to  $1.0 \text{ nm}^{-1}$  above a conservative resolution estimate for each crystal (`--push-res=1.0`). Hit rates and indexing rates were stable in the order of 1.0% and 70%, respectively, irrespective of the pulse index in the train (Appendix A). The lower hit rate is a consequence of diluting the crystalline slurry with the ligand/substrate. It has been shown that the X-ray pulse position in the train has no effect on the structure (Yefanov *et al.*, 2019). Structure-factor amplitudes were generated from the measured intensities using programs from the *CCP4* software suite (Winn *et al.*, 2011). Data-collection statistics are shown in Table 1.

As a control, and to investigate the result of the complete reaction of BlaC with SUB in the platelet crystal form, macroscopic crystals were grown in sitting drops ( $10 \mu\text{l}$  BlaC at  $45 \text{ mg ml}^{-1}$  mixed in a 1:1 ratio with  $2.1 \text{ M}$  AP pH 4.1). Crystals grew within three days. The crystals were soaked for 3 h in a cryobuffer consisting of  $2 \text{ M}$  AP, 20% glycerol and  $100 \text{ mM}$  SUB. The crystals were cooled in liquid nitrogen. Data were collected on beamline ID-19 of the Structural Biology Center, Advanced Photon Source, Argonne National Laboratory. Data were processed to  $2.7 \text{ \AA}$  using *HKL-3000* (Minor *et al.*, 2006). Details will be presented elsewhere.

### 2.3. Difference-map calculation and structure determination

The structures of BlaC and the BlaC–CEF complexes were determined as described previously (Kupitz *et al.*, 2017; Olmos *et al.*, 2018). Since the unit-cell constants change substantially after mixing (Table 1), isomorphous difference maps cannot be calculated and OMIT difference maps ( $\text{DED}_{\text{omit}}$ ) were used. An initial BlaC model, PDB (Berman *et al.*, 2002) entry 6b5x (Olmos *et al.*, 2018), was refined against the structure-factor amplitudes  $|F_o(t)|_{\text{CEF}}$  collected at a particular  $\Delta t_m$ . The content of the active sites (water and phosphate) was removed

during the refinement. From the refined model amplitudes,  $|F_c|$  were determined. From the amplitudes (and the phases obtained from the refined model), weighted  $m|F_o(t)|_{\text{CEF}} - D|F_c|$  OMIT maps ( $\text{DED}_{\text{omit}}$ ) were calculated. Polder difference maps (Liebschner *et al.*, 2017;  $\text{DED}_{\text{polder}}$ ) were calculated to display weak difference electron-density features. The CEF was modeled in the polder maps. To refine the structure and to determine the fractional concentration of both  $P_i$  and CEF, grouped occupancy refinement was performed using *Phenix* (Liebschner *et al.*, 2019). CEF was flagged together with  $P_i$  as a pair of molecules occupying the same space. The positions and *B* factors of all atoms as well as the occupancies of  $P_i$  and CEF were refined simultaneously. As a check, the sum of the occupancies of the flagged molecules should not deviate too much from unity.

Initial structures of the BlaC–SUB complexes were determined by inspecting both isomorphous and OMIT difference maps. The OMIT map was calculated in a similar way as described above except that amplitudes  $|F_o(t)|_{\text{SUB}}$  were used. A weighted  $\text{DED}_{\text{iso}}$  map was calculated from difference amplitudes  $w[|F_o(t)|_{\text{SUB}} - |F_o|_{\text{WAT}}]$ , where the reference amplitudes  $|F_o|_{\text{WAT}}$  were obtained by mixing with water. The weighting factor was calculated as described previously for photoactive yellow protein (Ren *et al.*, 2001; Pandey *et al.*, 2020) and for the needle crystal form of BlaC (Olmos *et al.*, 2018). The *trans*-EN and SUB molecules were inserted into the OMIT map. The positions and orientations were cross-examined to agree with the  $\text{DED}_{\text{iso}}$  map. The complexes were refined using *REFMAC* (Murshudov *et al.*, 2011) against the  $|F_o(t)|_{\text{SUB}}$  amplitudes. The refinement statistics for the BlaC–CEF and BlaC–SUB complexes are shown in Table 3.

### 2.4. Binding kinetics of CEF

Refined occupancies are fitted by functions that account for saturation of CEF and decline of  $P_i$ ,

$$C_{\text{CEF}}(t) = \frac{C_{\text{S,CEF}} \cdot t}{t_{1/2} + t}, \quad (1)$$

and

$$C_{P_i}(t) = \frac{C_{\text{ini},P_i} \cdot t_{1/2}}{t_{1/2} + t}, \quad (2)$$

**Table 3**  
Refinement statistics.

	Water	5 ms CEF	10 ms CEF	50 ms CEF	66 ms SUB	30 ms CEF (Olmos <i>et al.</i> , 2018, revisited)
Refinement program	<i>Phenix</i>	<i>Phenix</i>	<i>Phenix</i>	<i>Phenix</i>	<i>REFMAC</i>	<i>Phenix</i>
Resolution	2.8	2.4	2.6	2.6	2.7	2.75
Reflections used	36804	52163	43274	45264	36434	40951
$R_{\text{cryst}}/R_{\text{free}}$	0.21/0.27	0.24/0.25	0.22/0.26	0.22/0.27	0.21/0.29	0.22/0.26
Occupancy (CEF/phosphate) (%)	—	B, 46/60; D, 43/53	B, 61/35; D, 64/38	B, 84/11; D, 79/27	100, not refined	B, 76/20; D, 74/21
$\langle B \rangle_{\text{CEF}}$ ( $B/D$ ) ( $\text{\AA}^2$ )	—	51/48	55/58	53/50	—	70/67
R.m.s.d., bond lengths ( $\text{\AA}$ )	0.009	0.003	0.003	0.003	0.007	0.003
R.m.s.d., bond angles ( $^\circ$ )	1.09	1.07	1.03	1.34	1.67	1.10
H <sub>2</sub> O	129	246	251	247	201	146

respectively.  $C_{\text{S,CEF}}$  and  $C_{\text{ini,P}_i}$  are the occupancy of CEF after a long time (at saturation) and the initial occupancy of  $\text{P}_i$ , respectively. The constant  $t_{1/2}$  is either the time taken to reach half saturation of CEF or denotes the time when  $\text{P}_i$  has declined to half its initial concentration. The initial occupancy of  $\text{P}_i$  was set as 1.0, but the final occupancy of CEF was not constrained to 1.0 to account for a more realistic scenario.

### 2.5. The diffusion coefficient of CEF in the BlaC platelets

The occupancy of CEF bound noncovalently to the active center of BlaC was calculated with typical sized  $10 \times 10 \times 2 \mu\text{m}$  (platelet-like) crystals (Appendix A) by varying the diffusion coefficient  $D$  for the CEF in crystals until agreement with the experiment was achieved. The crystal was divided into 20 voxels along each direction and 20 time intervals were used. For each time interval, the concentration of the CEF substrate ( $C_{\text{CEF}}$ ) in each of the 8000 voxels in the crystal was determined using the known solution to Fick's second law for a rectangular volume, represented by the first 20 modes (Schmidt, 2013, 2020; Carslaw & Jaeger, 1959),

$$C_{\text{CEF}}(x, y, z, t) = C_{0,\text{CEF}} \left( 1 - \frac{64}{\pi^3} \sum_{l=0}^{19} \sum_{m=0}^{19} \sum_{n=0}^{19} \frac{(-1)^{l+m+n}}{(2l+1)(2m+1)(2n+1)} \times \cos \frac{(2l+1)\pi x}{2a} \cos \frac{(2m+1)\pi y}{2b} \cos \frac{(2n+1)\pi z}{2c} \times \exp \left\{ -\frac{D\pi^2}{4} \left[ \frac{(2l+1)^2}{a^2} + \frac{(2m+1)^2}{b^2} + \frac{(2n+1)^2}{c^2} \right] t \right\} \right) \quad (3)$$

where  $l, m, n$  are integer numbers that define the modes.  $x, y$  and  $z$  are coordinates within the crystal that extend from  $-a$  to  $+a, -b$  to  $+b$  and  $-c$  to  $c$ , where  $a, b, c$  are the half edge lengths of the platelet-shaped BlaC crystals.  $D$  is the diffusion coefficient,  $t$  is the time after mixing and  $C_{0,\text{CEF}}$  is the outside CEF concentration, which was set to 150 mM. This analytical approach to diffusion is strictly speaking only valid in the absence of substrate binding. However, here the substrate concentration ( $\sim 150 \text{ mM}$ ) is much higher than the concentration of the subunits that bind the CEF (7.8 mM). The concentration of substrate in the crystals increases rapidly to values much higher than the stoichiometric concentration. At saturation, the ES concentration is only 5.2% of that of the substrate. In addition, the speed (rate) of substrate binding is

low until sufficient substrate is present. Accordingly, substrate binding is a small perturbation of the free CEF concentration on all but the very shortest timescales.

On the timescales employed here, the formation of later intermediates and the catalytic turnover of BlaC with CEF do not play a role (Boyd & Lunn, 1979; Hugonnet & Blanchard, 2007; Tremblay *et al.*, 2010; Olmos *et al.*, 2018). Both processes unfold over much longer timescales (Fig. 3) than the time delays examined here.

CEF binding to the active sites of BlaC is dependent on the free BlaC concentration in the crystal and the rate coefficients that describe the binding kinetics (Fig. 3). Here, the rate coefficient  $k_{\text{on}}$  of  $3.2 \text{ M}^{-1} \text{ s}^{-1}$  as estimated by Olmos and coworkers was used. The  $k_{\text{off}}$  rate coefficient (dashed arrow in Fig. 3) was assumed to be negligible relative to the on-rate coefficient. There is only one free parameter, the diffusion coefficient  $D$ , which can be inferred by matching calculated occupancies to the refined occupancies observed at  $\Delta t_{\text{m}}$ . (3) provides substrate (CEF) concentrations in each individual voxel (at each position in the crystal) at any particular time  $t$ . CEF binding to BlaC was calculated for each voxel by numerically integrating the rate equation with time intervals  $dt$ ,

$$\begin{aligned} d[\text{ES}] &= [\text{E}(t)]_{\text{free}} \cdot [C_{\text{CEF}}(t)] \cdot k_{\text{on}} dt, \\ [\text{ES}(t_{i+1})] &= [\text{ES}(t_i)] + d[\text{ES}], \\ [\text{E}(t_{i+1})]_{\text{free}} &= [\text{E}(t_i)]_{\text{free}} - d[\text{ES}], \\ t_{i+1} &= t_i + dt. \end{aligned} \quad (4)$$

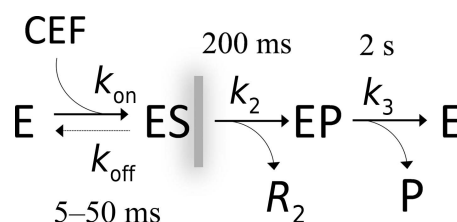


**Figure 3**  
Simplified enzymatic cycle of, and the timescales associated with, the reaction of BlaC with CEF. CEF is delivered to the crystals by diffusion. It noncovalently binds to the free BlaC enzyme (E) to form the enzyme-substrate complex (ES). The acyl intermediate EP, which is covalently bound to Ser70, is formed within  $\sim 200 \text{ ms}$ . The leaving group  $R_2$  is cleaved off the CEF. The modified CEF (EP) is hydrolyzed and released as product (P) and the free enzyme is recovered within about 2 s. In this paper, only the formation of the ES complex up to 50 ms (gray, blurred vertical line) was explored.

In (4),  $d[\text{ES}]$  is the change in concentration of the BlaC–CEF complex ([ES]) given the free enzyme ([E]) and free CEF ( $[C_{\text{CEF}}]$ ) concentrations at time  $t_i$  and the  $k_{\text{on}}$  rate. The free-enzyme concentration [E] decreases and that of the BlaC–CEF complex increases with each time step. (4) is repeated by increasing  $t_i$  by  $dt$  until  $t_i$  is larger than a given delay time, for example 10 ms. The substrate  $[C_{\text{CEF}}]$  is provided everywhere by diffusion (3) and its concentration is also dependent on  $t_i$ . The goal was to reproduce the approximate 50% BlaC–CEF occupancy in the *B* and *D* subunits ( $\text{occ}_{\text{obs}}$ ) which was observed in the experiment at around 5 ms. The calculated BlaC–CEF occupancy ( $\text{occ}_{\text{calc}}$ ) is the average of the calculated occupancies found in all voxels of the crystal.  $\text{Occ}_{\text{calc}}$  can then be compared with  $\text{occ}_{\text{obs}}$  and adjusted by varying the diffusion coefficient of CEF.

### 3. Results and discussion

#### 3.1. Formation of the enzyme–substrate complex

The EuXFEL 564 kHz pulse structure was used to measure the binding of the large CEF substrate to BlaC at a  $\Delta t_m$  of 5, 10 and 50 ms. The  $\Delta t_m$  of 5 ms is about an order of magnitude faster than the earliest (30 ms) time point collected previously (Olmos *et al.*, 2018). The  $\sim 2 \mu\text{m}$  thin, platelet-shaped BlaC microcrystals allow fast diffusion times across the thin dimension. Furthermore, diffusion is facilitated by large channels in the crystals (Olmos *et al.*, 2018). Therefore, these crystals are ideally suited for mix-and-inject investigations on fast timescales.

As observed in the previous studies at longer  $\Delta t_m$ , CEF only binds to BlaC subunits *B* and *D*. In Figs. 4(b)–4(d) polder difference electron-density maps (Liebschner *et al.*, 2017;  $\text{DED}_{\text{polder}}$ ) are shown in the active site of subunit *B*. On early timescales (5 and 10 ms after mixing) we simultaneously observe electron densities for CEF and the close-by phosphate ( $\text{P}_i$ ) molecule. Since CEF and  $\text{P}_i$  occupy the same space, their presence is mutually exclusive and the electron density reflects

an average over sites occupied by  $\text{P}_i$  and others occupied by CEF.  $\text{P}_i$  is also found near the CEF binding site in the unliganded (unmixed) form [Fig. 4(a)]. At  $\Delta t_m = 5$  ms, the  $\text{P}_i$  and CEF occupancies are both approximately 50%. The available catalytic sites in subunits *B* and *D* are equally occupied either by a CEF or by a  $\text{P}_i$ . At  $\Delta t_m = 50$  ms, the  $\text{P}_i$  density vanishes. Nevertheless, the  $\text{P}_i$  occupancy refines to 19% and that of CEF to 82% (Table 3). Here, an electron-rich compound ( $\text{P}_i$ ) is refined in conjunction with CEF, occupying equivalent spaces in different unit cells. This may result in an overestimate of the occupancy of  $\text{P}_i$ . As there is no indication of phosphate-shaped electron density at 50 ms [Fig. 4(d)], we consider this to be the error margin of our occupancy refinement.

In agreement with previous work (Olmos *et al.*, 2018), an additional CEF molecule is identified close to each active site that weakly interacts (stacks) with the CEF already bound there (Fig. 5). The stacking sites seem to be only transiently visited by CEF molecules until the active sites are fully occupied. The unit-cell parameter changes roughly follow CEF binding and  $\text{P}_i$  release [Fig. 6(a), inset; Table 1]. When subactam, which is about 2.5 times smaller, binds the  $\text{P}_i$  is not replaced and the unit-cell parameters do not change (see below and Table 1). We postulate that the displacement of the strongly negatively charged  $\text{P}_i$ , as well as the occupancy of the stacking site, may contribute to the unit-cell changes observed when CEF is mixed in. The needle crystal form described earlier (Olmos *et al.*, 2018) does not show unit-cell changes. There, neither the  $\text{P}_i$  nor the stacking site is present. In our BlaC platelets the CEF occupancy can be very heterogenous, in particular at 5 ms, which should result in different unit-cell parameters near the surface and in the center, respectively. However, the Bragg reflections are not split, which is in accordance with observations by others (Ramakrishnan *et al.*, 2021; Stagno *et al.*, 2017; Kupitz *et al.*, 2014). This may be a consequence of the fully coherent illumination of the entire microcrystal volume by the XFEL radiation or may be due to the plasticity of microcrystals that even supports phase transitions and space-group changes (Ramakrishnan *et al.*, 2021).

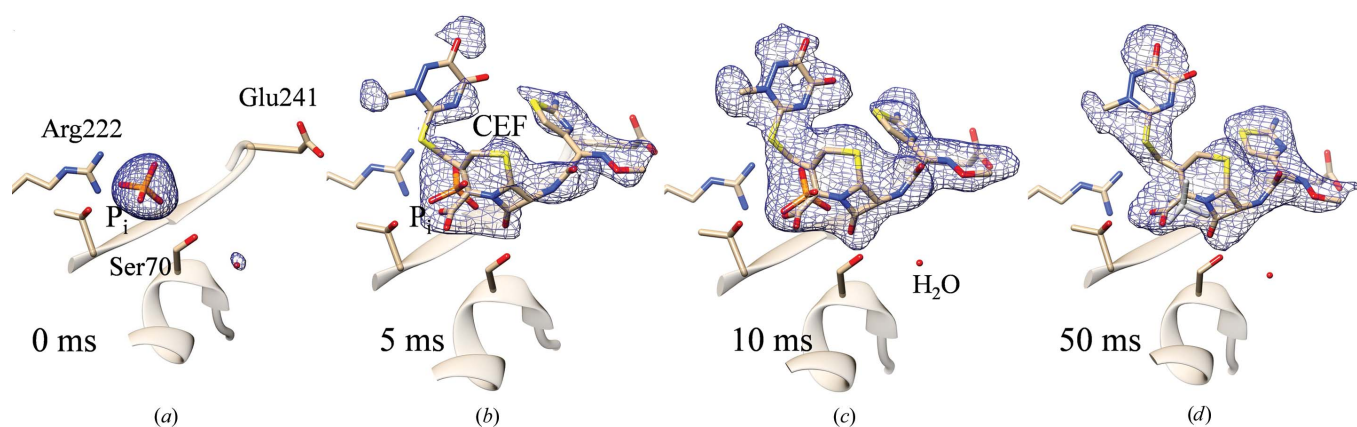
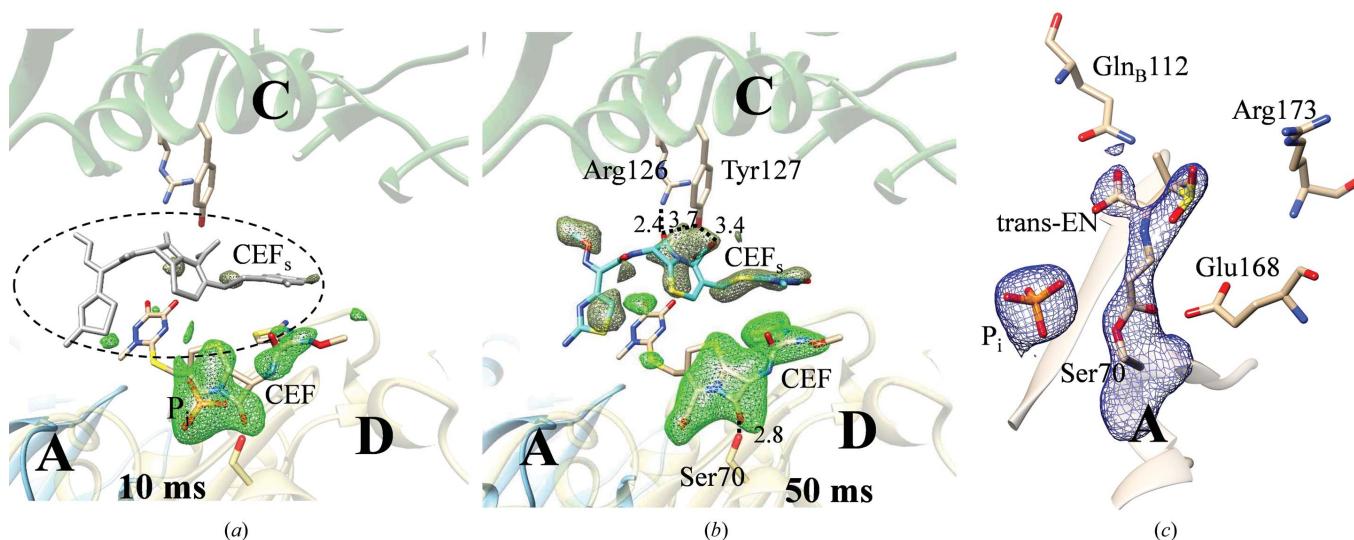


Figure 4

Polder difference electron density, contour level  $3\sigma$ , in the active center of BlaC subunit *B*. (a) The CEF ligand has not yet diffused in; the phosphate ( $\text{P}_i$ ) from the crystallization buffer is dominant in the active site. (b) 5 ms after mixing: the phosphate is beginning to be displaced by CEF. (c) 10 ms after mixing: the phosphate is no longer dominant. (d) 50 ms after mixing: little evidence of the phosphate remains and the density only has features of the antibiotic compound. Nearby amino acids are marked in (a).

As more CEF binds, Ser70 moves towards the  $P_i$  position (by about 1 Å) and the  $P_i$  is replaced at the same time (Table 4c). Other amino acids such as Asn172 and Asp241 move closer to the CEF. We can now develop a mini-movie for the formation of an enzyme–substrate (ES) complex (Supplementary Movie S1). This movie visualizes how CEF interacts with BlaC. The initial binding phase is complete when the CEF occupancy approaches saturation. Since the aminothiazole ring and, in particular, the dioxotriazine ring of

CEF stick out from the center [the  $\beta$ -lactam ring fused to the six-membered thiazine ring; Fig. 1(b)], they are more disordered and their electron densities are weaker. However, clear density features guide a structural refinement that shows that CEF binds through a succession of conformations which may be associated with distinct BlaC intermediates. The separation of these intermediates from the X-ray data is difficult since we have not collected a sufficiently large number of time delays to apply meaningful deconvolution algorithms (Schmidt *et al.*,



**Figure 5** Additional ligands. (a) CEF in the active site and the stacking site (dotted oval) located between subunits D and C. A  $DF_o - mF_c$  OMIT difference electron-density map in the active site is shown in green and that in the stacking site in gray–green (at a  $2.5\sigma$  contour level). Substantial CEF density in the active site is shown in green. There is also electron density for  $P_i$  present due to averaging over all unit cells in the crystal. The stacking site is not occupied (gray CEF<sub>s</sub> molecule). (b) At 50 ms the maximum occupancy of CEF in the active center is reached. The stacking site is substantially occupied (blue CEF molecule). Important residues and distances are marked in Å. (c) The covalently bound *trans*-EN is present in subunit A of the static cryostructure of BlaC when soaked with SUB (blue;  $2F_o - F_c$  map at a  $1.5\sigma$  contour level).

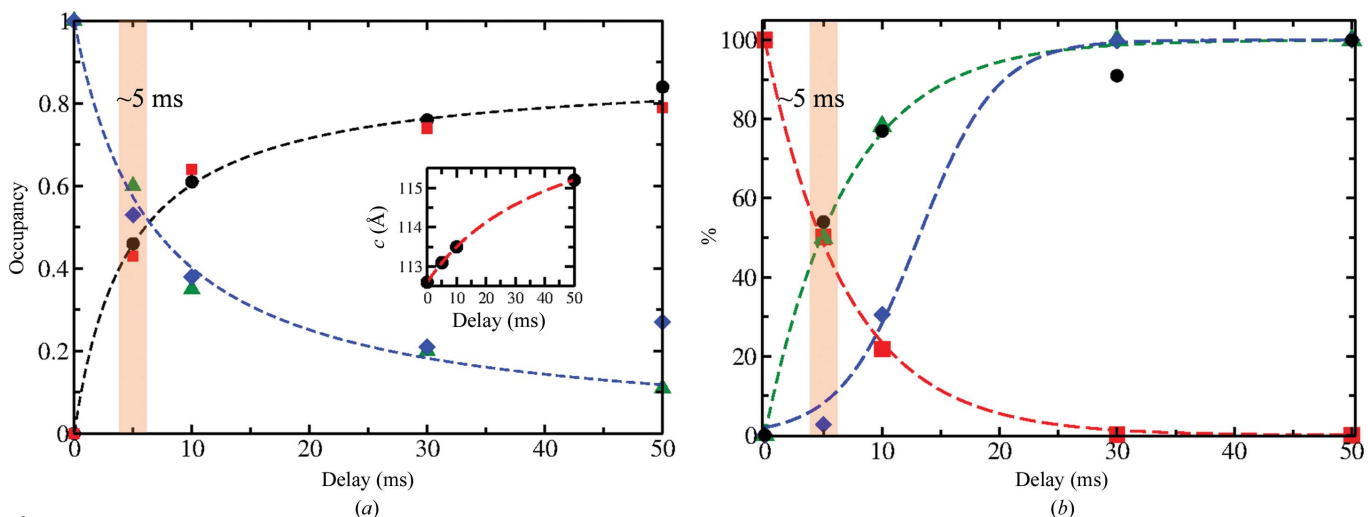


**Figure 6** BlaC–CEF complex formation as a function of time. (a) Occupancies of CEF in the active site of BlaC at 5, 10, 30 and 50 ms in subunits B (spheres) and D (squares) as well as those of  $P_i$  (green triangles and blue diamonds) are plotted as a function of delay (the 30 ms data are from Olmos *et al.*, 2018). The data are fitted with saturation curves [equations (1) and (2), black and blue dashed lines]. The two curves intersect at around 6 ms. Inset: the corresponding change in the unit-cell axis *c*. (b) Concentrations (in %) as calculated from diffusion and binding [equations (1)–(5)]; green dashed line and green triangles, increase of the calculated BlaC–CEF complex concentration averaged over all voxels in the crystal; red dashed line and squares, decrease of the free enzyme (BlaC); blue dashed line and diamonds, increase of the BlaC–CEF complex in the center of the platelet-shaped crystals. For comparison, the observed (refined) occupancies of the BlaC–CEF complex (normalized to 100% at 50 ms) are also shown (black spheres).

**Table 4**  
Important distances in the active centers of BlaC.

s, strong hydrogen bond up to 2.5 Å; h, hydrogen bond from 2.6 to 3.2 Å; w, weak interaction >3.2 Å (Jeffrey, 1997).

(a) Distances in (Å) in subunits *A* and *C* to the sulbactam (0RN).

	Subunit <i>A</i>	Subunit <i>C</i>
Ser70 OG to P <sub>i</sub> O	3.2 (h)	2.6 (h)
Ser70 OG to 0RN OAF	3.1 (h)	3.2 (h)
Gln112 OE1 to 0RN OX	Gln from <i>B</i> , 2.8 (h)	Gln from <i>D</i> , 3.3 (w)
Asn172 ND2 to 0RN OAF	3.2 (h)	3.1 (h)
Glu168 O2 to 0RN OAF	3.0 (h)	2.8 (h)
Arg173 NH1 to 0RN O	2.5 (s)	3.9 (w)
Thr239 O to 0RN OAO	3.9 (w)	2.9 (h)

(b) Distances in (Å) in subunits *B* and *D* to the Ser70 *trans*-enamine (TSS).

	Subunit <i>B</i>	Subunit <i>D</i>
Lys73 NZ to TSS O13	2.8 (h)	3.0 (h)
Gln109 OE1 to TSS O12	Gln from <i>A</i> , 2.7 (h)	Gln from <i>C</i> , 2.9 (h)
Thr239 O to TSS O8	2.9 (h)	2.9 (h)
Asp241 OD2 to TSS O11	6.4	4.1

(c) Distances in (Å) during ceftriaxone binding (CEF is only bound to subunits *B* and *D*).

	Subunit <i>B</i>				Subunit <i>D</i>			
	0 ms	5 ms	10 ms	50 ms	0 ms	5 ms	10 ms	50 ms
Ser70 OG to H <sub>2</sub> O	3.1 (h)	2.8 (h)	3.3 (w)	2.8 (h)	3.5 (w)	2.4† (s)	3.1 (h)	3.2 (h)
Ser70 OG to P <sub>i</sub> O4	3.6 (w)	3.5 (w)	3.4 (w)	2.6 (s)	2.7 (h)	3.7 (w)	3.9 (w)	2.7 (h)
Ser70 OG to CEF O	na‡	3.1 (h)	2.9 (h)	2.9 (h)	na	2.9 (h)	3.0 (h)	2.8 (h)
Ser128 OG to CEF OAD	na	2.4 (s)	2.4 (s)	2.5 (s)	na	2.3 (s)	2.4 (s)	2.6 (h)
Asn172 ND2 to CEF OAR	na	2.7 (h)	3.1 (h)	3.2 (h)	na	2.8 (h)	3.0 (h)	3.1 (h)
Thr237 OG1 to CEF OA1	na	2.7 (h)	3.1 (h)	3.0 (h)	na	2.7 (h)	2.6 (h)	3.1 (h)
Thr239 OG2 to CEF OA1	na	3.3 (w)	3.0 (h)	3.0 (h)	na	3.4 (w)	3.4 (w)	3.1 (h)
Asp241 OD1 to CEF NAC	na	<b>4.7</b>	<b>4.3</b>	<b>3.2 (h)</b>	<b>na</b>	<b>4.4</b>	<b>4.2</b>	<b>3.6 (w)</b>

† Weak OMIT difference electron density. ‡ Not applicable.

2003; Kostov & Moffat, 2011). The high X-ray pulse-repetition rate of the EuXFEL may make this possible since it allows the fast collection of data sets at tightly spaced delays. Given the resolution of our X-ray data (Table 1), it is challenging to make a distinction between ligand binding being supported by conformational disorder (Tzeng & Kalodimos, 2012) or by adaptation of the structure to a changing energy landscape, which would resemble an ‘induced fit’ (Changeux & Edelstein, 2011). Both scenarios (Vogt & Di Cera, 2012) would most likely result in the same (or a very similar) crystallographic signal. We hypothesize that both mechanisms are involved to some degree, which might be unraveled by single-particle experiments, as recently demonstrated for an unrelated biological system (Dashti *et al.*, 2020). However, the structures of BlaC as well as of CEF change [Table 4(c), Supplementary Movie S1], which might be interpreted as the signature of an induced fit after the initial binding event.

Formation of the ES complex is most important since it triggers the enzymatic cycle. Hence, it determines the time resolution of the MISC method. The ES complex consists of CEF noncovalently bound in the active site of BlaC (Fig. 4). CEF is delivered by diffusion into the crystals. The crystals must be small enough to enable short enough diffusion times so that the binding kinetics can be observed. However, MISC

does not measure the free substrate concentration in the crystals, and therefore diffusion is rather observed indirectly through the increase in the occupancies of well ordered substrate molecules in the active centers of BlaC. When the diffusion times are very short, occupancies may accumulate on a timescale longer than the diffusion time, as they are governed by the binding kinetics. The formation of the ES complex, and therefore the time resolution of the MISC method, is therefore not only dependent on the ligand concentration delivered by diffusion but also on the magnitude of the rate coefficients that characterize the kinetic mechanism.

### 3.2. Inhibitor binding

The structure of the BlaC–SUB complex was probed at  $\Delta t_m = 66$  ms. Strong positive  $DED_{iso}$  shows SUB binding to all four subunits of BlaC, which is in stark contrast to CEF, which only binds to subunits *B* and *D*. The absence of negative  $DED_{iso}$  at the P<sub>i</sub> position [Figs. 7(a) and 7(b)] shows that the P<sub>i</sub> does not move and stays in the active site. At the time delay of 66 ms sulbactam binding to BlaC is heterogeneous. In subunits *B* and *D* the

$DED_{iso}$  is elongated and stretches outwards from Ser70 [Fig. 7(b)]. In subunits *A* and *C* the  $DED_{iso}$  is pillow-like and is more distant from Ser70 [Fig. 7(a)]. The elongated  $DED_{iso}$  in subunits *B* and *D* [Fig. 7(b)] can be explained by a covalently bound *trans*-EN as a result of the reaction of the sulbactam with the catalytic Ser70. The diffusion time is fast enough that 66 ms after mixing all *B* and *D* subunits contain *trans*-EN, the position of which is stabilized by a network of BlaC residues [Fig. 7 and Table 4(b)]. This is quite unexpected, as it was suggested that it would take minutes for the enamine to form after binding of SUB to BlaC (Totir *et al.*, 2007; Cheng *et al.*, 2020; Tassoni *et al.*, 2019). In subunits *B* and *D* Arg173 displays a stretched, open conformation, allowing the SUB to orient correctly towards Ser70 and to react swiftly to the *trans*-EN, which then irreversibly inhibits BlaC (Tassoni *et al.*, 2019). The nearby P<sub>i</sub>, which is displaced when the much larger ligand CEF is present, stays in place in all subunits and is likely to add to the stability of both complexes.

The pillow-like  $DED_{iso}$  in a region more distant from Ser70 in subunits *A* and *C* [Fig. 7(a)] can be explained by an intact sulbactam molecule that is noncovalently bound to the active site. The SUB is oriented so that the ring sulfur dioxide points towards Ser70, with the  $\beta$ -lactam ring pointing away from Ser70. We hypothesize that this ‘upside-down’ orientation is

enforced by Arg173 and Gln112 [Fig. 7(a) and Table 4(a)], where Gln112 protrudes deep into the active sites from the adjacent, noncrystallographically related subunits [Fig. 7(a)]. As the noncovalently bound SUB is oriented incorrectly, Ser70 cannot attack and open the  $\beta$ -lactam ring within the  $\Delta t_m$  of 66 ms. However, the static (cryo) X-ray structure of this complex [Fig. 5(c)] shows that SUB indeed also reacts to the *trans*-EN in subunits A and C. Accordingly, the BlaC–SUB structure is an interesting intermediate on the catalytic pathway from SUB to *trans*-EN. The detection of this intermediate would be difficult if not impossible without the MISC experiment.

### 3.3. Diffusion of substrate in BlaC microcrystals

With  $D = 2.3 \times 10^{-6} \text{ cm}^2 \text{ s}^{-1}$  for CEF in water [Table 5(b)], the diffusion time into the center of a  $10 \times 10 \times 2 \text{ }\mu\text{m}$  crystal volume consisting of water is 1.6 ms. This means that at 5 ms the concentration of CEF molecules would be 96% of the outside concentration (about 144 mM), which is about 20 times higher than the stoichiometric concentration [Table 5(a)]. After integration of the rate equation, the

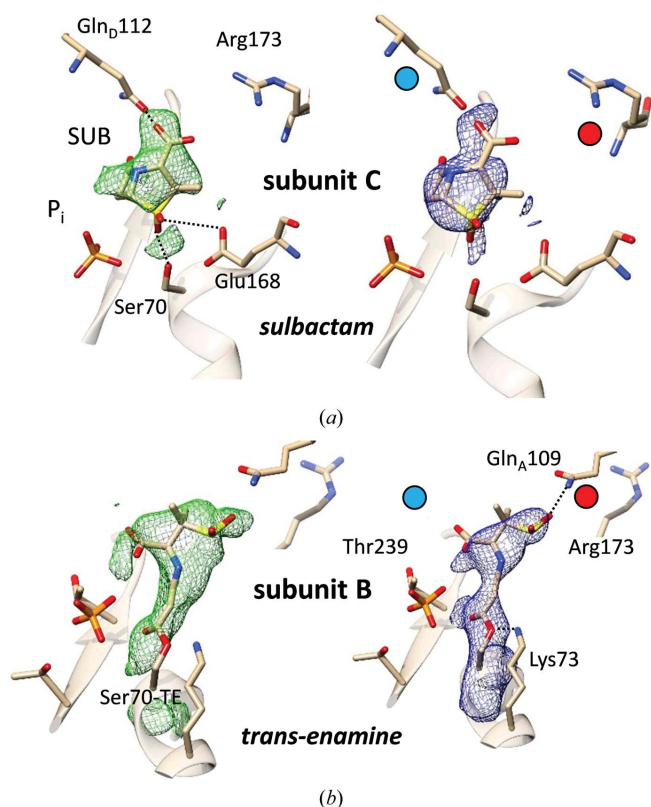


**Figure 7**  
BlaC–SUB complexes at  $\Delta t_m = 66 \text{ ms}$ . (a) Active site in subunit C with noncovalently bound intact sulbactam; left side,  $\text{DED}_{180}$  map (contour:  $3\sigma$ ); right side,  $2mF_o - DF_c$  map (contour:  $1.7\sigma$ ) after refinement. Close-by amino acids and the phosphate ( $\text{P}_i$ ) are marked. (b) Active site in subunit B with *trans*-enamine bound to Ser70; left side,  $\text{DED}_{180}$  map (contour:  $3\sigma$ ); right side,  $2mF_o - DF_c$  map (contour:  $1.7\sigma$ ) after refinement. Red and blue dots show important differences between the subunits. Gln112 from the adjacent subunit is not located close by and Arg173 is extended in subunit B, leaving subunit B more accessible to ligands and substrate.

**Table 5**  
Characterization of BlaC–CEF complex formation in crystals.

(a) Parameters for the binding of CEF to BlaC [see also Fig. 3 and equation (4)]. The concentration  $E_0$  of all subunits in the BlaC platelet crystal form is 15.5 mM. Only subunits B and D bind substrate.  $C_{0,\text{CEF}}$  is the mixed-in substrate concentration [see equation (3)].

$E_0$ (mM)	$C_{0,\text{CEF}}$ (mM)	$k_{\text{on}}$ ( $\text{M}^{-1} \text{ s}^{-1}$ )
7.8	150	3.2

(b) Parameters in equations (1)–(5) that were fitted to the respective refined occupancy values of CEF and  $\text{P}_i$ . The comparison of observed and calculated occupancies allows the determination of a diffusion coefficient  $D_{\text{eff}}$ .

BlaC–CEF increase, (1)	$\text{P}_i$ decrease, (2)	BlaC–CEF in the crystal center, (5)	$D$ ( $\text{cm}^2 \text{ s}^{-1}$ ) for CEF, (3) and (4)			
Observed†	Observed†	Sigmoidal increase‡			Water	$D_{\text{eff}}§$
$C_{\text{S,CEF}}$	$\tau_{1/2}$ (ms)	$\tau_{1/2}$ (ms)	$k$ ( $\text{ms}^{-1}$ )	$t_0$ (ms)		
88%	4.6	6.7	0.3	13.1	$2.3 \times 10^{-6}$	$2 \times 10^{-7}$

(c) Calculated occupancies which could be determined with the help of  $D_{\text{eff}}$ . The free CEF, free BlaC ( $[\text{E}_{\text{free}}]$ ) and BlaC–CEF complex ( $[\text{ES}]$ ) concentrations were averaged (angle brackets) over all voxels in the crystal.  $[\text{ES}]_{\text{center}}$  is the BlaC–CEF complex concentration in the center of the microcrystal platelets. Values in parentheses either denote the inside CEF concentration in terms of the percentage of the outside CEF concentration or represent the occupancy values of the relevant species.

$\Delta t_m$ (ms)	$[\text{CEF}]$ (mM)	$[\text{E}_{\text{free}}]$ (mM)	$[\text{ES}]$ (mM)	$[\text{ES}]_{\text{center}}$ (mM)
5	79.4 (53%)	3.9 (50%)	3.9 (50%)	0.2 (2.7%)
10	98.4 (66%)	1.7 (21%)	6.1 (79%)	2.4 (30%)
30	133.3 (89%)	0.0 (0.1%)	7.8 (99.9%)	7.7 (99%)
50	144.4 (96%)	0.0 (0%)	7.8 (100%)	7.8 (100%)

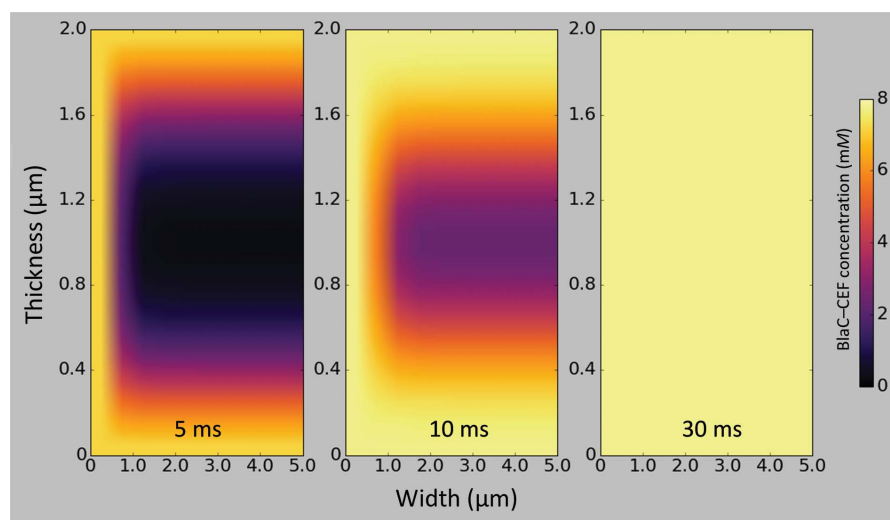
† From fitting saturation curves to refined occupancy values.  $C_{\text{S,CEF}}$  is the saturation concentration of CEF;  $\tau_{1/2}$  are characteristic times where 50% of the final concentrations of CEF and phosphate are reached, respectively. ‡ Parameters of the logistics function (5) fitted to occupancies determined in the centers of the BlaC platelets. §  $D_{\text{eff}}$  was obtained by matching the calculated and observed CEF binding kinetics.

average occupancy would be 99%, which is essentially saturation. This result does not reflect the crystallographically observed occupancy at 5 ms. When decreasing the diffusion coefficient to  $2.0 \times 10^{-7} \text{ cm}^2 \text{ s}^{-1}$ , the diffusion time into the crystal center increases to 19 ms [see Fig. 6(b) and Table 5(b)]. From this, the decrease of the free BlaC enzyme concentration, the increase of the free CEF concentration and the increase of the BlaC–CEF complex concentration were calculated as explained in Section 2.5. The results are shown in Fig. 6(b). The BlaC–CEF concentration in the center of the crystal lags behind [blue diamonds in Fig. 6(b)] since CEF requires additional time to reach the center and to bind to BlaC. The resulting sigmoidal-shaped response was fitted by a logistic function,

$$[\text{ES}]_{\text{center}} = \frac{100}{1 + \exp[-k(t - t_0)]}, \quad (5)$$

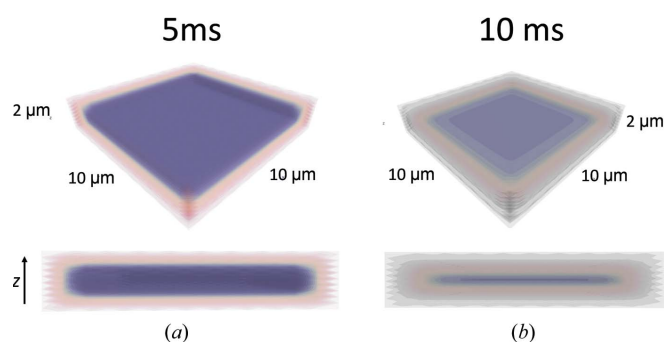
where  $t_0 = 13.1 \text{ ms}$  denotes the characteristic time when the binding reaction accelerates in the crystal center. With  $k = 0.3 \text{ ms}^{-1}$  a reasonable steepness of (5) was achieved [Fig. 6(b), blue dashed line]. The  $t_0$  roughly coincides with the diffusion time. Averaged over the entire crystal volume,  $\sim 50\%$  BlaC–CEF occupancy is reached at 5 ms, which is equal to the




**Figure 8**

Concentrations of the BlaC–CEF complex in  $10 \times 10 \times 2 \mu\text{m}$  platelet-shaped crystals (a) 5 ms, (b) 10 ms and (c) 30 ms after mixing with 200 mM ceftriaxone (150 mM final concentration assumed). The concentrations are shown in different colors (see the scale bar on the right) in central cross sections through half the width of the crystals. The drawings are not to scale, since the sections displayed are 5  $\mu\text{m}$  horizontally (width) and 2  $\mu\text{m}$  vertically (thickness). The enlargement along the short 2  $\mu\text{m}$  axis allows the display of the nuanced occupancy differences.

occupancy determined experimentally at  $\Delta t_m = 5 \text{ ms}$  [compare the green dashed line in Fig. 6(b) with Fig. 6(a)]. Fig. 8 shows a heatmap that plots BlaC–CEF occupancies through the center of half a BlaC crystal (see also Fig. 9 for a 3D representation). The concentrations of the BlaC–CEF complex are depicted with various colors (see the scale bar on the right). At the edge of the crystal, almost all active BlaC subunits (*B* and *D*) are already bound to CEF at 5 ms. In the center the BlaC–CEF complex concentration is 0.21 mM (2.7% of the total concentration of *B* and *D* subunits in the crystal), although the CEF concentration delivered by diffusion is already 35 mM (which is the mentioned 23% of the outside CEF concentration but is 5.5 times the stoichiometric concentration). The situation changes completely at 30 ms, where almost 100% occupancy is reached everywhere in the crystal, which is in accordance with earlier results (Olmos *et al.*, 2018) and with the occupancy at  $\Delta t_m = 50 \text{ ms}$  reported here (see also


**Figure 9**

3D representation of CEF occupancy values in the BlaC catalytic cleft 5 ms (a) and 10 ms (b) after mixing in a typical BlaC microcrystal platelet. Dark blue colors denote low occupancies and lighter hues denote high occupancies.

Supplementary Movie S2). As also discussed earlier, the variation of occupancy across microcrystals at faster mix-and-inject delays does not affect the enzyme kinetics, as the nucleophilic attack of Ser70 of BlaC on the  $\beta$ -lactam ring happens long after the crystals establish full CEF occupancy. It needs to be pointed out here that the simple model of CEF diffusion into BlaC microcrystals and the binding of CEF to BlaC molecules can be augmented by taking into account, for example, the exclusion volume occupied by reacting and nonreacting BlaC subunits (Geremia *et al.*, 2006), by the mentioned pointwise depletion of the free CEF concentration in each voxel by binding to BlaC active centers, or the diffusion of substrate directly through protein molecules facilitated by protein dynamics. Since the exact mechanism of diffusion through protein crystals (Geremia *et al.*, 2006) is difficult to

determine, the unknown parameters are tied up in the effective diffusion coefficient ( $D_{\text{eff}}$ ) determined here.

### 3.4. Reaction initiation by diffusion

CEF diffusion is about a factor of 12 slower in the BlaC crystals than in water, with a  $D_{\text{eff}}$  of about  $\sim 2 \times 10^{-7} \text{ cm}^2 \text{ s}^{-1}$  [Table 5(b)]. This slowdown is in agreement with findings that were previously obtained from simulations on substrate diffusion in enzyme crystals (Geremia *et al.*, 2006). Estimates of enzyme–ligand occupancies can now be directly deduced from time-resolved X-ray crystallography everywhere in a crystal after mixing. Not surprisingly, at 5 ms the occupancy is high (>90%) only near the crystal surface [Fig. 8(a)], where sufficient substrate is present to promote ES formation at a high rate. In the center of the crystals the ES complex concentration is initially small [Table 5(c), Figs. 8(a) and 9(a)]. The binding rate is not sufficiently high to generate significant occupancy. After  $\Delta t_m = 10 \text{ ms}$  the binding rate increases, until at 30 ms full occupancy of the BlaC–CEF complex is reached everywhere (Olmos *et al.*, 2018) [Fig. 6(b), green dashed line, Table 5(c)]. With the rapid diffusion of CEF into small BlaC crystals, we are now able to quantify variations of substrate, enzyme and ES concentrations across the enzyme crystal volume at any time [Table 5(c), Figs. 8 and 9]. The remarkable speed of ES accumulation shows that the mix-and-inject technique can be used to characterize enzymes with turnover times much faster than that of BlaC. The direct observation of the important initial ligand- and substrate-binding phase in biomedically relevant enzymes is possible at the EuXFEL.

Since the ES complex (here the BlaC–CEF complex) triggers the enzymatic cycle, accurate kinetics can be extracted to the point where the time required to accumulate sufficient ES

complex approaches the lifetime of the next intermediate in the catalytic cycle (Schmidt, 2013). This finding holds for any other technique (Šrajer & Schmidt, 2017) which aims to trigger enzymatic reactions, even in noncrystalline samples. Not only is it required to bring sufficient substrate into the vicinity of the enzyme, but the binding kinetics also need to be taken into account. With microcrystals below a certain crystal size, the binding of substrate, and not the diffusion of substrate into the crystal volume, may become rate-limiting. As a consequence, for BlaC crystals of a size of about 1  $\mu\text{m}$  the speed of ES complex formation is not substantially different from that in solution. The  $D_{\text{eff}}$  determined here suggests that accurate measurements of the substrate-binding kinetics would not be possible with significantly larger crystals. Enzymes with turnover times faster than that of BlaC will usually also display faster substrate-binding kinetics with larger  $k_{\text{on}}$  rate coefficients. In such cases, the crystal sizes (and their size distributions) or perhaps the temperature must be adjusted appropriately to ensure that the diffusion times can catch up with the substrate-binding rates.

Diffusion is an effective way to initiate reactions. Given a sufficient substrate concentration, and appropriately small crystals, all of the crystal volume is already infused with a multiple of the stoichiometric substrate concentration after a few milliseconds [Table 5(c)]. This is very important for fast reaction initiation since the rate (speed) of enzyme–substrate complex formation, and therefore the time resolution of the method, depends decisively, and primarily, on the concentration of the substrate, and of course also on the free enzyme concentration and the kinetic rate coefficients. Others (Mehrabi, Schulz, Dsouza *et al.*, 2019) have reported significant substrate occupancy in the active site only 30 ms after the activation of a caged substrate that is even located close by. This slow occupancy increase may be a result of (sub-)stoichiometric substrate concentrations in the unit cell, which strengthens our point of view. BlaC is not a fast enzyme. Apart from the possibility of investigating the initial substrate-

binding phase(s) potentially on submillisecond timescales, the benefits of XFEL-based mix-and-inject approaches may come to light once faster enzymes with turnover times of  $<50$  ms are investigated. These experiments require small crystals. Exploration of how to investigate these small crystals using either XFELs or synchrotrons, perhaps after upgrade to an advanced accelerator lattice (Eriksson, 2016; Wanzenberg *et al.*, 2019), remains to be performed.

#### 4. Outlook

In order to further investigate CEF and SUB binding and their reactions with Ser70, a time series should be collected that consists of data sets at multiple  $\Delta t_m$  values that span from a few milliseconds to seconds. To achieve this, the EuXFEL pulse structure must be exploited most efficiently. Every X-ray pulse in all pulse trains provides observations of the same time delay, and our experiments took maximum advantage of the high pulse rate (Fig. 2, inset). This is in contrast to optical pump–X-ray probe experiments, which require appropriate waiting times between laser excitations to guarantee that the laser-excited volume exits the X-ray interaction region, so that multiple laser activations can be avoided (Pandey *et al.*, 2020). We showed that diffraction data sufficient for good-quality structure determination can be collected in about half an hour, as demonstrated for the 50 ms CEF time point. This time can be reduced substantially by limiting the number of diffraction patterns per data set (around 25 000 is appropriate for this space group; Olmos *et al.*, 2018) and by optimizing the crystal density that flows through the mixing device. High crystal density will lead to higher hit rates, but might also cause frequent interruptions caused by injector clogging. In our experiments, a fine balance between crystal size and crystal density was found so that the mix-and-inject experiments with CEF and SUB could be completed successfully with acceptable hit rates (Table 1) given the high X-ray pulse-repetition rate at the EuXFEL. Previous experiments have shown that

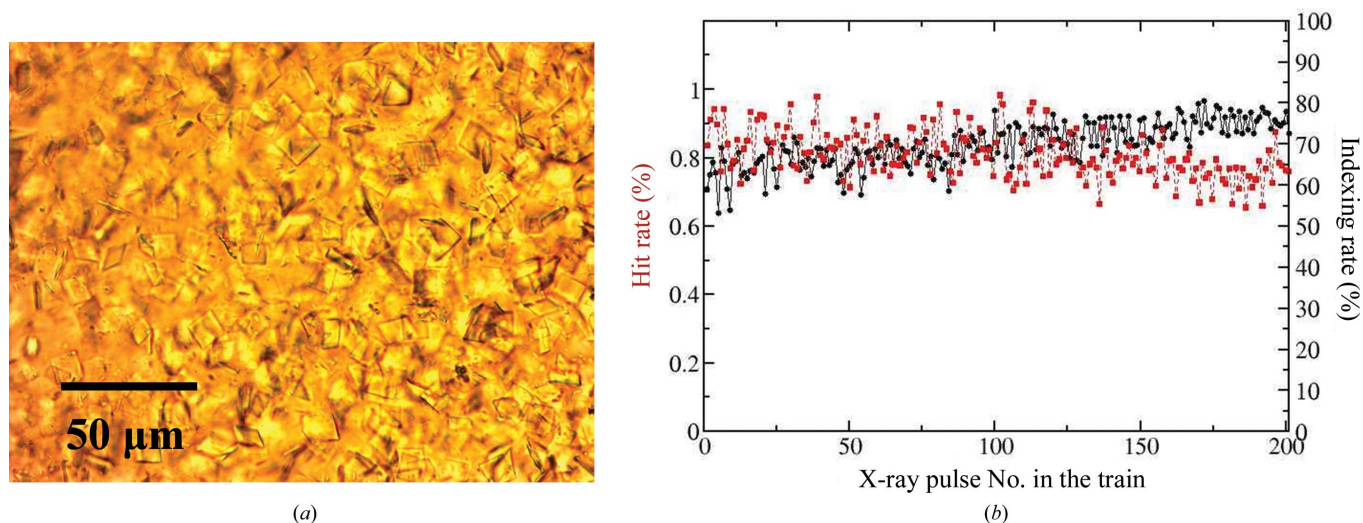


**Figure 10** Crystals, hit and indexing rates. (a) Microscopic image of the platelet crystal form of BlaC and (b) exemplary hit (red squares) and indexing (black spheres) rates from BlaC/CEF mixing as a function of the pulse ID in the train. Both rates are stable across the entire pulse train.

the collection of sufficient patterns for structure determination should be possible in less than 20 min at the detector-limited repetition rate of the EuXFEL (Yefanov *et al.*, 2019; Pandey *et al.*, 2020). This provides the tantalizing possibility of directly characterizing kinetic processes in biomolecules from single-digit millisecond to longer timescales within relatively short experimental times. The kinetics can rapidly change when environmental conditions are varied. It may be possible, for example, to control the temperature in the mixing injector delay line to determine barriers of activation from the resulting X-ray data (Schmidt *et al.*, 2013). The full analysis of such a multidimensional data set requires the development and deployment of user-friendly classification algorithms to separate mixtures into their pure components (Schmidt *et al.*, 2003) and to derive kinetics and energetics (Schmidt *et al.*, 2013) consistent with the electron-density maps and the structures of intermediate states along the reaction pathway.

## 5. Summary

Our experiments permitted a real-time view into the active sites of an enzyme during substrate binding. They facilitate more mix-and-inject experiments at the EuXFEL with unprecedented data-collection rates, allowing more structures to be determined per allocated experimental time. This capability will become an important tool for biomedically relevant research in years to come.

## APPENDIX A Microcrystals and data collection

Fig. 10(a) shows a microscopic image of the BlaC platelets used for the experiments. They appear to be uniform in size and shape. In Fig. 10(b) the hit and indexing rates achieved with these crystals in our MISC experiments are displayed across all of the pulses in the pulse train of the EuXFEL. A decay in the hit rate following pulse 1 is not observed. This is an indication that the jet is fast enough that a fresh jet volume is intercepted by the following X-ray pulses (Wiedorn, Oberthür *et al.*, 2018; Yefanov *et al.*, 2019; Pandey *et al.*, 2020).

## APPENDIX B Diffraction patterns and masks

The ability to mask out detector pixels and other parts of the diffraction pattern (Fig. 11) is important for the successful identification of DP-containing Bragg reflections (hits) from the stream of detector images (Wiedorn, Oberthür *et al.*, 2018; Carrillo *et al.*, 2021). Only peaks [blue squares in Figs. 11(a) and 11(b)] outside the mask are found. In the hit-finder *Cheetah* (Barty *et al.*, 2014) a convenient masking tool is available that facilitates the exclusion of any part of the detector image. The central 'hole' and the gaps (except for the tile edges) do not need to be masked since the detector geometry is known.

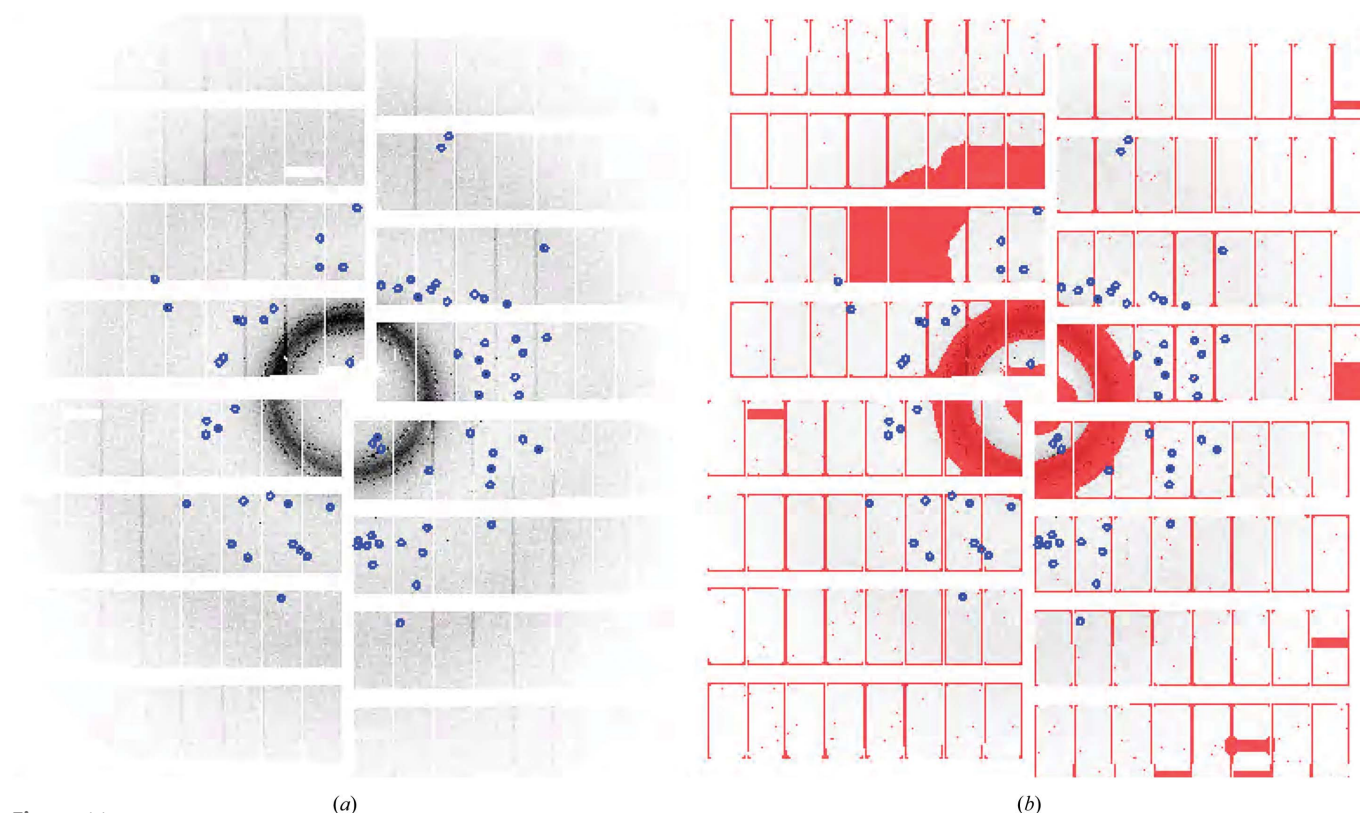


Figure 11

(a) Example of a diffraction pattern collected by the AGIPD. In (b) a mask (in red) is superposed that covers the strong rings at low resolution and inactive detector areas.

## Acknowledgements

We are very grateful to those who supported this experiment by being present in person at the European XFEL during the onset of the COVID-19 pandemic in March 2020. We acknowledge the European XFEL in Schenefeld, Germany for the provision of X-ray free-electron laser beamtime on the SPB/SFX scientific instrument and would like to thank the staff for their assistance. We acknowledge the use of the XBI facility at the European XFEL. The SFX stream files were deposited in the CXIDB with code 170. Individual contributions were as follows. SP, TM, JM-G, JH-Y, FK, IP, MM, RJ, MS, WX and JO expressed, purified and crystallized the protein. RB, KD, HK, MK, JK, GM, TS and MV operated the SPB/SFX instrument. LP, AMK, GC and KAZ designed and provided injector nozzles. MV, FK and MK assembled and operated the nozzles. FK, JM-G, J-HY, LG and PS collected the data. SP, IP, OY, VM, PS, AT and AB processed the data. SP, IP, TM, GP and MS analyzed the data. IP, MF, AS, FK, PS and MS logged the experiment. RB, APM, MS and GP designed the experiment. SP, PF, APM, RB, GP and MS wrote the manuscript with input from all other authors.

## Funding information

This work was supported by the National Science Foundation Science and Technology Center 'BioXFEL' through award STC-1231306, and in part by the US Department of Energy, Office of Science, Basic Energy Sciences under contract DE-SC0002164 (AO, algorithm design and development) and by the National Science Foundation under contract Nos. 1551489 (AO, underlying analytical models) and DBI-2029533 (AO, functional conformations). This material is based upon work supported by the National Science Foundation Graduate Research Fellowship Program under Grant No. 1450681 to JLO. The work was also supported by funds from the National Institutes of Health grant R01 GM117342-0404. Funding and support are also acknowledged from the National Institutes of Health grant R01 GM095583, from the Biodesign Center for Applied Structural Discovery at ASU, from National Science Foundation award No. 1565180 and the US Department of Energy through Lawrence Livermore National Laboratory under contract DE-AC52-07NA27344. KAZ was supported by the Cornell Molecular Biophysics Training Program (NIH T32-GM008267). This work was also supported by the Cluster of Excellence 'CUI: Advanced Imaging of Matter' of the Deutsche Forschungsgemeinschaft (DFG), EXC 2056, project ID 390715994. CFEL is supported by the Gottfried Wilhelm Leibniz Program of the DFG, the 'X-probe' project funded by the European Union 2020 Research and Innovation Program under Marie Skłodowska-Curie grant agreement 637295, the European Research Council, 'Frontiers in Attosecond X-ray Science: Imaging and Spectroscopy (AXSIS)', ERC-2013-SyG 609920, and the Human Frontiers Science Program grant RGP0010 2017. This work is also supported by the AXSIS project funded by the European Research Council under the European Union Seventh Framework Program (FP/2007-2013)/ERC Grant Agreement No. 609920.

## References

- Allahgholi, A., Becker, J., Delfs, A., Dinapoli, R., Goettlicher, P., Greiffenberg, D., Henrich, B., Hirsemann, H., Kuhn, M., Klanner, R., Klyuev, A., Krueger, H., Lange, S., Laurus, T., Marras, A., Mezza, D., Mozzanica, A., Niemann, M., Poehlsen, J., Schwandt, J., Sheviakov, I., Shi, X., Smoljanin, S., Steffen, L., Sztuk-Dambietz, J., Trunk, U., Xia, Q., Zeribi, M., Zhang, J., Zimmer, M., Schmitt, B. & Graafsma, H. (2019). *J. Synchrotron Rad.* **26**, 74–82.
- Barends, T. R. M., Foucar, L., Ardevol, A., Nass, K., Aquila, A., Botha, S., Doak, R. B., Falahati, K., Hartmann, E., Hilpert, M., Heinz, M., Hoffmann, M. C., Kofinger, J., Koglin, J. E., Kovacsova, G., Liang, M., Milathianaki, D., Lemke, H. T., Reinstein, J., Roome, C. M., Shoeman, R. L., Williams, G. J., Burghardt, I., Hummer, G., Boutet, S. & Schlichting, I. (2015). *Science*, **350**, 445–450.
- Barty, A., Kirian, R. A., Maia, F. R. N. C., Hantke, M., Yoon, C. H., White, T. A. & Chapman, H. (2014). *J. Appl. Cryst.* **47**, 1118–1131.
- Berman, H. M., Battistuz, T., Bhat, T. N., Bluhm, W. F., Bourne, P. E., Burkhardt, K., Feng, Z., Gilliland, G. L., Iype, L., Jain, S., Fagan, P., Marvin, J., Padilla, D., Ravichandran, V., Schneider, B., Thanki, N., Weissig, H., Westbrook, J. D. & Zardecki, C. (2002). *Acta Cryst.* **D58**, 899–907.
- Boutet, S., Lomb, L., Williams, G. J., Barends, T. R., Aquila, A., Doak, R. B., Weierstall, U., DePonte, D. P., Steinbrener, J., Shoeman, R. L., Messerschmidt, M., Barty, A., White, T. A., Kassemeyer, S., Kirian, R. A., Seibert, M. M., Montanez, P. A., Kenney, C., Herbst, R., Hart, P., Pines, J., Haller, G., Gruner, S. M., Philipp, H. T., Tate, M. W., Hromalik, M., Koerner, L. J., van Bakel, N., Morse, J., Ghonsalves, W., Arnlund, D., Bogan, M. J., Caleman, C., Fromme, R., Hampton, C. Y., Hunter, M. S., Johansson, L. C., Katona, G., Kupitz, C., Liang, M., Martin, A. V., Nass, K., Redecke, L., Stellato, F., Timneanu, N., Wang, D., Zatsepin, N. A., Schafer, D., DeFever, J., Neutze, R., Fromme, P., Spence, J. C. H., Chapman, H. N. & Schlichting, I. (2012). *Science*, **337**, 362–364.
- Boyd, D. B. & Lunn, W. H. (1979). *J. Med. Chem.* **22**, 778–784.
- Calvey, G. D., Katz, A. M. & Pollack, L. (2019). *Anal. Chem.* **91**, 7139–7144.
- Carrillo, M., Pandey, S., Sanchez, J., Noda, M., Poudyal, I., Aldama, L., Malla, T. N., Claesson, E., Wahlgren, W. Y., Feliz, D., Šrajcar, V., Maj, M., Castillon, L., Iwata, S., Nango, E., Tanaka, R., Tanaka, T., Fangjia, L., Tono, K., Owada, S., Westenhoff, S., Stojković, E. A. & Schmidt, M. (2021). *Structure*, **29**, 743–754.
- Carlsaw, H. S. & Jaeger, J. C. (1959). *Conduction Heat in Solids*, 2nd ed. Oxford: Clarendon Press.
- Cassini, A., Högberg, L. D., Plachouras, D., Quattrocchi, A., Hoxha, A., Simonsen, G. S., Colomb-Cotinat, M., Kretschmar, M. E., Devleeschauwer, B., Cecchini, M., Ouakrim, D. A., Oliveira, T. C., Struelens, M. J., Suetens, C., Monnet, D. L., Strauss, R., Mertens, K., Struyf, T., Catry, B., Latour, K., Ivanov, I. N., Dobreva, E. G., Tambic-Andrašević, A., Soprek, S., Budimir, A., Paphitou, N., Žemlicková, H., Schytte Olsen, S., Wolff Sönksen, U., Märtin, P., Ivanova, M., Lyytikäinen, O., Jalava, J., Coignard, B., Eckmanns, T., Abu Sin, M., Haller, S., Daikos, G. L., Gikas, A., Tsiodras, S., Kontopidou, F., Tóth, Á., Hajdu, Á., Guólaugsson, Ó., Kristinsson, K. G., Murchan, S., Burns, K., Pezzotti, P., Gagliotti, C., Dumpis, U., Liuimiene, A., Perrin, M., Borg, M. A., de Greeff, S. C., Monen, J. C., Koek, M. B., Elstrøm, P., Zabička, D., Deptula, A., Hryniewicz, W., Caniça, M., Nogueira, P. J., Fernandes, P. A., Managairo, V., Popescu, G. A., Serban, R. I., Schréterová, E., Litvová, S., Štefkovicová, M., Kolman, J., Klavs, I., Korošec, A., Aracil, B., Asensio, A., Pérez-Vázquez, M., Billström, H., Larsson, S., Reilly, J. S., Johnson, A. & Hopkins, S. (2019). *Lancet Infect. Dis.* **19**, 56–66.
- Changeux, J.-P. & Edelstein, S. (2011). *F1000 Biol. Rep.* **3**, 19.
- Chapman, H. N., Fromme, P., Barty, A., White, T. A., Kirian, R. A., Aquila, A., Hunter, M. S., Schulz, J., DePonte, D. P., Weierstall, U., Doak, R. B., Maia, F. R. N. C., Martin, A. V., Schlichting, I., Lomb, L., Coppola, N., Shoeman, R. L., Epp, S. W., Hartmann, R., Rolles,

- D., Rudenko, A., Foucar, L., Kimmel, N., Weidenspointner, G., Holl, P., Liang, M., Barthelmess, M., Caleman, C., Boutet, S., Bogan, M. J., Krzywinski, J., Bostedt, C., Bajt, S., Gumprecht, L., Rudek, B., Erk, B., Schmidt, C., Hömke, A., Reich, C., Pietschner, D., Strüder, L., Hauser, G., Gorke, H., Ullrich, J., Herrmann, S., Schaller, G., Schopper, F., Soltau, H., Kühnel, K.-U., Messerschmidt, M., Bozek, J. D., Hau-Riege, S. P., Frank, M., Hampton, C. Y., Sierra, R. G., Starodub, D., Williams, G. J., Hajdu, J., Timneanu, N., Seibert, M. M., Andreasson, J., Rocker, A., Jönsson, O., Svenda, M., Stern, S., Nass, K., Andritschke, R., Schröter, C.-D., Krasniqi, F., Bott, M., Schmidt, K. E., Wang, X., Grotjohann, I., Holton, J. M., Barends, T. R. M., Neutze, R., Marchesini, S., Fromme, R., Schorb, S., Rupp, D., Adolph, M., Gorkhover, T., Andersson, I., Hirsemann, H., Potdevin, G., Graafsma, H., Nilsson, B. & Spence, J. C. H. (2011). *Nature*, **470**, 73–77.
- Cheng, Q., Xu, C., Chai, J., Zhang, R., Wai Chi Chan, E. & Chen, S. (2020). *ACS Infect. Dis.* **6**, 577–587.
- Coquelle, N., Sliwa, M., Woodhouse, J., Schirò, G., Adam, V., Aquila, A., Barends, T. R. M., Boutet, S., Byrdin, M., Carbajo, S., De la Mora, E., Doak, R. B., Feliks, M., Fieschi, F., Foucar, L., Guillon, V., Hilpert, M., Hunter, M. S., Jakobs, S., Koglin, J. E., Kovacsova, G., Lane, T. J., Lévy, B., Liang, M. N., Nass, K., Ridard, J., Robinson, J. S., Roome, C. M., Ruckebusch, C., Seaberg, M., Thepaut, M., Cammarata, M., Demachy, I., Field, M., Shoeman, R. L., Bourgeois, D., Colletier, J.-P., Schlichting, I. & Weik, M. (2018). *Nat. Chem.* **10**, 31–37.
- Dashti, A., Mashayekhi, G., Shekhar, M., Ben Hail, D., Salah, S., Schwander, P., des Georges, A., Singharoy, A., Frank, J. & Ourmazd, A. (2020). *Nat. Commun.* **11**, 4734.
- Decking, W., Abeghyan, S., Abramian, P., Abramsky, A., Aguirre, A., Albrecht, C., Alou, P., Altarelli, M., Altmann, P., Amyan, K., Anashin, V., Apostolov, E., Appel, K., Auguste, D., Ayvazyan, V., Baark, S., Babies, F., Baboi, N., Bak, P., Balandin, V., Baldinger, R., Baranasic, B., Barbanotti, S., Belikov, O., Belokurov, V., Belova, L., Belyakov, V., Berry, S., Bertucci, M., Beutner, B., Block, A., Blocher, M., Bockmann, T., Bohm, C., Bohnert, M., Bondar, V., Bondarchuk, E., Bonezzi, M., Borowiec, P., Bosch, C., Bosenberg, U., Bosotti, A., Bospflug, R., Bousonville, M., Boyd, E., Bozhko, Y., Brand, A., Branlard, J., Briechle, S., Brinker, F., Brinker, S., Brinkmann, R., Brockhauser, S., Brovko, O., Bruck, H., Brudgam, A., Butkowski, L., Buttner, T., Calero, J., Castro-Carballo, E., Cattalanotto, G., Charrier, J., Chen, J., Cherepenko, A., Cheskidov, V., Chiodini, M., Chong, A., Choroba, S., Chorowski, M., Churanov, D., Cichalewski, W., Clausen, M., Clement, W., Cloue, C., Cobos, J. A., Coppola, N., Cunis, S., Czuba, K., Czwalińska, M., D'Almagne, B., Dammann, J., Danared, H., Wagner, A. D., Delfs, A., Delfs, T., Dietrich, F., Dietrich, T., Dohlus, M., Dommach, M., Donat, A., Dong, X., Doynikov, N., Dressel, M., Duda, M., Duda, P., Eckoldt, H., Ehsan, W., Eidam, J., Eints, F., Engling, C., English, U., Ermakov, A., Escherich, K., Eschke, J., Saldin, E., Faesing, M., Fallou, A., Felber, M., Fenner, M., Fernandes, B., Fernandez, J. M., Feuker, S., Filippakopoulos, K., Floettmann, K., Fogel, V., Fontaine, M., Frances, A., Martin, I. F., Freund, W., Freyermuth, T., Friedland, M., Frohlich, L., Fusetti, M., Fydrych, J., Gallas, A., Garcia, O., Garcia-Tabares, L., Geloni, G., Gerasimova, N., Gerth, C., Gessler, P., Gharibyan, V., Gloor, M., Glowinkowski, J., Goessel, A., Golebiewski, Z., Golubeva, N., Grabowski, W., Graeff, W., Grebentsov, A., Grecki, M., Grevsmuehl, T., Gross, M., Grosse-Wortmann, U., Grunert, J., Grunewald, S., Grzegory, P., Feng, G., Guler, H., Gusev, G., Gutierrez, J. L., Hage, L., Hamberg, M., Hanneken, R., Harms, E., Hartl, I., Hauberg, A., Hauf, S., Hauschildt, J., Hauser, J., Havlicek, J., Hedqvist, A., Heidbrook, N., Hellberg, F., Henning, D., Hensler, O., Hermann, T., Hidvegi, A., Hierholzer, M., Hintz, H., Hoffmann, F., Hoffmann, M., Hoffmann, M., Holler, Y., Huning, M., Ignatenko, A., Ilchen, M., Iluk, A., Iversen, J., Iversen, J., Izquierdo, M., Jachmann, L., Jardon, N., Jastrow, U., Jensch, K., Jensen, J., Dotabek, M. J. O., Jidda, M., Jin, H., Johansson, N., Jonas, R., Kaabi, W., Kaefer, D., Kammering, R., Kapitzka, H., Karabekyan, S., Karstensen, S., Kasprzak, K., Katalev, V., Keese, D., Keil, B., Kholopov, M., Killenberger, M., Kitaev, B., Klimchenko, Y., Klos, R., Knebel, L., Koch, A., Koepke, M., Kohler, S., Kohler, W., Kohlstrunk, N., Konopkova, Z., Konstantinov, A., Kook, W., Koprek, W., Korfer, M., Korth, O., Kosarev, A., Kosinski, K., Kostin, D., Kot, Y., Kotarba, A., Kozak, T., Kozak, V., Kramert, R., Krasilnikov, M., Krasnov, A., Krause, B., Kravchuk, L., Krebs, O., Kretschmer, R., Kreutzkamp, J., Kroplin, O., Krzysik, K., Kube, G., Kuehn, H., Kujala, N., Kulikov, V., Kuzminych, V., La Civita, D., Lacroix, M., Lamb, T., Lancetov, A., Larsson, M., Le Pinvidic, D., Lederer, S., Lensch, T., Lenz, D., Leuschner, A., Levenhagen, F., Li, Y., Liebing, J., Lilje, L., Limberg, T., Lipka, D., List, B., Liu, J., Liu, S., Lorbeer, B., Lorkiewicz, J., Lu, H. H., Ludwig, F., Machau, K., Maciocha, W., Madec, C., Magueur, C., Maiano, C., Maksimova, I., Malcher, K., Maltezosopoulos, T., Mamoshkina, E., Manschwetus, B., Marcellini, F., Marinkovic, G., Martinez, T., Martirosyan, H., Maschmann, W., Maslov, M., Matheisen, A., Mavric, U., Meissner, J., Meissner, K., Messerschmidt, M., Meyners, N., Michalski, G., Michelato, P., Mildner, N., Moe, M., Moglia, F., Mohr, C., Mohr, S., Moller, W., Mommerz, M., Monaco, L., Montiel, C., Moretti, M., Morozov, I., Morozov, P., Mross, D., Mueller, J., Muller, C., Muller, J., Muller, K., Munilla, J., Munnich, A., Muratov, V., Napoly, O., Naser, B., Nefedov, N., Neumann, R., Neumann, R., Ngada, N., Noelle, D., Obier, F., Okunev, I., Oliver, J. A., Omet, M., Oppelt, A., Ottmar, A., Oublaid, M., Pagani, C., Paparella, R., Paramonov, V., Peitzmann, C., Penning, J., Perus, A., Peters, F., Petersen, B., Petrov, A., Petrov, I., Pfeiffer, S., Pfluger, J., Philipp, S., Pienaud, Y., Pierini, P., Pivovarov, S., Planas, M., Plawski, E., Pohl, M., Polinski, J., Popov, V., Prat, S., Prenting, J., Priebe, G., Pryscheleski, H., Przygoda, K., Pyata, E., Racky, B., Rathjen, A., Ratuschni, W., Regnaud-Camperdos, S., Rehlich, K., Reschke, D., Robson, C., Roever, J., Roggli, M., Rothenburg, J., Rusinski, E., Rybaniec, R., Sahling, H., Salmani, M., Samoylova, L., Sanzone, D., Saretzki, F., Sawlanski, O., Schaffran, J., Schlarb, H., Schlosser, M., Schlott, V., Schmidt, C., Schmidt-Foehre, F., Schmitz, M., Schmokel, M., Schnautz, T., Schneidmiller, E., Scholz, M., Schoneburg, B., Schultze, J., Schulz, C., Schwarz, A., Sekutowicz, J., Sellmann, D., Semenov, E., Serkez, S., Sertore, D., Shehzad, N., Shemarykin, P., Shi, L., Sienkiewicz, M., Sikora, D., Sikorski, M., Silenzi, A., Simon, C., Singer, W., Singer, X., Sinn, H., Sinram, K., Skvorodnev, N., Smirnow, P., Sommer, T., Sorokin, A., Stadler, M., Steckel, M., Steffen, B., Steinhau-Kuhl, N., Stephan, F., Stodulski, M., Stolper, M., Sulimov, A., Susen, R., Swierblewski, J., Sydlo, C., Syresin, E., Sytchev, V., Szuba, J., Tesch, N., Thie, J., Thiebault, A., Tiedtke, K., Tischhauser, D., Tolkiehn, J., Tomin, S., Tonisch, F., Toral, F., Torbin, I., Trapp, A., Treyer, D., Trowitzsch, G., Trublet, T., Tschentscher, T., Ullrich, F., Vannoni, M., Varela, P., Varghese, G., Vashchenko, G., Vasic, M., Vazquez-Velez, C., Verguet, A., Vilcins-Czvitkovits, S., Villanueva, R., Visentin, B., Viti, M., Vogel, E., Volobuev, E., Wagner, R., Walker, N., Wamsat, T., Weddig, H., Weichert, G., Weise, H., Wenndorf, R., Werner, M., Wichmann, R., Wiebers, C., Wienczek, M., Wilksen, T., Will, I., Winkelmann, L., Winkowski, M., Wittenburg, K., Witzig, A., Wlk, P., Wohlenberg, T., Wojciechowski, M., Wolff-Fabris, F., Wrochna, G., Wrona, K., Yakopov, M., Yang, B., Yang, F., Yurkov, M., Zagorodnov, I., Zalden, P., Zavadtsev, A., Zavadtsev, D., Zhirnov, A., Zhukov, A., Ziemann, V., Zolotov, A., Zolotukhina, N., Zummack, F. & Zybin, D. (2020). *Nat. Photonics*, **14**, 391–397.
- Dods, R., Báth, P., Morozov, D., Gagnér, V. A., Arnlund, D., Luk, H. L., Kübel, J., Maj, M., Vallejos, A., Wickstrand, C., Bosman, R., Beyerlein, K. R., Nelson, G., Liang, M. N., Milathianaki, D., Robinson, J., Harimoorthy, R., Berntsen, P., Malmerberg, E., Johansson, L., Andersson, R., Carbajo, S., Claesson, E., Conrad, C. E., Dahl, P., Hammarin, G., Hunter, M. S., Li, C. F., Lisova, S., Royant, A., Safari, C., Sharma, A., Williams, G. J., Yefanov, O., Westenhoff, S., Davidsson, J., DePonte, D. P., Boutet, S., Barty, A., Katona, G., Groenhof, G., Brändén, G. & Neutze, R. (2021). *Nature*, **589**, 310–314.

- Eriksson, M. (2016). *AIP Conf. Proc.* **1741**, 020001.
- Fair, R. J. & Tor, Y. (2014). *Perspect. Medicin. Chem.* **6**, PMC.S14459.
- Geremia, S., Campagnolo, M., Demitri, N. & Johnson, L. N. (2006). *Structure*, **14**, 393–400.
- Gevorkov, Y., Yefanov, O., Barty, A., White, T. A., Mariani, V., Brehm, W., Tolstikova, A., Grigat, R.-R. & Chapman, H. N. (2019). *Acta Cryst.* **A75**, 694–704.
- Gourinchas, G., Etlz, S., Göbl, C., Vide, U., Madl, T. & Winkler, A. (2017). *Sci. Adv.* **3**, e1602498.
- Grünbein, M. L., Gorel, A., Foucar, L., Carbajo, S., Colocho, W., Gilevich, S., Hartmann, E., Hilpert, M., Hunter, M., Kloos, M., Koglin, J. E., Lane, T. J., Lewandowski, J., Lutman, A., Nass, K., Nass Kovacs, G., Roome, C. M., Sheppard, J., Shoeman, R. L., Stricker, M., van Driel, T., Vetter, S., Doak, R. B., Boutet, S., Aquila, A., Decker, F. J., Barends, T. R. M., Stan, C. A. & Schlichting, I. (2021). *Nat. Commun.* **12**, 1672.
- Han, H., Round, E., Schubert, R., Gül, Y., Makroczyová, J., Meza, D., Heuser, P., Aepfelbacher, M., Barák, I., Betzel, C., Fromme, P., Kursula, I., Nissen, P., Tereschenko, E., Schulz, J., Uetrecht, C., Ulicný, J., Wilmanns, M., Hajdu, J., Lamzin, V. S. & Lorenzen, K. (2021). *J. Appl. Cryst.* **54**, 7–21.
- Hartmann, N., Helml, W., Galler, A., Bionta, M. R., Grünert, J. L., Molodtsov, S., Ferguson, K. R., Schorb, S., Swiggers, M. L., Carron, S., Bostedt, C., Castagna, J., Bozek, J., Glowina, J. M., Kane, D. J., Fry, A. R., White, W. E., Hauri, C. P., Feurer, T. & Coffee, R. N. (2014). *Nat. Photonics*, **8**, 706–709.
- Holtorf, H., Reinbothe, S., Reinbothe, C., Bereza, B. & Apel, K. (1995). *Proc. Natl Acad. Sci. USA*, **92**, 3254–3258.
- Hugonnet, J. E. & Blanchard, J. S. (2007). *Biochemistry*, **46**, 11998–12004.
- Imming, P., Sinning, C. & Meyer, A. (2006). *Nat. Rev. Drug Discov.* **5**, 821–834.
- Ishigami, I., Lewis-Ballester, A., Echelmeier, A., Brehm, G., Zatsepin, N. A., Grant, T. D., Coe, J. D., Lisova, S., Nelson, G., Zhang, S., Dobson, Z. F., Boutet, S., Sierra, R. G., Batyuk, A., Fromme, P., Fromme, R., Spence, J. C. H., Ros, A., Yeh, S. R. & Rousseau, D. L. (2019). *Proc. Natl Acad. Sci. USA*, **116**, 3572–3577.
- Jeffrey, G. A. (1997). *An Introduction to Hydrogen Bonding*. Oxford University Press.
- Kern, J., Chatterjee, R., Young, I. D., Fuller, F. D., Lassalle, L., Ibrahim, M., Gul, S., Fransson, T., Brewster, A. S., Alonso-Mori, R., Hussein, R., Zhang, M., Douthit, L., de Lichtenberg, C., Cheah, M. H., Shevela, D., Wersig, J., Seuffert, I., Sokaras, D., Pastor, E., Weninger, C., Kroll, T., Sierra, R. G., Aller, P., Butryn, A., Orville, A. M., Liang, M., Batyuk, A., Koglin, J. E., Carbajo, S., Boutet, S., Moriarty, N. W., Holton, J. M., Dobbek, H., Adams, P. D., Bergmann, U., Sauter, N. K., Zouni, A., Messinger, J., Yano, J. & Yachandra, V. K. (2018). *Nature*, **563**, 421–425.
- Kostov, K. S. & Moffat, K. (2011). *Biophys. J.* **100**, 440–449.
- Kupitz, C., Basu, S., Grotjohann, I., Fromme, R., Zatsepin, N. A., Rendek, K. N., Hunter, M. S., Shoeman, R. L., White, T. A., Wang, D., James, D., Yang, J.-H., Cobb, D. E., Reeder, B., Sierra, R. G., Liu, H., Barty, A., Aquila, A. L., DePonte, D., Kirian, R. A., Bari, S., Bergkamp, J. J., Beyerlein, K. R., Bogan, M. J., Coleman, C., Chao, T.-C., Conrad, C. E., Davis, K. M., Fleckenstein, H., Galli, L., Hau-Riege, S. P., Kassemeyer, S., Laksmono, H., Liang, M., Lomb, L., Marchesini, S., Martin, A. V., Messerschmidt, M., Milathianaki, D., Nass, K., Ros, A., Roy-Chowdhury, S., Schmidt, K., Seibert, M., Steinbrener, J., Stellato, F., Yan, L., Yoon, C., Moore, T. A., Moore, A. L., Pushkar, Y., Williams, G. J., Boutet, S., Doak, R. B., Weierstall, U., Frank, M., Chapman, H. N., Spence, J. C. H. & Fromme, P. (2014). *Nature*, **513**, 261–265.
- Kupitz, C., Olmos, J. L. Jr, Holl, M., Tremblay, L., Pande, K., Pandey, S., Oberthür, D., Hunter, M., Liang, M., Aquila, A., Tenboer, J., Calvey, G., Katz, A., Chen, Y., Wiedorn, M. O., Knoska, J., Meents, A., Majriani, V., Norwood, T., Poudyal, I., Grant, T., Miller, M. D., Xu, W., Tolstikova, A., Morgan, A., Metz, M., Martin-Garcia, J. M., Zook, J. D., Roy-Chowdhury, S., Coe, J., Nagaratnam, N., Meza, D., Fromme, R., Basu, S., Frank, M., White, T., Barty, A., Bajt, S., Yefanov, O., Chapman, H. N., Zatsepin, N., Nelson, G., Weierstall, U., Spence, J., Schwander, P., Pollack, L., Fromme, P., Ourmazd, A., Phillips, G. N. Jr & Schmidt, M. (2017). *Struct. Dyn.* **4**, 044003.
- Li, J., Liu, Z., Tan, C., Guo, X., Wang, L., Sancar, A. & Zhong, D. (2010). *Nature*, **466**, 887–890.
- Liebschner, D., Afonine, P. V., Baker, M. L., Bunkóczi, G., Chen, V. B., Croll, T. I., Hintze, B., Hung, L.-W., Jain, S., McCoy, A. J., Moriarty, N. W., Oeffner, R. D., Poon, B. K., Prisant, M. G., Read, R. J., Richardson, J. S., Richardson, D. C., Sammito, M. D., Sobolev, O. V., Stockwell, D. H., Terwilliger, T. C., Urzhumtsev, A. G., Videau, L. L., Williams, C. J. & Adams, P. D. (2019). *Acta Cryst.* **D75**, 861–877.
- Liebschner, D., Afonine, P. V., Moriarty, N. W., Poon, B. K., Sobolev, O. V., Terwilliger, T. C. & Adams, P. D. (2017). *Acta Cryst.* **D73**, 148–157.
- Lomb, L., Barends, T. R. M., Kassemeyer, S., Aquila, A., Epp, S. W., Erk, B., Foucar, L., Hartmann, R., Rudek, B., Rolles, D., Rudenko, A., Shoeman, R. L., Andreasson, J., Bajt, S., Barthelmess, M., Barty, A., Bogan, M. J., Bostedt, C., Bozek, J. D., Coleman, C., Coffee, R., Coppola, N., DePonte, D. P., Doak, R. B., Ekeberg, T., Fleckenstein, H., Fromme, P., Gebhardt, M., Graafsma, H., Gumprecht, L., Hampton, C. Y., Hartmann, A., Hauser, G., Hirsemann, H., Holl, P., Holton, J. M., Hunter, M. S., Kabsch, W., Kimmel, N., Kirian, R. A., Liang, M., Maia, F. R. N. C., Meinhart, A., Marchesini, S., Martin, A. V., Nass, K., Reich, C., Schulz, J., Seibert, M. M., Sierra, R., Soltau, H., Spence, J. C. H., Steinbrener, J., Stellato, F., Stern, S., Timneanu, N., Wang, X., Weidenspointner, G., Weierstall, U., White, T. A., Wunderer, C., Chapman, H. N., Ullrich, J., Strüder, L. & Schlichting, I. (2011). *Phys. Rev. B*, **84**, 214111.
- Mancuso, A. P., Aquila, A., Batchelor, L., Bean, R. J., Bielecki, J., Borchers, G., Doerner, K., Giewekemeyer, K., Graceffa, R., Kelsey, O. D., Kim, Y., Kirkwood, H. J., Legrand, A., Letrun, R., Manning, B., Lopez Morillo, L., Messerschmidt, M., Mills, G., Raabe, S., Reimers, N., Round, A., Sato, T., Schulz, J., Signe Takem, C., Sikorski, M., Stern, S., Thute, P., Vagović, P., Weinhausen, B. & Tschentscher, T. (2019). *J. Synchrotron Rad.* **26**, 660–676.
- Mariani, V., Morgan, A., Yoon, C. H., Lane, T. J., White, T. A., O’Grady, C., Kuhn, M., Aplin, S., Koglin, J., Barty, A. & Chapman, H. N. (2016). *J. Appl. Cryst.* **49**, 1073–1080.
- Mehrabi, P., Schulz, E. C., Agthe, M., Horrell, S., Bourenkov, G., von Stetten, D., Leimkohl, J. P., Schikora, H., Schneider, T. R., Pearson, A. R., Tellkamp, F. & Miller, R. J. D. (2019). *Nat. Methods*, **16**, 979–982.
- Mehrabi, P., Schulz, E. C., Dsouza, R., Müller-Werkmeister, H. M., Tellkamp, F., Miller, R. J. D. & Pai, E. F. (2019). *Science*, **365**, 1167–1170.
- Minor, W., Cymborowski, M., Otwinowski, Z. & Chruszcz, M. (2006). *Acta Cryst.* **D62**, 859–866.
- Moffat, K. (2001). *Chem. Rev.* **101**, 1569–1582.
- Murshudov, G. N., Skubák, P., Lebedev, A. A., Pannu, N. S., Steiner, R. A., Nicholls, R. A., Winn, M. D., Long, F. & Vagin, A. A. (2011). *Acta Cryst.* **D67**, 355–367.
- Nass, K. (2019). *Acta Cryst.* **D75**, 211–218.
- Neutze, R., Wouts, R., van der Spoel, D., Weckert, E. & Hajdu, J. (2000). *Nature*, **406**, 752–757.
- Nogly, P., Weinert, T., James, D., Carbajo, S., Ozerov, D., Furrer, A., Gashi, D., Borin, V., Skopintsev, P., Jaeger, K., Nass, K., Bãth, P., Bosman, R., Koglin, J., Seaberg, M., Lane, T., Kekilli, D., Brünle, S., Tanaka, T., Wu, W., Milne, C., White, T., Barty, A., Weierstall, U., Panneels, V., Nango, E., Iwata, S., Hunter, M., Schapiro, I., Schertler, G., Neutze, R. & Standfuss, J. (2018). *Science*, **361**, eaat0094.
- Olmos, J. L. Jr, Pandey, S., Martin-Garcia, J. M., Calvey, G., Katz, A., Knoska, J., Kupitz, C., Hunter, M. S., Liang, M., Oberthuer, D., Yefanov, O., Wiedorn, M., Heyman, M., Holl, M., Pande, K., Barty, A., Miller, M. D., Stern, S., Roy-Chowdhury, S., Coe, J., Nagaratnam, N., Zook, J., Verburg, J., Norwood, T., Poudyal, I.,

- Xu, D., Koglin, J., Seaberg, M. H., Zhao, Y., Bajt, S., Grant, T., Mariani, V., Nelson, G., Subramanian, G., Bae, E., Fromme, R., Fung, R., Schwander, P., Frank, M., White, T. A., Weierstall, U., Zatsepin, N., Spence, J., Fromme, P., Chapman, H. N., Pollack, L., Tremblay, L., Ourmazd, A., Phillips, G. N. Jr & Schmidt, M. (2018). *BMC Biol.* **16**, 59.
- Pande, K., Hutchison, C. D. M., Groenhof, G., Aquila, A., Robinson, J. S., Tenboer, J., Basu, S., Boutet, S., DePonte, D., Liang, M., White, T., Zatsepin, N., Yefanov, O., Morozov, D., Oberthuer, D., Gati, C., Subramanian, G., James, D., Zhao, Y., Koralek, J., Brayshaw, J., Kupitz, C., Conrad, C., Roy-Chowdhury, S., Coe, J. D., Metz, M., Xavier, P. L., Grant, T. D., Koglin, J. E., Ketawala, G., Fromme, R., Šrajer, V., Henning, R., Spence, J. C. H., Ourmazd, A., Schwander, P., Weierstall, U., Frank, M., Fromme, P., Barty, A., Chapman, H. N., Moffat, K., van Thor, J. J. & Schmidt, M. (2016). *Science*, **352**, 725–729.
- Pandey, S., Bean, R., Sato, T., Poudyal, I., Bielecki, J., Cruz Villarreal, J., Yefanov, O., Mariani, V., White, T. A., Kupitz, C., Hunter, M., Abdellatif, M. H., Bajt, S., Bondar, V., Echelmeier, A., Doppler, D., Emons, M., Frank, M., Fromme, R., Gevorkov, Y., Giovanetti, G., Jiang, M., Kim, D., Kim, Y., Kirkwood, H., Klimovskaia, A., Knoska, J., Koua, F. H. M., Letrun, R., Lisova, S., Maia, L., Mazalova, V., Meza, D., Michelat, T., Ourmazd, A., Palmer, G., Ramilli, M., Schubert, R., Schwander, P., Silenzi, A., Sztuk-Dambietz, J., Tolstikova, A., Chapman, H. N., Ros, A., Barty, A., Fromme, P., Mancuso, A. P. & Schmidt, M. (2020). *Nat. Methods*, **17**, 73–78.
- Ramakrishnan, S., Stagno, J. R., Conrad, C. E., Ding, J., Yu, P., Bhandari, Y. R., Lee, Y. T., Pauly, G., Yefanov, O., Wiedorn, M. O., Knoska, J., Oberthür, D., White, T. A., Barty, A., Mariani, V., Li, C., Brehm, W., Heinz, W. F., Magidson, V., Lockett, S., Hunter, M. S., Boutet, S., Zatsepin, N. A., Zuo, X., Grant, T. D., Pandey, S., Schmidt, M., Spence, J. C. H., Chapman, H. N. & Wang, Y.-X. (2021). *Nat. Commun.* **12**, 1762.
- Ren, Z., Perman, B., Šrajer, V., Teng, T.-Y., Pradervand, C., Bourgeois, D., Schotte, F., Ursby, T., Kort, R., Wulff, M. & Moffat, K. (2001). *Biochemistry*, **40**, 13788–13801.
- Schmidt, M. (2008). *Ultrashort Laser Pulses in Medicine and Biology*, edited by M. Braun, P. Gilch & W. Zinth, pp. 201–241. Berlin, Heidelberg, New York: Springer
- Schmidt, M. (2013). *Adv. Condens. Matter Phys.* **2013**, 1–10.
- Schmidt, M. (2020). *Crystals*, **10**, 116.
- Schmidt, M., Rajagopal, S., Ren, Z. & Moffat, K. (2003). *Biophys. J.* **84**, 2112–2129.
- Schmidt, M., Šrajer, V., Henning, R., Ihee, H., Purwar, N., Tenboer, J. & Tripathi, S. (2013). *Acta Cryst. D* **69**, 2534–2542.
- Skopintsev, P., Ehrenberg, D., Weinert, T., James, D., Kar, R. K., Johnson, P. J. M., Ozerov, D., Furrer, A., Martiel, I., Dworkowski, F., Nass, K., Knopp, G., Cirelli, C., Arrell, C., Gashi, D., Mous, S., Wranik, M., Gruhl, T., Kekilli, D., Brünle, S., Deupi, X., Schertler, G. F. X., Benoit, R. M., Panneels, V., Nogly, P., Schapiro, I., Milne, C., Heberle, J. & Standfuss, J. (2020). *Nature*, **583**, 314–318.
- Smith, T., Wolff, K. A. & Nguyen, L. (2013). *Curr. Top. Microbiol. Immunol.* **374**, 53–80.
- Sorigué, D., Hadjidemetriou, K., Blangy, S., Gotthard, G., Bonvalet, A., Coquelle, N., Samire, P., Aleksandrov, A., Antonucci, L., Benachir, A., Boutet, S., Byrdin, M., Cammarata, M., Carbajo, S., Cuiné, S., Doak, R. B., Foucar, L., Gorel, A., Grünbein, M., Hartmann, E., Hiernerwadel, R., Hilpert, M., Kloos, M., Lane, T. J., Légeret, B., Legrand, P., Li-Beisson, Y., Moulin, S. L. Y., Nurizzo, D., Peltier, G., Schirò, G., Shoeman, R. L., Sliwa, M., Solinas, X., Zhuang, B., Barends, T. R. M., Colletier, J., Joffre, M., Royant, A., Berthomieu, C., Weik, M., Domratheva, T., Brettel, K., Vos, M. H., Schlichting, I., Arnoux, P., Müller, P. & Beisson, F. (2021). *Science*, **372**, eabd5687.
- Sorigué, D., Légeret, B., Cuiné, S., Blangy, S., Moulin, S., Billon, E., Richaud, P., Brugière, S., Couté, Y., Nurizzo, D., Müller, P., Brettel, K., Pignol, D., Arnoux, P., Li-Beisson, Y., Peltier, G. & Beisson, F. (2017). *Science*, **357**, 903–907.
- Šrajer, V. & Schmidt, M. (2017). *J. Phys. D Appl. Phys.* **50**, 373001.
- Stagno, J. R., Liu, Y., Bhandari, Y. R., Conrad, C. E., Panja, S., Swain, M., Fan, L., Nelson, G., Li, C., Wendel, D. R., White, T. A., Coe, J. D., Wiedorn, M. O., Knoska, J., Oberthuer, D., Tuckey, R. A., Yu, P., Dyba, M., Tarasov, S. G., Weierstall, U., Grant, T. D., Schwieters, C. D., Zhang, J., Ferré-D'Amaré, A. R., Fromme, P., Draper, D. E., Liang, M., Hunter, M. S., Boutet, S., Tan, K., Zuo, X., Ji, X., Barty, A., Zatsepin, N. A., Chapman, H. N., Spence, J. C. H., Woodson, S. A. & Wang, Y.-X. (2017). *Nature*, **541**, 242–246.
- Takala, H., Björling, A., Berntsson, O., Lehtivuori, H., Niebling, S., Hoernke, M., Kosheleva, I., Henning, R., Menzel, A., Ihalainen, J. A. & Westenhoff, S. (2014). *Nature*, **509**, 245–248.
- Tassoni, R., Blok, A., Pannu, N. S. & Ubbink, M. (2019). *Biochemistry*, **58**, 997–1009.
- Tenboer, J., Basu, S., Zatsepin, N., Pande, K., Milathianaki, D., Frank, M., Hunter, M., Boutet, S., Williams, G. J., Koglin, J. E., Oberthuer, D., Heymann, M., Kupitz, C., Conrad, C., Coe, J., Roy-Chowdhury, S., Weierstall, U., James, D., Wang, D., Grant, T., Barty, A., Yefanov, O., Scales, J., Gati, C., Seuring, C., Šrajer, V., Henning, R., Schwander, P., Fromme, R., Ourmazd, A., Moffat, K., Van Thor, J. J., Spence, J. C. H., Fromme, P., Chapman, H. N. & Schmidt, M. (2014). *Science*, **346**, 1242–1246.
- Totir, M. A., Helfand, M. S., Carey, M. P., Sheri, A., Buynak, J. D., Bonomo, R. A. & Carey, P. R. (2007). *Biochemistry*, **46**, 8980–8987.
- Tremblay, L. W., Xu, H. & Blanchard, J. S. (2010). *Biochemistry*, **49**, 9685–9687.
- Tzeng, S. R. & Kalodimos, C. G. (2012). *Nature*, **488**, 236–240.
- Vogt, A. D. & Di Cera, E. (2012). *Biochemistry*, **51**, 5894–5902.
- Wanzenberg, R., Agapov, I., Brefeld, W., Brinkmann, R., Chae, Y., Chao, H., Keil, J., Gavalda, X. N., Röhlberger, R., Schroer, C. G., Tischer, M. & Weckert, E. (2019). *AIP Conf. Proc.* **2054**, 030002.
- White, T. A., Mariani, V., Brehm, W., Yefanov, O., Barty, A., Beyerlein, K. R., Chervinskii, F., Galli, L., Gati, C., Nakane, T., Tolstikova, A., Yamashita, K., Yoon, C. H., Diederichs, K. & Chapman, H. N. (2016). *J. Appl. Cryst.* **49**, 680–689.
- Wiedorn, M. O., Awel, S., Morgan, A. J., Ayyer, K., Gevorkov, Y., Fleckenstein, H., Roth, N., Adriano, L., Bean, R., Beyerlein, K. R., Chen, J., Coe, J., Cruz-Mazo, F., Ekeberg, T., Graceffa, R., Heymann, M., Horke, D. A., Knoška, J., Mariani, V., Nazari, R., Oberthür, D., Samanta, A. K., Sierra, R. G., Stan, C. A., Yefanov, O., Rompotis, D., Correa, J., Erk, B., Treusch, R., Schulz, J., Hogue, B. G., Gañán-Calvo, A. M., Fromme, P., Küpper, J., Rode, A. V., Bajt, S., Kirian, R. A. & Chapman, H. N. (2018). *IUCrJ*, **5**, 574–584.
- Wiedorn, M. O., Oberthür, D., Bean, R., Schubert, R., Werner, N., Abbey, B., Aepfelbacher, M., Adriano, L., Allahgholi, A., Al-Qudami, N., Andreasson, J., Aplin, S., Awel, S., Ayyer, K., Bajt, S., Barák, I., Bari, S., Bielecki, J., Botha, S., Boukhelef, D., Brehm, W., Brockhauser, S., Cheviakov, I., Coleman, M. A., Cruz-Mazo, F., Danilevski, C., Darmanin, C., Doak, R. B., Domaracky, M., Dörner, K., Du, Y., Fangohr, H., Fleckenstein, H., Frank, M., Fromme, P., Gañán-Calvo, A. M., Gevorkov, Y., Giewekemeyer, K., Ginn, H. M., Graafsma, H., Graceffa, R., Greiffenberg, D., Gumprecht, L., Göttlicher, P., Hajdu, J., Hauf, S., Heymann, M., Holmes, S., Horke, D. A., Hunter, M. S., Imlau, S., Kaukher, A., Kim, Y., Klyuev, A., Knoška, J., Kobe, B., Kuhn, M., Kupitz, C., Küpper, J., Lahey-Rudolph, J. M., Laurus, T., Le Cong, K., Letrun, R., Xavier, P. L., Maia, L., Maia, F., Mariani, V., Messerschmidt, M., Metz, M., Mezza, D., Michelat, T., Mills, G., Monteiro, D. C. F., Morgan, A., Mühlig, K., Munke, A., Münnich, A., Nette, J., Nugent, K. A., Nuguid, T., Orville, A. M., Pandey, S., Pena, G., Villanueva-Perez, P., Poehlsen, J., Previtali, G., Redecke, L., Riekehr, W. M., Rohde, H., Round, A., Safenreiter, T., Sarrou, I., Sato, T., Schmidt, M., Schmitt, B., Schönherr, R., Schulz, J., Sellberg, J. A., Seibert, M. M., Seuring, C., Shelby, M. L., Shoeman, R. L., Sikorski, M., Silenzi, A., Stan, C. A., Shi, X., Stern, S., Sztuk-Dambietz, J., Szuba, J., Tolstikova, A., Trebbin, M., Trunk, U., Vagovic, P., Ve, T.,

- Weinhausen, B., White, T. A., Wrona, K., Xu, C., Yefanov, O., Zatsepin, N., Zhang, J., Perbandt, M., Mancuso, A. P., Betzel, C., Chapman, H. & Barty, A. (2018). *Nat. Commun.* **9**, 4025.
- Winn, M. D., Ballard, C. C., Cowtan, K. D., Dodson, E. J., Emsley, P., Evans, P. R., Keegan, R. M., Krissinel, E. B., Leslie, A. G. W., McCoy, A., McNicholas, S. J., Murshudov, G. N., Pannu, N. S., Potterton, E. A., Powell, H. R., Read, R. J., Vagin, A. & Wilson, K. S. (2011). *Acta Cryst.* **D67**, 235–242.
- Yefanov, O., Mariani, V., Gati, C., White, T. A., Chapman, H. N. & Barty, A. (2015). *Opt. Express*, **23**, 28459–28470.
- Yefanov, O., Oberthür, D., Bean, R., Wiedorn, M. O., Knoska, J., Pena, G., Awel, S., Gumprecht, L., Domaracky, M., Sarrou, I., Lourdu Xavier, P., Metz, M., Bajt, S., Mariani, V., Gevorkov, Y., White, T. A., Tolstikova, A., Villanueva-Perez, P., Seuring, C., Aplin, S., Estillore, A. D., Küpper, J., Klyuev, A., Kuhn, M., Laurus, T., Graafsma, H., Monteiro, D. C. F., Trebbin, M., Maia, F. R. N. C., Cruz-Mazo, F., Gañán-Calvo, A. M., Heymann, M., Darmanin, C., Abbey, B., Schmidt, M., Fromme, P., Giewekemeyer, K., Sikorski, M., Graceffa, R., Vagovic, P., Kluyver, T., Bergemann, M., Fangohr, H., Sztuk-Dambietz, J., Hauf, S., Raab, N., Bondar, V., Mancuso, A. P., Chapman, H. & Barty, A. (2019). *Struct. Dyn.* **6**, 064702.
- Yun, J.-H., Li, X., Yue, J., Park, J.-H., Jin, Z., Li, C., Hu, H., Shi, Y., Pandey, S., Carbajo, S., Boutet, S., Hunter, M. S., Liang, M., Sierra, R. G., Lane, T. J., Zhou, L., Weierstall, U., Zatsepin, N. A., Ohki, M., Tame, J. R. H., Park, S. Y., Spence, J. C. H., Zhang, W., Schmidt, M., Lee, W. & Liu, H. (2021). *Proc. Natl Acad. Sci. USA*, **118**, e2020486118.
- Zaitsev-Doyle, J. J., Puchert, A., Pfeifer, Y., Yan, H., Yorke, B. A., Müller-Werkmeister, H. M., Uetrecht, C., Rehbein, J., Huse, N., Pearson, A. R. & Sans, M. (2019). *RSC Adv.* **9**, 8695–8699.





# 3D diffractive imaging of nanoparticle ensembles using an x-ray laser

KARTIK AYYER,<sup>1,2,3,\*</sup> P. LOURDU XAVIER,<sup>1,3,4,†</sup> JOHAN BIELECKI,<sup>5</sup> ZHOU SHEN,<sup>6</sup> BENEDIKT J. DAURER,<sup>6</sup> AMIT K. SAMANTA,<sup>4</sup> SALAH AWEL,<sup>4</sup> RICHARD BEAN,<sup>5</sup> ANTON BARTY,<sup>4</sup> MARTIN BERGEMANN,<sup>5</sup> TOMAS EKEBERG,<sup>7</sup> ARMANDO D. ESTILLORE,<sup>4</sup> HANS FANGOHR,<sup>5</sup> KLAUS GIEWEKEMEYER,<sup>5</sup> MARK S. HUNTER,<sup>8</sup> MIKHAIL KARNEVSKIY,<sup>5</sup> RICHARD A. KIRIAN,<sup>9</sup> HENRY KIRKWOOD,<sup>5</sup> YOONHEE KIM,<sup>5</sup> JAYANATH KOLIYADU,<sup>5</sup> HOLGER LANGE,<sup>3,10</sup> ROMAIN LETRUN,<sup>5</sup> JANNIK LÜBKE,<sup>3,4,11</sup> THOMAS MICHELAT,<sup>5</sup> ANDREW J. MORGAN,<sup>12</sup> NILS ROTH,<sup>4,11</sup> TOKUSHI SATO,<sup>5</sup> MARCIN SIKORSKI,<sup>5</sup> FLORIAN SCHULZ,<sup>10</sup> JOHN C. H. SPENCE,<sup>9</sup> PATRIK VAGOVIC,<sup>4,5</sup> TAMME WOLLWEBER,<sup>1,2,3</sup> LENA WORBS,<sup>4,11</sup> OLEKSANDR YEFANOV,<sup>4</sup> YULONG ZHUANG,<sup>1,2</sup> FILIPE R. N. C. MAIA,<sup>7,13</sup> DANIEL A. HORKE,<sup>3,4,14</sup> JOCHEN KÜPPER,<sup>3,4,11,15</sup> N. DUANE LOH,<sup>6,16</sup> ADRIAN P. MANCUSO,<sup>5,17</sup> AND HENRY N. CHAPMAN<sup>3,4,11</sup>

<sup>1</sup>Max Planck Institute for the Structure and Dynamics of Matter, 22761 Hamburg, Germany

<sup>2</sup>Center for Free-Electron Laser Science, 22761 Hamburg, Germany

<sup>3</sup>The Hamburg Center for Ultrafast Imaging, Universität Hamburg, 22761 Hamburg, Germany

<sup>4</sup>Center for Free-Electron Laser Science, DESY, 22607 Hamburg, Germany

<sup>5</sup>European XFEL, 22869 Schenefeld, Germany

<sup>6</sup>Center for BioImaging Sciences, National University of Singapore, Singapore 117557, Singapore

<sup>7</sup>Department of Cell and Molecular Biology, Uppsala University, 75124 Uppsala, Sweden

<sup>8</sup>Linac Coherent Light Source, SLAC National Accelerator Laboratory, Menlo Park, California 94025, USA

<sup>9</sup>Department of Physics, Arizona State University, Tempe, Arizona 85287, USA

<sup>10</sup>Institute of Physical Chemistry, Universität Hamburg, 20146 Hamburg, Germany

<sup>11</sup>Department of Physics, Universität Hamburg, 22761 Hamburg, Germany

<sup>12</sup>University of Melbourne, Physics, Melbourne, VIC 3010, Australia

<sup>13</sup>NERSC, Lawrence Berkeley National Laboratory, Berkeley, California 94720, USA

<sup>14</sup>Institute for Molecules and Materials, Radboud University, 6525 AJ Nijmegen, The Netherlands

<sup>15</sup>Department of Chemistry, Universität Hamburg, 20146 Hamburg, Germany

<sup>16</sup>Department of Physics, National University of Singapore, Singapore 117551, Singapore

<sup>17</sup>Department of Chemistry and Physics, La Trobe Institute for Molecular Science, La Trobe University, Melbourne, VIC 3086, Australia

\*Corresponding author: kartik.ayyer@mpsd.mpg.de

Received 7 October 2020; revised 3 November 2020; accepted 20 November 2020 (Doc. ID 410851); published 24 December 2020

Single particle imaging at x-ray free electron lasers (XFELs) has the potential to determine the structure and dynamics of single biomolecules at room temperature. Two major hurdles have prevented this potential from being reached, namely, the collection of sufficient high-quality diffraction patterns and robust computational purification to overcome structural heterogeneity. We report the breaking of both of these barriers using gold nanoparticle test samples, recording around 10 million diffraction patterns at the European XFEL and structurally and orientationally sorting the patterns to obtain better than 3-nm-resolution 3D reconstructions for each of four samples. With these new developments, integrating advancements in x-ray sources, fast-framing detectors, efficient sample delivery, and data analysis algorithms, we illuminate the path towards sub-nanometer biomolecular imaging. The methods developed here can also be extended to characterize ensembles that are inherently diverse to obtain their full structural landscape.

Published by The Optical Society under the terms of the [Creative Commons Attribution 4.0 License](https://creativecommons.org/licenses/by/4.0/). Further distribution of this work must maintain attribution to the author(s) and the published article's title, journal citation, and DOI.

<https://doi.org/10.1364/OPTICA.410851>

## 1. INTRODUCTION

The determination of the structures of biomolecules at atomic resolution requires bright sources of radiation, which are unfortunately also energetic enough to degrade the object under

observation [1]. All approaches to structure determination are dedicated primarily to overcoming, or working around, the effects of this radiation damage. In x-ray crystallography, large numbers of aligned molecules amplify the diffraction signal that can be

obtained within the exposure that the sample can tolerate. The tolerable dose can be increased somewhat by cooling the crystals to cryogenic temperatures. Such cooling also allows electron microscopy—where the ratio of the image-forming to damage-causing radiation is more favorable—to record faint and noisy images of many uncrystallized molecules, which can then be used to build up a three-dimensional image. The extreme intensity and ultrashort pulses of x-ray free electron lasers (XFELs) potentially offer another way to obtain structural information from single macromolecules, but without the need for cooling [2]. Pulses of femtosecond duration can outrun radiation damage and essentially freeze the molecule in time [3,4].

Single particle imaging (SPI) at XFELs consists of collecting coherent diffraction patterns from individual particles intersecting bright XFEL pulses. Theoretical work predicts that currently available XFEL sources generate enough scattered photons from single macromolecules to solve for their unknown orientations and reconstruct 3D structures of large reproducible biomolecules [5–7]. Proof-of-principle SPI experiments on biological particles [8–14] have highlighted the challenges of the approach, i.e., the recording of a large number of patterns, all with sufficiently low background, and from structurally homogeneous samples.

Here, we present experimental results that address these challenges and show the path towards single-particle imaging of macromolecules. We overcame the first challenge by aerosol injection of gold nanoparticles (AuNPs) and collected millions of patterns by using the megahertz-rate European XFEL [15] and a relatively large illumination area of the XFEL beam. The particles were chosen for two reasons, the first being the high scattering power of gold, which balances the reduced intensity from the large beam size to provide scattering signals at the levels expected from biological materials once tight focusing is achieved.

The other reason is that their inherent heterogeneity from the synthesis reflects what is expected with biomolecules, especially at higher resolutions.

To recover a high-resolution 3D structure, a structurally homogeneous dataset must be generated. This challenge was performed computationally using an extension of the well-known Expand-Maximize-Compress (EMC) algorithm [16]. Even though individual diffraction patterns contained as few as 0.0012 photons per pixel on average, we show that this is sufficient not only to extract the orientations of particles, but also to disentangle structural variations. We obtain a 3D structure approaching 2 nm resolution, which is significantly improved compared to what could be achieved without structural sorting.

With further improvements in aerosol sample delivery to increase the particle density in the x-ray focus [17–19], more highly focused x-ray beams can be used to obtain similar data from biomolecules. The computational techniques developed here also open the way to experiments that can reveal thermodynamically rare states in an ensemble and characterize heterogeneous ensembles with statistical rigor. The short exposure times set by the femtosecond pulse duration will also offer unprecedented opportunities for capturing the dynamics of macromolecules in real time.

In Section 2, we describe the experimental setup and data collection process, including observation of beam-induced melting of some samples for 1 MHz repetition rate. This is followed in Section 3 by the classification of diffraction patterns using 2D averaging and per-pattern size and incident fluence determination. Finally, 3D reconstructions are performed on subsets of the data in Section 4, showing an improvement in structure quality when the appropriate selection is performed and demonstrating the power of the serial data collection method.

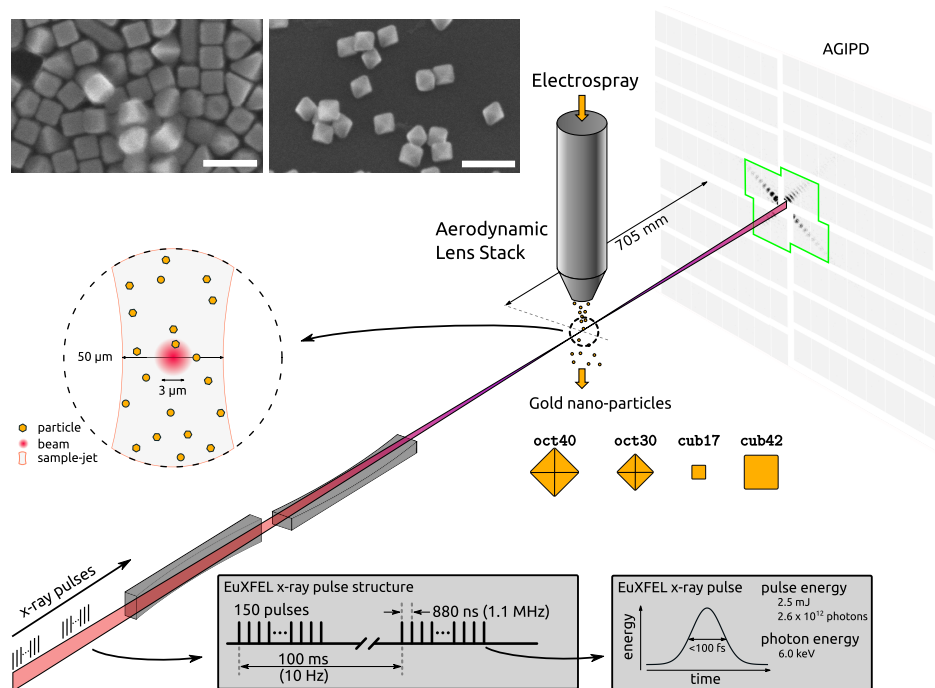


**Fig. 1.** Experimental setup. XFEL pulses were focused by a series of Kirkpatrick–Baez mirrors into a  $3 \times 3 \mu\text{m}^2$  spot and scattered off particles in the aerosol stream to produce diffraction patterns on the AGIPD. The lower inset shows the timing structure of the XFEL pulses at the instrument, while the top inset shows representative SEM images of the cub42 and oct30 samples; scale bars are 100 nm. The low-resolution part of the detector used for the structural sorting is highlighted in green.

**Table 1. Data Collection Statistics for the Four Nanocrystal Samples<sup>a</sup>**

Parameter	oct30	oct40	cub42	cub17
No. frames	15,805,472	29,309,832	34,197,950	36,966,286
No. hits	2,117,732	2,133,041	2,451,068	3,307,723
Hit ratio	13.40%	7.28%	7.17%	8.95%
Hits/hour	376,947	233,553	228,633	402,954
Hits/train <sup>b</sup>	5.2/10.4/15.6	2.8/6.4/8.4	2.4/5.6/9.1	NA/7.2/12.1
No. “good” hits	1,430,086	1,249,328	433,259	564121
Sphere fraction (%) <sup>b</sup>	3.4/4.0/19.2	2.7/7.2/33.5	2.4/10.4/29.1	NA <sup>c</sup>
Resolution (nm) <sup>d</sup>	3.50 (2.10–4.54)	5.32 (1.89–7.17)	4.89 (1.98–6.56)	2.11 (1.81–3.31)

<sup>a</sup>Sample names refer to their nominal shape (octahedron or cube) and edge length in nanometers.

<sup>b</sup>The three numbers correspond to values for 0.28 MHz, 0.55 MHz, and 1.1 MHz intra-train repetition rates, respectively.

<sup>c</sup>There was no clear sign of spherical particles for the cub17 sample.

<sup>d</sup>The first number is the azimuthal average resolution, while numbers in parentheses show minimum and maximum values, respectively.

## 2. MILLION-PATTERN DATA COLLECTION

Data was collected at the SPB/SFX (single particles, biomolecules, and clusters/serial femtosecond crystallography) instrument [20] of the European XFEL using 6 keV photons focused into a  $3 \times 3 \mu\text{m}^2$  spot, as measured by a  $20 \mu\text{m}$  thick YAG screen in the focal plane. Individual x-ray pulses were generated with 2.5 mJ of energy on average ( $2.6 \times 10^{12}$  photons). The pulses were delivered in 150-pulse trains with an intra-train repetition rate of 1.1 MHz and trains arriving every 0.1 s, leading to a maximum data collection rate of 1500 frames/second. A detector built specifically for this burst mode operation, the Adaptive Gain Integrating Pixel Detector (AGIPD) [21], was placed 705 mm downstream of the interaction region to collect the diffraction patterns for each pulse individually up to a scattering angle of  $8.3^\circ$  at the center-edge of the detector (Fig. 1).

Gold octahedra and cubes, each of two different sizes, were sequentially injected into the x-ray beam using an electrospray-ionization aerodynamic-lens-stack sample delivery system. The nominal sizes of the particles measured using scanning electron microscopy were 30 and 40 nm for the octahedra and 42 and 17 nm for the cubes. In the rest of the paper, these samples are described using the codes oct30, oct40, cub42, and cub17, respectively. The octahedra and cubes were prepared using different protocols, generating different heterogeneity profiles, as will be seen later.

Diffraction patterns were observed in around 10% of the collected frames. This relatively high hit ratio compared to those achieved with biological particles in similar conditions was due to a combination of the relatively large x-ray focal spot size, high particle concentration and high mass and density of the larger AuNPs, leading to lower speeds after acceleration by the gas flow in the aerodynamic lens stack [17,22,23]. Lower speeds lead to higher spatial densities, and thus higher hit ratios for the same particle beam size. Table 1 shows the statistics of the number of frames collected for each sample as well as the various filtration steps after the analyses described below.

When using the peak repetition rate of 1.1 MHz and 150 pulses per train, diffraction patterns corresponding to the shapes of cubes and octahedra could be observed, but a high fraction of the diffraction patterns appeared to originate from spherical particles (see Table 1 and third column of Fig. 2). This was found to be caused by the melting of particles in the wings of the previous XFEL pulse in the train, as the particles approached the focus. To reduce this occurrence, we therefore reduced the intra-train repetition rate

from 1.1 MHz to 550 kHz, providing only half the available pulses; further reduction of the repetition rate was tested but not found to be necessary. This reduced-rate mode was used to collect most of the data for the three larger samples (but not the cub17 sample).

## 3. SINGLE-HIT SELECTION BY 2D CLASSIFICATION

Frames with diffraction from particles were detected by setting a threshold on the number of pixels in the AGIPD detector that recorded at least one photon. Unfortunately, not all the particles are of interest, even accounting for the heterogeneity. The extraneous patterns include those from spheres formed after melting, multi-particle aggregates, and other possible contaminants. In previous work, either manual selection [10,13] or manifold learning methods [12,24] have been used to classify patterns and reject outliers. We adopt an alternative approach, similar to one commonly used in cryo-EM [25], but implemented in diffraction space. Two-dimensional orientation determination into multiple models was performed in the detector plane using the EMC algorithm [16,26] implemented in *Dragonfly* [27]. The in-plane rotation angle ( $\theta$ ) and relative incident fluence ( $\phi$ ) of each diffraction pattern were determined collectively, and multiple independent 2D intensity models were reconstructed. Each of these intensities represents an average of aligned copies of a subset of the patterns from the whole set. In addition to the EMC algorithm being highly noise tolerant [7,28,29], one can also use it to examine the average models to understand what type of particles are in the dataset.

In this experiment, 50 random white noise 2D intensity models were used as initial guesses to perform the classification for each sample, using only the low resolution part of the detector highlighted at this stage (Fig. 1). Some of the reconstructed intensities are shown in Fig. 2. The first two columns of the figure show representative examples of “good” models of each sample, chosen manually to be those with high contrast and strong streaks for further processing. The third column shows an average of diffraction from rounded particles (except in the cub17 case where a dimer average is highlighted). These models were used to determine the sphere fraction shown in Table 1. Finally, the last column shows low-contrast models where a diverse set of particles was averaged.

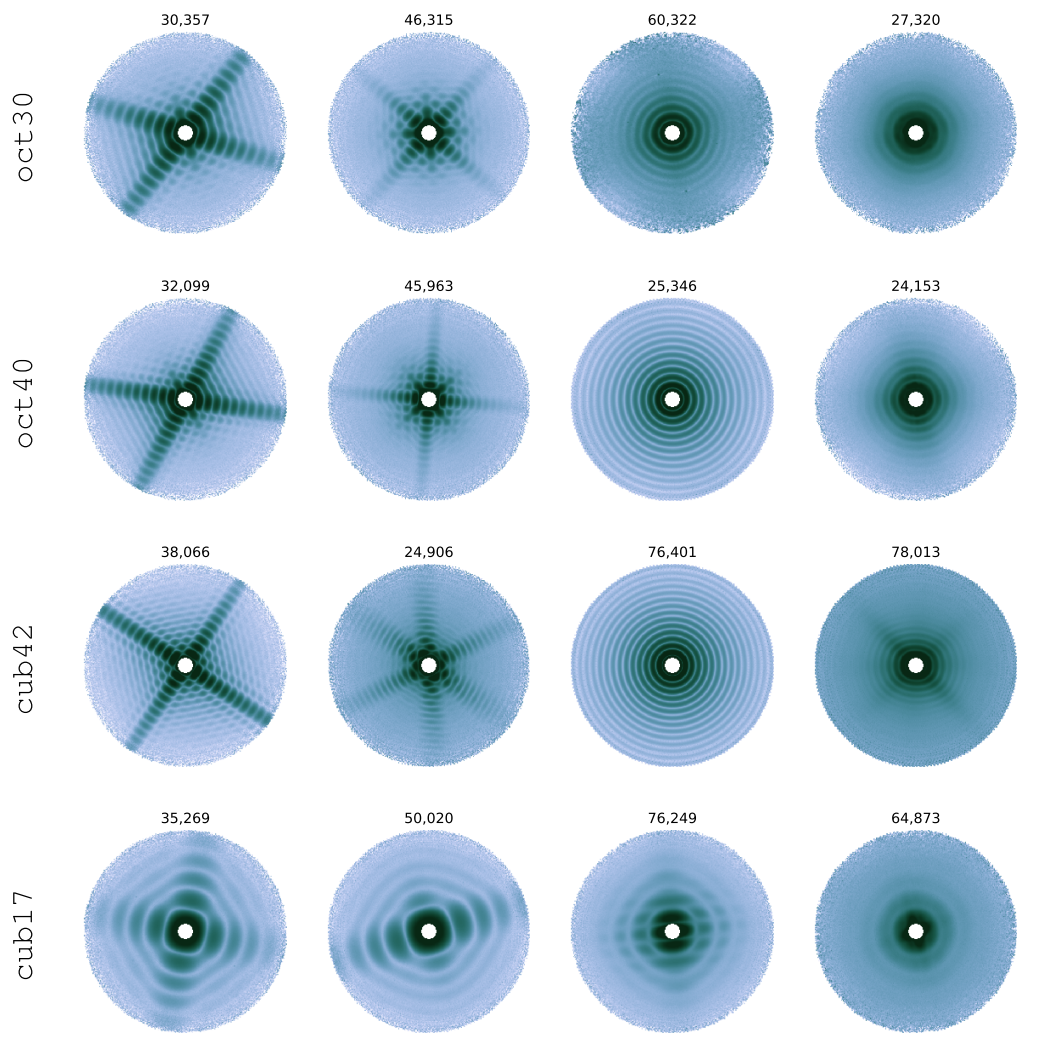


**Fig. 2.** 2D classification. Representative examples of reconstructed 2D models shown on a logarithmic scale, with each row representing a different sample. The numbers indicate how many patterns had that model as the most likely one. The first two columns show models selected for further processing. The third column shows diffraction from rounded/spherical particles, except in the cub17 case where there were no spherical particles and the model shows diffraction from a dimer instead. The fourth column shows some of the low-contrast models generated by averaging patterns from a diverse set of particles. The resolution at the edge of the circle is 3.3 nm.

### A. Single-Shot Characterization

The 2D classification also enabled the analysis of size heterogeneity from those models where the faces of the nanoparticles were parallel to the x-ray beam. In these cases, one observes strong streaks on the detector, and the fringe spacing indicates the distance between these parallel faces. The size distributions of the samples inferred this way are shown in Fig. 3(a). The octahedral samples had a much broader size distribution than the cubic ones. While some of the breadth of the peaks is due to apparent size variations when the faces are not perfectly parallel to the beam, the much broader size distributions of the octahedra suggest that they had more heterogeneity.

In addition, the octahedra were also noticeably asymmetric, as seen in Figs. 3(c) and 3(d). These histograms were made by identifying patterns that belonged to models with two strong streaks (e.g., top left model in Fig. 2). Another run of 2D classification with just these two-streak patterns showed no variation in the angle

between the streaks, but only in the fringe spacing. This is to be expected since the angle is fixed by the  $\langle 111 \rangle$  growth direction, while the size is not restricted by symmetry. The equivalent figures for the cubic samples showed no asymmetry.

Due to the low polydispersity of the cubes, they were used to determine the incident fluence distribution of the x-ray beam. Since the Fourier transform of a cube is the product of three orthogonal sinc functions, the size fitting procedure also generated a predicted incident fluence. The distribution from 102,480 patterns is shown in Fig. 3(b), yielding a maximum fluence of around  $60 \mu\text{J}/\mu\text{m}^2$ , which leads to a lower bound estimate of around  $540 \mu\text{J}$  in the focal spot from the measured spot size. The actual fluence was likely higher, as the particles were not ideal cubes and the scattering efficiency is reduced at high fluences [30]. One can also see that most diffraction patterns were obtained with lower incident fluences, because the particles interacted with the outer regions of the x-ray focus. The expected behavior of a Gaussian focal spot is shown as a red dashed line and shows a much

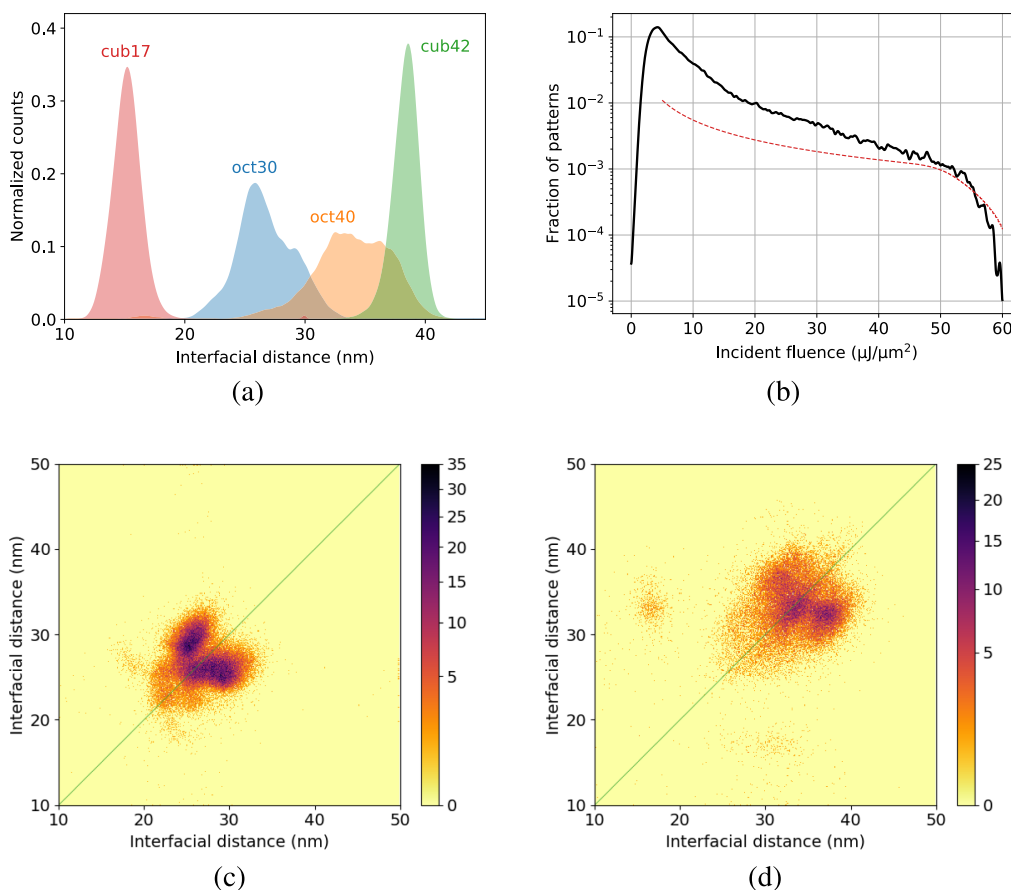


**Fig. 3.** Size and incident fluence distributions from 2D classification. (a) Size distribution for the four samples. The sizes are represented by the distance between opposing parallel faces. The cubes have narrow distributions, while the octahedral distributions are broader. (b) Distribution of incident fluence on the particle calculated from the cub42 sample assuming they are ideal cubes. The red dashed line represents the expected behavior from an ideal Gaussian focus weighted by the measured pulse energy distribution. (c), (d) 2D histogram of size distributions from two-streak patterns for the oct 30 and oct 40 samples, respectively. High density in the off-diagonal regions suggests the particles are asymmetric. The horizontal axis represents the brighter of the two streaks.

lower fraction of weak hits [31]. This difference can be accounted for by the stronger wings of the x-ray focus than for a Gaussian spot, which are also responsible for the melting observed at high repetition rates.

#### 4. 3D RECONSTRUCTION WITH STRUCTURAL SORTING

The fraction of good hits used for 3D structure reconstruction varied from 17% for the cube samples to around 60% for the octahedra (Table 1). The 3D intensity distribution was obtained using these patterns before recovering the structures by performing phase retrieval using a combination of the difference map and error reduction algorithms [7]. For computational efficiency, the 3D orientations were first determined using the low-resolution part of the detector where the corner resolution was 3.3 nm. A refinement procedure similar to that developed for serial crystallography with the EMC algorithm [32] was used with the whole detector to get the full-resolution 3D intensities. In this procedure, only orientations in the neighborhood of the most likely orientation of a given pattern from the low-resolution run were searched.

#### A. Octahedral Samples oct30 and oct40

For the octahedra, the results from this conventional single-model approach are shown in Fig. 4(a). The intensities have noticeably lower contrast than the equivalent slices in the 2D models. From the size distributions seen in Fig. 3, this could be attributed to structural heterogeneity. To counter this, the patterns were probabilistically partitioned into five intensity volumes in a manner equivalent to the 2D classification procedure. However, the initial guesses were not random white noise, but rather isotropically stretched/scaled versions of the single model reconstructed above. Five models, with stretch factors ranging from 0.9 to 1.1 were used as these initial seeds. The rest of the reconstruction proceeded without any restraints between these models or any symmetry constraints.

Once again, this structural sorting was performed at low resolution before refining the orientations of a subset of patterns from a single model to get full-resolution intensities. Slices through the 3D intensity for the oct30 sample are shown in Fig. 4(a). The left column, showing the single-model reconstruction with 1.4 million patterns has noticeably worse fringe contrast and background than the equivalent slices in the right column or in the first two columns of the 2D classification output shown in Fig. 2. The homogeneous

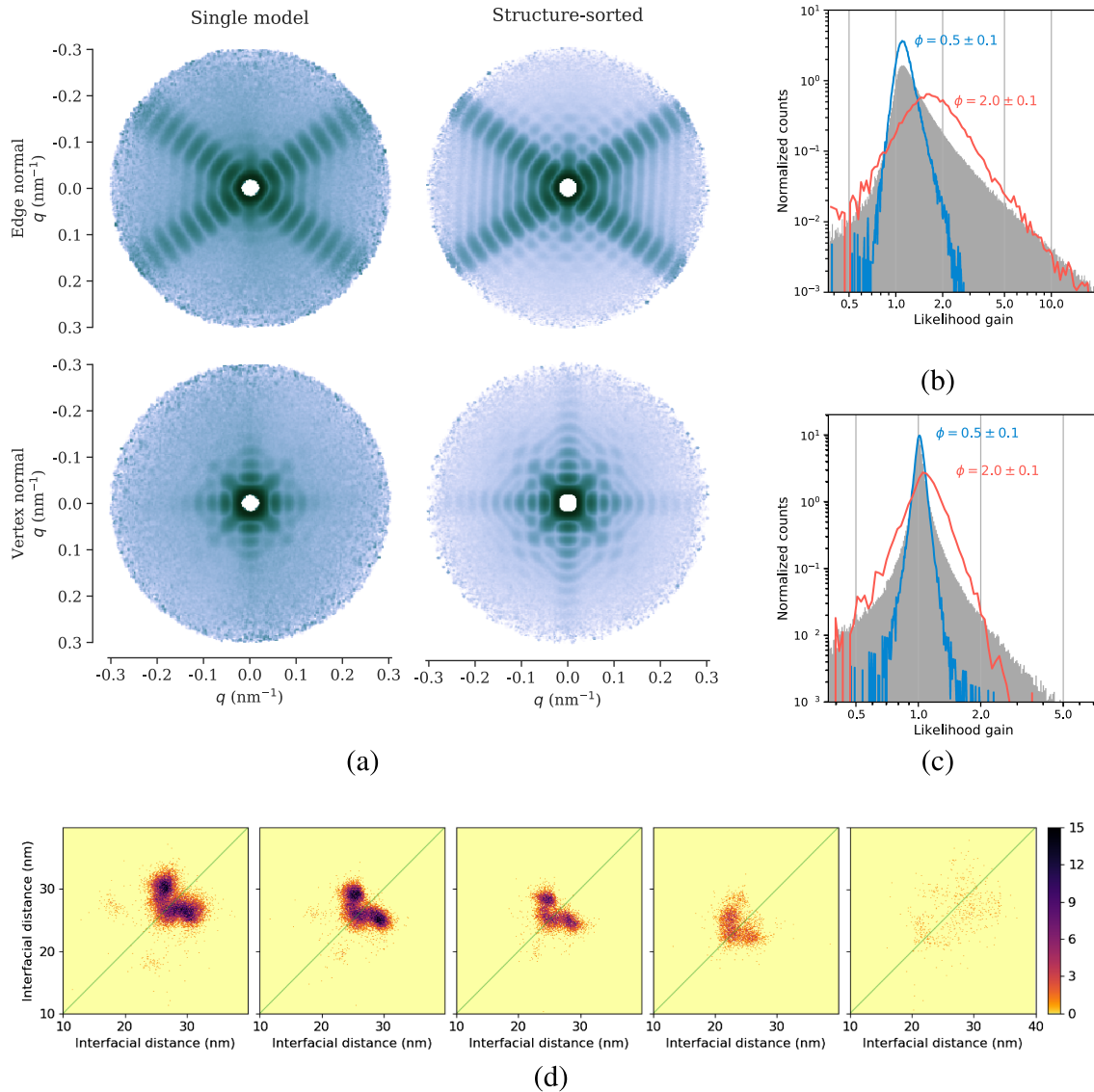


**Fig. 4.** Effect of structural sorting. Comparison of 3D intensity reconstructions for the octahedra before and after structural sorting. (a) Low-resolution logarithmic intensities of the oct30 sample comparing the standard single-model reconstruction with one of the sorted models. The two rows represent slices normal to an edge and vertex of the octahedron. (b) Likelihood gain distribution for the patterns shared with the sorted model shown in (a). The blue and red curves show distributions for weak and strong patterns, as identified by the relative fluence factor  $\phi$ , respectively. (c) Same gain plot for the oct40 sample. (d) Two-streak size histograms [Fig. 3(c)] for the oct30 sample separated into the five reconstructed models.

set had 0.53 million patterns selected using the multi-model EMC reconstruction. The visual improvement is accompanied by an increase in likelihood of the model intensities outside the central speckle for the common patterns in both sets, as shown in Fig. 4(b). The filled histogram shows the distribution of the per-pattern increase in likelihood, which we refer to as likelihood gain (see Supplement 1, Section 6), while the two traces show the distributions for weak (relative scale  $0.5 \pm 0.1$ ) and strong (relative scale  $2.0 \pm 0.1$ ) patterns. The latter shows how brighter patterns are more selective towards an improved model. Figure 4(c) shows the same information for the oct40 sample, where the gain ratio is smaller, but still greater than one. The 2D size distributions shown in Fig. 3(c) were re-calculated for each subset of patterns belonging to the five models and plotted in Fig. 4(d), confirming the different

sizes for each model, but also exhibiting a simpler structure than that of the full dataset.

## B. Cubic Samples cub42 and cub17

For the cubic particles, a single-model 3D reconstruction was deemed sufficient, due to the relative monodispersity of the sample. The selection of good hits from the 2D classification was more stringent, including only high-contrast cube-like patterns. The incident fluence factors were estimated in the first few iterations where the calculated probability distributions were broad and then later kept fixed (see Supplement 1).

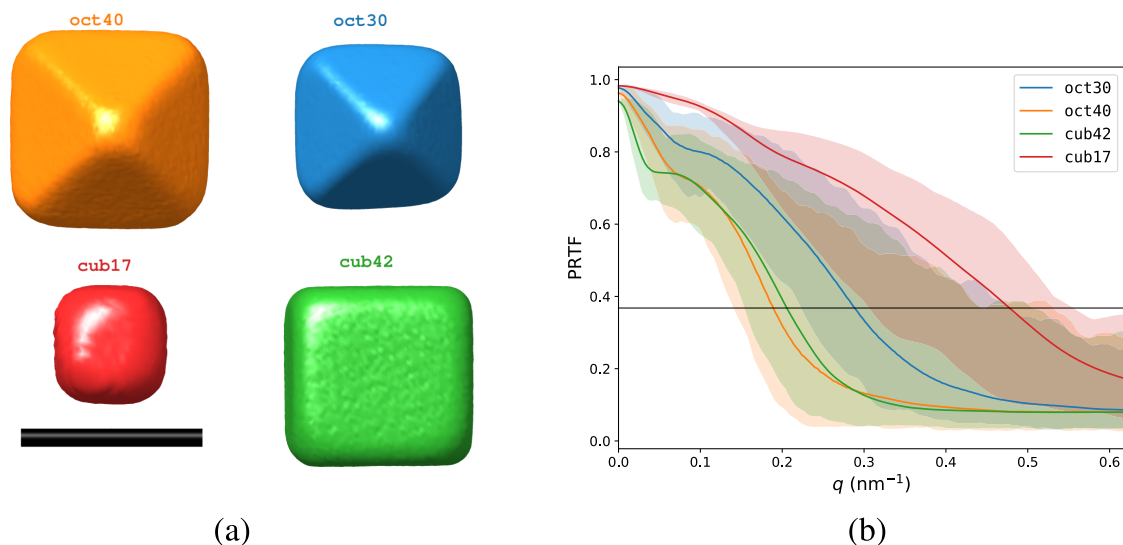


**Fig. 5.** Phase retrieval. (a) Isosurface plots of electron densities recovered after phase retrieval (scale bar is 40 nm). The asymmetric structures of the octahedra are clearly evident (see Visualization 2 and Fig. S7). (b) Smoothed phase retrieval transfer function (PRTF) measuring reproducibility of phases as a function of  $q$ . The solid lines represent the azimuthal average PRTF conventionally used to determine the resolution of the structure. The shaded region around each line indicates the range of values at each  $q$ . The typical  $1/e$  cutoff is shown in black.

### C. Phase Retrieval

The electron densities were reconstructed by performing 3D iterative phase retrieval on the full-resolution intensity volumes (see Visualization 1 for details and Fig. S6 for intensity slices). Figure 5(a) shows the reconstructed electron densities as isosurface plots. The contour levels were chosen where the gradient of the density was highest. Other views of the particles are shown in Fig. S7. The phase retrieval transfer function (PRTF) metric as a function of wave-vector  $q$  is shown in Fig. 5(b). This metric is a measure of the reproducibility of recovered phases when starting from 128 random models. The 3D PRTF distribution was smoothed using a Gaussian kernel with a width equal to one-third of the fringe width. The shaded region around each line shows the range of values in each  $q$  shell, highlighting the strong anisotropy of the metric due to the faceted nature of the objects. The intersection with the common  $1/e$  threshold determining the resolution is shown in Table 1. The resolution normal to the flat faces is 2 nm or better for all samples, while the resolution is relatively low, far from any strong streaks in Fourier space. This angle-dependent resolution is a property of the diffractive-domain averaging before phase retrieval, but also due to the strongly faceted shape and lack of internal structure of these objects, both of which are not representative of biological objects.

## 5. CONCLUSION

We have demonstrated an order-of-magnitude increase in data collection efficiency along with much higher imaging resolution than previously achieved for x-ray single particle diffractive imaging, setting a template for future SPI experiments at the European XFEL and elsewhere. We have also shown that with these large data sets, one can structurally sort the particles and average a narrow size and shape range to obtain higher resolution. A similar problem is expected to be faced when imaging biological particles, and the method developed here shows the way towards overcoming conformational variability in the Fourier domain.

Although we benefited from the strong scattering cross section of gold compared to organic materials, with the commissioning of a sub-micrometer focus at the SPB/SFX instrument, we can expect comparable signal strengths from organic materials. Unfortunately, smaller x-ray foci would also mean lower hit ratios with the current sample delivery setup. Improvements could be made through optimized focusing for the targeted size distribution [17] or cryogenic injection systems [19] that additionally allow conformational selection [33]. Another approach is to keep using the larger focus and conjugate the particles with AuNPs to assist hitfinding and orientation determination [34]. The effective hit rate can also be increased by using more pulses in each train from the European XFEL (max. 2700) than the AGIPD detector can save (max. 352) and vetoing in real time those frames that do not contain diffraction signal.

The class of experiments exemplified here can also be applied to study rare events such as transient states in a spontaneous phase transition or high-free-energy states. Since each image is collected serially, one can identify relevant subsets corresponding to interesting states without averaging over all patterns. In this work, we have taken the approach of treating the objects as general 3D contrast functions with no *a priori* information. One can also envision a parameterized refinement approach that should enable a finer characterization of the structural landscape of the ensemble. Another direction for future development is the automatic classification of 2D intensity models to find the ones that correspond to single, non-spherical particles. In addition to improving the efficiency of the applications mentioned above, this would also enable the study of highly heterogeneous samples where the motifs themselves vary [35,36].

**Funding.** Deutsche Forschungsgemeinschaft (AIM, EXC 2056, ID 390715994, CUI, EXC 1074, ID 194651731); European Research Council (ERC-614507-Küpper); Helmholtz Association (Impuls-und Vernetzungsfond); Human Frontier Science Program (RGP0010/2017); Vetenskapsrådet; Carl

Tryggers Stiftelse för Vetenskaplig Forskning; Röntgen-Ångström Cluster; BioXFEL Science and Technology Center (STC-1231306); Joachim Herz Stiftung.

**Acknowledgment.** We thank Rick Millane for helpful discussions. We acknowledge European XFEL in Schenefeld, Germany, for provision of x-ray free-electron laser beamtime at Scientific Instrument SPB/SFX and thank the staff for their assistance. We thank the DESY NanoLab, CSSB cryoEM user facility and the XBI labs at EuXFEL for access to electron microscopy resources and their staff for their help. J.C.H.S. and R.A.K. acknowledge support from the National Science Foundation BioXFEL. J.R.N.C.M. acknowledges support from the Swedish Research Council, Röntgen-Ångström Cluster, and Carl Tryggers Foundation for Scientific Research. P.L.X. acknowledges a fellowship from the Joachim Herz Stiftung. P.L.X. and H.N.C. acknowledge support from the Human Frontiers Science Program.

**Disclosures.** The authors declare no conflicts of interest.

See [Supplement 1](#) for supporting content.

†These authors contributed equally to this paper.

## REFERENCES

1. R. Henderson, "The potential and limitations of neutrons, electrons and x-rays for atomic resolution microscopy of unstained biological molecules," *Q. Rev. Biophys.* **28**, 171–193 (1995).
2. R. Neutze, R. Wouts, D. Van der Spoel, E. Weckert, and J. Hajdu, "Potential for biomolecular imaging with femtosecond x-ray pulses," *Nature* **406**, 752–757 (2000).
3. H. N. Chapman, A. Barty, M. J. Bogan, S. Boutet, M. Frank, S. P. Hau-Riege, S. Marchesini, B. W. Woods, S. Bajt, W. H. Benner, R. A. London, E. Plönjes, M. Kuhlmann, R. Treusch, S. Düsterer, T. Tschentscher, J. R. Schneider, E. Spiller, T. Möller, C. Bostedt, M. Hoener, D. A. Shapiro, K. O. Hodgson, D. van der Spoel, F. Burmeister, M. Bergh, C. Caleman, G. Huldt, M. M. Seibert, F. R. N. C. Maia, R. W. Lee, A. Szöke, N. Timneanu, and J. Hajdu, "Femtosecond diffractive imaging with a soft-x-ray free-electron laser," *Nat. Phys.* **2**, 839–843 (2006).
4. A. Barty, C. Caleman, A. Aquila, N. Timneanu, L. Lomb, T. A. White, J. Andreasson, D. Arnlund, S. Bajt, T. R. M. Barends, M. Barthelmess, M. J. Bogan, C. Bostedt, J. D. Bozek, R. Coffee, N. Coppola, J. Davidsson, D. P. DePonte, R. B. Doak, T. Ekeberg, V. Elser, S. W. Epp, B. Erk, H. Fleckenstein, L. Foucar, P. Fromme, H. Graafsma, L. Gumprecht, J. Hajdu, C. Y. Hampton, R. Hartmann, A. Hartmann, G. Hauser, H. Hirsemann, P. Holl, M. S. Hunter, L. Johansson, S. Kassemeyer, N. Kimmel, R. A. Kirian, M. Liang, F. R. N. C. Maia, E. Malmerberg, S. Marchesini, A. V. Martin, K. Nass, R. Neutze, C. Reich, D. Rolles, B. Rudek, A. Rudenko, H. Scott, I. Schlichting, J. Schulz, M. M. Seibert, R. L. Shoeman, R. G. Sierra, H. Soltau, J. C. H. Spence, F. Stellato, S. Stern, L. Strüder, J. Ullrich, X. Wang, G. Weidenspointner, U. Weierstall, C. B. Wunderer, and H. N. Chapman, "Self-terminating diffraction gates femtosecond x-ray nanocrystallography measurements," *Nat. Photonics* **6**, 35–40 (2012).
5. C. Fortmann-Grote, A. Buzmakov, Z. Jurek, N.-T. D. Loh, L. Samoylova, R. Santra, E. A. Schneidmiller, T. Tschentscher, S. Yakubov, C. H. Yoon, M. V. Yurkov, B. Ziaja-Motyka, and A. P. Mancuso, "Start-to-end simulation of single-particle imaging using ultra-short pulses at the European x-ray free-electron laser," *IUCrJ* **4**, 560–568 (2017).
6. K. Ayyer, G. Geloni, V. Kocharyan, E. Saldin, S. Serkez, O. Yefanov, and I. Zagorodnov, "Perspectives for imaging single protein molecules with the present design of the European XFEL," *Struct. Dyn.* **2**, 041702 (2015).
7. K. Ayyer, A. J. Morgan, A. Aquila, H. DeMirici, B. G. Hogue, R. A. Kirian, P. L. Xavier, C. H. Yoon, H. N. Chapman, and A. Barty, "Low-signal limit of x-ray single particle diffractive imaging," *Opt. Express* **27**, 37816–37833 (2019).
8. M. J. Bogan, W. H. Benner, S. Boutet, U. Rohner, M. Frank, A. Barty, M. M. Seibert, F. Maia, S. Marchesini, S. Bajt, B. Woods, V. Riot, S. P. Hau-Riege, M. Svenda, E. Marklund, E. Spiller, J. Hajdu, and H. N. Chapman, "Single particle x-ray diffractive imaging," *Nano Lett.* **8**, 310–316 (2008).
9. M. M. Seibert, T. Ekeberg, F. R. N. C. Maia, M. Svenda, J. Andreasson, O. Jönsson, D. Odić, B. Iwan, A. Rocker, D. Westphal, M. Hantke, D. P. DePonte, A. Barty, J. Schulz, L. Gumprecht, N. Coppola, A. Aquila, M. Liang, T. A. White, A. Martin, C. Caleman, S. Stern, C. Abergel, V. Seltzer, J.-M. Claverie, C. Bostedt, J. D. Bozek, S. Boutet, A. A. Miahnahri, M. Messerschmidt, J. Krzywinski, G. Williams, K. O. Hodgson, M. J. Bogan, C. Y. Hampton, R. G. Sierra, D. Starodub, I. Andersson, S. Bajt, M. Barthelmess, J. C. H. Spence, P. Fromme, U. Weierstall, R. Kirian, M. Hunter, R. B. Doak, S. Marchesini, S. P. Hau-Riege, M. Frank, R. L. Shoeman, L. Lomb, S. W. Epp, R. Hartmann, D. Rolles, A. Rudenko, C. Schmidt, L. Foucar, N. Kimmel, P. Holl, B. Rudek, B. Erk, A. Hömke, C. Reich, D. Pietschner, G. Weidenspointner, L. Strüder, G. Hauser, H. Gorke, J. Ullrich, I. Schlichting, S. Herrmann, G. Schaller, F. Schopper, H. Soltau, K.-U. Kühnel, R. Andritschke, C.-D. Schröter, F. Krasniqi, M. Bott, S. Schorb, D. Rupp, M. Adolph, T. Gorkhover, H. Hirsemann, G. Potdevin, H. Graafsma, B. Nilsson, H. N. Chapman, and J. Hajdu, "Single mimivirus particles intercepted and imaged with an x-ray laser," *Nature* **470**, 78–81 (2011).
10. T. Ekeberg, M. Svenda, C. Abergel, F. R. N. C. Maia, V. Seltzer, J.-M. Claverie, M. Hantke, O. Jönsson, C. Nettelblad, G. van der Schot, M. Liang, D. P. DePonte, A. Barty, M. M. Seibert, B. Iwan, I. Andersson, N. D. Loh, A. V. Martin, H. Chapman, C. Bostedt, J. D. Bozek, K. R. Ferguson, J. Krzywinski, S. W. Epp, D. Rolles, A. Rudenko, R. Hartmann, N. Kimmel, and J. Hajdu, "Three-dimensional reconstruction of the giant mimivirus particle with an x-ray free-electron laser," *Phys. Rev. Lett.* **114**, 098102 (2015).
11. A. Munke, J. Andreasson, A. Aquila, S. Awel, K. Ayyer, A. Barty, R. J. Bean, P. Berntsen, J. Bielecki, S. Boutet, M. Bucher, H. N. Chapman, B. J. Daurer, H. DeMirici, V. Elser, P. Fromme, J. Hajdu, M. F. Hantke, A. Higashiura, B. G. Hogue, A. Hosseinizadeh, Y. Kim, R. A. Kirian, H. K. N. Reddy, T.-Y. Lan, D. S. D. Larsson, H. Liu, N. D. Loh, F. R. N. C. Maia, A. P. Mancuso, K. Mühlig, A. Nakagawa, D. Nam, G. Nelson, C. Nettelblad, K. Okamoto, A. Ourmazd, M. Rose, G. van der Schot, P. Schwander, M. M. Seibert, J. A. Sellberg, R. G. Sierra, C. Song, M. Svenda, N. Timneanu, I. A. Vartanyants, D. Westphal, M. O. Wiedorn, G. J. Williams, P. L. Xavier, C. H. Yoon, and J. Zook, "Coherent diffraction of single Rice Dwarf virus particles using hard x-rays at the Linac coherent light source," *Sci. Data* **3**, 160064 (2016).
12. H. K. Reddy, C. H. Yoon, A. Aquila, S. Awel, K. Ayyer, A. Barty, P. Berntsen, J. Bielecki, S. Bobkov, M. Bucher, G. A. Carini, S. Carron, H. Chapman, B. J. Daurer, H. DeMirici, T. Ekeberg, P. Fromme, J. Hajdu, M. F. Hantke, P. Hart, B. G. Hogue, A. Hosseinizadeh, Y. Kim, R. A. Kirian, R. P. Kurta, D. S. Larsson, N. Duane Loh, F. R. Maia, A. P. Mancuso, K. Mühlig, A. Munke, D. Nam, C. Nettelblad, A. Ourmazd, M. Rose, P. Schwander, M. Seibert, J. A. Sellberg, C. Song, J. C. Spence, M. Svenda, G. Van der Schot, I. A. Vartanyants, G. J. Williams, and P. L. Xavier, "Coherent soft x-ray diffraction imaging of coliphage PR772 at the Linac coherent light source," *Sci. Data* **4**, 170079 (2017).
13. I. V. Lundholm, J. A. Sellberg, T. Ekeberg, M. F. Hantke, K. Okamoto, G. van der Schot, J. Andreasson, A. Barty, J. Bielecki, P. Bruza, M. Bucher, S. Carron, B. J. Daurer, K. Ferguson, D. Hasse, J. Krzywinski, D. S. D. Larsson, A. Morgan, K. Mühlig, M. Müller, C. Nettelblad, A. Pietrini, H. K. N. Reddy, D. Rupp, M. Sauppe, M. Seibert, M. Svenda, M. Swiggers, N. Timneanu, A. Ulmer, D. Westphal, G. Williams, A. Zani, G. Faigel, H. N. Chapman, T. Möller, C. Bostedt, J. Hajdu, T. Gorkhover, and F. R. N. C. Maia, "Considerations for three-dimensional image reconstruction from experimental data in coherent diffractive imaging," *IUCrJ* **5**, 531–541 (2018).
14. E. Sobolev, S. Zolotarev, K. Giewekemeyer, J. Bielecki, K. Okamoto, H. K. N. Reddy, J. Andreasson, K. Ayyer, I. Barak, S. Bari, A. Barty, R. Bean, S. Bobkov, H. N. Chapman, G. Chojnowski, B. J. Daurer, K. Dörner, T. Ekeberg, L. Flückiger, O. Galzitskaya, L. Gelisio, S. Hauf, B. G. Hogue, D. A. Horke, A. Hosseinizadeh, V. Ilyin, C. Jung, C. Kim, Y. Kim, R. A. Kirian, H. Kirkwood, O. Kulyk, J. Küpper, R. Letrun, N. D. Loh, K. Lorenzen, M. Messerschmidt, K. Mühlig, A. Ourmazd, N. Raab, A. V. Rode, M. Rose, A. Round, T. Sato, R. Schubert, P. Schwander, J. A. Sellberg, M. Sikorski, A. Silenzi, C. Song, J. C. H. Spence, S. Stern, J.



- Sztuk-Dambietz, A. Teslyuk, N. Timneanu, M. Trebbin, C. Uetrecht, B. Weinhausen, G. J. Williams, P. L. Xavier, C. Xu, I. A. Vartanyants, V. S. Lamzin, A. Mancuso, and F. R. N. C. Maia, "Megahertz single-particle imaging at the European XFEL," *Commun. Phys.* **3**, 97 (2020).
15. W. Decking, S. Abeghyan, P. Abramian, A. Abramsky, A. Aguirre, C. Albrecht, P. Alou, M. Altarelli, P. Altmann, K. Amyan, V. Anashin, E. Apostolov, K. Appel, D. Auguste, V. Ayvazyan, S. Baark, F. Babies, N. Baboi, P. Bak, V. Balandin, R. Baldinger, B. Baranasic, S. Barbanotti, O. Belikov, V. Belokurov, L. Belova, V. Belyakov, S. Berry, M. Bertucci, B. Beutner, A. Block, M. Blöcher, T. Böckmann, C. Bohm, M. Böhnert, V. Bondar, E. Bondarchuk, M. Bonezzi, P. Borowiec, C. Bösch, U. Bösenberg, A. Bosotti, R. Böspflug, M. Bousonville, E. Boyd, Y. Bozhko, A. Brand, J. Branlard, S. Briechle, F. Brinker, S. Brinker, R. Brinkmann, S. Brockhauser, O. Brovko, H. Brück, A. Brüdgam, L. Butkowski, T. Büttner, J. Calero, E. Castro-Carballo, G. Cattalanotto, J. Charrier, J. Chen, A. Cherepenko, V. Cheskidov, M. Chiodini, A. Chong, S. Choroba, M. Chorowski, D. Churanov, W. Cichalewski, M. Clausen, W. Clement, C. Cloué, J. A. Cobos, N. Coppola, S. Cunis, K. Czuba, M. Czwalińska, B. D'Almagne, J. Dammann, H. Danared, A. de Zubiare Wagner, A. Delfs, T. Delfs, F. Dietrich, T. Dietrich, M. Dohlus, M. Dommach, A. Donat, X. Dong, N. Doynikov, M. Dressel, M. Duda, P. Duda, H. Eckoldt, W. Ehsan, J. Eidam, and F. Eints, et al., "A MHz-repetition-rate hard x-ray free-electron laser driven by a superconducting linear accelerator," *Nat. Photonics* **14**, 391–397 (2020).
  16. N.-T. D. Loh and V. Elser, "Reconstruction algorithm for single-particle diffraction imaging experiments," *Phys. Rev. E* **80**, 026705 (2009).
  17. N. Roth, S. Awel, D. A. Horke, and J. Küpper, "Optimizing aerodynamic lenses for single-particle imaging," *J. Aerosol Sci.* **124**, 17–29 (2018).
  18. J. Bielecki, M. F. Hantke, B. J. Daurer, H. K. N. Reddy, D. Hasse, D. S. D. Larsson, L. H. Gunn, M. Svenda, A. Munke, J. A. Sellberg, L. Flueckiger, A. Pietrini, C. Nettelblad, I. Lundholm, G. Carlsson, K. Okamoto, N. Timneanu, D. Westphal, O. Kulyk, A. Higashiura, G. van der Schot, N.-T. D. Loh, T. E. Wysocki, C. Bostedt, T. Gorkhover, B. Iwan, M. M. Seibert, T. Osipov, P. Walter, P. Hart, M. Bucher, A. Ulmer, D. Ray, G. Carini, K. R. Ferguson, I. Andersson, J. Andreasson, J. Hajdu, and F. R. N. C. Maia, "Electrospray sample injection for single-particle imaging with x-ray lasers," *Sci. Adv.* **5**, eaav8801 (2019).
  19. A. K. Samanta, M. Amin, A. D. Estillone, N. Roth, L. Worbs, D. A. Horke, and J. Küpper, "Controlled beams of shock-frozen, isolated, biological and artificial nanoparticles," *Struct. Dyn.* **7**, 024304 (2020).
  20. A. P. Mancuso, A. Aquila, L. Batchelor, R. J. Bean, J. Bielecki, G. Borchers, K. Doerner, K. Giewekemeyer, R. Graceffa, O. D. Kelsey, Y. Kim, H. J. Kirkwood, A. Legrand, R. Letrun, B. Manning, L. Lopez Morillo, M. Messerschmidt, G. Mills, S. Raabe, N. Reimers, A. Round, T. Sato, J. Schulz, C. Signe Takem, M. Sikorski, S. Stern, P. Thute, P. Vagovič, B. Weinhausen, and T. Tschentscher, "The single particles, clusters and biomolecules and serial femtosecond crystallography instrument of the European XFEL: initial installation," *J. Synchrotron Radiat.* **26**, 660–676 (2019).
  21. B. Henrich, J. Becker, R. Dinapoli, P. Goettlicher, H. Graafsma, H. Hirsemann, R. Klanner, H. Krueger, R. Mazzocco, A. Mozzanica, H. Perrey, G. Potdevin, B. Schmitt, X. Shi, A. Srivastava, U. Trunk, and C. Youngman, "The adaptive gain integrating pixel detector AGIPD a detector for the European XFEL," *Nucl. Instrum. Methods Phys. A* **633**, S11–S14 (2011).
  22. S. Awel, R. A. Kirian, N. Eckerskorn, M. Wiedorn, D. A. Horke, A. V. Rode, J. Küpper, and H. N. Chapman, "Visualizing aerosol-particle injection for diffractive-imaging experiments," *Opt. Express* **24**, 6507–6521 (2016).
  23. M. F. Hantke, J. Bielecki, O. Kulyk, D. Westphal, D. S. Larsson, M. Svenda, H. K. Reddy, R. A. Kirian, J. Andreasson, J. Hajdu, and F. R. N. C. Maia, "Rayleigh-scattering microscopy for tracking and sizing nanoparticles in focused aerosol beams," *IUCrJ* **5**, 673–680 (2018).
  24. M. Rose, S. Bobkov, K. Ayyer, R. P. Kurta, D. Dzhigaev, Y. Y. Kim, A. J. Morgan, C. H. Yoon, D. Westphal, J. Bielecki, J. A. Sellberg, G. Williams, F. R. Maia, O. M. Yefanov, V. Ilyin, A. P. Mancuso, H. N. Chapman, B. G. Hogue, A. Aquila, A. Barty, and I. A. Vartanyants, "Single-particle imaging without symmetry constraints at an x-ray free-electron laser," *IUCrJ* **5**, 727–736 (2018).
  25. S. H. Scheres, M. Valle, R. Nuñez, C. O. Sorzano, R. Marabini, G. T. Herman, and J.-M. Carazo, "Maximum-likelihood multi-reference refinement for electron microscopy images," *J. Mol. Biol.* **348**, 139–149 (2005).
  26. N. D. Loh, M. J. Bogan, V. Elser, A. Barty, S. Boutet, S. Bajt, J. Hajdu, T. Ekeberg, F. R. N. C. Maia, J. Schulz, M. M. Seibert, B. Iwan, N. Timneanu, S. Marchesini, I. Schlichting, R. L. Shoeman, L. Lomb, M. Frank, M. Liang, and H. N. Chapman, "Cryptotomography: reconstructing 3D Fourier intensities from randomly oriented single-shot diffraction patterns," *Phys. Rev. Lett.* **104**, 225501 (2010).
  27. K. Ayyer, T.-Y. Lan, V. Elser, and N. D. Loh, "Dragonfly: an implementation of the expand–maximize–compress algorithm for single-particle imaging," *J. Appl. Crystallogr.* **49**, 1320–1335 (2016).
  28. H. T. Philipp, K. Ayyer, M. W. Tate, V. Elser, and S. M. Gruner, "Solving structure with sparse, randomly-oriented x-ray data," *Opt. Express* **20**, 13129–13137 (2012).
  29. K. Giewekemeyer, A. Aquila, N.-T. D. Loh, Y. Chushkin, K. S. Shanks, J. Weiss, M. W. Tate, H. T. Philipp, S. Stern, P. Vagovic, M. Mehrjoo, C. Teo, M. Barthelmeß, F. Zontone, C. Chang, R. C. Tiberio, A. Sakdinawat, G. J. Williams, S. M. Gruner, and A. P. Mancuso, "Experimental 3D coherent diffractive imaging from photon-sparse random projections," *IUCrJ* **6**, 357–365 (2019).
  30. P. J. Ho, B. J. Daurer, M. F. Hantke, J. Bielecki, A. Al Haddad, M. Bucher, G. Doumy, K. R. Ferguson, L. Flückiger, T. Gorkhover, B. Iwan, C. Knight, S. Moeller, T. Osipov, D. Ray, S. H. Southworth, M. Svenda, N. Timneanu, A. Ulmer, P. Walter, J. Hajdu, L. Young, F. R. N. C. Maia, and C. Bostedt, "The role of transient resonances for ultra-fast imaging of single sucrose nanoclusters," *Nat. Commun.* **11**, 167 (2020).
  31. N. D. Loh, D. Starodub, L. Lomb, C. Y. Hampton, A. V. Martin, R. G. Sierra, A. Barty, A. Aquila, J. Schulz, J. Steinbrener, R. L. Shoeman, S. Kassemeyer, C. Bostedt, J. Bozek, S. W. Epp, B. Erk, R. Hartmann, D. Rolles, A. Rudenko, B. Judek, L. Foucar, N. Kimmel, G. Weidenspointner, G. Hauser, P. Holl, E. Pedersoli, M. Liang, M. S. Hunter, L. Gumprecht, N. Coppola, C. Wunderer, H. Graafsma, F. R. Maia, T. Ekeberg, M. Hantke, H. Fleckenstein, H. Hirsemann, K. Nass, T. A. White, H. J. Tobias, G. R. Farquar, W. H. Benner, S. Hau-Riege, C. Reich, A. Hartmann, H. Soltau, S. Marchesini, S. Bajt, M. Barthelmeß, L. Strueder, J. Ullrich, P. Bucksbaum, M. Frank, I. Schlichting, H. N. Chapman, and M. J. Bogan, "Sensing the wavefront of x-ray free-electron lasers using aerosol spheres," *Opt. Express* **21**, 12385–12394 (2013).
  32. T.-Y. Lan, J. L. Wierman, M. W. Tate, H. T. Philipp, V. Elser, and S. M. Gruner, "Reconstructing three-dimensional protein crystal intensities from sparse unoriented two-axis x-ray diffraction patterns," *J. Appl. Crystallogr.* **50**, 985–993 (2017).
  33. Y.-P. Chang, D. A. Horke, S. Trippel, and J. Küpper, "Spatially-controlled complex molecules and their applications," *Int. Rev. Phys. Chem.* **34**, 557–590 (2015).
  34. K. Ayyer, "Reference-enhanced x-ray single-particle imaging," *Optica* **7**, 593–601 (2020).
  35. I. Barke, H. Hartmann, D. Rupp, L. Flückiger, M. Sauppe, M. Adolph, S. Schorb, C. Bostedt, R. Treusch, C. Peltz, S. Bartling, T. Fennel, K.-H. Meiwes-Broer, and T. Möller, "The 3D-architecture of individual free silver nanoparticles captured by x-ray scattering," *Nat. Commun.* **6**, 6187 (2015).
  36. B. Langbehn, K. Sander, Y. Ovcharenko, C. Peltz, A. Clark, M. Coreno, R. Cucini, M. Drabfels, P. Finetti, M. Di Fraia, L. Giannessi, C. Grazioli, D. Iablonskyi, A. C. LaForge, T. Nishiyama, V. Oliver Álvarez de Lara, P. Piseri, O. Plekan, K. Ueda, J. Zimmermann, K. C. Prince, F. Stienkemeier, C. Callegari, T. Fennel, D. Rupp, and T. Möller, "Three-dimensional shapes of spinning helium nanodroplets," *Phys. Rev. Lett.* **121**, 255301 (2018).

---

## Staff-driven publications

This section includes the following staff-driven publications.

### **The Single Particles, Clusters and Biomolecules and Serial Femtosecond Crystallography instrument of the European XFEL: initial installation**

A.P. Mancuso et al.: J. Synchrotron Rad. **26** (3), 1–17 (2019)

doi:10.1107/S1600577519003308

### **Megahertz x-ray microscopy at x-ray free-electron laser and synchrotron sources**

P. Vagovič et al.: Optica **6** (9), 1106 (2019)

doi:10.1364/OPTICA.6.001106

### **Femtosecond timing synchronization at megahertz repetition rates for an x-ray free-electron laser**

T. Sato et al.: Optica **7** (6), 716 (2020)

doi:10.1364/OPTICA.396728



Received 4 November 2018  
Accepted 7 March 2019

<sup>†</sup>This article will form part of a virtual special issue on X-ray free-electron lasers.

‡ Current address: SLAC National Accelerator Laboratory, 2575 Sand Hill Road, Menlo Park, CA, 94025, USA.

§ Current address: Arizona State University, School of Molecular Sciences and Biodesign Institute – Center for Applied Structural Discovery, Tempe, AZ 85287, USA.

¶ Current address: Deutsches Elektronen-Synchrotron, Notkestraße 85, 22607 Hamburg, Germany.

**Keywords:** XFEL; serial crystallography; instrumentation.

# The Single Particles, Clusters and Biomolecules and Serial Femtosecond Crystallography instrument of the European XFEL: initial installation<sup>1</sup>

Adrian P. Mancuso,<sup>a,b\*</sup> Andrew Aquila,<sup>a,‡</sup> Lewis Batchelor,<sup>a</sup> Richard J. Bean,<sup>a</sup> Johan Bielecki,<sup>a</sup> Gannon Borchers,<sup>a</sup> Katerina Doerner,<sup>a</sup> Klaus Giewekemeyer,<sup>a</sup> Rita Graceffa,<sup>a</sup> Oliver D. Kelsey,<sup>a</sup> Yoonhee Kim,<sup>a</sup> Henry J. Kirkwood,<sup>a</sup> Alexis Legrand,<sup>a</sup> Romain Letrun,<sup>a</sup> Bradley Manning,<sup>a</sup> Luis Lopez Morillo,<sup>a</sup> Marc Messerschmidt,<sup>a,§</sup> Grant Mills,<sup>a</sup> Steffen Raabe,<sup>a,c</sup> Nadja Reimers,<sup>a</sup> Adam Round,<sup>a</sup> Tokushi Sato,<sup>a,c</sup> Joachim Schulz,<sup>a</sup> Cedric Signe Takem,<sup>a</sup> Marcin Sikorski,<sup>a</sup> Stephan Stern,<sup>a,¶</sup> Prasad Thute,<sup>a</sup> Patrik Vagovič,<sup>a,c</sup> Britta Weinhausen<sup>a</sup> and Thomas Tschentscher<sup>a</sup>

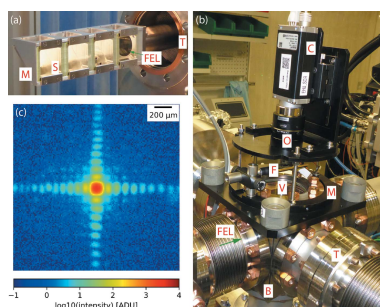
<sup>a</sup>European XFEL, Holzkoppel 4, 22869 Schenefeld, Germany, <sup>b</sup>Department of Chemistry and Physics, La Trobe Institute for Molecular Science, La Trobe University, Melbourne, Victoria 3086, Australia, and <sup>c</sup>Center for Free Electron Laser Science, Deutsches Elektronen-Synchrotron, Notkestraße 85, 22607 Hamburg, Germany.

\*Correspondence e-mail: adrian.mancuso@xfel.eu

The European X-ray Free-Electron Laser (FEL) became the first operational high-repetition-rate hard X-ray FEL with first lasing in May 2017. Biological structure determination has already benefitted from the unique properties and capabilities of X-ray FELs, predominantly through the development and application of serial crystallography. The possibility of now performing such experiments at data rates more than an order of magnitude greater than previous X-ray FELs enables not only a higher rate of discovery but also new classes of experiments previously not feasible at lower data rates. One example is time-resolved experiments requiring a higher number of time steps for interpretation, or structure determination from samples with low hit rates in conventional X-ray FEL serial crystallography. Following first lasing at the European XFEL, initial commissioning and operation occurred at two scientific instruments, one of which is the Single Particles, Clusters and Biomolecules and Serial Femtosecond Crystallography (SPB/SFX) instrument. This instrument provides a photon energy range, focal spot sizes and diagnostic tools necessary for structure determination of biological specimens. The instrumentation explicitly addresses serial crystallography and the developing single particle imaging method as well as other forward-scattering and diffraction techniques. This paper describes the major science cases of SPB/SFX and its initial instrumentation – in particular its optical systems, available sample delivery methods, 2D detectors, supporting optical laser systems and key diagnostic components. The present capabilities of the instrument will be reviewed and a brief outlook of its future capabilities is also described.

## 1. Introduction

The recently operational European X-ray Free-Electron Laser (EuXFEL) is the first high-repetition-rate hard X-ray FEL in the world (Abela *et al.*, 2006). The initial suite of six scientific instruments is designed to pursue a wide range of science applications exploiting both the ultrafast and ultrabright pulses of X-ray FEL radiation produced, as well as uniquely utilizing the megahertz (MHz) peak repetition rate of this unprecedented facility (Tschentscher *et al.*, 2017). The Single Particles, Clusters and Biomolecules and Serial Femtosecond Crystallography (SPB/SFX) instrument is one of the first two



OPEN ACCESS

instruments to come online and perform experiments with the EuXFEL beam and has produced first results less than a year after first experiments (Grünbein *et al.*, 2018; Wiedorn *et al.*, 2018).

The SPB/SFX instrument is primarily concerned with 3D structure determination of both crystalline and non-crystalline micrometre-scale and smaller objects. A particular emphasis is placed on biological objects, including viruses, biomolecules and protein crystals. Nevertheless, the instrument will also be capable of investigating non-biological samples using similar techniques. The instrument exploits the unique high peak repetition rate of the facility and brings benefit to these structural biology applications. The major benefits are the reduction in the experimental time required to measure a complete dataset for structure determination, particularly in time-resolved experiments and potential reduction in sample consumption in some methods.

The goal of this paper is to describe the capabilities of the SPB/SFX instrument in its early operational phase. Future capabilities, such as additional interaction regions for further experiments (such as in-atmosphere experiments) are also briefly outlined. The instrument relies on a variety of complex systems, many of which are described in more detail in this journal. These systems include the accelerator (Decking *et al.*, 2019), the photon transport systems (Sinn *et al.*, 2019) from EuXFEL's undulator source (Abeghyan *et al.*, 2019) to the instrument and the detector systems (Henrich *et al.*, 2011); in addition, the optical laser systems (Palmer *et al.*, 2019) that provide optical pulses at the same repetition rate as the EuXFEL for so-called pump–probe experiments that excite ('pump') a system with an optical pulse and investigate ('probe') it with the X-ray FEL pulses (or vice versa). All of this activity is supported by the controls system (Heisen *et al.*, 2013; Hauf *et al.*, 2019) while the extreme data rate due to the high repetition rate is managed by a state-of-the-art data acquisition and storage system (Boukhelef *et al.*, 2013). An essential part of fully utilizing the instrument is the data analysis tools to make sense of the so-called 'data deluge' which, while essential to the successful realization of experiments, is beyond the scope of this paper. EuXFEL data analysis tools are discussed in general by Fangohr *et al.* (2018).

This paper primarily documents the initial configuration of the instrument as commissioned for early user experiments in late 2017 and 2018. Some outlook is given towards the additional instrumentation to be installed in 2019, in particular brief descriptions of the additional interaction regions contributed by the SFX user consortium (SFX User Consortium, 2013), which will both broaden the instrument capability and increase its capacity in the near future.

## 2. Science targets for the instrument

The SPB/SFX instrument predominantly caters to structure determination of biological systems, both crystalline samples and single particles. Potentially, any sample that can be investigated by forward-scattering methods may be probed at SPB/SFX, with the major use cases outlined below. These use

cases are very similar to those of the Coherent X-ray Imaging (CXI) instrument at LCLS (Boutet & Williams, 2010), which has pioneered this science at 120 Hz repetition rate.

### 2.1. Serial crystallography

The relatively recent advent of structure determination from micrometre- and sub-micrometre-sized crystals of biomolecules using X-ray FEL sources (Chapman *et al.*, 2011; Aquila *et al.*, 2012; Boutet *et al.*, 2012; Redecke *et al.*, 2013; Liu *et al.*, 2013; Barends *et al.*, 2014) represents a significant broadening of the scope of crystallography for biological structure determination (Standfuss & Spence, 2017). Importantly, serial crystallography at FELs addresses three major classes of sample: (i) those that do not form large enough crystals to provide an adequate signal-to-noise ratio for analysis of their diffraction using a synchrotron source (Redecke *et al.*, 2013), (ii) those containing metal atoms that may be easily altered chemically by longer duration synchrotron radiation (and hence not reflect the native structure of the sample) (Suga *et al.*, 2014), and (iii) time-resolved systems, where either femtosecond time resolution is needed or, for example, irreversible reactions such as mixing which requires small crystals to minimize the mixing time and define a clear  $t_0$  as the start of the reaction (Schmidt, 2013).

### 2.2. Single particle imaging

Arguably one of the most exciting classes of samples for structure determination at an X-ray FEL facility encompasses those samples where each individual sample exhibits the same, or markedly similar, structure as the others. A so-called 'reproducible' sample allows for the collection of data from many copies of such samples. Naively, each individual sample illuminated with the X-ray FEL beam scatters 2D data into a 2D detector at the instrument. Reproducible samples allow the aggregation of that data from many randomly oriented copies of the sample into a single piece of 3D information about the sample (Neutze *et al.*, 2000; Ekeberg *et al.*, 2015). This method is referred to as single particle imaging (SPI). The method is presently under development (Aquila *et al.*, 2015a; Daurer *et al.*, 2017; Hantke *et al.*, 2018) and typically requires a large amount of diffraction data for successful three-dimensional reconstruction (Rose *et al.*, 2018; Lundholm *et al.*, 2018). The SPB/SFX instrument has the potential to collect SPI data almost 30 times faster than the X-ray FEL with the next highest repetition rate, potentially a significant step in this method's development to application.

### 2.3. Time-resolved experiments

One of the key advantages of X-ray FELs is in the ability to access the time domain on femtosecond timescales. This can be done either by exploiting the femtosecond pulse duration of an X-ray FEL to probe femtosecond timescale science, such as in the switching of magnetic structures (Beaurepaire *et al.*, 2004; Higley *et al.*, 2016), or by using an X-ray FEL's extraordinary pulse intensities to allow the probing of irreproducible processes that require sufficient information to be

acquired at each time point from a single measurement, such as mixing a protein with an antibiotic, or other mixing processes (Stagno *et al.*, 2016). The EuXFEL's vastly greater repetition rate than other X-ray FEL sources is particularly attractive for time-resolved studies, as it allows for the collection of sufficient data from multiple time points within a realistic and manageable experiment duration. This then allows for a far greater number of time points to be explored, which is useful when changes in a sample occur over a variety of timescales or when one simply does not know the ideal timescale to make observations *a priori* and a survey in time is needed to establish the appropriate measurement parameters.

In addition to mixing experiments (Schmidt, 2013; Stagno *et al.*, 2016), reactions in bio-systems started by optical pulses are the other most common type of time-resolved experiment considered here. Pump–probe experiments excite a sample by an optical ‘pump’, causing changes to its structure. The subsequent X-ray FEL ‘probe’ is used to observe its structure some defined time after the excitation. Doing so for a number of different delay times between pump and probe allows for a so-called ‘molecular movie’ of the structural changes to be made (Tenboer *et al.*, 2014; Barends *et al.*, 2015; Levantino *et al.*, 2015a; Pande *et al.*, 2016; Nango *et al.*, 2016), giving insights into the dynamics of such light-activated systems.

#### 2.4. Further science goals

Additional science cases include those supported by other classes of forward-scattering experiments, such as time-resolved small-angle X-ray scattering (Graceffa *et al.*, 2013; Levantino *et al.*, 2015b; Bruetzel *et al.*, 2018; Röllen *et al.*, 2018) and X-ray photon correlation spectroscopy (XPCS) (Carnis *et al.*, 2014; Lehmkuhler *et al.*, 2015).

### 3. Science requirements

The science requirements of the instrument are derived directly from the science cases above and have not changed markedly since their publication in the SPB Technical Design Report (TDR) (Mancuso *et al.*, 2013). Importantly, the sample–detector distance must be compatible with the resolution and sampling requirements of samples of the order of less than 100 nm to approximately 1  $\mu\text{m}$  in size [typical protein and/or protein (micro-/nano-)crystal sizes] (The AGIPD Consortium, 2012; Giewekemeyer *et al.*, 2013). The 2D detector used must have a very high dynamic range to accommodate not only the brightest signals from crystal Bragg peaks but also low signal on a single photon level, *e.g.* from the continuous diffraction between Bragg peaks (Ayyer *et al.*, 2016), which may fall into adjacent pixels in any practical detector. Single-photon sensitivity is also essential for SPI applications where a weakly scattering non-crystalline sample is envisaged and only a few photons per frame may be collected by the 2D detector (Loh & Elser, 2009; Ayyer *et al.*, 2014).

The X-ray focal spot size must also match these size ranges to optimally illuminate these smaller and larger samples. In

**Table 1**

Summary of basic parameters of the the SPB/SFX instrument.

Parameter	Value/range	Units
Photon energy	3–16	keV
Pulse energy (maximum)	~1–5	mJ
Photons per pulse (maximum)	~1–8	$10^{12}$ photons
Focal spot size	~100s, 1	nm, $\mu\text{m}$
Repetition rate	$10 \times 1350$ (maximum at highest pulse energy) $10 \times 2700$ (maximum at lower pulse energies)	$\text{s}^{-1}$
Pulse duration (range)	A few 100	fs
Detector pixel size (AGIPD)	$200 \times 200$	$\mu\text{m}$
Upstream detector	AGIPD, four independent quadrants ( $4 \times 512 \times 512$ pixels)	NA
Downstream detectors (to be installed in future)	AGIPD and Jungfrau, both 4 megapixel	NA
Single-photon sensitivity	Yes	NA
Detector dynamic range at 12 keV	$>10^4$	photons
Detector frame rate AGIPD (burst)	4.5	MHz
Sample–detector distances	0.12 to ~6	m
Sample delivery options	Liquid jet, aerosol jet, fixed targets	NA
Miscellanea	Pump–probe laser	NA

practice, a variation of focal spot sizes at the sample position differing by an order of magnitude in lateral extent is desirable, realized at SPB/SFX by two independent focusing mirror systems.

Updated instrument parameters are shown in Table 1. While there have been a great deal of developments in serial crystallography and single particle imaging since the TDR (Mancuso *et al.*, 2013) was written, only relatively minor updates to the target parameters have been necessary.

### 4. Instrumentation

The SPB/SFX instrument layout and instrumentation have been designed to accommodate experiments that lie within the main science goals while maintaining flexibility for future upgrades and alternative experiment types (Mancuso *et al.*, 2013). SPB/SFX is a forward-scattering instrument, with multiple optical systems to focus the FEL beam, a flexible sample–X-ray beam interaction environment with integrated sample-pump laser system, and an X-ray detector that is designed to collect scattering around the incident beam axis. These principal components are complemented by an array of X-ray beam conditioning and diagnostic devices. An iconographic overview of the instrument with the currently installed instrumentation is shown in Fig. 1.

The SPB/SFX instrument is designed to operate at photon energies from 3 to 16 keV, with peak performance expected between about 6 and 15 keV. The SPB/SFX instrument is located behind the SASE1 undulator, with X-ray beam delivered via a dedicated branch in the XTD9 photon tunnel (Sinn *et al.*, 2019). Instrumentation is installed in the XTD9 tunnel, an instrument optics hutch and an experiment hutch.

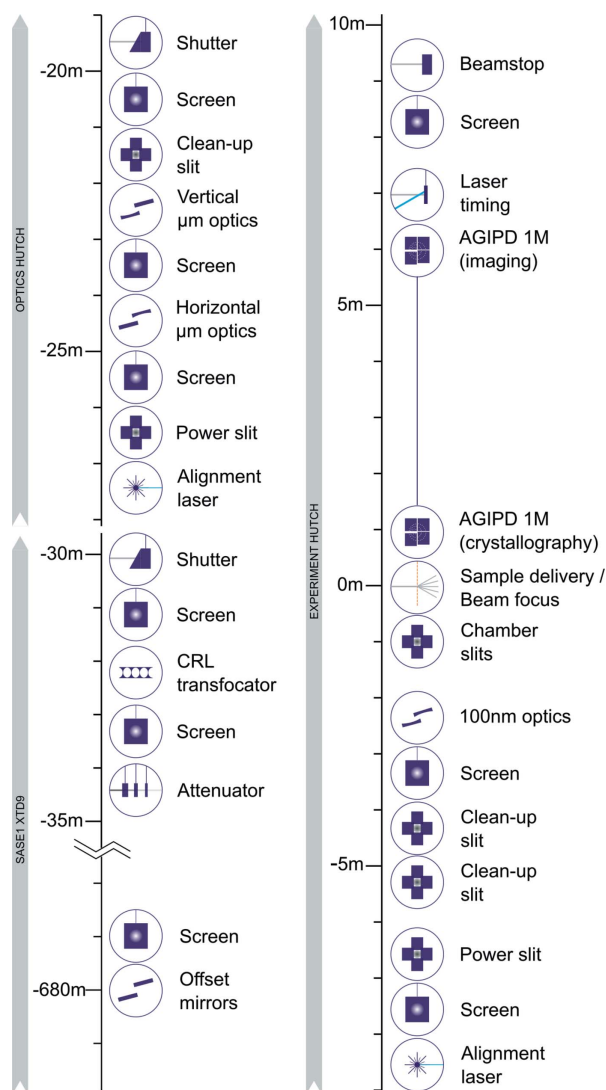


**Figure 1** Iconographic layout of components of the SPB/SFX instrument. Approximate distances of components in the SASE1 XTD9 tunnel, SPB/SFX optics hutch and SPB/SFX experiment hutch are given relative to the common focal plane of the upstream interaction region. X-ray beam direction is indicated by the grey arrows.

The geographical layout of SPB/SFX, including the relevant tunnel and hutches, is shown in Fig. 2.

The most upstream components of the SPB/SFX instrument – train picker, attenuator array and incoming beam diagnostic screen – are housed in the last metres of the SPB/SFX photon branch line in the XTD9 tunnel, upstream of the instrument shutter. A compound refractive lens system, used to provide focusing prior to the commissioning of the mirror-based focusing systems, was also installed at this location.

Directly following the tunnel downstream wall, the optics hutch houses a reference laser system (also sometimes called an alignment laser system), an aperture-defining B<sub>4</sub>C blade slit system, two vacuum chambers containing mirror optics of the micrometre-scale KB focusing system, clean-up slits to remove scatter around the beam, and a shutter to control transmission of the X-ray beam to the experiment hutch. Three diagnostic

screens are located at the upstream, centre and downstream ends of the mirror chambers to aid mirror alignment.

Following ~12 m of beam transport, the most upstream component in the SPB/SFX experiment hutch is a second reference laser system followed by a diagnostic screen and a second aperture-defining B<sub>4</sub>C blade slit system. Two sets of beam clean-up slits and a beam diagnostic screen immediately precede a vacuum chamber containing mirror optics of the 100 nm-scale focusing system.

Downstream of the 100 nm-scale optical chamber, a differential pumping system is installed to support sample-injection compatible vacuum conditions in the X-ray beam-sample interaction region. The interaction region comprises a large vacuum chamber ~600 mm × 600 mm × 800 mm (w × h × l), with infrastructure for several sample delivery methods, pump-laser in-coupling, imaging and diagnostics. The 100 nm-scale optical system and interaction chamber breadboard share a common granite support, which is designed to minimize any effect of vibration on the X-ray optical alignment of the 100 nm-scale beam.

The centralized SASE1 pump-laser system (Palmer *et al.*, 2019) is installed in an adjacent hutch and supplies the SPB/SFX instrument laser hutch with optical laser light at a repetition rate matched to that of the EuXFEL. Additional frequency conversion, beam conditioning and delay adjustment are implemented in the instrument laser hutch prior to delivery into the experiment hutch and interaction region.

The principal X-ray detector for the SPB/SFX instrument, the AGIPD 1 megapixel, is mounted into a carriage mated directly to the downstream flange of the interaction region chamber. The interaction region chamber and downstream devices including AGIPD are mounted onto a common rail system – the component support structure (CSS) – designed to move in order to track the X-ray beam trajectory, while preserving the alignment of downstream components. The detector carriage can be moved longitudinally along the rail, supporting sample-detector distances between 120 mm and 6000 mm.

A diagnostics screen and instrument beamstop occupy the downstream end of the CSS and are currently the final components of the SPB/SFX instrument, pending installation and commissioning of a second interaction region.

#### 4.1. Optics and beam conditioning

**4.1.1. Compound refractive lenses: initial focusing optics.** For the initial operation of the instrument during early user experiments (September 2017 to June 2018), focusing optics based on beryllium compound refractive lenses (CRLs) were installed to focus the beam to the X-ray-sample interaction point. The lenses are housed in a dedicated translocator containing ten arms, each capable of holding up to ten lenses (JJ X-ray AS, Denmark). An image of the translocator is shown in Fig. 3. The installation position at the end of the XTD9 tunnel and the long source-to-translocator (~888 m) and translocator-to-focus (~32 m) distances set the parameters of the lenses required.

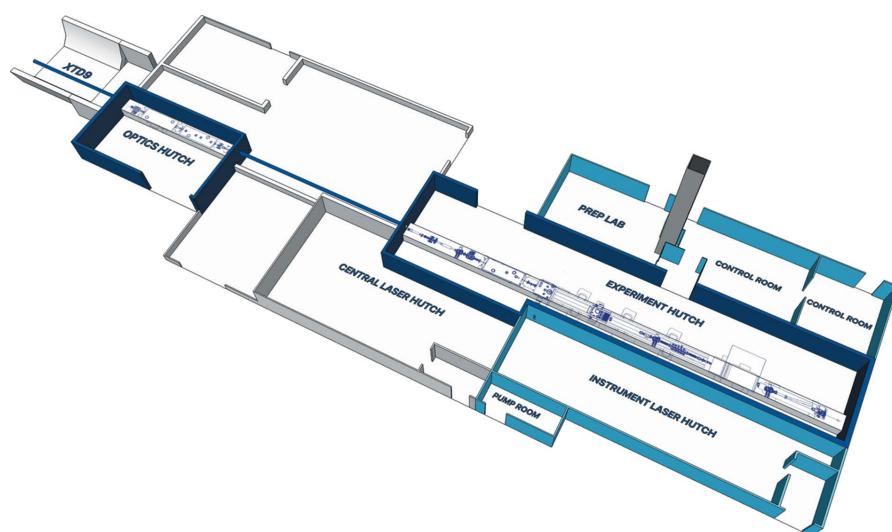


**Figure 2**  
Overview of SASE1 hutches. X-ray beam direction is left to right, top to bottom. SPB/SFX X-ray radiation hutches are depicted in dark blue with SPB/SFX laser hutches, laboratory, control rooms and service rooms depicted in light blue. The vertical column in grey is the so-called ‘sample elevator’ used to transport material from the upstairs biological laboratory to the preparation laboratory adjacent to the SPB/SFX experiment hatch. A 2D overhead engineering view of the instrumentation is placed into the hatch model for context.



**Figure 3**  
CAD-model of the JJ X-ray translocator unit (left) and photograph of the lens cassettes inside the chamber installed in the XTD9 tunnel (right).

To be able to focus over such long distances, lenses with large radii of curvature are required. Given the initial incoming X-ray beam parameters and minimal required energy range, 30 lenses with radii of curvature 5.8 mm and aperture 3 mm with beryllium grade IS50 (purchased from RXOPTICS GmbH & Co. KG, Germany) were installed, the largest radius of curvature available at the time of purchase.

Lenses were mounted into the lens cassettes in a binary configuration to enable a minimum increment of one lens for any lens configuration, as shown in Fig. 4. With the limitations on radius of curvature, the addition or removal of one lens adjusts the focus position by more than 1 m, larger than the longitudinal movement range of the translocator. Fine tuning of the focus position to match the sample interaction point was successfully achieved by adjustment of the undulator gap and hence shifting the photon energy.

An image of the CRL-focused beam interaction with a 20  $\mu\text{m}$ -thick cerium-doped yttrium aluminium garnet crystal (YAG:Ce) (Crytur, Turnov, Czech Republic) produced an upper bound on the focus size of  $\sim 16 \mu\text{m}$ . This is larger than modelling would suggest and could be due to a number of reasons. Possibilities include (i) the chromaticity of the beam being greater than expected, (ii) the XFEL source being different from that expected, or even (iii) non-optimal alignment of the lens units. In practice, this limitation has been addressed by the replacement of the CRLs as the temporary, primary focusing optic by a super-polished mirror focusing system described in the next section.

**4.1.2. Super-polished mirror focusing systems.** The SPB/SFX instrument has two independent KB super-polished elliptical-mirror-based systems, focusing to the micrometre scale and 100 nm scale, to meet the variable X-ray beam size requirements of the science targets discussed in the preceding

Arm Number		10	9	8	7	6	5	4	3	2	1
Position in lens cassette	1										
	2										
	3										
	4										
	5										
	6										
	7										
	8										
	9										
	10										
Total number of lenses in cassette		0	0	0	1	2	4	5	8	10	0

**Figure 4**  
Arrangement of the beryllium lenses in the translocator unit, where green colour indicates in which position within the lens cassette the lens is placed. The arrangement is such that differing numbers of lenses can be placed into the beam by moving arms in or out, allowing for the focusing of different photon energies to the same plane in the interaction region.

section. KB mirror systems were chosen as they are highly transmissive, achromatic and expected to survive the pulse train structure of the EuXFEL and largely preserve the wavefront properties of the FEL beam, critical for coherent imaging-type experiments. Both systems are designed to focus the X-ray beam to a common focal plane at the upstream interaction region of the instrument (see Fig. 1). At the time of writing, the micrometre-scale system has recently been commissioned and used in a small number of experiments. The focused beam from these optics was initially imaged at 5  $\mu\text{m}$ , and recently improved to better than 3  $\mu\text{m}$  as imaged with a 3.7  $\mu\text{m}$ -thick LYSO:Ce ( $\text{Lu}_{1.8}\text{Y}_{0.2}\text{SiO}_5\text{:Ce}$ ) scintillator at the interaction point. Continued commissioning and optimization of this focal spot is ongoing.

The optics of the 100 nm-scale system have recently been installed, with commissioning and first experimental use expected for mid-2019. Details of the performance of both mirror optical systems will be the subject of future publications.

The SPB/SFX instrument occupies the central branch of the SASE1 undulator beamline, minimizing the number of optical elements between the source and instrument focusing optics. The source point, estimated to be in the second-to-last undulator cell, is  $918 \pm 2$  m from the instrument common focal plane (Bean *et al.*, 2016). The first optical elements in the SASE1 beamline are two  $\text{B}_4\text{C}$ -coated flat offset mirrors installed for radiation protection. The second mirror includes a bender to allow flatness correction or to produce an intermediate focus between the offset mirrors and instrument optics (Sinn *et al.*, 2012; Tschentscher *et al.*, 2017). The position of the KB optic systems between the undulator source and instrument focus is determined by geometrical optics arguments, accounting for the predicted source size, desired focal size and source-to-focus distance. Given the large source–focus distance and expected beam divergence, 1000 mm silicon substrate mirrors (with 950 mm super-polished length) are installed. To maximize the available aperture, the mirror optics are designed for relatively high incidence angles of 4 mrad in the micrometre-scale case and 3.5 mrad in the 100 nm-scale case, with resulting apertures of 3.8 mm and 3.3 mm, respectively (Bean *et al.*, 2016). All mirrors are coated with two stripes,  $\text{B}_4\text{C}$  and ruthenium, each 50 nm thick, for good transmission across the 3–16 keV working energy range of the instrument. Test measurements suggest that the coatings will survive the oper-

ating conditions at the SPB/SFX instrument (Aquila *et al.*, 2015b). Further details on the polishing and control specifications of the mirrors are given by Bean *et al.* (2016).

The micrometre-scale system is located in the optics hutch, centred 23.2 m from the upstream interaction region common focal plane and 894.8 m from the predicted SASE1 source point. The two KB ellipses are incorporated into a four-bounce mirror system, with two additional flat mirrors of the same polishing and coating specifications, resulting in a focused beam with parallel trajectory and small offset from the direct beam. The depth of focus of the micrometre-scale system is calculated to be  $\sim 10$  mm.

The 100 nm-scale system is located directly upstream of the interaction region, centred 2.75 m upstream of the common focal plane. The 100 nm system uses a traditional two-bounce KB mirror scheme resulting in a 7 mrad angular deviation of the 100 nm-scale focused beam with respect to the direct beam. The depth of focus of the 100 nm-scale system is  $\sim 0.15$  mm.

Representation of the horizontal and vertical optical paths of the direct, micrometre-scale and 100 nm-scale beams through the SPB/SFX instrument are shown in Figs. 5 and 6.

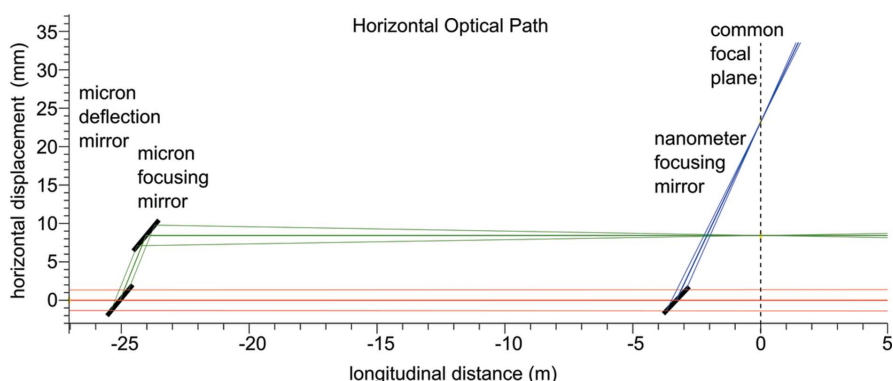


**Figure 5** Representation of the horizontal optical layout of the SPB/SFX instrument. The incident beam from XTD9 is shown in red, with the 1  $\mu\text{m}$ -scale system in green and the 100 nm-scale system in blue. The 0 m mark in the longitudinal distance denotes the common focal plane of the two systems. Figure adapted from Bean *et al.* (2016).

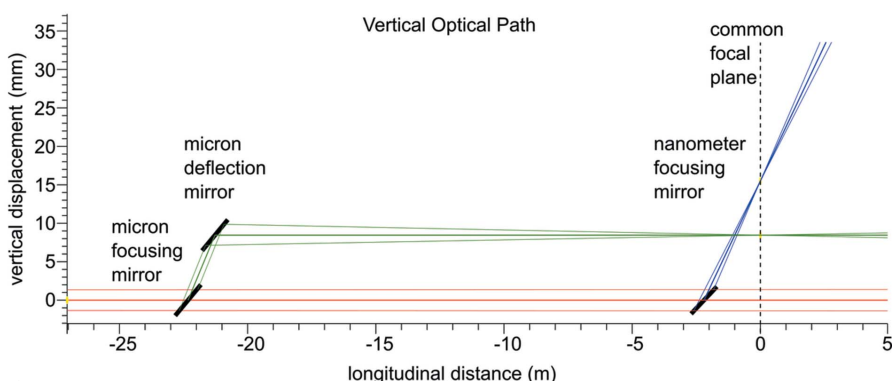


**Figure 6** Representation of the vertical optical layout of the SPB/SFX instrument. The incident beam from XTD9 is shown in red, with the 1  $\mu\text{m}$ -scale system in green and the 100 nm-scale system in blue. The 0 m mark in the longitudinal distance denotes the common focal plane of the two systems. Figure adapted from Bean *et al.* (2016).



**4.1.3. Train picker.** A train-picker device is installed as the most upstream component of the SPB/SFX instrumentation in the XTD9 photon tunnel. This device is designed to pass individual (10 Hz) trains from the accelerator to the experiment either ‘on demand’ or synchronized with sample environment hardware. The key component is a notched disc which rotates to alternately block the beam or allow it to pass. The disc is composed of 2 mm B<sub>4</sub>C and 0.5 mm alloy of 98.5% tungsten with Ni and Fe. The train picker is intended for use only in low-power beam modes of 30 pulses per train or fewer.

**4.1.4. Beam conditioning.** To define the shape of the X-ray beam incident on the focusing optics, both the micrometre-scale and nano-scale focusing optics are accompanied by a slit system optimized for high incident beam power (JJ X-ray AS, Denmark). These so-called ‘power’ slits are equipped with four mechanically independent B<sub>4</sub>C ‘blades’ with a thickness of 75 mm along the beam direction. While B<sub>4</sub>C is among the materials with the lowest single-shot damage threshold for FEL radiation, it has a relatively long absorption length, especially at high X-ray energies. To more fully suppress radiation at higher energies, the B<sub>4</sub>C blocks are equipped with a 5 mm-thick sheet of tungsten on the downstream side. While the power slits are capable of blocking the unfocused incident beam at 10 Hz operation, they are not designed to withstand full pulse trains at 4.5 MHz with full beam power under all possible experimental conditions. In order to avoid overheating of the aperture-defining blocks under UHV conditions, each block is actively water-cooled.

A second set of slit systems is used to suppress scattering from the power slits and other sources of scattering such as the edges of the focusing mirrors. Permanent ‘cleanup’ slit installations (JJ X-ray AS, Denmark) are located between the micrometre-scale and the 100 nm-scale KB systems (see Fig. 1). Blade edges are composed of polished cylinders, fabricated in silicon nitride (low-*Z* option; JJ X-ray AS, Denmark) or wedge-shaped tantalum/tungsten (high-*Z* option; Xenocs SAS, France). Additional slit sets (customized development) can be installed inside the interaction region chamber to block remaining scatter close to the focus position. Polished cylinder-based blade edges of silicon nitride, tantalum/tungsten or germanium are available.

A solid attenuator array is installed to attenuate beam intensity in beam modes of up to tens of pulses per train. This compact device (JJ X-ray AS, Denmark) has four water-cooled arms, each equipped with six filters. Filters are primarily single crystal silicon, with thicknesses between 25 µm and 6.4 mm and polycrystalline synthetic diamond with thicknesses between 100 µm and 3.2 mm. Each arm can be inserted independently, giving a large range of possible attenuation options, roughly at least one combination in every magnitude interval of the transmission factors between 1 and  $<10^{-12}$  over the 3–16 keV operating energy range of the SPB/SFX instrument.

**4.1.5. Beam diagnostics.** To ensure an efficient alignment process of the complex X-ray optical focusing system and to maintain a high focus quality in the interaction region, 2D beam diagnostic devices are essential, especially for an FEL

instrument (Tono *et al.*, 2011, 2013; Juranić *et al.*, 2018). For the first operation phase (before completion of the downstream interaction region), seven such devices are available at the SPB/SFX instrument, monitoring the beam at locations starting in the photon tunnel, before interaction with any focusing optics, down to the end of the instrument, immediately upstream of the instrument beam stop. To accommodate various beam sizes and positions at different locations within the instrument and also for different focusing schemes, two variations of the screen devices have been devised with different scintillator sizes (Type I and Type II, see below). Both screen types are non-transmissive. The series of screens allow monitoring of the beam position, trajectory, shape and internal structure.

The diagnostic screens, designed and built in-house, are based on flat scintillating screens with a standard thickness of 100 µm, made of single-crystal cerium-doped yttrium aluminium garnet (YAG:Ce) (Crytur, Turnov, Czech Republic). Scintillators are placed at 90° with respect to the X-ray optical axis, and an optically flat,  $\lambda/10$ , Al-coated fused silica mirror at 45° incidence angle is used to reflect the scintillation light through a high-grade anti-reflection-coated optical viewport, with flatness specification in the central region of  $\lambda/8$ , into an objective outside the vacuum chamber. Scintillators and mirrors are mounted to an aluminium frame inserted into the beam using a linear manipulator. Each Type I aluminium frame has four possible positions for scintillators, and each Type II has two, minimizing maintenance time in case a scintillator is damaged by the FEL beam. The additional mounting positions also allow the installation of additional diagnostic probes, such as area diodes.

The main purpose of the diagnostic screens is to locate the beam centroid position in a relatively large field of view and are hence not optimized for high spatial resolution. While for Type I devices the resolution is limited by the pixel pitch of the sensor (effective pixel pitch  $\sim 13.1$  µm), for Type II devices it is limited by the objective’s object-side Rayleigh resolution (at maximum zoom around 9.5 µm, with an effective pixel pitch of about 3.0 µm). Installing higher-resolution optics for special applications is possible without opening up vacuum connections and only limited by the minimum working distance set by the distance between the scintillating screen and the viewport ( $\sim 93$  mm for Type I devices and  $\sim 119$  mm for Type II devices). An image of a diagnostic screen and scintillator carriage is shown in Fig. 7 alongside a demonstration image.

**4.1.6. Instrument beam stop.** The instrument beam stop (IBS) is the most downstream component of the SPB/SFX instrument. Its main purpose is to attenuate and stop the FEL beam. The attenuating components are made from low-*Z* materials – diamond, B<sub>4</sub>C, and aluminium – with a large single-shot damage threshold.

The main attenuating components are three B<sub>4</sub>C blocks that are arranged in an asymmetric V-shape, so that the X-ray incidence angle is about 10° with respect to the surface (see Fig. 8). Each B<sub>4</sub>C block has a heat sink terminal brazed to it, which is clamped in a water-cooled copper baseplate. All heat-sink terminals are electrically isolated from the B<sub>4</sub>C using

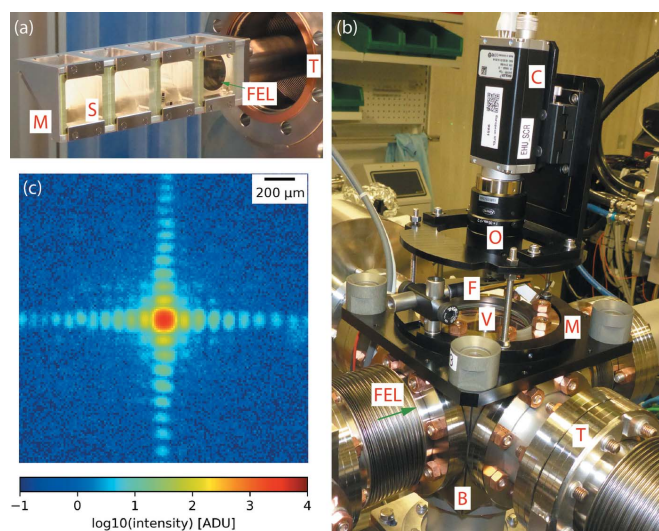


**Figure 7** Overview of a beam diagnostic device at the SPB/SFX instrument. (a) UHV-compatible mounting block for four scintillators (S) and optical mirrors (M). (b) Overview of a Type I diagnostic device with a standard DN63CF cube as its basic building block (B). The three-point mount (M) for camera (C) and optics (O) can be removed without breaking the vacuum inside the cube for maintenance and baking. The scintillators are inserted into the beam via a motorized translation (T). An optical filter (F) is used to block transmission of the blue light from the reference laser which causes fluorescence emission from the scintillator just like the X-ray beam and thus can be visualized in the same way. (c) Illustrative example output from a Type I diagnostic device: diffraction from an instrument slit system closed to a gap of a few tens of micrometres in the horizontal and vertical direction, as imaged in a plane more than 22 m downstream at a photon energy of 9.3 keV. Only a very small fraction from the much larger incident beam was selected here. The image is a background-corrected average of 647 single-FEL-pulse images.

sapphire discs, which makes it possible to read out an X-ray-induced photocurrent from each absorber as a diagnostic of beam intensity.

B<sub>4</sub>C is known to be among the most robust low-Z materials commonly used for the protection of X-ray components. Nevertheless, in-house front-end module (FEM) simulations indicate that even B<sub>4</sub>C would not withstand the full pulse train of the EuXFEL with the expected minimal beam size at the IBS position. The reason is high mechanical stress resulting from the thermal expansion of the B<sub>4</sub>C, following illumination. Therefore, the first component in the IBS that faces the direct X-ray beam is a diamond disc (diameter: 800 mm; thickness: 500 μm), which is composed of alternating layers of microcrystalline (thickness: 50 μm) and nanocrystalline (thickness: 5 μm) diamond (Diamond Materials GmbH, Freiburg, Germany). This composition was chosen to mitigate the risk of strong Bragg reflections from larger crystal grains, while maintaining the good thermal conduction properties of microcrystalline diamond. An incidence angle of about 2° further enhances heat distribution so that the disc can withstand the full pulse train, even in the worst case scenario. The diamond disc is clamped in a water-cooled copper arm. To monitor the X-ray beam during an experiment, fluorescence from this boron-doped diamond can be imaged using an out-of-vacuum camera setup (see Fig. 8).

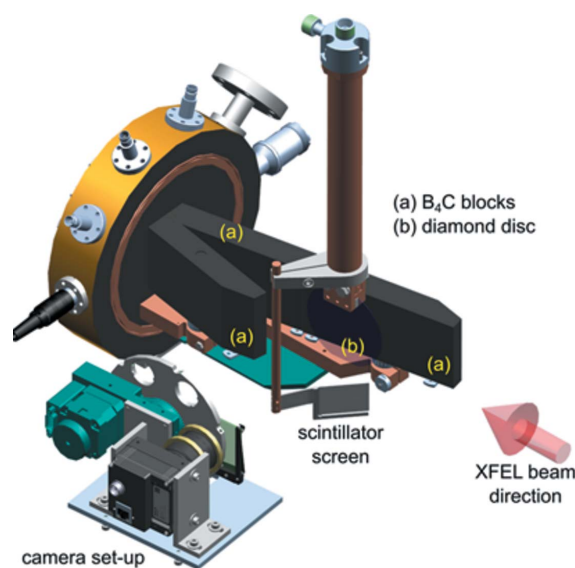


**Figure 8** Schematic of the core components in the instrument beam stop (IBS). While a large fraction of the beam is attenuated by B<sub>4</sub>C blocks (a) arranged in a V-shaped layout, the initial material to attenuate the X-ray beam is a diamond disc at an incidence angle of about 2°. A camera setup is used to monitor the fluorescence signal caused by the X-ray beam incident on the diamond.

#### 4.2. Vacuum scheme

The vacuum scheme of the SPB/SFX instrument is designed to provide appropriate conditions for instrumentation with differing vacuum requirements based on their position. Due to the potential power of the pulse train from the SASE1 undulators, and the desire to minimize background scattering from gas or windows, SPB/SFX is a windowless instrument from accelerator to undulator to sample injection to beamstop. Primary beam conditioning components and the KB mirror optical systems require UHV conditions (better than  $1 \times 10^{-8}$  mbar), while a higher pressure must be tolerated in the sample–X-ray interaction regions due to liquid- and gas-based sample injection. The upstream sections containing the conditioning and optical components are pumped using ion pumps and the downstream sections of the sample interaction regions and detectors are pumped with high-throughput turbomolecular pumps.

In order to maintain the UHV vacuum of the 100 nm-scale KB optics, a differential pumping system is installed between the optics vacuum tank and the interaction region chamber. The system is a three-stage differential pump design based on a series of pre-aligned straws with internal diameters of 3 mm mounted between sealed chambers, which are individually pumped using turbomolecular pumps. The narrow internal diameter of the connecting straws maintains a differential of approximately five decades between the interaction region chamber and the 100 nm-scale optics chamber. The differential system is mounted onto a four-axis stage – providing vertical, horizontal, pitch and yaw movements – to accommodate the differing trajectories of the 1 μm-scale, 100 nm-scale and direct X-ray beams.

Pumping of the X-ray–sample interaction region is provided by turbomolecular pumps attached to the chamber. The primary chamber pump is a 2300 L s<sup>-1</sup> magnetically levitated pump, chosen to reduce vibrations transmitted to the chamber and, due to the continuous rotation axis adjustment, an anticipated improved performance under variable gas loads and potential particle contamination. An additional turbomolecular pump is connected to a port directly underneath the sample delivery mechanism ‘catcher’. This catcher provides a seal between the sample delivery and pump, establishing a differential vacuum, which allows the safe operation of the 2D X-ray detector (with high voltage and cooling systems interlocked to a pressure better than 1 × 10<sup>-4</sup> mbar).

The turbomolecular pumps of the differential pumping system, interaction chamber and downstream sections of the instrument are supported with a distributed rough vacuum system. The outputs of the turbomolecular pumps are connected, via DN100 ISO-K standard aluminium tubing, to Ebara EV-S200P multi-stage dry roots pumps located in a pump room well separated from the experiment hutch to reduce noise and vibration. The ‘dirty’ rough vacuum of the interaction region and the ‘clean’ rough vacuum of the differential pump, detector and other downstream components are separated to avoid contamination, each having dedicated tubing and roots pump. A rough vacuum level of ~5 × 10<sup>-2</sup> mbar is maintained at the exhaust of the interaction chamber turbo pumps during sample injection.

### 4.3. Sample environment

The SPB/SFX instrument deploys three main classes of sample delivery: (i) liquid jets for delivering (primarily) small crystals to the X-ray FEL beam for serial crystallography, (ii) focused aerosol beams for delivering (primarily) non-crystalline particles to the X-ray FEL beam for single particle imaging, and (iii) samples arranged on fixed targets, which may be crystalline or non-crystalline. All three sample delivery methods are supported in the upstream interaction region (IRU) of the SPB/SFX instrument. Additional, downstream interaction regions (IRD) are planned as extensions of the baseline instrumentation and are outlined in Section 4.6.

**4.3.1. Liquid jet sample delivery.** Liquid jets are the principal sample delivery method for serial femtosecond crystallography experiments. The liquid jet delivery system at the SPB/SFX instrument is designed to maintain compatibility with established jet delivery systems developed at other FEL facilities while allowing flexibility in nozzle design. More details are given by Schulz *et al.* (2019).

Sample delivery nozzles are mounted at the end of a hollow rod, inserted via a load lock to position the nozzle above the X-ray focus position. Currently, two configurations are available: a 1/2-inch outer-diameter rod and a 25 mm version suitable for more complicated nozzle designs.

The nozzle rod mates to a catcher centred around the interaction region. The catcher includes apertures for the FEL beam, a 100° solid angle diffraction exit cone, as well as

windows for microscopes and optical laser coupling. The catcher restricts the majority of sample residue to a small easy-to-clean volume and provides differential pumping of the liquid and gas loads. Both nozzle rod and catcher assembly are modular in design for easy upgrade.

The most frequently used liquid jet devices are gas dynamic virtual nozzles (GDVNs) (DePonte *et al.*, 2008). GDVNs compress a liquid sample jet from a 50–100 µm capillary to a few micrometres diameter using a surrounding gas stream. These nozzles can provide fast jets with velocities over 80 m s<sup>-1</sup> (Grünbein *et al.*, 2018b), recently shown to successfully deliver sample jets compatible with the current operational pulse train structure of the FEL beam at SPB/SFX (Grünbein *et al.*, 2018a; Wiedorn *et al.*, 2018).

While not ideally suited to the pulse train structure of the EuXFEL, high-viscosity extrusion jet sample delivery (Weierstall *et al.*, 2014) can be installed into the nozzle rod and catcher infrastructure. Initial experiments with this delivery method have been limited to a single pulse per train, at a train rate of 10 Hz.

**4.3.2. Aerosol sample delivery.** Aerosol sample delivery is expected to be the primary method for delivering single particles into the X-ray beam for imaging experiments at the SPB/SFX instrument. The small scattering cross section and non-crystalline nature of single particles require that the scattering background is reduced to a minimum. In aerosol-based sample delivery, the aim is to isolate the sample from any surrounding liquid, removing scattering from the delivery medium that would otherwise overwhelm the weak sample scattering signal.

An aerosol of (sub-)micrometre-sized droplets, each containing ideally one sample particle, is generated from a nozzle in a chamber at the entrance to an aerodynamic lens stack. The droplets in this aerosol mist evaporate, in principle leaving behind isolated sample particles that are funnelled into an aerodynamic lens (Hantke *et al.*, 2018). Within the aerodynamic lens, the particle flow is focused into a narrow beam that intersects the X-ray beam at the exit of the lens stack.

With the aerodynamic lens stack available at SPB/SFX (see Fig. 9), efficient delivery of particles ranging from 30 to 3000 nm in diameter is possible. The nozzle-to-interaction particle transmission varies with both particle size and gas flow, and can reach >70% (Hantke *et al.*, 2014) for particles of a few hundred nanometres in diameter. The exit velocity also depends on particle diameter and gas flow, with sub-100 nm particles reaching 200 m s<sup>-1</sup>, while micrometre-sized particles travel slower at approximately 20 m s<sup>-1</sup> (Hantke *et al.*, 2018).

Potential complications of limited liquid jet speeds in the high peak repetition rate FEL beam, such as sample replacement and jet disruption (Stan *et al.*, 2016), can be alleviated with aerosol sample delivery, where no surrounding liquid is present.

The lack of surrounding liquid also enables the use of ion time-of-flight spectroscopy as a potential means to provide detector veto signals within a single pulse train (Andreasson *et al.*, 2014; Pietrini *et al.*, 2018). These features make aerosol

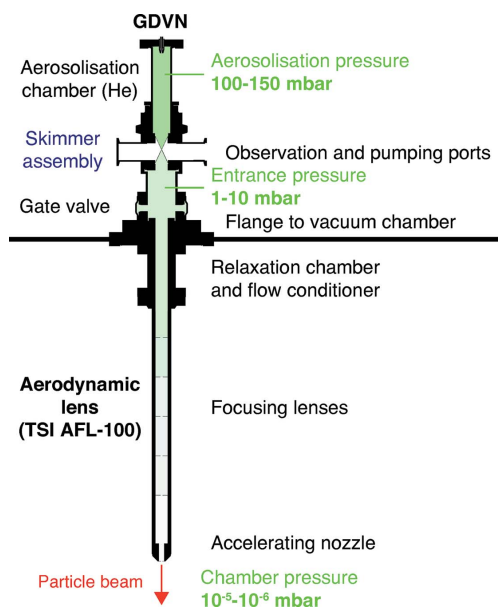


**Figure 9** Schematic of an aerosol injector. The droplets are formed inside the aerosolization chamber from the Rayleigh instability in a thin liquid jet originating from a flow focusing nozzle. The gas necessary for the flow focusing is further used both to create an atmosphere where the droplets are able to evaporate and to provide the stream-lines inside the aerodynamic lens used to focus the particles into a narrow beam. Between the aerosolization chamber and the lens stack, a nozzle-skimmer stage is inserted to limit the gas load inside the lens stack. Adapted from Hantke *et al.* (2018).

sample delivery an intriguing possibility for delivering crystalline samples into the X-ray beam (Awel *et al.*, 2018).

#### 4.4. Detectors: overview and present installation

Crystallographic and single-particle experiments rely on high-performance 2D X-ray photon detectors. Suitable detectors must be capable of measuring fully integrated 2D diffraction patterns from single tens of femtosecond X-ray exposures. They must have a high dynamic range to capture intense Bragg peaks as well as low scattering signals from non-crystalline samples, all at the maximum 4.5 MHz pulse rate of the EuXFEL (Giewekemeyer *et al.*, 2013).

One of the area detectors developed specifically to capture diffraction patterns at the unique time structure of X-ray pulses produced by the EuXFEL is the Adaptive Gain Integrating Pixel Detector (AGIPD) (Allahgholi *et al.*, 2016; Mezza *et al.*, 2016; Allahgholi *et al.*, 2019). Two instances of AGIPD will ultimately be deployed at SPB/SFX, a 1 megapixel (1Mpx) version, already in use at the upstream interaction region since September 2017, and a 4 megapixel (4Mpx) version planned for the downstream interaction region. A Jungfrau 4Mpx detector (Jungmann-Smith *et al.*, 2016) will be available for use as a secondary detector at experiments at the downstream interaction region of SPB/SFX.

The specifications of the AGIPD 1Mpx are described below, and the AGIPD 4Mpx and Jungfrau are outlined later in the

description of the future downstream interaction region. The mechanical setups of each AGIPD implementation and the Jungfrau detector feature motorized longitudinal motion in order to vary the sample–detector distance.

**4.4.1. The Adaptive Gain Integrating Pixel Detector.** AGIPD is a hybrid pixel array, silicon sensor-based detector with  $200\ \mu\text{m} \times 200\ \mu\text{m}$  pixels (Allahgholi *et al.*, 2016). It is an integrating detector (rather than counting) and hence able to acquire full diffraction patterns from single EuXFEL shots, which is essential for the diffraction-before-destruction approach of serial femtosecond crystallography.

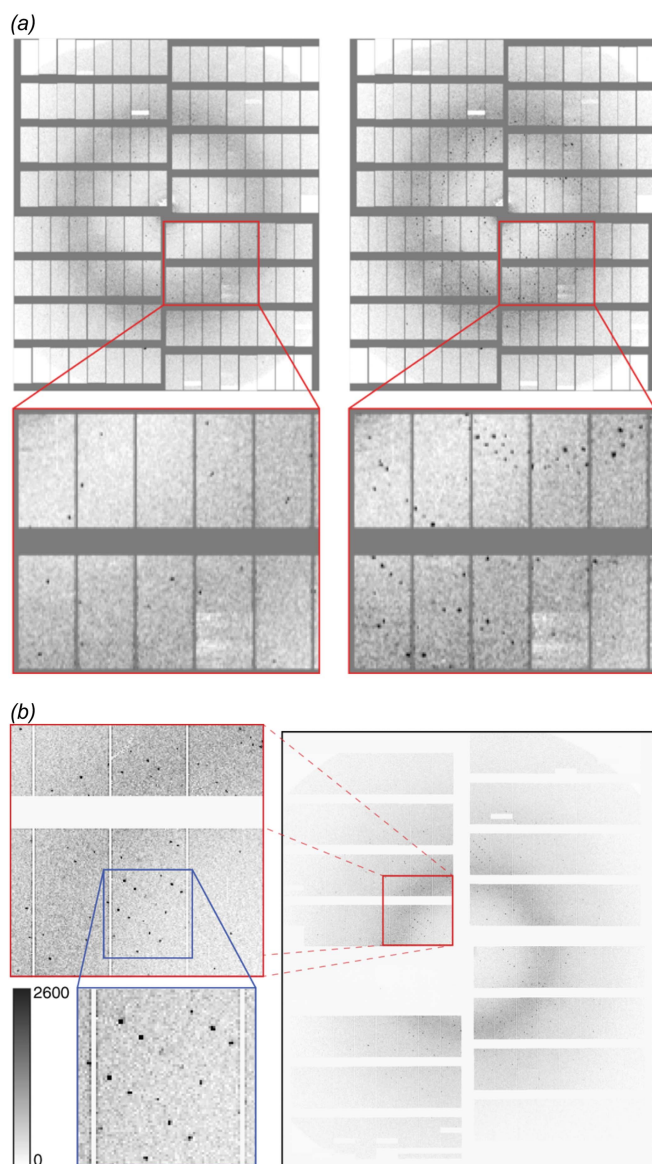
The smallest unit of AGIPD is a single FEM, consisting of  $128 \times 512$  pixels, an active area of  $\sim 26\ \text{mm} \times 103\ \text{mm}$ . Multiple FEMs can be assembled to form a large 2D area detector. Each FEM is constructed from a  $500\ \mu\text{m}$ -thick silicon sensor, giving a high absorption efficiency over the 3–16 keV photon energy operation range at SPB/SFX. The sensor surface facing the interaction region is coated with a 500 nm layer of aluminium to prevent the absorption of optical light photons, especially important for maintaining a low background level in optical-pump-type experiments. The sensor is bump-bonded to an application-specific integrated circuit (ASIC) for detection of the absorbed X-ray photons.

The ASIC is optimized for the high dynamic range, high peak repetition rate demands of experiments at SPB/SFX. It features a radiation-hard electronic design to ensure several years of operation. High dynamic range is achieved via ‘adaptive gain’ switching of individual pixels between three gain levels in adaptation to the incident signal. At a photon energy of  $\sim 12\ \text{keV}$ , signal levels of  $10^4$ – $10^5$  photons  $\text{pixel}^{-1}$  pulse $^{-1}$  (*i.e.*  $10^4$  at 12 keV, more at lower energies) can be recorded in low gain mode, alongside single-photon sensitivity in high gain mode.

Data acquisition at up to 4.5 MHz is achieved by storing signal values in on-pixel analogue memory for the duration of the pulse-train, and read out and subsequently digitized during the idle time (99.4 ms) in between pulse trains. Up to 352 values per pulse train can be stored in the on-pixel memory, resulting in a maximum data rate from AGIPD of 3520 recorded images per second (Allahgholi *et al.*, 2016).

**4.4.2. AGIPD 1Mpx.** The first produced AGIPD 1Mpx detector is installed at the upstream interaction of the SPB/SFX instrument and has been used for both crystallography and single-particle imaging-type experiments. Fig. 10 shows some examples of serial crystallography data taken to date. AGIPD 1Mpx comprises 16 FEMs, grouped into four quadrants centred around the X-ray beam, to form a  $1024 \times 1024$  pixel, 1Mpx detector. Each quadrant is designed to be individually positioned around the X-ray beam such that the position, size and shape of the central aperture can be adjusted.

AGIPD 1Mpx is installed in a vacuum chamber mounted in a detector carriage with large-diameter bellows between the upstream and downstream flanges of the cage. An engineering model of AGIPD 1Mpx in its vacuum chamber is shown in Fig. 11. This construction provides up to 200 mm longitudinal movement of AGIPD without breaking vacuum and supports

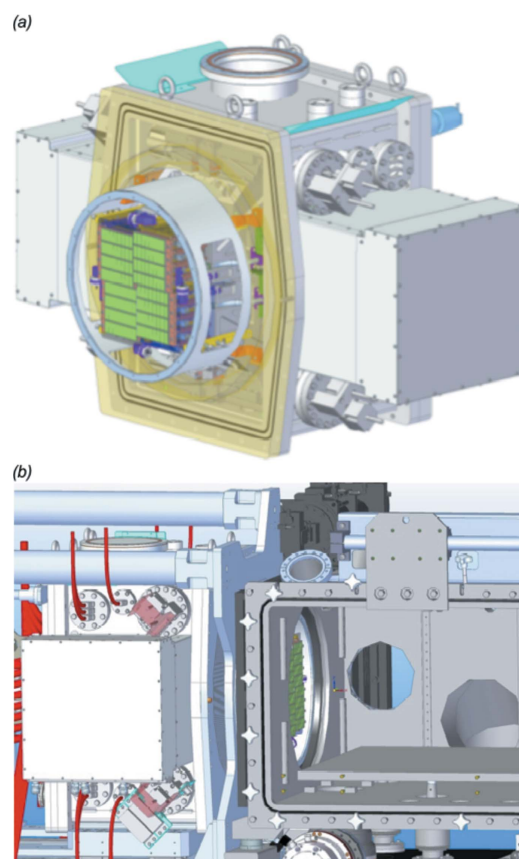

**Figure 10**

Example serial crystallography data taken using the AGIPD 1Mpx during early user experiments at SPB/SFX. Note the well defined Bragg peaks that span a large fraction of the detector's dynamic range. This figure was originally published in (a) Grünbein *et al.* (2018a) and (b) Wiedorn *et al.* (2018) and is licenced under a Creative Commons Attribution 4.0 International Licence.

a minimum sample–sensor distance of 120 mm ( $2\theta$  angle of  $\sim 45^\circ$  at the upper/lower edges). The carriage can either be mounted directly to the exit flange of the interaction region chamber or behind a modular flight tube for sample–sensor distances of up to 6 m.

#### 4.5. Optical laser systems

There are three optical laser systems relevant to operation of experiments at the SPB/SFX instrument. The first are the reference lasers, a simple setup for allowing alignment of components when the FEL beam is not present. The second


**Figure 11**

(a) Mechanical design of the AGIPD 1Mpx detector inside its vacuum tank. The detector consists of four movable quadrants, which are predominantly moved in an iris fashion to adjust the central hole size. Each quadrant in turn consists of four AGIPD FEMs. (b) CAD-model of the AGIPD in its most upstream position (sample-to-detector distance  $\sim 120$  mm). The compressed bellows can also be seen between the sample chamber and the AGIPD vacuum chamber. The sample chamber is deliberately shown empty so one can see the AGIPD sensors (in green) that detect the X-ray photons.

are a collection of commercial nanosecond lasers, used for pump–probe timing where the dynamics of the sample are longer than nanoseconds. The third is a EuXFEL-developed central laser system (Palmer *et al.*, 2019) that offers femto-second and picosecond pulses at the repetition rate of the accelerator, suitable for pump–probe experiments on sample systems with nano-, pico- or femtosecond timescale dynamics.

**4.5.1. Reference lasers.** A preliminary alignment of the instrument requires a reference laser, collinear with the X-ray beam. A reference laser can be used to align components and apertures without the X-ray beam, minimizing installation effort when changing experimental environments and reducing the risk to X-ray sensitive components.

The specific needs of the SPB/SFX instrument require  $\pm 5$  mm horizontal and vertical positioning to match the  $1 \mu\text{m}$ -scale focused beam and 100 nm-scale focused beam trajectories, variable longitudinal focus position along the instrument, microradian-order angular precision, and remote control of in-coupling.

**Table 2**  
Description of basic laser parameters.

The 800 nm source is tunable from 750 to 850 nm (longer than 15 fs).

Wavelength $\lambda$	800 nm	1030 nm
Pulse duration (FWHM)	15–300 fs (nearly Fourier-transform-limited)	<1 ps or 400 ps (chirped)

The reference lasers (Wavespectrum WSL-445-001m-4) are installed in locations at the upstream ends of the optics and experiment hutches, upstream of the respective mirror focusing systems (see Figs. 1 and 2). Each reference-laser beam can be introduced into the X-ray vacuum beam path by an in-coupling optical mirror that may be remotely driven into a fixed kinematic mount to guarantee positional reproducibility.

The 445 nm wavelength laser excites the Ce:YAG scintillators of the beam diagnostic screens, and the resulting fluorescence can be viewed with the screen cameras to establish target positions for the X-ray beam on each screen and ensure a clear path through the interaction region equipment and detectors.

**4.5.2. Commercial nanosecond lasers for pump–probe experiments.** Three nanosecond optical parametric oscillators (OPOs), Opolette HE 355 LD UV from Oportek (Carlsbad, CA, USA), are available at SPB/SFX. These OPOs can provide 4–7 ns pulses of mJ order, continuously tunable in the range 210–2400 nm, relevant for a number of biological systems with microsecond or even millisecond response times. These lasers are, however, limited to 10 Hz operation. Up to three OPOs can be used concurrently for experiments that require multi-step excitation sequences.

**4.5.3. Optical femtosecond and picosecond lasers and their conditioning.** Optical pump–X-ray probe experiments require a synchronized optical laser as a pump source. The EuXFEL Optical Lasers group provides 800 nm, 15–300 fs near-transform-limited pulses, with central wavelength tuneable across a 750–850 nm range and 1030 nm, 1, 400 ps (compressed, stretched, respectively) pulses to the SPB/SFX instrument laser hutch (ILH) (Palmer *et al.*, 2019), see Table 2.

Parameters of the two laser systems at various set points are summarized in Table 3, and detailed information has been given by Pergament *et al.* (2016). The ILH contains beam diagnostics, beam conditioning and delay stages to prepare an appropriate pump beam for biological samples. Additional optical components in the experiment hutch and chamber guide the laser beam to the X-ray–sample interaction point. The 800 nm femtosecond laser pulses are delivered negatively chirped to the ILH

**Table 3**  
Laser set points.

Set point	Repetition rate (MHz)	E1030 nm (mJ)	E800 nm (mJ)
1	4.5	1	0.05
2	1.13	4	0.3
3	0.188	21	1.5
4	0.1	40	2.5

to compensate for dispersion introduced by the windows of the beam transport pipes and the sample chamber as well as the air path, ensuring optimal pulse duration at the sample position.

Harmonic generation – up to the third harmonic for the 800 nm system and fourth harmonic for the 1030 nm system – is provided in the experiment hutch to enable alternative pump wavelengths. An optical parametric amplifier, TOPAS Prime with NirUVis and NDFG units (Light Conversion, Vilnius, Lithuania), will be installed to provide continuous tunability of the femtosecond laser system, covering the wavelength range 240–15000 nm. Specific transport optics can then be installed to support a given subset of that wavelength range for any given experiment.

Fig. 12 shows the optical layout in the SPB/SFX instrument laser hutch. The optical laser paths (800 nm, 1030 nm) have delay lines to control the pump-pulse time of arrival with respect to the X-ray pulse. All beam paths have a consistent 15 m length in the ILH.

All reflective mirrors are equipped with very low dispersion coatings appropriate for the respective wavelength operation regime. The mirrors and other optics require sufficient damage thresholds and low group delay dispersion (GDD) to maintain performance for high peak power and high intensities at high-

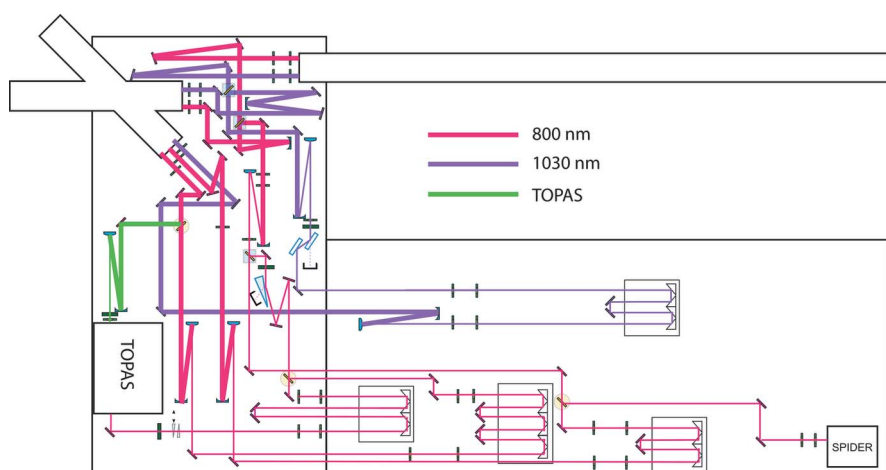


**Figure 12**  
Laser optics layout in the SPB/SFX instrument laser hutch (ILH) for the upstream interaction region (IRU). The optics table size is 1500 mm × 3000 mm (h × w) (left area) and 3600 mm × 1500 mm (h × w) (right area). Beam from the SASE1 common pump laser installed in the central laser hutch (CLH) enters from the left. The optical path to IRU exits top left, and transport of the common pump laser to the optical table for the downstream interaction region (IRD) is shown at the top.

repetition-rate conditions. For the shortest 15 fs pulses, high specification coated mirrors are in use [e.g. Ag + multilayer HRs (45°, 680–940 nm) > 99.5% |GDD| < 10 fs<sup>2</sup> and HR 45° Rp > 99.97% Tp ≤ 0.02% for 1030 nm high-power ps-pulses from Layertec (Mellingen, Germany)].

Different wavelengths require different mirror solutions. Mirrors with silver-based coatings can be used in a wavelength range from 440 nm to the near-infrared. For other cases, which require high-power damage threshold or low GDD in the UV region, customized dielectric coatings are used.

Air humidity and temperature stability are key for consistent delivery of ultrashort pulses. For example, a 10% relative humidity change will alter the refractive index of air by 0.07 p.p.m. (Telada, 2009), introducing a 5 fs timing jitter for a path length of 20 m (approximate total path length to the sample). A 1 K temperature change can induce a 660 fs arrival time offset for the same 20 m path length (thermal expansion coefficient of type SUS410 stainless steel  $9.9 \times 10^{-6} \text{ K}^{-1}$ ). To minimize these effects, a high-precision air-conditioning system is installed in the central laser hutch and ILH, specified to a  $21 \pm 0.1 \text{ K}$  temperature range and  $50 \pm 1\%$  humidity. Recently, very first measurements of the arrival time jitter between X-ray and optical pulses have been made (Kirkwood *et al.*, 2019). The measured jitter is expected to improve significantly in the near future.

#### 4.6. Downstream interaction region: overview

As the popularity of serial crystallography increases, the opportunity for an additional experimental region is advantageous to improve the efficiency and throughput of the SPB/SFX instrument as a whole. The downstream interaction region (IRD) aims to maximize the use of the X-ray pulses of the EuXFEL by refocusing and reusing the direct beam after it has passed through the upstream interaction region (IRU) to a second experimental setup (Boutet *et al.*, 2015; Hunter *et al.*, 2016). Refocusing the used beam with CRLs mounted on the CSS, it is intended to enable two experiments to be performed simultaneously – one upstream and one downstream. This additional instrumentation has been contributed by the SFX user consortium (SFX User Consortium, 2013).

The downstream interaction region, in practice, comprises two separate (and mutually exclusive) interaction regions. One will be operable in atmosphere or a helium environment (IRDa), while the other will operate in vacuum (IRDb).

IRDa gives users increased flexibility in their choice of sample delivery; for example, allowing studies for thermal- and pressure-sensitive samples. Additional scope for developments of novel concepts for sample delivery are also possible (without the complication of vacuum compatibility) as well as accessing longer timescales where the sample may freeze in vacuum and for more complex multi-stage optical pumping to access intermediate states in multi-stage reaction cycles.

As reliable and reproducible data collection is a prerequisite, standardized sample environments will be available, such as the Roadrunner system (Roedig *et al.*, 2017) (version III, in

atmosphere) with an option for nozzle mounting, which will allow for crystal injection in liquids of viscous media and fixed target data collection. Crystallography data is planned to be collected at atmospheric pressure using Jungfrau detector modules. To enable experiments at atmospheric pressure, safe outcoupling of the beam downstream of the CRL refocusing optics will use an in-house-designed sonic delay line to protect the upstream components in case of failure of the outcoupling diamond window. Commissioning of IRDa is planned for 2019 with more regular operation expected from early 2020.

IRDb consists of an in-vacuum sample environment and a 4 megapixel AGIPD for detection and is presently planned for an early 2020 installation.

**4.6.1. AGIPD 4Mpx.** The in-vacuum downstream interaction region of SPB/SFX will be equipped with a 4 megapixel AGIPD. The mechanical design is optimized for crystallographic experiments to match the primary scientific scope of the downstream interaction region. In addition to the primary use as the principal detector of the downstream interaction region, AGIPD 4Mpx can serve as a second detection plane for upstream interaction region experiments requiring recording of very small angle signal. The AGIPD 4Mpx sensor plane is located  $\sim 10 \text{ m}$  downstream of the IRU focus position.

AGIPD 4Mpx consists of 56 AGIPD FEMs (3.7 megapixel) of the same type as AGIPD 1Mpx, arranged in two halves of 28 FEMs each. The detector halves are vertically offset by half of the FEM pitch to ensure continuous reciprocal space coverage for samples with a delivery orientation preference (Redecke *et al.*, 2013). The total detection plane area is larger than  $400 \text{ mm} \times 400 \text{ mm}$ , requiring an 800 mm-diameter entrance flange.

The detector halves can be independently positioned, both transversely and longitudinally. Each half can move horizontally up to 50 mm to control the position and size of the central slot, with a maximum separation of 100 mm. Sample–sensor distances in the range of  $\sim 150 \text{ mm}$  ( $2\theta$  angle of  $\sim 60^\circ$  at the upper/lower edges) to 550 mm will be achievable. In contrast to AGIPD 1Mpx, most of the electronics of AGIPD 4Mpx, including digitizers and FPGAs, will be installed in-vacuum, directly attached to the output of each FEM.

The AGIPD 4Mpx detector of the IRD is also planned to be used as a second detection plane for samples injected in the upstream interaction region (IRU) with the two regions connected by a long evacuated flight tube to facilitate single particle imaging, solution scattering measurements, and other experiments requiring very low angle (scattering/diffraction) data to be collected.

**4.6.2. Jungfrau.** In the in-atmosphere downstream interaction region, SPB/SFX will integrate a Jungfrau 4Mpx detector (Jungmann-Smith *et al.*, 2016). The Jungfrau detector has many similarities with AGIPD. Jungfrau is an integrating hybrid-pixel array detector, based on  $512 \times 1024$  pixel FEMs using a 320  $\mu\text{m}$ -thick silicon sensor. The interaction-region facing surface of the sensor is coated in aluminium to prevent the absorption of optical light. High dynamic range is realized with gain switching. At a photon energy of 12 keV, signal levels of  $10^4$  photons  $\text{pixel}^{-1} \text{ pulse}^{-1}$  at 12 keV can be

recorded in low gain mode with single-photon sensitivity in high gain mode in an adjacent pixel.

Data acquisition at possibly up to megahertz rates is achieved by storing signal values in on-pixel analogue memory for the duration of the pulse train, and read out and subsequently digitized during the idle time (99.4 ms) in between pulse trains. Sixteen values per pulse train can be stored in the on-pixel memory, resulting in a maximum data rate from Jungfrau of 160 recorded images per second (Jungmann-Smith *et al.*, 2016).

In comparison with AGIPD, Jungfrau has a smaller pixel size of  $75\ \mu\text{m} \times 75\ \mu\text{m}$  and reduced electronic noise, leading to enhanced single-photon sensitivity at the low end of the SPB/SFX photon-energy operation range. Prior to full integration and commissioning of the SPB/SFX downstream interaction region, a preliminary implementation of Jungfrau at SPB/SFX will consist of four FEMs (2 megapixel), arranged in two independently movable halves. An upgrade to 4 megapixel will be completed upon receipt of additional modules. This detector will initially be housed in a manner compatible with a helium sample environment (see Section 4.6 with later upgrades to a vacuum housing possible).

## 5. Conclusions

The SPB/SFX instrument has been described, including its early operation optical system, sample delivery systems, detection systems and basic diagnostics. Importantly, the first scientific results from user experiments at the EuXFEL (Grünbein *et al.*, 2018a; Wiedorn *et al.*, 2018) have been published demonstrating that serial crystallography is indeed possible at MHz rates. This, in turn, allows for unprecedented data rates, which supports high-throughput experiments, finer time steps in time-resolved work, or both. The possibilities of more than an order of magnitude faster data collection than any other similar source are just being explored.

Beyond this advantage of higher repetition rate, at present, a whole suite of additional instrumentation is being installed that will provide further capabilities to EuXFEL users in the not-too-distant future. The capabilities include detectors with more pixels, alternate sample delivery mechanisms, additional diagnostics, and more. With both MHz repetition rates and a suite of instrumentation tailored to the needs of structural studies, the future promises to hold a number of exciting possibilities at the SPB/SFX instrument of the EuXFEL.

## Acknowledgements

The SFX User Consortium (UC) has provided instrumentation, personnel and ideas that have directly contributed to the instrument. The SFX UC is composed of scientific partners from Germany, Sweden, UK, Slovakia, Switzerland, Australia and USA. In particular, the SFX UC executive committee, composed of James Naismith, Richard Neutze and Henry Chapman, have provided invaluable advice and support. The SPB/SFX Advisory Review Team – consisting of David Stuart, Anton Barty, Sebastien Boutet, Daniel DePonte, Victor

Lamzin, Franz Pfeiffer, Ilme Schlichting and Garth Williams – are acknowledged for their expert advice and contributions to the instrument design. The members of the European XFEL Scientific Advisory Committee are also thanked for their sound advice and robust feedback on the instrument design and scope. All staff of the European XFEL are thanked for their continuing commitment to this and all instrumentation at the European XFEL. We gratefully acknowledge the contributions of Viktor Lyamayev (†2016) to the instrument, particularly for developing the Instrument Beam Stop. Susanne Fangohr is acknowledged for editing and improving the text and structure of the paper.

## Funding information

In addition to the baseline funding provided by the European XFEL members, we acknowledge funding of instrumentation and staff by the following sources: the Wellcome Trust, the German Federal Ministry for Education and Research (BMBF) via projects 05K13GU7 and 05E13GU1, the Ministry of Education, Science, Research and Sport of the Slovak Republic, The Swedish Research Council (822-2013-2014), the Knut and Alice Wallenberg Foundation, the Röntgen-Ångström Cluster, the Swedish Foundation for Strategic Research, the Australian Research Council Center of Excellence in Advanced Molecular Imaging (CE140100011), the Australian Nuclear Science and Technology Organisation (ANSTO), the Max Planck Society for Medical Research, the NSF-STC ‘BioXFEL’ through award STC-1231306 and the Helmholtz Association Strategic Investment funds.

## References

- Abeghyan, S., Bagha-Shanjani, M., Chen, G., Englisch, U., Karabekyan, S., Li, Y., Preisskorn, F., Wolff-Fabris, F., Wuenschel, M., Yakopov, M. & Pflueger, J. (2019). *J. Synchrotron Rad.* **26**, 302–310.
- Abela, R., Aghababayan, A., Altarelli, M., Altucci, C., Amatuni, G., Anfinrud, P., Audebert, P., Ayvazyan, V., Baboi, N., Baehr, J., Balandin, V., Bandelmann, R., Becker, J., Beutner, B., Blome, C. *et al.* (2006). *The European X-ray Free-Electron Laser*. Technical Design Report, European XFEL, Hamburg, Germany.
- Allahgholi, A., Becker, J., Bianco, L., Bradford, R., Delfs, A., Dinapoli, R., Goettlicher, P., Gronewald, M., Graafsma, H., Greiffenberg, D., Henrich, B. H., Hirsemann, H., Jack, S., Klanner, R., Klyuev, A., Krueger, H., Lange, S., Marras, A., Mezza, D., Mozzanica, A., Perova, I., Xia, Q., Schmitt, B., Schwandt, J., Sheviakov, I., Shi, X., Trunk, U. & Zhang, J. (2016). *J. Instrum.* **11**, C02066.
- Allahgholi, A., Becker, J., Delfs, A., Dinapoli, R., Goettlicher, P., Greiffenberg, D., Henrich, B., Hirsemann, H., Kuhn, M., Klanner, R., Klyuev, A., Krueger, H., Lange, S., Laurus, T., Marras, A., Mezza, D., Mozzanica, A., Niemann, M., Poehlsen, J., Schwandt, J., Sheviakov, I., Shi, X., Smoljanin, S., Steffen, L., Sztuk-Dambietz, J., Trunk, U., Xia, Q., Zeribi, M., Zhang, J., Zimmer, M., Schmitt, B. & Graafsma, H. (2019). *J. Synchrotron Rad.* **26**, 74–82.
- Andreasson, J., Martin, A. V., Liang, M., Timneanu, N., Aquila, A., Wang, F., Iwan, B., Svenda, M., Ekeberg, T., Hanke, M., Bielecki, J., Rolles, D., Rudenko, A., Foucar, L., Hartmann, R., Erk, B., Rudek, B., Chapman, H. N., Hajdu, J. & Barty, A. (2014). *Opt. Express*, **22**, 2497–2510.
- Aquila, A., Barty, A., Bostedt, C., Boutet, S., Carini, G., de Ponte, D., Drell, P., Doniach, S., Downing, K. H., Earnest, T., Elmlund, H., Elser, V., Gühr, M., Hajdu, J., Hastings, J., Hau-Riege, S. P., Huang,



- Z., Lattman, E. E., Maia, F. R. N. C., Marchesini, S., Ourmazd, A., Pellegrini, C., Santra, R., Schlichting, I., Schroer, C., Spence, J. C. H., Vartanyants, I. A., Wakatsuki, S., Weis, W. I. & Williams, G. J. (2015a). *Struct. Dyn.* **2**, 041701.
- Aquila, A., Hunter, M. S., Doak, R. B., Kirian, R. A., Fromme, P., White, T. A., Andreasson, J., Arnlund, D., Bajt, S., Barends, T. R. M., Barthelmess, M., Bogan, M. J., Bostedt, C., Bottin, H., Bozek, J. D., Caleman, C., Coppola, N., Davidsson, J., DePonte, D. P., Elser, V., Epp, S. W., Erk, B., Fleckenstein, H., Foucar, L., Frank, M., Fromme, R., Graafsma, H., Grotjohann, I., Gumprecht, L., Hajdu, J., Hampton, C. Y., Hartmann, A., Hartmann, R., Hau-Riege, S., Hauser, G., Hirsemann, H., Holl, P., Holton, J. M., Hömke, A., Johansson, L., Kimmel, N., Kassemeyer, S., Krasniqi, F., Kühnel, K.-U., Liang, M., Lomb, L., Malmerberg, E., Marchesini, S., Martin, A. V., Maia, F. R., Messerschmidt, M., Nass, K., Reich, C., Neutze, R., Rolles, D., Rudek, B., Rudenko, A., Schlichting, I., Schmidt, C., Schmidt, K. E., Schulz, J., Seibert, M. M., Shoeman, R. L., Sierra, R., Soltau, H., Starodub, D., Stellato, F., Stern, S., Strüder, L., Timneanu, N., Ullrich, J., Wang, X., Williams, G. J., Weidenspointner, G., Weierstall, U., Wunderer, C., Barty, A., Spence, J. C. H. & Chapman, H. N. (2012). *Opt. Express*, **20**, 2706–2716.
- Aquila, A., Sobierajski, R., Ozkan, C., Hájková, V., Burian, T., Chalupský, J., Juha, L., Störmer, M., Bajt, S., Klepka, M. T., Dłużewski, P., Morawiec, K., Ohashi, H., Koyama, T., Tono, K., Inubushi, Y., Yabashi, M., Sinn, H., Tschentscher, T., Mancuso, A. P. & Gaudin, J. (2015b). *Appl. Phys. Lett.* **106**, 241905.
- Awel, S., Kirian, R. A., Wiedorn, M. O., Beyerlein, K. R., Roth, N., Horke, D. A., Oberthür, D., Knoska, J., Mariani, V., Morgan, A., Adriano, L., Tolstikova, A., Xavier, P. L., Yefanov, O., Aquila, A., Barty, A., Roy-Chowdhury, S., Hunter, M. S., James, D., Robinson, J. S., Weierstall, U., Rode, A. V., Bajt, S., Küpper, J. & Chapman, H. N. (2018). *J. Appl. Cryst.* **51**, 133–139.
- Ayyer, K., Philipp, H. T., Tate, M. W., Elser, V. & Gruner, S. M. (2014). *Opt. Express*, **22**, 2403–2413.
- Ayyer, K., Yefanov, O. M., Oberthür, D., Roy-Chowdhury, S., Galli, L., Mariani, V., Basu, S., Coe, J., Conrad, C. E., Fromme, R., Schaffer, A., Dörner, K., James, D., Kupitz, C., Metz, M., Nelson, G., Xavier, P. L., Beyerlein, K. R., Schmidt, M., Sarrou, I., Spence, J. C. H., Weierstall, U., White, T. A., Yang, J.-H., Zhao, Y., Liang, M., Aquila, A., Hunter, M. S., Robinson, J. S., Koglin, J. E., Boutet, S., Fromme, P., Barty, A. & Chapman, H. N. (2016). *Nature*, **530**, 202–206.
- Barends, T. R. M., Foucar, L., Ardevol, A., Nass, K., Aquila, A., Botha, S., Doak, R. B., Falahati, K., Hartmann, E., Hilpert, M., Heinz, M., Hoffmann, M. C., Kofinger, J., Koglin, J. E., Kovacsova, G., Liang, M., Milathianaki, D., Lemke, H. T., Reinstein, J., Roome, C. M., Shoeman, R. L., Williams, G. J., Burghardt, I., Hummer, G., Boutet, S. & Schlichting, I. (2015). *Science*, **350**, 445–450.
- Barends, T. R. M., Foucar, L., Botha, S., Doak, R. B., Shoeman, R. L., Nass, K., Koglin, J. E., Williams, G. J., Boutet, S., Messerschmidt, M. & Schlichting, I. (2014). *Nature*, **505**, 244–247.
- Bean, R. J., Aquila, A., Samoylova, L. & Mancuso, A. P. (2016). *J. Opt.* **18**, 074011.
- Beaurepaire, E., Turner, G. M., Harrel, S. M., Beard, M. C., Bigot, J. Y. & Schmuttenmaer, C. A. (2004). *Appl. Phys. Lett.* **84**, 3465–3467.
- Boukhelef, D., Szuba, J., Wrona, K. & Youngman, C. (2013). *Proceedings of the 14th International Conference on Accelerator and Large Experimental Physics Control Systems (ICALPECS 2013)*, 6–11 October 2013, San Francisco, CA, USA, pp. 665–668. TUPPC045.
- Boutet, S., Foucar, L., Barends, T. R. M., Botha, S., Doak, R. B., Koglin, J. E., Messerschmidt, M., Nass, K., Schlichting, I., Seibert, M. M., Shoeman, R. L. & Williams, G. J. (2015). *J. Synchrotron Rad.* **22**, 634–643.
- Boutet, S., Lomb, L., Williams, G. J., Barends, T. R. M., Aquila, A., Doak, R. B., Weierstall, U., DePonte, D. P., Steinbrener, J., Shoeman, R. L., Messerschmidt, M., Barty, A., White, T. A., Kassemeyer, S., Kirian, R. A., Seibert, M. M., Montanez, P. A., Kenney, C., Herbst, R., Hart, P., Pines, J., Haller, G., Gruner, S. M., Philipp, H. T., Tate, M. W., Hromalik, M., Koerner, L. J., van Bakel, N., Morse, J., Ghonsalves, W., Arnlund, D., Bogan, M. J., Caleman, C., Fromme, R., Hampton, C. Y., Hunter, M. S., Johansson, L. C., Katona, G., Kupitz, C., Liang, M., Martin, A. V., Nass, K., Redecke, L., Stellato, F., Timneanu, N., Wang, D., Zatsepin, N. A., Schafer, D., Defever, J., Neutze, R., Fromme, P., Spence, J. C. H., Chapman, H. N. & Schlichting, I. (2012). *Science*, **337**, 362–364.
- Boutet, S. & Williams, G. J. (2010). *New J. Phys.* **12**, 035024.
- Bruetzel, L. K., Walker, P. U., Gerling, T., Dietz, H. & Lipfert, J. (2018). *Nano Lett.* **18**, 2672–2676.
- Carnis, J., Cha, W., Wingert, J., Kang, J., Jiang, Z., Song, S., Sikorski, M., Robert, A., Gutt, C., Chen, S.-W., Dai, Y., Ma, Y., Guo, H., Lurio, L. B., Shpyrko, O., Narayanan, S., Cui, M., Kosif, I., Emrick, T., Russell, T. P., Lee, H. C., Yu, C.-J., Grübel, G., Sinha, S. K. & Kim, H. (2014). *Sci. Rep.* **4**, 6017.
- Chapman, H. N., Fromme, P., Barty, A., White, T. A., Kirian, R. A., Aquila, A., Hunter, M. S., Schulz, J., DePonte, D. P., Weierstall, U., Doak, R. B., Maia, F. R. N. C., Martin, A. V., Schlichting, I., Lomb, L., Coppola, N., Shoeman, R. L., Epp, S. W., Hartmann, R., Rolles, D., Rudenko, A., Foucar, L., Kimmel, N., Weidenspointner, G., Holl, P., Liang, M., Barthelmess, M., Caleman, C., Boutet, S., Bogan, M. J., Krzywinski, J., Bostedt, C., Bajt, S., Gumprecht, L., Rudek, B., Erk, B., Schmidt, C., Hömke, A., Reich, C., Pietschner, D., Strüder, L., Hauser, G., Gorke, H., Ullrich, J., Herrmann, S., Schaller, G., Schopper, F., Soltau, H., Kühnel, K.-U., Messerschmidt, M., Bozek, J. D., Hau-Riege, S. P., Frank, M., Hampton, C. Y., Sierra, R. G., Starodub, D., Williams, G. J., Hajdu, J., Timneanu, N., Seibert, M. M., Andreasson, J., Rucker, A., Jönsson, O., Svenda, M., Stern, S., Nass, K., Andritschke, R., Schröter, C.-D., Krasniqi, F., Bott, M., Schmidt, K. E., Wang, X., Grotjohann, I., Holton, J. M., Barends, T. R. M., Neutze, R., Marchesini, S., Fromme, R., Schorb, S., Rupp, D., Adolph, M., Gorkhover, T., Andersson, I., Hirsemann, H., Potdevin, G., Graafsma, H., Nilsson, B. & Spence, J. C. H. (2011). *Nature*, **470**, 73–77.
- Daurer, B. J., Okamoto, K., Bielecki, J., Maia, F. R. N. C., Mühlig, K., Seibert, M. M., Hantke, M. F., Nettelblad, C., Benner, W. H., Svenda, M., Timneanu, N., Ekeberg, T., Loh, N. D., Pietrini, A., Zani, A., Rath, A. D., Westphal, D., Kirian, R. A., Awel, S., Wiedorn, M. O., van der Schot, G., Carlsson, G. H., Hasse, D., Sellberg, J. A., Barty, A., Andreasson, J., Boutet, S., Williams, G., Koglin, J., Andersson, I., Hajdu, J. & Larsson, D. S. D. (2017). *IUCrJ*, **4**, 251–262.
- Decking, W. *et al.* (2019). Submitted.
- DePonte, D. P., Weierstall, U., Schmidt, K., Warner, J., Starodub, D., Spence, J. C. H. & Doak, R. B. (2008). *J. Phys. D Appl. Phys.* **41**, 195505.
- Ekeberg, T., Svenda, M., Abergel, C., Maia, F. R., Seltzer, V., Claverie, J.-M., Hantke, M., Jönsson, O., Nettelblad, C., van der Schot, G., Liang, M., DePonte, D. P., Barty, A., Seibert, M. M., Iwan, B., Andersson, I., Loh, N. D., Martin, A. V., Chapman, H., Bostedt, C., Bozek, J. D., Ferguson, K. R., Krzywinski, J., Epp, S. W., Rolles, D., Rudenko, A., Hartmann, R., Kimmel, N. & Hajdu, J. (2015). *Phys. Rev. Lett.* **114**, 098102.
- Fangohr, H., Beg, M., Bondar, V., Boukhelef, D., Brockhauser, S., Danilevicius, C., Ehsan, W., Esenov, S. G., Flucke, G., Giovanetti, G., Goerics, D., Hauf, S., Heisen, B., Hickin, D. G., Khakhulin, D., Klimovskaia, A., Kuster, M., Lang, P. M., Maia, L., Mekinda, T., Michelat, A., Parenti, G., Previtali, H., Santos, A., Silenzi, J., Sztuk-Dambietz, J., Szuba, M., Teichmann, K., Weger, J., Wiggins, K., Wrona, L., Xu, C., Aplin, S., Barty, A., Kuhn, M., Mariani, V. & Kluyver, T. (2018). *Proceedings of the 16th International Conference on Accelerator and Large Experimental Control Systems (ICALPECS'17)*, 8–13 October 2017, Barcelona, Spain, pp. 245–252. TUCPA01.
- Giewekemeyer, K., Turcato, M. & Mancuso, A. P. (2013). *Detector Geometries for Coherent X-ray Diffractive Imaging at the SPB*

- Instrument*, XFEL.EU Technical Report TR-2013-007. European XFEL, Hamburg, Germany (doi:10.3204/XFEL.EU/TR-2013-007).
- Graceffa, R., Nobrega, R. P., Barrea, R. A., Kathuria, S. V., Chakravarthy, S., Bilsel, O. & Irving, T. C. (2013). *J. Synchrotron Rad.* **20**, 820–825.
- Grünbein, M. L., Bielecki, J., Gorel, A., Stricker, M., Bean, R., Cammarata, M., Dörner, K., Fröhlich, L., Hartmann, E., Hauf, S., Hilpert, M., Kim, Y., Kloos, M., Letrun, R., Messerschmidt, M., Mills, G., Nass Kovacs, G., Ramilli, M., Roome, C. M., Sato, T., Scholz, M., Sliwa, M., Sztuk-Dambietz, J., Weik, M., Weinhausen, B., Al-Qudami, N., Boukhelef, D., Brockhauser, S., Ehsan, W., Emons, M., Esenov, S., Fangohr, H., Kaukher, A., Kluyver, T., Lederer, M., Maia, L., Manetti, M., Michelat, T., Münnich, A., Pallas, F., Palmer, G., Previtali, G., Raab, N., Silenzi, A., Szuba, J., Venkatesan, S., Wrona, K., Zhu, J., Doak, R. B., Shoeman, R. L., Foucar, L., Colletier, J.-P., Mancuso, A. P., Barends, T. R. M., Stan, C. A. & Schlichting, I. (2018a). *Nat. Commun.* **9**, 3487.
- Grünbein, M. L., Shoeman, R. L. & Doak, R. B. (2018b). *Opt. Express*, **26**, 7190–7203.
- Hantke, M. F., Bielecki, J., Kulyk, O., Westphal, D., Larsson, D. S. D., Svenda, M., Reddy, H. K. N., Kirian, R. A., Andreasson, J., Hajdu, J. & Maia, F. R. N. C. (2018). *IUCrJ*, **5**, 673–680.
- Hantke, M. F., Hasse, D., Maia, F. R. N. C., Ekeberg, T., John, K., Svenda, M., Loh, N. D., Martin, A. V., Timneanu, N., Larsson, D. S. D., Schot, G., van der Carlsson, G. H., Ingelman, M., Andreasson, J., Westphal, D., Liang, M., Stellato, F., DePonte, D. P., Hartmann, R., Kimmel, N., Kirian, R. A., Seibert, M. M., Mühlig, K., Schorb, S., Ferguson, K., Bostedt, C., Carron, S., Bozek, J. D., Rolles, D., Rudenko, A., Epp, S., Chapman, H. N., Barty, A., Hajdu, J. & Andersson, I. (2014). *Nat. Photon.* **8**, 943–949.
- Hauf, S., Heisen, B., Aplin, S., Beg, M., Bergemann, M., Bondar, V., Boukhelef, D., Danilevsky, C., Wajid, E., Esenov, S., Fabbri, R., Flucke, G., Fulla Marsa, D., Görjes, D., Giovanetti, G., Hickin, D., Jarosiewicz, T., Kamil, E., Khakhulin, D., Klimovskaia, A., Kluyver, T., Kirienko, Y., Kuhn, M., Maia, L., Mamchik, D., Mariani, V., Mekinda, L., Michelat, T., Münnich, A., Padee, A., Parenti, A., Santos, H., Silenzi, A., Teichmann, M., Weger, K., Wiggins, J., Wrona, K., Xu, C., Youngman, C., Zhu, J., Fangohr, H. & Brockhauser, S. (2019). *J. Synchrotron Rad.* **26**. To be published.
- Heisen, B., Boukhelef, D., Esenov, S., Hauf, S., Kozlova, I., Maia, L., Parenti, A., Szuba, J., Weger, K., Wrona, K. & Youngman, C. (2013). *14th International Conference on Accelerator and Large Experimental Physics Control Systems (ICALPEPCS2013)*, 6–11 October 2013, San Francisco, CA, USA. FRCOAAB02.
- Henrich, B., Becker, J., Dinapoli, R., Goettlicher, P., Graafsma, H., Hirsemann, H., Klanner, R., Krueger, H., Mazzocco, R., Mozzanica, A., Perrey, H., Potdevin, G., Schmitt, B., Shi, X., Srivastava, A., Trunk, U. & Youngman, C. (2011). *Nucl. Instrum. Methods Phys. Res. A*, **633**, S11–S14.
- Higley, D. J., Hirsch, K., Dakovski, G. L., Jal, E., Yuan, E., Liu, T., Lutman, A. A., MacArthur, J. P., Arenholz, E., Chen, Z., Coslovich, G., Denes, P., Granitzka, P. W., Hart, P., Hoffmann, M. C., Joseph, J., Le Guyader, L., Mitra, A., Moeller, S., Ohldag, H., Seaberg, M., Shafer, P., Stöhr, J., Tsukamoto, A., Nuhn, H.-D., Reid, A. H., Dürr, H. A. & Schlotter, W. F. (2016). *Rev. Sci. Instrum.* **87**, 033110.
- Hunter, M. S., Yoon, C. H., DeMirci, H., Sierra, R. G., Dao, E. H., Ahmadi, R., Aksit, F., Aquila, A. L., Ciftci, H., Guillet, S., Hayes, M. J., Lane, T. J., Liang, M., Lundström, U., Koglin, J. E., Mgbam, P., Rao, Y., Zhang, L., Wakatsuki, S., Holton, J. M. & Boutet, S. (2016). *Nat. Commun.* **7**, 13388.
- Jungmann-Smith, J. H., Bergamaschi, A., Brückner, M., Cartier, S., Dinapoli, R., Greiffenberg, D., Huthwelker, T., Maliakal, D., Mayilyan, D., Medjoubi, K., Mezza, D., Mozzanica, A., Ramilli, M., Ruder, C., Schädlér, L., Schmitt, B., Shi, X. & Tinti, G. (2016). *J. Synchrotron Rad.* **23**, 385–394.
- Juranić, P., Rehanek, J., Arrell, C. A., Pradervand, C., Ischebeck, R., Erny, C., Heimgartner, P., Gorgisyan, I., Thominet, V., Tiedtke, K., Sorokin, A., Follath, R., Makita, M., Seniutinas, G., David, C., Milne, C. J., Lemke, H., Radovic, M., Hauri, C. P. & Patthey, L. (2018). *J. Synchrotron Rad.* **25**, 1238–1248.
- Kirkwood, H. J., Letrun, R., Tanikawa, T., Liu, J., Nakatsutsumi, M., Emons, M., Jezynski, T., Palmer, G., Lederer, M., Bean, R., Buck, J., Di Dio Cafisio, S., Graceffa, R., Grünert, J., Göde, S., Höppner, H., Kim, Y., Konopkova, Z., Mills, G., Makita, M., Pelka, A., Preston, T. R., Sikorski, M., Takem, C. M. S., Giewekemeyer, K., Chollet, M., Vagovic, P., Chapman, H. N., Mancuso, A. P. & Sato, T. (2019). *Opt. Lett.* **44**, 1650–1653.
- Lehmkuhler, F., Kwaśniewski, P., Roseker, W., Fischer, B., Schroer, M. A., Tono, K., Katayama, T., Sprung, M., Sikorski, M., Song, S., Glownia, J., Chollet, M., Nelson, S., Robert, A., Gutt, C., Yabashi, M., Ishikawa, T. & Grübel, G. (2015). *Sci. Rep.* **5**, 17193.
- Levantino, M., Schirò, G., Lemke, H. T., Cottone, G., Glownia, J. M., Zhu, D., Chollet, M., Ihee, H., Cupane, A. & Cammarata, M. (2015a). *Nat. Commun.* **6**, 6772.
- Levantino, M., Yorke, B. A., Monteiro, D. C., Cammarata, M. & Pearson, A. R. (2015b). *Curr. Opin. Struct. Biol.* **35**, 41–48.
- Liu, W., Wacker, D., Gati, C., Han, G. W., James, D., Wang, D., Nelson, G., Weierstall, U., Katritsch, V., Barty, A., Zatsepin, N. A., Li, D., Messerschmidt, M., Boutet, S., Williams, G. J., Koglin, J. E., Seibert, M. M., Wang, C., Shah, S. T. A., Basu, S., Fromme, R., Kupitz, C., Rendek, K. N., Grotjohann, I., Fromme, P., Kirian, R. A., Beyerlein, K. R., White, T. A., Chapman, H. N., Caffrey, M., Spence, J. C. H., Stevens, R. C. & Cherezov, V. (2013). *Science*, **342**, 1521–1524.
- Loh, N. D. & Elser, V. (2009). *Phys. Rev. E*, **80**, 026705.
- Lundholm, I. V., Sellberg, J. A., Ekeberg, T., Hantke, M. F., Okamoto, K., van der Schot, G., Andreasson, J., Barty, A., Bielecki, J., Bruza, P., Bucher, M., Carron, S., Daurer, B. J., Ferguson, K., Hasse, D., Krzywinski, J., Larsson, D. S. D., Morgan, A., Mühlig, K., Müller, M., Nettelblad, C., Pietrini, A., Reddy, H. K. N., Rupp, D., Sauppe, M., Seibert, M., Svenda, M., Swiggers, M., Timneanu, N., Ulmer, A., Westphal, D., Williams, G., Zani, A., Faigel, G., Chapman, H. N., Möller, T., Bostedt, C., Hajdu, J., Gorkhover, T. & Maia, F. R. N. C. (2018). *IUCrJ*, **5**, 531–541.
- Mancuso, A. P., Aquila, A., Borchers, G., Giewekemeyer, K. & Reimers, N. (2013). *Technical Design Report: Scientific Instrument Single Particles, Clusters and Biomolecules (SPB)*. Technical Report. European XFEL GmbH, Hamburg, Germany.
- Mezza, D., Allahgholi, A., Arino-Estrada, G., Bianco, L., Delfs, A., Dinapoli, R., Goettlicher, P., Graafsma, H., Greiffenberg, D., Hirsemann, H., Jack, S., Klanner, R., Klyuev, A., Krueger, H., Marras, A., Mozzanica, A., Poehlsen, J., Schmitt, B., Schwandt, J., Sheviakov, I., Shi, X., Trunk, U., Xia, Q., Zhang, J. & Zimmer, M. (2016). *Nucl. Instrum. Methods Phys. Res. A*, **838**, 39–46.
- Nango, E., Royant, A., Kubo, M., Nakane, T., Wickstrand, C., Kimura, T., Tanaka, T., Tono, K., Song, C., Tanaka, R., Arima, T., Yamashita, A., Kobayashi, J., Hosaka, T., Mizohata, E., Nogly, P., Sugahara, M., Nam, D., Nomura, T., Shimamura, T., Im, D., Fujiwara, T., Yamanaka, Y., Jeon, B., Nishizawa, T., Oda, K., Fukuda, M., Andersson, R., Båth, P., Dods, R., Davidsson, J., Matsuoka, S., Kawatake, S., Murata, M., Nureki, O., Owada, S., Kameshima, T., Hatsui, T., Joti, Y., Schertler, G., Yabashi, M., Bondar, A. N., Standfuss, J., Neutze, R. & Iwata, S. (2016). *Science*, **354**, 1552–1557.
- Neutze, R., Wouts, R., van der Spoel, D., Weckert, E. & Hajdu, J. (2000). *Nature*, **406**, 752–757.
- Palmer, G., Kellert, M., Wang, J., Emons, M., Wegner, U., Kane, D., Pallas, F., Jezynski, T., Venkatesan, S., Rompotis, D., Brambrink, E., Monoszlai, B., Jiang, M., Meier, J., Kruse, K., Pergament, M. & Lederer, M. J. (2019). *J. Synchrotron Rad.* **26**, 328–332.
- Pande, K., Hutchison, C. D., Groenhof, G., Aquila, A., Robinson, J. S., Tenboer, J., Basu, S., Boutet, S., DePonte, D. P., Liang, M., White, T. A., Zatssepin, N. A., Yefanov, O., Morozov, D., Oberthuer, D., Gati, C., Subramanian, G., James, D., Zhao, Y., Koralek, J., Brayshaw, J., Kupitz, C., Conrad, C., Roy-Chowdhury, S., Coe, J. D., Metz, M., Xavier, P. L., Grant, T. D., Koglin, J. E., Ketawala, G., Fromme, R., rajer, V., Henning, R., Spence, J. C., Ourmazd, A., Schwander, P., Weierstall, U., Frank, M., Fromme, P., Barty, A.,

- Chapman, H. N., Moffat, K., van Thor, J. J. & Schmidt, M. (2016). *Science*, **352**, 725–729.
- Pergament, M., Palmer, G., Kellert, M., Kruse, K., Wang, J., Wissmann, L., Wegner, U., Emons, M., Kane, D., Priebe, G., Venkatesan, S., Jezynski, T., Pallas, F. & Lederer, M. J. (2016). *Opt. Express*, **24**, 29349–29359.
- Pietrini, A., Bielecki, J., Timneanu, N., Hantke, M. F., Andreasson, J., Loh, N. D., Larsson, D. S. D., Boutet, S., Hajdu, J., Maia, F. R. N. C. & Nettelblad, C. (2018). *Commun. Phys.* **1**, 92.
- Redecke, L., Nass, K., DePonte, D. P., White, T. A., Rehders, D., Barty, A., Stellato, F., Liang, M., Barends, T. R. M., Boutet, S., Williams, G. J., Messerschmidt, M., Seibert, M. M., Aquila, A., Arnlund, D., Bajt, S., Barth, T., Bogan, M. J., Caleman, C., Chao, T.-C., Doak, R. B., Fleckenstein, H., Frank, M., Fromme, R., Galli, L., Grotjohann, I., Hunter, M. S., Johansson, L. C., Kassemeyer, S., Katona, G., Kirian, R. A., Koopmann, R., Kupitz, C., Lomb, L., Martin, A. V., Mogk, S., Neutze, R., Shoeman, R. L., Steinbrener, J., Timneanu, N., Wang, D., Weierstall, U., Zatsepin, N. A., Spence, J. C. H., Fromme, P., Schlichting, I., Duszynski, M., Betzel, C. & Chapman, H. N. (2013). *Science*, **339**, 227–230.
- Roedig, P., Ginn, H. M., Pakendorf, T., Sutton, G., Harlos, K., Walter, T. S., Meyer, J., Fischer, P., Duman, R., Vartiainen, I., Reime, B., Warmer, M., Brewster, A. S., Young, I. D., Michels-Clark, T., Sauter, N. K., Kotecha, A., Kelly, J., Rowlands, D. J., Sikorski, M., Nelson, S., Damiani, D. S., Alonso-Mori, R., Ren, J., Fry, E. E., David, C., Stuart, D. I., Wagner, A. & Meents, A. (2017). *Nat. Methods*, **14**, 805–810.
- Röllén, K., Granzin, J., Batra-Safferling, R. & Stadler, A. M. (2018). *Plos ONE*, **13**, e0200746.
- Rose, M., Bobkov, S., Ayer, K., Kurta, R. P., Dzhigaev, D., Kim, Y. Y., Morgan, A. J., Yoon, C. H., Westphal, D., Bielecki, J., Sellberg, J. A., Williams, G., Maia, F. R. N. C., Yefanov, O. M., Ilyin, V., Mancuso, A. P., Chapman, H. N., Hogue, B. G., Aquila, A., Barty, A. & Vartanyants, I. A. (2018). *IUCrJ*, **5**, 727–736.
- Schmidt, M. (2013). *Adv. Condens. Matter Phys.* **2013**, 167276.
- Schulz, J., Bielecki, J., Doak, R. B., Dörner, K., Graceffa, R., Shoeman, R. L., Sikorski, M., Thute, P., Westphal, D. & Mancuso, A. P. (2019). *J. Synchrotron Rad.* **26**, 339–345.
- SFX User Consortium (2013). *SFX user consortium*, [https://www.xfel.eu/facility/instruments/spb\\_sfx/sfx\\_user\\_consortium/index\\_eng.html](https://www.xfel.eu/facility/instruments/spb_sfx/sfx_user_consortium/index_eng.html).
- Sinn, H., Dommach, M., Dickert, B., Di Felice, M., Dong, X., Eidam, J., Finze, D., Freijo-Martin, I., Gerasimova, N., Kohlstrunk, N., La Civita, D., Meyn, F., Music, V., Neumann, M., Petrich, M., Rio, B., Samoylova, L., Schmidtchen, S., Stoermer, M., Trapp, A., Vannoni, M., Villanueva, R. & Yang, F. (2019). *J. Synchrotron Rad.* **26**, 000–000 [XQ5004].
- Sinn, H., Dommach, M., Dong, X., La Civita, D., Samoylova, L., Villanueva, R. & Yang, F. (2012). Technical Report XFEL EU TR-2012–006. The European XFEL, Hamburg, Germany.
- Stagno, J. R., Liu, Y., Bhandari, Y. R., Conrad, C. E., Panja, S., Swain, M., Fan, L., Nelson, G., Li, C., Wendel, D. R., White, T. A., Coe, J. D., Wiedorn, M. O., Knoska, J., Oberthuer, D., Tuckey, R. A., Yu, P., Dyba, M., Tarasov, S. G., Weierstall, U., Grant, T. D., Schwieters, C. D., Zhang, J., Ferré-D’Amaré, A. R., Fromme, P., Draper, D. E., Liang, M., Hunter, M. S., Boutet, S., Tan, K., Zuo, X., Ji, X., Barty, A., Zatsepin, N. A., Chapman, H. N., Spence, J. C. H., Woodson, S. A. & Wang, Y. X. (2016). *Nature*, **541**, 242–246.
- Stan, C. A., Milathianaki, D., Laksmono, H., Sierra, R. G., McQueen, T. A., Messerschmidt, M., Williams, G. J., Koglin, J. E., Lane, T. J., Hayes, M. J., Guillet, S. A. H., Liang, M., Aquila, A. L., Willmott, P. R., Robinson, J. S., Gumerlock, K. L., Botha, S., Nass, K., Schlichting, I., Shoeman, R. L., Stone, H. A. & Boutet, S. (2016). *Nat. Phys.* **12**, 966–971.
- Standfuss, J. & Spence, J. (2017). *IUCrJ*, **4**, 100–101.
- Suga, M., Akita, F., Hirata, K., Ueno, G., Murakami, H., Nakajima, Y., Shimizu, T., Yamashita, K., Yamamoto, M., Ago, H. & Shen, J.-R. (2014). *Nature*, **517**, 99–103.
- Telada, S. (2009). *J. Vac. Soc. Jpn.* **52**, 347–350.
- Tenboer, J., Basu, S., Zatsepin, N., Pande, K., Milathianaki, D., Frank, M., Hunter, M., Boutet, S., Williams, G. J., Koglin, J. E., Oberthuer, D., Heymann, M., Kupitz, C., Conrad, C., Coe, J., Roy-Chowdhury, S., Weierstall, U., James, D., Wang, D., Grant, T., Barty, A., Yefanov, O., Scales, J., Gati, C., Seuring, C., Srajer, V., Henning, R., Schwander, P., Fromme, R., Ourmazd, A., Moffat, K., Van Thor, J. J., Spence, J. C. H., Fromme, P., Chapman, H. N. & Schmidt, M. (2014). *Science*, **346**, 1242–1246.
- The AGIPD Consortium (2012). Adaptive Gain Integrating Pixel Detector (AGIPD): System Parameters. The AGIPD Consortium.
- Tono, K., Kudo, T., Yabashi, M., Tachibana, T., Feng, Y., Fritz, D., Hastings, J. & Ishikawa, T. (2011). *Rev. Sci. Instrum.* **82**, 023108.
- Tono, K., Togashi, T., Inubushi, Y., Sato, T., Katayama, T., Ogawa, K., Ohashi, H., Kimura, H., Takahashi, S., Takeshita, K., Tomizawa, H., Goto, S., Ishikawa, T. & Yabashi, M. (2013). *New J. Phys.* **15**, 083035.
- Tschentscher, T., Bressler, C., Grünert, J., Madsen, A., Mancuso, A. P., Meyer, M., Scherz, A., Sinn, H. & Zastra, U. (2017). *Appl. Sci.*, **7**, 592.
- Weierstall, U., James, D., Wang, C., White, T. A., Wang, D., Liu, W., Spence, J. C., Bruce Doak, R., Nelson, G., Fromme, P., Fromme, R., Grotjohann, I., Kupitz, C., Zatsepin, N. A., Liu, H., Basu, S., Wacker, D., Won Han, G., Katritch, V., Boutet, S., Messerschmidt, M., Williams, G. J., Koglin, J. E., Marvin Seibert, M., Klinker, M., Gati, C., Shoeman, R. L., Barty, A., Chapman, H. N., Kirian, R. A., Beyerlein, K. R., Stevens, R. C., Li, D., Shah, S. T. A., Howe, N., Caffrey, M. & Cherezov, V. (2014). *Nat. Commun.* **5**, 3309.
- Wiedorn, M. O., Oberthür, D., Bean, R., Schubert, R., Werner, N., Abbey, B., Aepfelbacher, M., Adriano, L., Allahgholi, A., Al-Qudami, N., Andreasson, J., Aplin, S., Awel, S., Ayer, K., Bajt, S., Barák, I., Bari, S., Bielecki, J., Botha, S., Boukhelef, D., Brehm, W., Brockhauser, S., Cheviakov, I., Coleman, M. A., Cruz-Mazo, F., Danilevski, C., Darmanin, C., Doak, R. B., Domaracky, M., Dörner, K., Du, Y., Fangohr, H., Fleckenstein, H., Frank, M., Fromme, P., Gañán-Calvo, A. M., Gevorkov, Y., Giewekemeyer, K., Ginn, H. M., Graafsma, H., Graceffa, R., Greiffenberg, D., Gumprecht, L., Göttlicher, P., Hajdu, J., Hauf, S., Heymann, M., Holmes, S., Horke, D. A., Hunter, M. S., Imlau, S., Kaukher, A., Kim, Y., Klyuev, A., Knoška, J., Kobe, B., Kuhn, M., Kupitz, C., Küpper, J., Lahey-Rudolph, J. M., Laurus, T., Le Cong, K., Letrun, R., Xavier, P. L., Maia, L., Maia, F. R. N. C., Mariani, V., Messerschmidt, M., Metz, M., Mezza, D., Michelat, T., Mills, G., Monteiro, D. C. F., Morgan, A., Mühlig, K., Munke, A., Münnich, A., Nette, J., Nugent, K. A., Nuguid, T., Orville, A. M., Pandey, S., Pena, G., Villanueva-Perez, P., Poehlsen, J., Previtali, G., Redecke, L., Riekehr, W. M., Rohde, H., Round, A., Safenreiter, T., Sarrou, I., Sato, T., Schmidt, M., Schmitt, B., Schönherr, R., Schulz, J., Sellberg, J. A., Seibert, M. M., Seuring, C., Shelby, M. L., Shoeman, R. L., Sikorski, M., Silenzi, A., Stan, C. A., Shi, X., Stern, S., Sztuk-Dambietz, J., Szuba, J., Tolstikova, A., Trebbin, M., Trunk, U., Vagovic, P., Ve, T., Weinhausen, B., White, T. A., Wrona, K., Xu, C., Yefanov, O., Zatsepin, N., Zhang, J., Perbandt, M., Mancuso, A. P., Betzel, C., Chapman, H. & Barty, A. (2018). *Nat. Commun.* **9**, 4025.



# Megahertz x-ray microscopy at x-ray free-electron laser and synchrotron sources

PATRIK VAGOVIČ,<sup>1,2,3,\*</sup> TOKUSHI SATO,<sup>1,2</sup> LADISLAV MIKEŠ,<sup>2</sup> GRANT MILLS,<sup>2</sup> RITA GRACEFFA,<sup>2</sup> FRANS MATTSSON,<sup>4</sup> PABLO VILLANUEVA-PEREZ,<sup>4,1</sup> ALEXEY ERSHOV,<sup>5</sup> TOMÁŠ FARAGÓ,<sup>5</sup> JOZEF ULIČNÝ,<sup>6</sup> HENRY KIRKWOOD,<sup>2</sup> ROMAIN LETRUN,<sup>2</sup> RAJMUND MOKSO,<sup>4</sup> MARIE-CHRISTINE ZDORA,<sup>7,8,9</sup> MARGIE P. OLBINADO,<sup>10</sup> ALEXANDER RACK,<sup>10</sup> TILO BAUMBACH,<sup>5</sup> JOACHIM SCHULZ,<sup>2</sup> ALKE MEENTS,<sup>1</sup> HENRY N. CHAPMAN,<sup>1</sup> AND ADRIAN P. MANCUSO<sup>2,11</sup>

<sup>1</sup>Center for Free-Electron Laser, Notkestraße 85, 22607 Hamburg, Germany

<sup>2</sup>European XFEL, Holzkoppel 4, 22869 Schenefeld, Germany

<sup>3</sup>Institute of Physics, Academy of Sciences of the Czech Republic v.v.i., Na Slovance 2, 182 21, Praha 8, Czech Republic

<sup>4</sup>Lund University, Sweden

<sup>5</sup>Institute for Photon Science and Synchrotron Radiation, Karlsruhe Institute of Technology (KIT), Hermann-von-Helmholtz-Platz 1, 76344 Eggenstein-Leopoldshafen, Germany

<sup>6</sup>Faculty of Science, Department of Biophysics, P. J. Šafárik University, Jesenná 5, 04154 Košice, Slovakia

<sup>7</sup>Diamond Light Source, Harwell Science and Innovation Campus, Didcot, Oxfordshire OX11 0DE, UK

<sup>8</sup>Department of Physics & Astronomy, University College London, London, WC1E 6BT, UK

<sup>9</sup>Department of Physics & Astronomy, University of Southampton, Southampton SO17 1BJ, UK

<sup>10</sup>ESRF – The European Synchrotron, 71 Avenue des Martyrs, 38000 Grenoble, France

<sup>11</sup>Department of Chemistry and Physics, La Trobe Institute for Molecular Science, La Trobe University, Melbourne, Victoria 3086, Australia

\*Corresponding author: patrik.vagovic@xfel.eu

Received 13 June 2019; revised 22 July 2019; accepted 26 July 2019 (Doc. ID 369962); published 23 August 2019

**Modern emerging technologies, such as additive manufacturing, bioprinting, and new material production, require novel metrology tools to probe fundamental high-speed dynamics happening in such systems. Here we demonstrate the application of the megahertz (MHz) European X-ray Free-Electron Laser (EuXFEL) to image the fast stochastic processes induced by a laser on water-filled capillaries with micrometer-scale spatial resolution. The EuXFEL provides superior contrast and spatial resolution compared to equivalent state-of-the-art synchrotron experiments. This work opens up new possibilities for the characterization of MHz stochastic processes on the nanosecond to microsecond time scales with object velocities up to a few kilometers per second using XFEL sources.** © 2019 Optical Society of America under the terms of the OSA Open Access Publishing Agreement

<https://doi.org/10.1364/OPTICA.6.001106>

Hard x-ray beams are well suited for microscopic two-dimensional (2D) and three-dimensional (3D) imaging of samples not transparent to visible light due to their high penetration power. Over the last two decades, the field of x-ray imaging has developed considerably, mainly due to the availability of modern third-generation synchrotrons producing x rays of high brilliance [1]. These sources have provided access to the structural determination of specimens down to nanometer-scale resolutions. Exploiting the (partial) spatial coherence of synchrotron x-ray

probes, several phase-sensitive techniques have been developed providing access to the electron density of specimens either via x-ray optical analyzers [2–4] or sophisticated algorithms [5,6]. While much attention has been paid to improving the spatial resolution of x-ray imaging to its limits, fewer resources have been used to explore the boundaries of the temporal domain. With the progress in the development of detectors over the last decade [7], fast radiography and tomography with kilohertz frame rates are available, allowing, for example, ~100 tomograms per second [8,9]. Only relatively recently has the stroboscopic nature of synchrotrons been exploited. For example, imaging with synchronized or individual x-ray pulses applied to fast stochastic transient processes has been demonstrated [10–12]. Further advancement of ultrafast x-ray imaging could be introduced by megahertz (MHz) x-ray free-electron laser (XFEL) sources, where the high flux per pulse can reveal dynamics of stochastic processes with velocities up to the scale of several kilometers per second with submicron-scale resolutions with high sensitivity to projected densities. In this work, we exploit the unique properties of the first operational hard x-ray MHz XFEL source European XFEL (EuXFEL) and explore its possibilities for ultrafast x-ray microscopy with MHz sampling. The laser-induced dynamic processes in an open-ended glass capillary filled with water was used as a dynamic sample. We use this simple model system to show the advantages of microsecond temporal resolution, micrometer spatial resolution, and the improved signal-to-noise in the images all brought about by using a MHz repetition rate XFEL. We compare the results obtained at EuXFEL to that at European

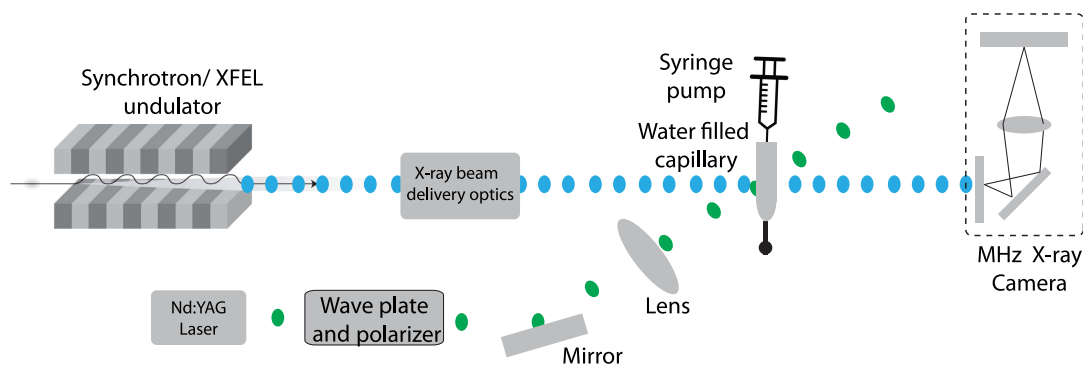


**Fig. 1.** Schematics of the time-resolved MHz x-ray microscopy of laser-induced dynamics in a water-filled glass capillary.

Synchrotron Radiation Facility (ESRF) ID19 beamline with the setup depicted in Fig. 1. The first results obtained at EuXFEL are already comparable to the state-of-the-art synchrotron performance [12] and are still subject to improvement. Further developments will allow for improving the spatial resolution beyond the reach of most brilliant synchrotron sources with potential acquisition of 3D MHz movies by employing x-ray multiprojection imaging [13].

It has been reported that liquid jets with velocities as high as 850 m/s can be generated by focusing a visible light laser into a capillary filled with water [14]. A jet based on this principle may be considered for needle-free drug-delivery injection or for sample delivery applications at MHz XFEL sources as a jet on demand, which can significantly minimize the sample usage. The characterization of the laser-induced jets and fluidics on the nanosecond to microsecond time scales is typically done by visible light microscopy. However, details on the microstructure are difficult or impossible to access with light microscopy due to the large refraction angle and strong multiple light scattering at the interfaces caused, for example, by microcavitations [15]. To explore the dynamics induced by the focused frequency-doubled Nd:YAG laser (Minilite II, Continuum) in the glass capillaries filled with water, we constructed conceptually similar time-resolved microscopy setups at the ID19 beamline at ESRF and at the Single Particles, Clusters and Biomolecules and Serial Femtosecond Crystallography (SPB/SFX) instrument of the EuXFEL using an indirect scintillator-based detector coupled to the MHz frame transfer CMOS camera SHIMADZU HPV-X2 schematically depicted in Fig. 1.

For the experiment at EuXFEL, we used the SPB/SFX instrument [16]. For the x-ray microscopy measurements, we reused the spent beam from the upstream interaction region and was outcoupled into air via a 180  $\mu\text{m}$  thick diamond window. A photon energy of 9.3 keV was used, and the pulse train was filled with 128 x-ray pulses with a repetition rate of 1.128 MHz. The effective pixel size of the imaging system was 3.2  $\mu\text{m}$  (see Supplement 1).

For the experiment at the ESRF synchrotron, we used the 16-bunch filling mode, providing a bunch separation of 176 ns; the MHz camera was recording every third frame with an interframe time of 530 ns. The harmonics of the undulator with central photon energy 32 keV were conditioned by a set of 1D compound refractive lenses to enhance the flux density at the detector. The effective pixel size of the imaging system was 8  $\mu\text{m}$  (see Supplement 1).

Stable jetting conditions were achieved at ESRF, with an incident laser pulse energy of 2 mJ and approximately 0.05 total absorbency of the laser power in water mixed with Nile blue dye, resulting in approximately 100  $\mu\text{J}$  absorbed energy per pulse. This was enough to form the repeatable jet [Fig. 3(a)]. This result is consistent with previous reported results [14]. The measured water jet speed is 184 m/s, and the wall velocity of the laser cavity expanding wall reaches 272 m/s. The transformation of the meniscus into the jet during first frames is also clearly visible with clear detail. Due to limited time during the EuXFEL experiment, jetting conditions were not achieved. However, due to the high contrast achieved and high spatial resolution, the microstructure of the laser interaction with the sample is revealed with great detail (Fig. 2), which is not possible by visible light microscopy. To compare quantitatively the imaging performance for both experiments, we used a signal-to-noise ratio (SNR) analysis and power spectrum analysis. Detailed description about applied analysis is described in the supplementary document. As a result, the SNR analyzed for both ESRF and EuXFEL sequences show almost 2 times higher values for the maximum SNR from each analyzed sequence for EuXFEL with SNR = 10.69 and for ESRF with SNR = 6.19 [Figs. 3(b) and 3(d)]. A more objective comparison using spectral power [Fig. 3(c)] clearly indicates the superior performance of EuXFEL microscopy over ESRF. However, stronger fluctuation in the mean values and SNR are observed for XFEL data. This is a natural behavior of XFEL beams and is related to the origin of x-ray pulse generation using the self-amplified spontaneous emission (SASE) process. Such fluctuations are the reason for the lack of a procedure for correct data normalization, as every sequence and pulse has a different intensity distribution. Simple normalization of such data leads to image flickering and the increase of the standard deviation of the signal. Another contribution responsible for the increase of the standard deviation for the actual EuXFEL data is attributed to the high-frequency noise caused by the focusing kilobyte optics. To remove normalization artifacts and high-frequency noise for the EuXFEL data, we performed an adaptive high-pass filtering by subtracting a low-pass filtered (Gaussian convolution with the standard deviation  $\sigma = 5$  pixels) image from its original version. This procedure significantly suppressed spatiotemporal image flickering. Using such image processing, we visualized the velocities of breaking glass reaching 35 m/s using flow analysis based on variational optical flow methods [17]. The computed velocities provide quantitative information about complex kinematics of the burst process

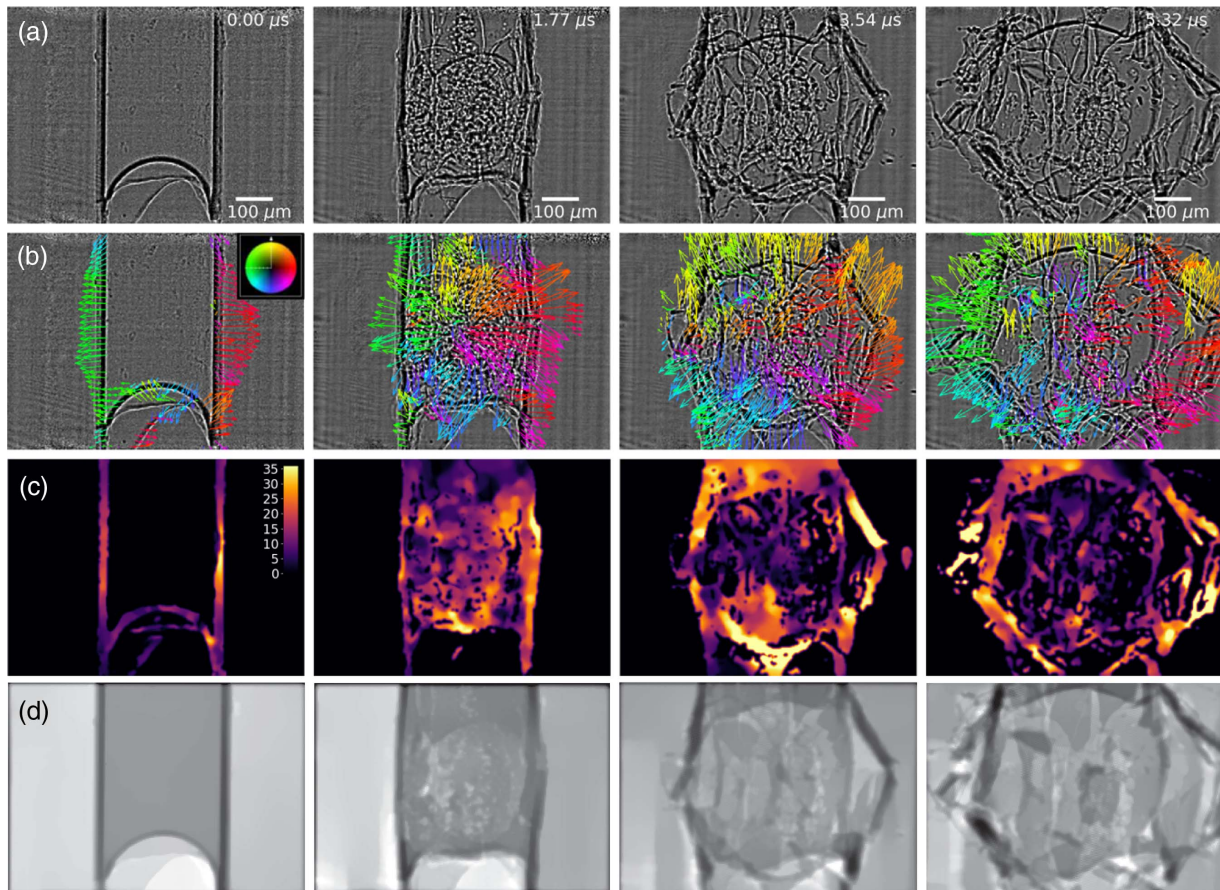


**Fig. 2.** Image sequence of laser-driven explosion of a capillary filled with water imaged at EuXFEL. Sequence (a) is the result of high-pass adaptive filtering to remove the high-frequency noise and image flickering; sequences (b) and (c) are the result of optical flow analysis [17] shown as a directional vector for the movement of debris (b) and the velocity maps (c) (see Visualization 1). The phase retrieval of the corresponding sequence (d) is performed using an ADMM-CTF algorithm [18].

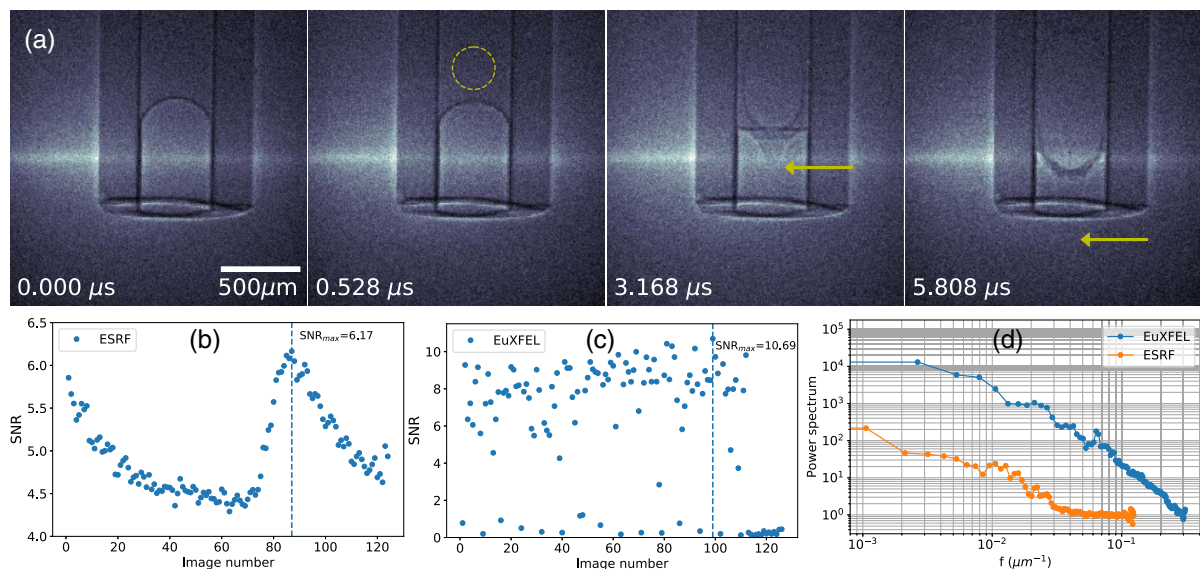


**Fig. 3.** (a) Image sequence of a water jet generated by absorbed power ( $\sim 2$  mJ pulse energy) of a focused visible-light laser inside the glass capillary (see Visualization 2) imaged at the ESRF synchrotron. The circle on the second frame shows the laser-induced cavitation with radius of 144 μm indicating an initial velocity of 272 m/s of the expanding wall. The arrows on the third and fourth frame indicate the tip of the water jet reaching a velocity of 184 m/s. The signal to noise analysis for (b) ESRF and (c) EuXFEL and (d) power spectrum curves shows superior image performance of EuXFEL data. For detailed description of SNR (b) and (c) and power spectrum analysis (d), see Supplement 1 for supporting content.

(see Supplement 1 for supporting content). The high spatial coherence of XFEL data allowed us to apply a contrast-transfer function (CTF)-based phase-retrieval method utilizing the alternating direction method of multipliers (ADMM) [18]. The high spatial coherence of XFEL data allowed us to apply a contrast-transfer function (CTF)-based phase-retrieval method utilizing the alternating direction method of multipliers (ADMM) [18], shown in Fig. 2(d). Here the data were first normalized using a set of empty beam sequences; then the ADMM-CTF phase-retrieval algorithm was applied. High-frequency noise introduced by this process was removed by nonlocal-means denoising [19]. ADMM-CTF phase retrieval of the synchrotron data failed to provide meaningful phase reconstruction, which is attributed to the weak signal.

In conclusion, we have successfully demonstrated x-ray microscopy sampled at greater than 1 MHz at EuXFEL, and with the full performance of EuXFEL, maximum frame-rate of 4.5 MHz will be achievable. Our model system shows a significant improvement in the contrast of the data obtained at EuXFEL compared to data obtained at ESRF. This is due to the much higher photon flux per pulse as well as the much higher spatial coherence at EuXFEL. Such performance at EuXFEL additionally allowed for a 2.5-fold increase in the spatial resolution and a significant improvement in power spectrum over the entire range of frequencies, which enabled us to apply a single-distance phase-retrieval algorithm. This study opens up new perspectives for imaging, especially of irreversible stochastic processes not accessible via visible light imaging or with less intense x-ray sources. At hard x-ray MHz rate XFEL facilities, this method enables the observation of stochastic object motions at high velocities on the order of meters per second to several kilometers per second. High flux per pulse at EuXFEL will enable 3D MHz rate microscopy by employing beam splitters, which is the scope of our future development.

**Funding.** Bundesministerium für Bildung und Forschung (BMBF) (05K18XXA); Vetenskapsrådet (VR) (2017-06719).

**Acknowledgment.** We acknowledge Klaus Giewekemeyer, Luis Morillo Lopez, Cedric Michel Signe Takem, Alexis Legrand, Bradley Manning, and Nadja Reimers for technical support during preparation of the EuXFEL experiment. Beamtime was granted at ESRF beamline ID19 in the frame of proposal MI-1267.






See Supplement 1 for supporting content.

## REFERENCES

1. C. Kunz, *J. Phys. Condens. Matter* **13**, 7499 (2001).
2. U. Bonse and M. Hart, *Appl. Phys. Lett.* **6**, 155 (1965).
3. D. Chapman, W. Thomlinson, R. E. Johnston, D. Washburn, E. Pisano, N. Gmür, Z. Zhong, R. Menk, F. Arfelli, and D. Sayers, *Phys. Med. Biol.* **42**, 2015 (1997).
4. C. David, B. Nöhammer, H. H. Solak, and E. Ziegler, *Appl. Phys. Lett.* **81**, 3287 (2002).
5. D. Paganin, S. C. Mayo, T. E. Gureyev, P. R. Miller, and S. W. Wilkins, *J. Microsc.* **206**, 33 (2002).
6. J. M. Rodenburg and H. M. L. Faulkner, *Appl. Phys. Lett.* **85**, 4795 (2004).
7. T. Hatsui and H. Graafsma, *IUCrJ* **2**, 371 (2015).
8. R. Mokso, C. M. Schlepütz, G. Theidel, H. Billich, E. Schmid, T. Celcer, G. Mikuljan, L. Sala, F. Marone, N. Schlumpf, and M. Stampanoni, *J. Synchrotron Radiat.* **24**, 1250 (2017).
9. W. Yashiro, D. Noda, and K. Kajiwara, *Appl. Phys. Express* **10**, 052501 (2017).
10. K. Fezzaa and Y. Wang, *Phys. Rev. Lett.* **100**, 104501 (2008).
11. M. P. Olbinado, X. Just, J.-L. Gelet, P. Lhuissier, M. Scheel, P. Vagovic, T. Sato, R. Graceffa, J. Schulz, A. Mancuso, J. Morse, and A. Rack, *Opt. Express* **25**, 13857 (2017).
12. N. D. Parab, C. Zhao, R. Cunningham, L. I. Escano, K. Fezzaa, W. Everhart, A. D. Rollett, L. Chen, and T. Sun, *J. Synchrotron Radiat.* **25**, 1467 (2018).
13. P. Villanueva-Perez, B. Pedrini, R. Mokso, P. Vagovic, V. A. Guzenko, S. J. Leake, P. R. Willmott, P. Obera, C. David, H. N. Chapman, and M. Stampanoni, *Optica* **5**, 1521 (2018).
14. Y. Tagawa, N. Oudalov, C. W. Visser, I. R. Peters, D. van der Meer, C. Sun, A. Prosperetti, and D. Lohse, *Phys. Rev. X* **2**, 031002 (2012).
15. D. Hudgins and R. S. Abhari, *Phys. Rev. E* **99**, 031102 (2019).
16. A. P. Mancuso, A. Aquila, L. Batchelor, R. J. Bean, J. Bielecki, G. Borchers, K. Doerner, K. Giewekemeyer, R. Graceffa, O. D. Kelsey, Y. Kim, H. J. Kirkwood, A. Legrand, R. Letrun, B. Manning, L. L. Morillo, M. Messerschmidt, G. Mills, S. Raabe, N. Reimers, A. Round, T. Sato, J. Schulz, C. S. Takem, M. Sikorski, S. Stern, P. Thute, P. Vagovič, B. Weinhausen, and T. Tschentscher, *J. Synchrotron Radiat.* **26**, 660 (2019).
17. A. Myagotin, A. Ershov, L. Helfen, R. Verdejo, A. Belyaev, and T. Baumbach, *J. Synchrotron Radiat.* **19**, 483 (2012).
18. P. Villanueva-Perez, F. Arcadu, P. Cloetens, and M. Stampanoni, *Opt. Lett.* **42**, 1133 (2017).
19. A. Buades, B. Coll, and J.-M. Morel, *Image Processing On Line* **1**, 208 (2011).



# Femtosecond timing synchronization at megahertz repetition rates for an x-ray free-electron laser

TOKUSHI SATO,<sup>1,2,†,\*</sup>  ROMAIN LETRUN,<sup>2,†</sup>  HENRY J. KIRKWOOD,<sup>2,†</sup>  JIA LIU,<sup>2,8,†</sup>   
 PATRIK VAGOVIČ,<sup>1,2,3</sup> GRANT MILLS,<sup>2</sup> YOONHEE KIM,<sup>2</sup> CEDRIC M. S. TAKEM,<sup>2</sup> MARC PLANAS,<sup>2</sup>  
 MORITZ EMONS,<sup>2</sup> TOMASZ JEZYNSKI,<sup>2</sup> GUIDO PALMER,<sup>2</sup> MAX LEDERER,<sup>2</sup> SEBASTIAN SCHULZ,<sup>4</sup>  
 JOST MUELLER,<sup>4</sup> HOLGER SCHLARF,<sup>4</sup> ALESSANDRO SILENZI,<sup>2</sup> GABRIELE GIOVANETTI,<sup>2</sup>  
 ANDREA PARENTI,<sup>2</sup> MARTIN BERGEMANN,<sup>2</sup> THOMAS MICHELAT,<sup>2</sup> JANUSZ SZUBA,<sup>2</sup> JAN GRÜNERT,<sup>2</sup>  
 HENRY N. CHAPMAN,<sup>1,5,6</sup>  AND ADRIAN P. MANCUSO<sup>2,7</sup>

<sup>1</sup>Center for Free-Electron Laser Science, Deutsches Elektronen-Synchrotron DESY, Notkestrasse 85, 22607 Hamburg, Germany

<sup>2</sup>European XFEL, Holzkoppel 4, 22869 Schenefeld, Germany

<sup>3</sup>Institute of Physics, Academy of Sciences of the Czech Republic v.v.i., Na Slovance 2, 182 21, Praha 8, Czech Republic

<sup>4</sup>Deutsches Elektronen-Synchrotron DESY, Notkestrasse 85, 22607 Hamburg, Germany

<sup>5</sup>Department of Physics, Universität Hamburg, Luruper Chaussee 149, Hamburg, Germany

<sup>6</sup>The Hamburg Center for Ultrafast Imaging, Universität Hamburg, Luruper Chaussee 149, Hamburg, Germany

<sup>7</sup>Department of Chemistry and Physics, La Trobe Institute for Molecular Science, La Trobe University, Melbourne, Victoria 3086, Australia

<sup>8</sup>e-mail: jia.liu@xfel.eu

\*Corresponding author: tokushi.sato@xfel.eu

Received 5 May 2020; accepted 7 May 2020 (Doc. ID 396728); published 17 June 2020

**A critical challenge of pump-probe experiments with x-ray free-electron lasers (XFELs) is accurate synchronization of x-ray and optical pulses. At the European XFEL we observed megahertz rate timing jitter of  $24.0 \pm 12.4$  fs.**

Published by The Optical Society under the terms of the [Creative Commons Attribution 4.0 License](https://creativecommons.org/licenses/by/4.0/). Further distribution of this work must maintain attribution to the author(s) and the published article's title, journal citation, and DOI.

<https://doi.org/10.1364/OPTICA.396728>

The emergence of x-ray free-electron lasers (XFELs) operating at photon energies of around 10 keV (hard x-rays) over the past decade has opened up new possibilities for the physical, chemical, and biological sciences due to their high brightness and femtosecond (fs) pulses [1]. These intense and ultrashort x-ray pulses are used to record so-called molecular movies on fs time scales using a pump-probe (PP) measurement to achieve both high temporal and spatial resolution—a necessary step to truly understand the dynamics of matter. One of the greatest difficulties to achieve fs time resolution in PP experiments is the shot-to-shot timing jitter, which can be hundreds of fs in XFELs [2]. Therefore, the temporal resolution of an experiment may be severely limited by the timing jitter if the relative PP delay time is not monitored on a single-shot basis, prohibiting studies of fs dynamics. Unlike other hard x-ray FELs so far, which have been operating at  $\leq 120$  Hz, the European XFEL (EuXFEL) has been designed to deliver up to 27,000 pulses per second at megahertz (MHz) repetition rates with burst operation [1]. In order to fully benefit from the increased

number of x-ray pulses that the EuXFEL can provide for PP experiments, a unique optical PP laser system was developed to deliver pulses as short as 15 fs with a burst structure matching that of the x-rays while maintaining minimal jitter between the XFEL and the optical laser using an optical synchronization system [3].

Characterization of the PP jitter at MHz repetition rate in the hard x-ray regime, which is presented here, was made possible with the installation of the photon arrival time monitor (PAM) at the Single Particles, Clusters, and Biomolecules and Serial Femtosecond Crystallography (SPB/SFX) instrument [4]. The PAM uses the spectral encoding technique that has already been successfully applied at other hard x-ray FELs [5] at up to 120 Hz. A 100  $\mu\text{m}$  thick Ce:YAG was utilized as a target sample. Two GOTTHARD (Gain Optimizing microSTrip sysTEM with Analog ReaDout) detectors [6] operating at 564 kHz recorded alternating optical pulses in each MHz pulse train. Using radiofrequency (RF) pre-lock synchronization [7], the inter-train RMS jitter was measured to be  $279 \pm 32$  fs. Figure 1 shows the relative time of arrival of x-ray and optical pulses using the RF and optical synchronization (OS) systems. An extremely low inter-train RMS jitter of 24.0 fs with an uncertainty of 12.4 fs was observed over a period of 10 min using OS [Fig. 1]. Additionally, measurements over a period of 2 h show no significant slow drift while using OS. These results demonstrate a significant advance towards fs PP experiments at MHz repetition rates.

In conclusion, the spectral encoding technique was developed for operation in the hard x-ray regime at a MHz repetition rate. The PP inter- and intra-train timing jitter was characterized at the EuXFEL with optical synchronization. Since the previous report [7], the inter-train RMS jitter has been reduced by 1 order of magnitude, down to 24.0 fs with 12.4 fs uncertainty, which

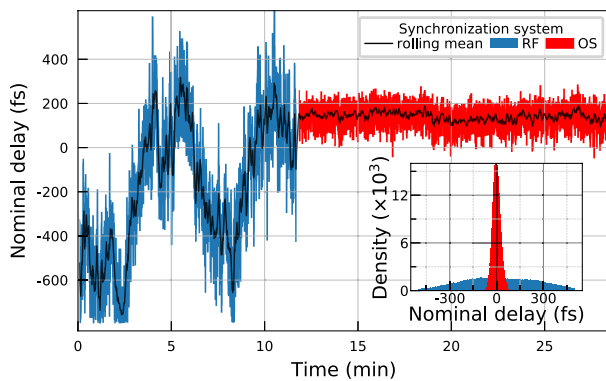


**Fig. 1.** The black line shows the rolling mean over a 5 s window. The inset shows a histogram of the relative arrival times using 100 x-ray pulses per train (10 Hz inter-train and 1.128 MHz intra-train repetition rates) with RF synchronization (blue, 854,430 pulses) measured using a 3.1 ps temporal window and optical synchronization (red, 431,300 x-ray pulses) measured using a 1.2 ps temporal window.

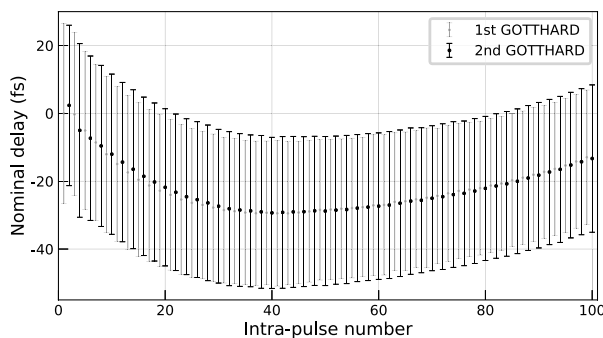


**Fig. 2.** Arrival time for each pulse with respect to the first pulse in its train when averaging over 5000 x-ray trains. The error bars show the standard deviation for each pulse in the train over a period of about 500 s.

can be attributed to the OS system and improved optical laser beam transport. Furthermore, the intra-train jitter was measured at 1.128 MHz repetition rate using a device that is available for users of the SPB/SFX instrument [Fig. 2]. Our work highlights the importance of the OS for future PP studies at high repetition rate and ultrashort x-ray sources. Owing to the excellent synchronization between the XFEL and the PP laser at EuXFEL, experiments requiring a temporal resolution above 100 fs will not require the conventional “measure and sort” approach and can thus be performed much more readily.

**Funding.** Helmholtz Association Strategic Investment funds; BioXFEL Science and Technology Center (STC-1231306); Max Planck Society for Medical Research; Australian Nuclear Science and Technology Organisation; Australian Research Council Center of Excellence in Advanced Molecular Imaging (CE140100011); Stiftelsen för Strategisk Forskning; Röntgen-Ångström Cluster; Knut och Alice Wallenbergs Stiftelse; Vetenskapsrådet (822-2013-2014); Ministerstvo školstva, vedy, výskumu a športu Slovenskej republiky; Bundesministerium für Bildung und Forschung (05E13GU1, 05K13GU7); Wellcome Trust.

**Acknowledgment.** We acknowledge European XFEL GmbH in Schenefeld, Germany, for provision of x-ray free-electron laser beamtime at the SPB/SFX instrument, and we thank the instrument group and facility staff for their great assistance. We thank T. Katayama and S. Owada for fruitful discussions.

**Disclosures.** The authors declare no conflicts of interest.

<sup>†</sup>These authors contributed equally to this work.

## REFERENCES

1. B. W. J. McNeil and N. R. Thompson, *Nat. Photonics* **4**, 814 (2010).
2. J. M. Glowina, K. Gumerlock, H. T. Lemke, T. Sato, D. Zhu, and M. Chollet, *J. Synchrotron Radiat.* **26**, 685 (2019).
3. G. Palmer, M. Kellert, J. Wang, M. Emons, U. Wegner, D. Kane, F. Pallas, T. Jezynski, S. Venkatesan, D. Rompotis, E. Brambrink, B. Monoszlai, M. Jiang, J. Meier, K. Kruse, M. Pergament, and M. J. Lederer, *J. Synch. Radiat.* **26**, 328 (2019).
4. A. P. Mancuso, A. Aquila, L. Batchelor, R. J. Bean, J. Bielecki, G. Borchers, K. Doerner, K. Giewekemeyer, R. Graceffa, O. D. Kelsey, Y. Kim, H. J. Kirkwood, A. Legrand, R. Letrun, B. Manning, L. Lopez Morillo, M. Messerschmidt, G. Mills, S. Raabe, N. Reimers, A. Round, T. Sato, J. Schulz, C. Signe Takem, M. Sikorski, S. Stern, P. Thute, P. Vagovič, B. Weinhausen, and T. Tschentscher, *J. Synch. Radiat.* **26**, 660 (2019).
5. M. R. Bionta, H. T. Lemke, J. P. Cryan, J. M. Glowina, C. Bostedt, M. Cammarata, J.-C. Castagna, Y. Ding, D. M. Fritz, A. R. Fry, J. Krzywinski, M. Messerschmidt, S. Schorb, M. L. Swiggers, and R. N. Coffee, *Opt. Express* **19**, 21855 (2011).
6. A. Mozzanica, A. Bergamaschi, R. Dinapoli, H. Graafsma, D. Greiffenberg, B. Henrich, I. Johnson, M. Lohmann, R. Valeria, B. Schmitt, and S. Xintian, *J. Instrum.* **7**, C01019 (2012).
7. H. J. Kirkwood, R. Letrun, T. Tanikawa, J. Liu, M. Nakatsutsumi, M. Emons, T. Jezynski, G. Palmer, M. Lederer, R. Bean, J. Buck, S. D. D. Cafisio, R. Graceffa, J. Grünert, S. Göde, H. Höppner, Y. Kim, Z. Konopkova, G. Mills, M. Makita, A. Pelka, T. R. Preston, M. Sikorski, C. M. S. Takem, K. Giewekemeyer, M. Chollet, P. Vagovič, H. N. Chapman, A. P. Mancuso, and T. Sato, *Opt. Lett.* **44**, 1650 (2019).